A Petrophysical Joint Inversion of Magnetotelluric and Gravity Data for Enhanced Subsurface Imaging of Sedimentary Environments

by

Rachel E. Maier

Thesis submitted for the degree of
Doctor of Philosophy
in
The University of Adelaide
School of Earth and Environmental Sciences
January, 2011

for Norbert A. Maier
1950-2007

Contents

Abstract

An emerging field in geophysics is that of joint inversions, in which multiple technique data sets are analysed and inverted simultaneously. This helps to integrate the complementary data sets and reduce model ambiguity, common in single technique inversions. In this thesis a new implementation of a magnetotelluric (MT) and gravity 2D joint inversion scheme is developed based on a petrophysical approach. In sedimentary rock environments, electrical conductivity (which underpins the MT technique) can be approximated by Archie's Law, whereas density (which underpins the gravity technique) can be derived from the porosity-density relationship. Since both expressions are themselves dependent on porosity, this petrophysical property provides the crucial link exploited by the 2D joint inversion. The 2D joint inversion approach devised here inverts directly for a porosity model, which is converted to resistivity and density models through Archie's Law and the porosity-density relationship, then constrained (fitted) by the MT and gravity data. Thus, a single porosity model is produced that satisfies both data sets.

By means of synthetic data inversions, it was established that the joint inversion is more effective in reproducing the true subsurface model than can be achieved by an MT or gravity inversion alone. Models produced by the joint inversion show improved placement of subsurface features and a greater accuracy of reconstructing the original subsurface (physical property) values. For optimal joint inversion results, broadband MT data should be used in favour of long period MT data, and the number of gravity stations should be greater than or equal to the number of MT stations. The joint inversion is particularly useful in extracting coherent information from noisy MT data when combined with good quality gravity data. While evaluating the MT and gravity compatibility, a new method was developed for evaluating

the information contained in the MT Jacobian (sensitivity) matrix.

The Renmark Trough in South Australia is an area of current geothermal interest for which multi-technique data (seismic, gravity, MT) exists. These field data were used to demonstrate and verify the effective use of the joint inversion in a practical real-world example. The Renmark Trough is a half graben structure with the Hamley Fault delineating the north-east boundary. At the Hamley Fault, the base of the trough is 3.5 km deep and rises gradually in a south-west direction. The inversion of the MT data alone produced a model inconsistent with seismic knowledge of the basement depths and geometries. In contrast, the joint inversion yielded a more geologically accurate image of the trough and faithfully reconstructed the basement depths and geometries.

In the process of developing the joint inversion scheme, a 2D gravity inversion algorithm, based on the Occam maximum smoothness approach, was produced. This inversion algorithm demonstrated the inherent non-uniqueness of gravity interpretation by only placing strong density contrasts at the surface. Attempts to improve the gravity inversion results, such as the use of depth weighting functions and fixing structure locations in parts of the model, were not as effective as the joint inversion in producing an accurate representation of the subsurface.

Statement of Originality

This work contains no material which has been accepted for the award of any other degree or diploma in any university or other tertiary institution and, to the best of my knowledge and belief, contains no material previously published or written by another person, except where due reference has been made in the text.

I give consent to this copy of my thesis when deposited in the University Library, being made available for loan and photocopying, subject to the provisions of the Copyright Act 1968.

I also give permission for the digital version of my thesis to be made available on the web, via the University's digital research repository, the library catalogue, the Australian Digital Thesis Program (ADTP) and also through web search engines, unless permission has been granted by the University to restrict access for a period of time.

SIGNED: .....

DATE: .....

Supervisors: Prof. Graham Heinson,
Prof. Stewart Greenhalgh
and Dr Mark Tingay.

Acknowledgements

Firstly, I would like thank my supervisors Graham Heinson, Stewart Greenhalgh and Mark Tingay. Their guidance and scientific input has been greatly valued. Stewart Greenhalgh, I also want to thank you for your work in helping me to improve my thesis and giving me a greater understanding of the English language.

I would like to thank the people of the MT group, fellow PhD students, and staff members of the Geology and Geophysics Discipline. In particular, thanks are expressed to Graham Baines, Robert Dart, Mike Hatch, Stephan Thiel and Jared Peacock. I'm very thankful for having had two of the best office mates! Stephan, thank you for being my sounding board and Jared you have been very patient when I've vocalised my internal dialogue.

I am very grateful to Steve Constable from Scripps Institute of Oceanography. An insightful chat about inversions in December 2008 proved to be a defining moment in my research. I also consider myself very lucky to have been invited on one of your cruises where I not only learnt about conducting research, but I thoroughly enjoyed myself too. Thanks to Luis Gallardo for willingly discussing joint inversions with me. Thanks also to Alan Jones and his research group at Dublin Institute of Advance Studies for their hospitality when I visited

I wish to thank Petratherm Pty. Ltd. which funded the acquisition of the MT Renmark Trough data and am grateful to them for allowing this work to be presented.

On a personal note I would like to thank my family and in particular my two sisters, Julie and Catherine and Julie's husband and daughter, Anton and Maddison. You were all a wonderful source of both encouragement and distraction. David, your love and reassurance has been a great source of support, helping me to both get

through the tough times and appreciate the good. Finally, I would like to thank my Mum. Quite simply I could not have done this without you!

List of Symbols

Throughout this thesis, numerous symbols will be used repeatedly to represent specific quantities or parameters. In this section, a list of symbols and a short description of each is given for the readers convenience. Every effort has been made to maintain conformity of symbols used here and wherever possible, standard symbols and notations have been used. However, standards have dictated a single symbol be used to represent more than one quantity. As a result, variations in symbol type, which are non-standard, have been used. The most significant double use of a symbol is ρ, which is typically used to represent both density and resistivity. To resolve this double use of this symbol, the slightly modified typeface ϱ has been used to represent resistivity.

α ... MT RMS weighting

β ... Gravity RMS weighting

β_* ... Gravity depth weighting constant

γ ... Complex propagation constant (wave number)

δ ... Skin depth

δm ... Small amount a model parameter is changed

$\underline{\partial}$ ... Differential operator

$\underline{\partial}_y$ ... Horizontal roughness matrix

$\underline{\partial}_z$ ... Vertical roughness matrix

ε ... Dielectric permittivity

ε_0 ... Dielectric permittivity of free space

ε_r ... Relative dielectric permittivity or dielectric constant

$\widehat{\zeta}$ ... Scale of the step length in the steepest decent inversion scheme

η ... Expansion coefficient for data space inversion scheme

ϑ ... Width of the cells in the Occam regularisation grid

κ ... Real component of the complex propagation constant

λ ... Tikhonov regularisation parameter

λ_c ... Compaction coefficient

μ ... Lagrange multiplier

μ_* ... Magnetic permeability

μ_0 ... Magnetic permeability of free space

μ_r ... Relative magnetic permeability

ν ... Volume

ϖ ... Weighting term in the model norm

ρ ... Density

ρ_{air} ... Density of air

ρ_{bulk} ... Bulk rock density

ρ_{fluid} ... Density of the formation fluid

ρ_{matrix} ... Density of the rock matrix

ρ_w ... Density of fresh water

σ ... Electrical conductivity

σ_{bulk} ... Bulk rock conductivity

σ_{fluid} ... Conductivity of the formation fluid

σ_w ... Conductivity of water

σ_{w_o} ... Conductivity of water at zero temperature and fixed salinity

σ^* ... Standard deviation

ϕ ... Porosity

ϕ_o ... Surface porosity

φ ... Phase

χ ... Chi distribution

χ_* ... Target misfit

ω	...	Angular frequency
ϱ	...	Electrical resistivity
ϱ_a	...	Apparent resistivity
ϱ_{bulk}	...	Bulk rock resistivity
ϱ_{fluid}	...	Resistivity of the formation fluid
ϱ_w	...	Resistivity of water
ϱ_{w_o}	...	Resistivity of water at zero temperature and fixed salinity
$\Delta\phi$	...	The change in porosity due to incorrect petrophysical parameters
Δg	...	Gravity offset term
Δm	...	Perturbation in the model space
A	...	Cross-sectional area of a regularisation grid cell
$\mathbf{a}$	...	Acceleration
a	...	Tortuosity factor
$\mathbf{B}$	...	Magnetic induction
B_0 B_1	...	Components of the surface magnetic induction
B_x B_y B_z	...	Components of the magnetic induction
b	...	Width of a rectangular prism
C_d	...	Data covariance matrix
c	...	Cut in the Occam inversion step size
$\mathbf{D}$	...	Electric displacement current
$\mathbf{d}$	...	Data vector
d	...	Data vector component
$\mathbf{E}$	...	Electric field
E_0 E_1	...	Components of the surface electric field
E_x E_y E_z	...	Components of the electric field
$\mathbf{F}$	...	Forward model operator
$\mathbf{F}_g$	...	Gravitational force
$\mathbf{F}_{GV}$	...	Gravity forward model operator
$\mathbf{F}_{MT}$	...	MT forward model operator

$\mathbf{F}_{new}$ ... New set of models after the Occam step size has been cut

f ... Frequency

$\mathbf{G}$ ... Linear forward model operator

G_c ... Gravitational constant

$\mathbf{g}$ ... Gravitational acceleration

g_z ... Vertical component of the gravitational acceleration

$\mathbf{H}$ ... Magnetic field

h ... Number of linearly independent equations

$\mathbf{I}$ ... Identity matrix

$\mathbf{J}$ ... Jacobian matrix

$\mathbf{J}_c$ ... Electric current density

J_{cy} ... Component of the electric current density

$\mathbf{J}_{GV}$ ... Gravity component of the joint inversion Jacobian

$\mathbf{J}_{MT}$ ... MT component of the joint inversion Jacobian

k ... Imaginary component of the complex propagation constant

l_1 ... l_1-norm

l_2 ... Euclidean norm or l_2-norm

M ... Mass

$\mathbf{m}$ ... Model parameter vector

m ... Component of the model parameter vector

$\mathbf{m}_\phi$ ... Model parameter vector containing only the porosity model components

m_{cf} ... Cementation factor

$\mathbf{m}_0$ ... Reference or starting model

n ... Number of model parameters

$\widehat{\mathbf{n}}$ ... Unit normal vector

n_s ... Saturation exponent

$\widehat{o}$ ... Vector of the direction of maximum decent in the steepest decent inversion scheme

$\mathbf{P}$ ... A point in space

P	...	Pressure
p	...	Number of MT data points
q	...	Number of data points
q_f	...	Free charge density
$\mathbf{R}$	...	Rotation matrix
r	...	Distance between points
$\widehat{\mathbf{r}}$	...	Unit distance vector
S	...	Fractional saturation
Sal	...	Salinity
SA	...	Sensitivity vector
s	...	Number of gravity data points
s_f	...	The surface over which an itergral is performed
T	...	Temperature
t	...	Time
U	...	Objective function
U_d	...	Data norm
U_g	...	Gravitational Potential
U_m	...	Model norm
U_{Tik}	...	Objective function of the Tikhonov Regularisation
v	...	Height of the cells in the Occam regularisation grid
$\mathbf{W}_d$	...	Data weighting matrix
$\mathbf{W}_{GV}$	...	Data weighting matrix used to implement the gravity data weighting
$\mathbf{W}_m$	...	Model weighting matrix
$\mathbf{W}_{MT}$	...	Data weighting matrix used to implement the MT data weighting
w	...	Gravity depth weighting function
w_y	...	Number of elements in the y-direction in the Occam regularisation grid
w_z	...	Number of elements in the z-direction in the Occam regularisation grid

$X_{xx}\ X_{yy}\ X_{xy}\ X_{yx}$	...	Real components of the impedance tensor
x	...	Spatial direction in Cartesian coordinates
$Y_{xx}\ Y_{yy}\ Y_{xy}\ Y_{yx}$	...	Imaginary components of the impedance tensor
y	...	Spatial direction in Cartesian coordinates
$\mathbf{Z}$	...	Impedance tensor
$Z_{xx}\ Z_{yy}\ Z_{xy}\ Z_{yx}$	...	Components of the impedance tensor
z	...	Spatial direction in Cartesian coordinates
$\widehat{\mathbf{z}}$	...	Unit vector vertically downwards
z_0	...	Gravity depth weighting constant
z_1	...	Depth to the top of a rectangular prism
z_2	...	Depth to the bottom of a rectangular prism

List of Figures

List of Tables

Chapter 1

Introduction

The aim of the research described in this thesis is to develop, test and apply a magnetotelluric (MT) and gravity 2D joint inversion scheme. Joint inversions take data sets from two complementary geophysical survey techniques, measured over the same subsurface geology, and simultaneously invert them to produce an integrated model [1] [2]. They provide an effective and efficient means of combining and jointly analysing the different data sets such that there is an increased confidence in the final interpretation [3]. Joint inversions also aid in reducing model non-uniqueness, which plagues single technique inversions, without having to introduce external constraints or geological prejudice [4] [5]. However, the difficulty with joint inversions is in developing a suitable and pervasive link between the two techniques on which the inversion is based.

The MT and gravity techniques were chosen for this study because they are relatively cheap and popular techniques. There exist readily available large open-file MT and gravity data sets, thus ensuring a demand for MT and gravity joint inversions in the future. The theory of the MT and gravity techniques is relatively simple when compared to the more complex seismic and controlled source electromagnetic (CSEM) techniques [6]. This allows for a more simplistic environment in which to develop a new joint inversion approach, before potentially adapting and extending it to more complicated techniques. Further details on the theoretical benefits of combining the MT and gravity techniques are provided in Chapter 5.

There are two previously reported attempts to combine the MT and gravity

techniques in a simultaneous inversion [7] [8]. Both research groups based their inversions on a structural approach, whereby it is assumed that each technique should sense the same position and orientation of any subsurface geological structure. Thus, the geology is the structural control on the distribution of the parameters. As a result, boundaries in the model parameters are expected at the same locations for each of the data sets [4]. Although boundaries or gradients of the parameter values in the models are expected to be the same, absolute values for each of the parameters are independent.

Santos *et al.* [7] and Jegen *et al.* [8] jointly inverted MT and gravity by using a simple form of structural approach, that of a 2D layered Earth model which has lateral changes in the thickness of the layers. The joint inversion produced resistivity and density models that were connected by having co-incident layer boundaries. The resistivity and density values between the layer boundaries were assumed to be constant and independent of each other. This style of joint inversion is restricted to simple geological provinces and is very much dependent on the model parameterisation used (number of layers) as well as the actual starting model [9]. Layered earth joint inversions have also been used by other researchers to combine various geophysical data sets [10] [11] [12] [13] [14] [15] [16] [17].

Structural approaches have been the mainstay of joint inversions to date. More sophisticated versions define the structure of a smooth 2D model in terms of the gradients between adjacent cells. Once there is a measure of structure, a constraint is placed on the joint inversion such that it fits the observed data sets and minimises the structural variation between models corresponding to the different techniques [1] [2]. The cross-gradient method developed by Gallardo and Meju [4] [5] is the most popular structural joint inversion approach. Initially, the 2D cross-gradient method was applied to seismic traveltimes and DC resistivity data for shallow investigations. Subsequently, the cross-gradient method has been adapted by numerous other researchers and applied in a variety of geophysical techniques and investigations, although it has never been applied to MT and gravity [3] [18] [19] [20] [21] [22] [23] [24].

An alternative way of performing a joint inversion is the petrophysical approach,

whereby the different parameters of the joint inversion (i.e. physical properties of the subsurface to which each technique is individually responsive) are linked through an *a priori* relationship. No analytical formulae exist that uniquely link the various parameters measured by geophysical techniques, although there do exist several well established empirical formulae. The petrophysical approach has shortcomings in terms of the absence of a robust link between parameters that can be applied to diverse geological situations. Thus, this approach has been mainly overlooked in favour of a structural approach.

To date there have been no attempts at MT and gravity petrophysical joint inversions cited. However, a petrophysical approach involving other geophysical techniques has been undertaken by Tiberi *et al.* [25] and Lees and VanDecar [26]. In these studies Birch's Law, which relates the P-wave velocity to density, was used to combine seismic and gravity data. Hoversten *et al.* [27] sought to recover reservoir properties by using rock-property models and jointly inverting marine seismic AVA data (amplitude variation with angle of incidence) and CSEM data. Tseng and Lee [28] jointly inverted electromagnetic (EM) and seismic traveltime data by inverting for porosity and fluid conductivity, which are related to conductivity and P-wave velocity through Archie's Law and Wyllie's Law. However, it was found that this type of joint inversion was ill-posed and would not produce reasonable models without heavy user intervention.

In this thesis, the objective of the research was to gain greater insight into the petrophysical approach by developing a new petrophysical joint inversion between MT and gravity data. Current MT and gravity joint inversions are restricted to layered (2D) Earth environments. Therefore, the petrophysical joint inversion developed here is intended to be applied to more structurally complicated areas, which entail complex 2D structure. This research is not necessarily to be restricted to just 2D MT and gravity data. Rather a general methodology is sought which can be extended to three dimensions for elucidating 3D structure, and to three or more techniques (e.g. adding seismic data). Equally, such an approach could be adapted for jointly inverting different techniques.

An outline of the thesis chapters, the key ideas and processes used to achieve

	Description	Key Ideas
Chapter 2	• Establishes MT and gravity theory. • Describes relationships that could be used to link resistivity and density in the joint inversion.	• MT is frequency dependent and contains more information about the subsurface than gravity. • Bouguer anomaly gravity data is sensitive to the density contrast of the subsurface.
Chapter 3	• Establishes inversion theory. • Reviews state of the art MT and gravity inversions.	• The Occam 2D non-linear scheme forms the basis of the joint inversion. • There is a pre-existing MT but not a gravity Occam inversion.
Chapter 4	• Develops an Occam gravity inversion, which forms the gravity component of the joint inversion. • Synthetic data is used to test the new gravity inversion.	• The gravity inversion only places model structure at surface. • An MT specific inversion grid has no adverse effect on the gravity inversion.
Chapter 5	• Determines the best relationships from chapter 2 to be used in the new petrophysical joint inversion. • Discusses the benefits of combining MT and gravity.	• Porosity though Archie's Law and the porosity-density relationship form the basis of linking MT and gravity in the joint inversion.
Chapter 6	• Presents the joint inversion methodology. • Discusses the characteristics of the new joint inversion.	• The joint inversion inverts directly for a single porosity model that is constrained by both MT and gravity data.
Chapter 7	• Synthetic data is used to test the joint inversion. • Includes investigating the effect of data errors, station configurations and resolution capabilities.	• The joint inversion is effective at reproducing the subsurface and produces a more accurate representation than the MT and gravity inversion alone.
Chapter 8	• A sensitivity analysis evaluates MT and gravity's compatibility in determining sub surface features. • Differential weighting of the MT and gravity data sets is attempted.	• A joint inversion produces better results using broadband rather than long period MT data. • Differential weighting does not significantly improve the joint inversion results.
Chapter 9	• The joint inversion is applied to the Renmark Trough in South Australia. • Determines the validity of the new joint inversion on real world data.	• The joint inversion produces a significantly better structural representation of the Trough than the MT or gravity inversion alone.

Figure 1.1: A description of, and the key ideas contained in, the chapters of this thesis.

the objectives are shown in Figure 1.1. The early chapters concentrate on the physical principles of MT and gravity and the background theory of modelling and inversion (Chapters 2, 3 and 4). This is followed by a detailed examination of the important petrophysical relationships (Chapter 5). The joint inversion methodology is developed in Chapter 6 and it is applied to synthetic data in Chapter 7, including a study into the effect of data errors and station placement. Chapter 8 continues with synthetic data testing but is primarily concerned with model sensitivities and related matters. Finally, the joint inversion is successfully applied to field data from South Australia (Chapter 9).

Chapter 2

Magnetotellurics and Gravity Theory

Magnetotellurics and gravity are two fundamentally different techniques that will be combined in a petrophysical joint inversion in Chapter 6. The gravity method is based on Newton's Law of Gravitation and can be mathematically described by potential theory (the Laplace and Poisson equations), whereas MT is an electromagnetic induction technique that satisfies the diffusion equation. These techniques have different characteristics and are sensitive to different properties of the Earth. Gravity is sensitive to density variations whereas MT is sensitive to resistivity variations.

This chapter provides an overview of the basic theory of the MT and gravity techniques. The equations for bulk conductivity and density in relation to other properties of the Earth are also summarised. These equations will be discussed further in Section 5.2 to determine the relationships used in the joint inversion.

2.1 Magnetotellurics

Magnetotellurics was first introduced by Cagniard [29] and Tikhonov [30] in the 1950's. It is a passive electromagnetic technique which exploits natural variations in the Earth's magnetic field to determine the subsurface resistivity distribution [31]. The sources that are utilised by MT have frequency fluctuations between 10^{-7} and

10^5 Hz, which makes it ideal for investigating shallow (tens of metres) as well as deep (hundreds of kilometres) structures of the Earth. In this section the basic theory of the MT technique and the conductivity equations, which could be used by the petrophysical joint inversion, are summarised.

2.1.1 Basic Magnetotelluric Theory

Source Field

Magneto-hydrodynamic processes occurring in the Earth's outer core generate the main component of the Earth's magnetic field [32]. This is superimposed upon by relatively low amplitude, natural time fluctuations called geomagnetic fluctuations. Geomagnetic fluctuations occur at frequencies between 10^{-7} and 10^5 Hz and are used as the MT source [33]. This source is assumed to be a time-invariant, uniform magnetic plane wave with normal incidence at the Earth's surface [31].

The causes of the geomagnetic fluctuations can be divided into several naturally occurring phenomena; meteorological activity, diurnal (solar) variations, magnetospheric ring currents and pulsations [9]. Meteorological activity, in particular lightning, is responsible for generating sources with frequencies higher than 1 Hz. The EM signal discharged by lightning is known as sferics. Sferics travel radially out from the lightning strike and propagate around the earth in the resistive zone between the ground and the conductive ionosphere, which acts as a waveguide. The majority of thunderstorms occur over land masses in the equatorial latitudes and the sferics appear as plane waves by the time these reach higher latitudes.

Diurnal fields occur at frequencies between $10^{-6} - 10^{-4}$ Hz and are caused by the heating and cooling of the ionosphere due to sun exposure. This produces large-scale circulating currents in each hemisphere. The eastward flowing currents at the magnetic equator are referred to as the equatorial electrojets.

The interaction between the Earth's magnetic field and charged particles in the solar winds and magnetic storms create magnetospheric ring currents [9]. Magnetospheric ring currents flow in a westward direction with their strength measured by the 'Dst' (disturbance storm index). Variations in the magnetospheric ring currents range from minute-by-minute fluctuations during magnetic storms that can last for

hours, to the 27 day rotation of the sun and the 11 year sun cycle. This results in a diverse range of frequencies that can be utilised as an MT source.

Geomagnetic pulsations generate an MT source at frequencies lower than 1 Hz. The constant exposure of the magnetosphere to solar winds causes the magnetosphere to be compressed on the sun's side and tail off on the opposing side. Variations in the density, velocity and intensity of the solar wind cause the magnetosphere to be further distorted. These distortions cause a sinusoidal oscillation of the magnetosphere through inductive and magneto-hydrodynamic processes [34].

Little signal occurs between frequencies of 0.5 and 5 Hz, with the minimum in signal strength being at 1 Hz. This is because there are almost no natural processes that generate frequencies in this band.

Maxwell's Equations

The MT technique, being an EM phenomena, is based on Maxwell's equations. These equations define the behaviour of electromagnetic waves at all frequencies. Maxwell's equations in differential form for a polarisable and magnetisable material containing no electric or magnetic sources can be written as [35]

$$\nabla \cdot \mathbf{D} = q_f \tag{2.1a}$$

$$\nabla \cdot \mathbf{B} = 0 \tag{2.1b}$$

$$\nabla \times \mathbf{E} = -\frac{\partial \mathbf{B}}{\partial t} \tag{2.1c}$$

$$\nabla \times \mathbf{H} = \mathbf{J}_c + \frac{\partial \mathbf{D}}{\partial t} \quad , \tag{2.1d}$$

where $\mathbf{D}$ is the electric displacement in Cm^{-2}, q_f is the free charge density in Cm^{-3}, $\mathbf{B}$ is the magnetic induction in T, $\mathbf{E}$ is the electric field in Vm^{-1}, $\mathbf{H}$ is the magnetic field in Am^{-1} and $\mathbf{J}_c$ is the electric current density in Am^{-2}.

Gauss' Law (Equation 2.1a) states that the source of displacement current is time invariant free charge, which arises from bound charge or polarisation of a medium. However, there is no point source for the generation of magnetic fields, meaning there are no free magnetic poles (Equation 2.1b). The magnetic source

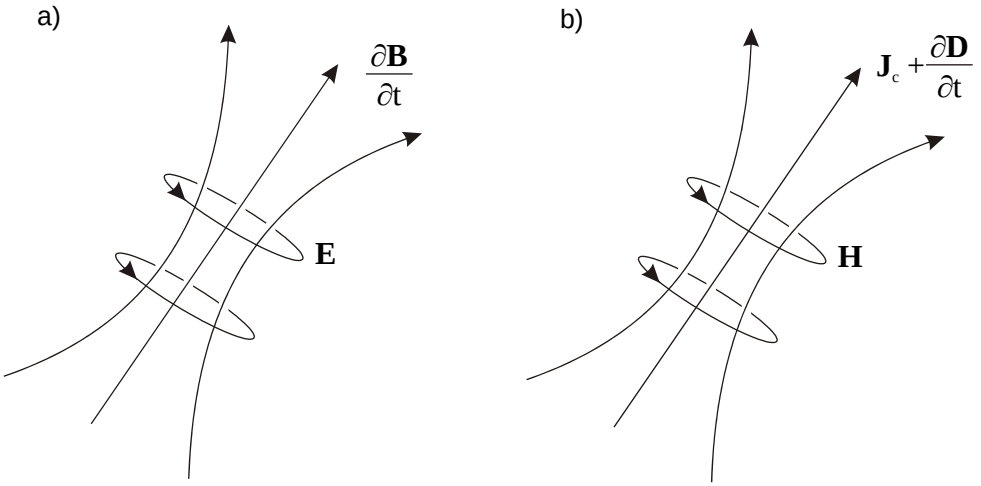

Figure 2.1: A schematic of the relationship between electric and magnetic fields for a) Faraday's Law and b) Ampere's Law.

is dipolar in nature and so the flux of **B** across any closed surface is zero. In Faraday's Law (Equation 2.1c), a time varying magnetic field generates an electric field that curls around it (Figure 2.1a). Similarly, by Ampere's Law (Equation 2.1d), a time varying displacement current and/or an ohmic current density will produce a magnetic intensity that forms closed loops around the current lines (Figure 2.1b).

Equation 2.1 does not define the electromagnetic fields but shows the inter-relationship between them. In the given form, **E** and **H** are decoupled and constitutive relations are required to establish the coupling. The following relationships apply in a linear, isotropic medium

$$\mathbf{B} = \mu_* \mathbf{H} \tag{2.2a}$$

$$\mathbf{D} = \varepsilon \mathbf{E} \quad , \tag{2.2b}$$

where ε is the dielectric permittivity in $\mathrm{AsV^{-1}m^{-1}}$ and μ_* is the magnetic permeability in $\mathrm{VsA^{-1}m^{-1}}$. The dielectric permittivity can be expressed as $\varepsilon = \varepsilon_0 \varepsilon_r$, where ε_r is the relative dielectric permittivity (or dielectric constant) and $\varepsilon_0 = 8.85 \times 10^{-12}$ $\mathrm{AsV^{-1}m^{-1}}$ is the permittivity of free space. Magnetic permeability is given by $\mu_* = \mu_0 \mu_r$, where μ_r is the relative magnetic permeability and $\mu_0 = 4\pi \times 10^{-7}$ $\mathrm{VsA^{-1}m^{-1}}$ is the magnetic permeability of free space. These relationships describe a material's

ability to become electrically polarized or magnetically polarized (magnetized) in the presence of an electric or magnetic field, respectively. Other non-linear relationships apply for ferroelectric and ferromagnetic materials.

In addition to displacement current, conduction current also exists inside a material. Conduction currents are related to the electric field through Ohm's Law

$$\mathbf{J}_c = \sigma \mathbf{E} \quad , \tag{2.3}$$

where σ is conductivity in Sm^{-1} and the relationship between conductivity and resistivity, ϱ, in Ωm is $\varrho = \frac{1}{\sigma}$. The quantities ε_r and μ_r exhibit a small range of variations in Earth materials when compared to conductivity σ, which can span 12 orders of magnitude [6].

The relationships given by Equations 2.2 and 2.3, when substituted into Maxwell's equations (Equation 2.1), yield

$$\begin{aligned}
\nabla \cdot \mathbf{E} &= \frac{q_f}{\varepsilon} && \text{(2.4a)} \\
\nabla \cdot \mathbf{B} &= 0 && \text{(2.4b)} \\
\nabla \times \mathbf{E} &= -\frac{\partial \mathbf{B}}{\partial t} && \text{(2.4c)} \\
\nabla \times \mathbf{B} &= \mu_* \sigma \mathbf{E} + \mu_* \varepsilon \frac{\partial \mathbf{E}}{\partial t} \quad . && \text{(2.4d)}
\end{aligned}$$

This is the modified form of Maxwell's equations in a conductive media and shows the coupling between the electric and magnetic fields.

EM Theory of a Homogeneous Half Space

The modified Maxwell equations (Equation 2.4) are used to examine the EM behaviour in the subsurface. This is initially done for a homogeneous half space. First, taking the curl of Ampere's Law (Equation 2.4d) gives

$$\nabla \times (\nabla \times \mathbf{B}) = \nabla \times \left(\mu_* \sigma \mathbf{E} + \mu_* \varepsilon \frac{\partial \mathbf{E}}{\partial t} \right) \quad , \tag{2.5}$$

and using the vector identity $\nabla \times (\nabla \times \,) = \nabla \cdot (\nabla \cdot \,) - \nabla^2$ it becomes

$$\nabla \cdot (\nabla \cdot \mathbf{B}) - \nabla^2 \mathbf{B} = \mu_* \sigma \nabla \times \mathbf{E} + \mu_* \varepsilon \frac{\partial \nabla \times \mathbf{E}}{\partial t} \quad . \tag{2.6}$$

Then substituting in Equation 2.4b and 2.4c it follows that

$$\nabla^2 \mathbf{B} = \mu_* \sigma \frac{\partial \mathbf{B}}{\partial t} + \mu_* \varepsilon \frac{\partial^2 \mathbf{B}}{\partial t^2} \quad . \tag{2.7}$$

This can be recognised as a damped wave equation. The first term on the right hand side is the diffusion term, expressing the decay of $\mathbf{B}$, whereas the second term on the right hand side is the propagation term. Equation 2.7 is expressed in the time domain and can be expressed as the vector Helmholtz equation in the frequency domain. Assuming an $e^{i\omega t}$ time dependency of the magnetic field, where $i = \sqrt{-1}$ is the imaginary number and $\omega = 2\pi f$ is angular frequency in rads^{-1} with f as frequency in Hz, it follows that

$$(\nabla^2 - \gamma^2)\mathbf{B} = \mathbf{0} \quad , \tag{2.8}$$

where γ^2 is the complex propagation constant (wave number) and is given by

$$\gamma^2 = i\omega\mu_*\sigma - \omega^2\mu_*\varepsilon = k^2 - \kappa^2 \quad . \tag{2.9}$$

The MT technique is based on a quasi-static approximation, which is where the source field changes sufficiently slowly as to appear to be static [33]. This behaviour occurs at low source frequencies ($< 10^5$ Hz). The quasi-static approximation means the diffusion term dominates over the propagation term in Equation 2.7. In other words, $\sigma \gg \varepsilon\omega$ and thus the first term in Equation 2.9 is the most significant. Neglecting κ^2, Equation 2.8 then becomes

$$(\nabla^2 - k^2)\mathbf{B} = \mathbf{0} \quad . \tag{2.10}$$

In the time domain, the quasi-static approximation is equivalent to neglecting the time derivative term of Equation 2.4d (no displacement current). Therefore Equation 2.7 becomes

$$\nabla^2 \mathbf{B} = \mu_* \sigma \frac{\partial \mathbf{B}}{\partial t} \quad . \tag{2.11}$$

A similar expression for the electric field can be derived following the same approach as used for the magnetic field. It then follows that the electric field equivalent to Equation 2.6 is given by

$$\nabla \cdot (\nabla \cdot \mathbf{E}) - \nabla^2 \mathbf{E} = -\frac{\partial \nabla \times \mathbf{B}}{\partial t} \quad . \tag{2.12}$$

In regions away from current sources ($q_f = 0$), the current density is divergence free, $\nabla \cdot \mathbf{J}_c = \frac{\partial q_f}{\partial t} = 0$, which implies $\nabla \cdot (\sigma \mathbf{E}) = \sigma \nabla \cdot \mathbf{E} + \mathbf{E} \cdot \nabla \sigma = 0$. There is no free charge in a homogeneous half space therefore $\nabla \sigma = 0$, hence $\nabla \cdot \mathbf{J}_c = \sigma \nabla \cdot \mathbf{E} = \boldsymbol{\nabla} \cdot \mathbf{E} = 0$. Substituting $\nabla \cdot \mathbf{E} = 0$ and Equation 2.4d (with the neglected time derivative due to the quasi-static approximation) into Equation 2.12 yields

$$\nabla^2 \mathbf{E} = \mu_* \sigma \frac{\partial \mathbf{E}}{\partial t} \quad , \tag{2.13}$$

and in the frequency domain

$$(\nabla^2 - k^2)\mathbf{E} = \mathbf{0} \quad . \tag{2.14}$$

Equations 2.11 and 2.13 show that the electric and magnetic fields obey the diffusion equation for the frequency range used by MT.

In a very poor conductor ($\sigma = 0$), the diffusion equation becomes the Laplace equation

$$\nabla^2 \mathbf{E} = 0 \tag{2.15a}$$

$$\nabla^2 \mathbf{B} = 0 \quad , \tag{2.15b}$$

and, at any moment in time, the diffusion equation becomes the Poisson equation

$$\nabla^2 \mathbf{E} = \mu_* \sigma \left. \frac{\partial \mathbf{E}}{\partial t} \right|_t \tag{2.16a}$$

$$\nabla^2 \mathbf{B} = \mu_* \sigma \left. \frac{\partial \mathbf{B}}{\partial t} \right|_t \quad . \tag{2.16b}$$

For both the Laplace and Poisson equations the magnetic and electric fields are static (no time dependence).

In Cartesian coordinates, where x, y, z, are north, east and vertically down, a solution to Equation 2.7 can be expressed as

$$\mathbf{B} = (B_0 e^{-ikz} + B_1 e^{+ikz}) e^{-iwt} \tag{2.17a}$$

$$\mathbf{E} = (E_0 e^{-ikz} + E_1 e^{+ikz}) e^{-iwt} \quad , \tag{2.17b}$$

where B_0, B_1, E_0 and E_1 are the electromagnetic fields at the surface of the Earth. The positive growth term e^{+ikz} in Equation 2.17 is not required as $\mathbf{B}$ and $\mathbf{E}$ fields have to vanish as $z \to \infty$. The quasi-static approximation also means the propagation term in Equation 2.7 is insignificant. This means fields are established instantaneously throughout the region of interest and the time dependent term in Equation 2.17 can be neglected.

In Equation 2.17, $k^2 = i\omega\mu_*\sigma$ and using the identity $\sqrt{i} = \frac{1+i}{\sqrt{2}}$ yields

$$k = (1+i)\sqrt{\frac{\omega\mu_*\sigma}{2}} \quad . \tag{2.18}$$

The skin depth, or the penetration depth (δ), is taken as the inverse real part of the propagation constant k, that is

$$\delta = \sqrt{\frac{2}{\omega\mu_*\sigma}} \quad . \tag{2.19}$$

This can be simplified since $\omega = 2\pi f$, and magnetic permeability does not vary substantially through the Earth, allowing its free space value to be used. The simplified skin depth is given by

$$\delta \approx 500\sqrt{\frac{\varrho}{f}} \quad , \tag{2.20}$$

where ϱ is the resistivity of the homogeneous half space. The skin depth, in m, is the depth at which the surface EM fields have been attenuated by $\frac{1}{e}$, or approximately 37% of the surface values. This shows that the depth of penetration of the MT technique is only dependent on bulk resistivity and source frequency.

Apparent Resistivity and Phase

Expressions for apparent resistivity and phase for a homogeneous half space can be obtained using the diffusion solution (Equation 2.17). Expanding the curl operator in Faraday's Law (Equation 2.4c) and assuming harmonic time dependence yields

$$\frac{\partial E_z}{\partial y} - \frac{\partial E_y}{\partial z} = -i\omega B_x \tag{2.21a}$$

$$\frac{\partial E_x}{\partial z} - \frac{\partial E_z}{\partial x} = -i\omega B_y \tag{2.21b}$$

$$\frac{\partial E_y}{\partial x} - \frac{\partial E_x}{\partial y} = -i\omega B_z \quad . \tag{2.21c}$$

Equation 2.21 shows the relationships between the different components of the electric and magnetic field.

The magnetic field source of MT is assumed to be a vertically travelling plane wave only changing in the horizontal direction, therefore $B_z = 0$. Equation 2.21c implies $\frac{\partial E_y}{\partial x}$ and $\frac{\partial E_x}{\partial y}$ are zero or equal. The MT source is also assumed to have normal incident at the surface and thus, the resulting induced electric field will have no vertical component ($E_z = 0$). Using these simplifications, Equation 2.21 becomes

$$\frac{\partial E_y}{\partial z} = i\omega B_x \tag{2.22a}$$

$$\frac{\partial E_x}{\partial z} = -i\omega B_y \quad . \tag{2.22b}$$

Substituting into the diffusion solution (Equation 2.17) leads to

$$kE_{y0}e^{-kz} = -i\omega B_{x0}e^{-kz} \quad (2.23a)$$

$$kE_{x0}e^{-kz} = i\omega B_{y0}e^{-kz} \quad . \quad (2.23b)$$

Based on Equation 2.23, the complex magnetotelluric impedance Z can be written as

$$Z_{yx} = \frac{E_{y0}}{B_{x0}} = -\frac{i\omega}{k} = -\sqrt{\frac{\omega\varrho}{\mu_*}}\sqrt{i} \quad (2.24a)$$

$$Z_{xy} = \frac{E_{x0}}{B_{y0}} = \frac{i\omega}{k} = \sqrt{\frac{\omega\varrho}{\mu_*}}\sqrt{i} \quad , \quad (2.24b)$$

where Z_{yx} and Z_{xy} are equal but of opposite sign. The impedance is the ratio of the orthogonal surface components of the electric and magnetic field. Rearranging Equation 2.24, the apparent resistivity ϱ_a of a half space is given by

$$\varrho_a = \frac{\mu_*}{\omega}|Z|^2 \quad . \quad (2.25)$$

Equation 2.25 shows that the Earth's resistivity can be defined in terms of the horizontal components of the magnetic and electric fields at different frequencies. The associated phase φ is

$$\varphi = \arg Z = \arg\left(\sqrt{\frac{\omega\varrho}{\mu_*}}\sqrt{i}\right) = \arg\left(\sqrt{\frac{\omega\varrho}{\mu_*}}e^{i\frac{\pi}{4}}\right) = \frac{\pi}{4} = 45^{\circ} \quad . \quad (2.26)$$

The phase is always 45° in homogenous half space, with the electric field leading the magnetic field, regardless of resistivity.

The above approach used to investigate a homogeneous half space can be extended to an arbitrary 3D subsurface resistivity distribution. However, all the orthogonal components of the electric and magnetic field in a 3D Earth are related and expressed using an impedance tensor, or MT transfer function $\mathbf{Z}$, where

$$\begin{bmatrix} E_x \\ E_y \end{bmatrix} = \begin{bmatrix} Z_{xx} & Z_{xy} \\ Z_{yx} & Z_{yy} \end{bmatrix} \begin{bmatrix} B_x \\ B_y \end{bmatrix} \quad . \quad (2.27)$$

Since the impedance tensor is complex, it can be expressed in terms of its real and imaginary parts

$$\begin{bmatrix} Z_{xx} & Z_{xy} \\ Z_{yx} & Z_{yy} \end{bmatrix} = \begin{bmatrix} X_{xx} & X_{xy} \\ X_{yx} & X_{yy} \end{bmatrix} + i \begin{bmatrix} Y_{xx} & Y_{xy} \\ Y_{yx} & Y_{yy} \end{bmatrix} \quad . \tag{2.28}$$

The associated apparent resistivity is

$$\varrho_{aij} = \frac{1}{\mu_0 \omega} |Z_{ij}(\omega)|^2 \quad , \tag{2.29}$$

and the phase is

$$\varphi_{ij} = \tan^{-1} \left(\frac{\mathrm{Re}\, Z_{ij}}{\mathrm{Im}\, Z_{ij}} \right) \quad , \tag{2.30}$$

where the subscripts i and j are indexes for the rows and columns of the impedance tensor.

The apparent resistivity or phase for different subsurface orientations can be obtained from Equations 2.29 and 2.30 by using multiple combinations of elements in the impedance tensor. The various frequencies of the MT source have different depths of penetration. Therefore, evaluating the apparent resistivity and phase for the various frequencies will give a range of depth information.

Model Dimensionality

The resistivity distribution can have different dimensionality depending on the geological scenario, and this is reflected in the impedance tensor (Equation 2.28). The following discussion applies to an isotropic Earth. Anisotropy can be incorporated into the impedance tensor, but is not considered in this thesis. For a 1D Earth $Z_{xx} = Z_{yy} = 0$ and $Z_{xy} = -Z_{yx}$. The frequency dependent phase behaviour for a two layered Earth will be greater than 45° at high frequencies if the top layer is more resistive than the bottom layer. Conversely, the phase will be less than 45° at high frequencies if the top layer is less resistive than the bottom layer. For both two layer configurations the phase will approach 45° at low frequencies. For a multilayered Earth, the apparent resistivity at the high and low frequencies will asymptotically

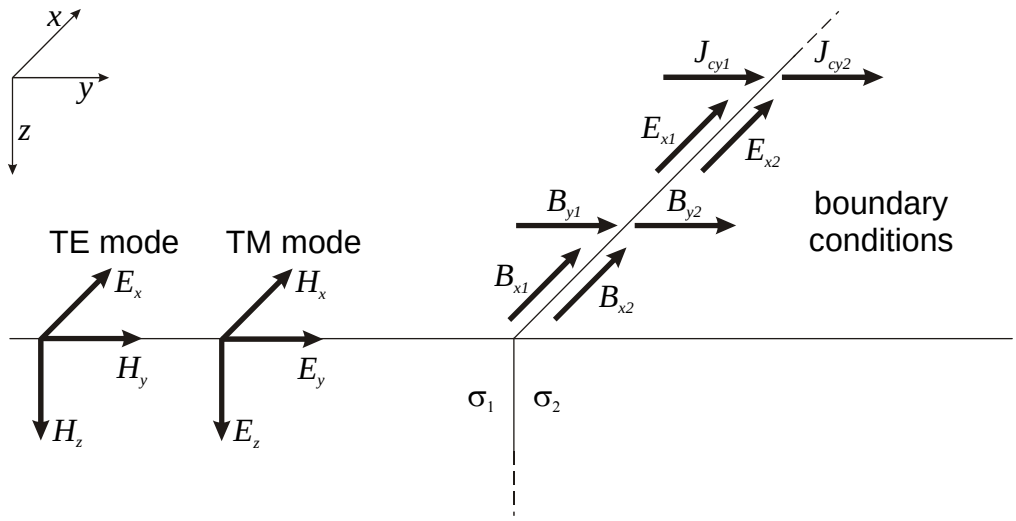

Figure 2.2: Example of a horizontal conductivity boundary, where $\sigma_1 < \sigma_2$, illustrating the TE and TM mode configurations and the electric and magnetic boundary conditions.

approach the resistivities of the top and bottom layers, respectively. The ability to resolve any intermediate layer depends on their relative resistivity and thickness, with conductive layers easier to resolve than resistive ones [36].

A simple model of a two dimensional Earth comprising a vertical boundary separating two conductivity zones is depicted in Figure 2.2. The boundary extends in the x-direction to a distance greater than the skin depth. For such a 2D Earth where the coordinate system aligns with the resistive strike, the pattern in the impedance tensor follows $Z_{xx} = Z_{yy} = 0$ and $Z_{xy} \neq Z_{yx}$. The orientation of field MT measurements rarely coincides with the resistive strike. Thus, the diagonal elements of the impedance tensor $\mathbf{Z}'$ will not equal zero. The impedance tensor can be rotated, by an angle θ, which rotates it into a coordinate frame parallel or perpendicular to the strike. This is implemented by

$$\mathbf{Z}' = \mathbf{R}\mathbf{Z}_{2D}\mathbf{R}^T \quad , \tag{2.31}$$

where

$$\mathbf{R} = \begin{bmatrix} \cos\theta & \sin\theta \\ -\sin\theta & \cos\theta \end{bmatrix} \quad . \tag{2.32}$$

The governing principle for a 2D conductivity boundary such as the model in Figure 2.2 is charge conservation. The current density across the discontinuity is equal on both sides in the y-direction (perpendicular to strike)

$$J_{cy1} = J_{cy2} \quad , \tag{2.33}$$

with $J_{cy1} = \sigma_1 E_{y1}$ and $J_{cy2} = \sigma_2 E_{y2}$, which gives

$$\sigma_1 E_{y1} = \sigma_2 E_{y2} \quad . \tag{2.34}$$

Equation 2.34 means there is an associated discontinuity in the perpendicular component of the electric field when there is a conductivity boundary, $\sigma_1 \neq \sigma_2$. This discontinuity will cause a jump in the total **E** field value. The parallel components of the **E** field are continuous in both the x and z-directions. All components of the **B** field are continuous across the boundary due to the magnetic permeability being assumed to be homogeneous and even if not, because the **B** field is non-divergent.

For an ideal 2D situation, the electric and magnetic fields are mutually orthogonal. This allows for the source field to be decomposed into two differently polarised modes, the TE and TM modes. The TE mode (transverse electric), also referred to as E-polarisation, has magnetic fields perpendicular to the discontinuity plane which induces an electric field parallel to strike (transverse to propagation direction). The TE mode describes current flowing parallel to strike and can be expressed mathematically as

$$\frac{\partial E_x}{\partial y} = \frac{\partial B_z}{\partial t} = i\omega B_z \tag{2.35a}$$

$$\frac{\partial E_x}{\partial z} = \frac{\partial B_y}{\partial t} = -i\omega B_y \tag{2.35b}$$

$$\frac{\partial B_z}{\partial y} - \frac{\partial B_y}{\partial z} = \mu_0 \sigma E_x \quad . \tag{2.35c}$$

The TM mode (transverse magnetic) also referred to as B-polarisation, has a magnetic field parallel to strike and induces electric fields perpendicular and parallel (vertical) to the discontinuity plane. The TM mode describes current flowing perpendicular to strike and can be expressed mathematically as

$$\frac{\partial B_x}{\partial y} = \mu_0 \sigma E_z \tag{2.36a}$$

$$-\frac{\partial B_x}{\partial z} = \mu_0 \sigma E_y \tag{2.36b}$$

$$\frac{\partial E_z}{\partial y} - \frac{\partial E_y}{\partial z} = i\omega B_x \quad . \tag{2.36c}$$

The TM mode expression contains E_y, which is discontinuous across a conductivity boundary. From Equation 2.34, the magnitude of the E_y discontinuity is $\frac{\sigma_2}{\sigma_1}$. The associated discontinuity in the apparent resistivity is of magnitude $\left(\frac{\sigma_2}{\sigma_1}\right)^2$. Consequently, the TM mode tends to be better at resolving lateral boundaries than the TE mode. However, near the boundary, the TM mode over-estimates the apparent resistivity value in conductive zones and under-estimates it in resistive zones. The TE mode provides a more reliable apparent resistivity value.

Resistivity values can vary in any direction in a 3D Earth. Therefore, the elements of the impedance tensor are independent of each other, irrespective of the coordinate system. All elements of the impedance tensor need to be considered to determine the subsurface resistivity.

Distortion

The MT response often suffers from galvanic distortion, which includes static shift [37]. Near-surface conductive heterogeneities at skin-depths shallower than that of the shortest measured wavelength cannot be resolved inductively and contribute to galvanic distortion of the impedance tensor. Charges accumulate along conductive boundaries which cause a redistribution of the electric field [38]. This non-inductive response is frequency independent and becomes superimposed on the frequency dependent regional MT response [37]. A distorted MT response has a shift in the apparent resistivity for all frequencies, but phase is unaffected. Such galvanic dis-

tortion hampers the ability to reconstruct targeted large scale conductive features. Methods for removing galvanic distortion include those by Bibby *et al.* [37], Groom and Bailey [39], Ledo *et al.* [38].

2.1.2 Conductivity Equations

Conductivity is a measure of the ease with which a material can transmit current. This can occur in any of three ways: electronic, electrolytic (ionic), and dielectric conduction (displacement current). Current transmission is inherently non-linear and complex in nature, therefore a universal equation does not exist that quantifies conduction for all geological settings [51]. This section provides a brief overview of the important conductivity relationships in multiphase media (summarised in Table 2.1).

Maxwell [52] first used effective medium theory to derive the bulk conductivity of a mixed medium. He derived the conductivity of spheres dispersed in a continuous medium. Wagner [53] developed the Maxwell-Wagner model that has more complicated spherical distributions than Maxwell's model, whereas Fricke [54] used ellipsoids instead of spheres. Continued research into effective medium theory has produced the Hashin-Shtrikman bounds [40][41][42] and the Waff model [43]. Hashin-Shtrikman bounds describe the extreme upper and lower conductivity bounds for the mixing of two conductive phases. The upper bound (HS^+) corresponds to non-connected resistive inclusions in a conductive phase, whereas the lower bound (HS^-) corresponds to non-connected conductive inclusions in a resistive phase. The shape of the inclusions are generally spheres, however they can be thin disks or needles, which lead to tighter bounds [55]. The Waff model assumes the medium is made up of an infinite number of varying sized composite connected spheres. For each sphere the core is phase 2, which is completely encapsulated by phase 1 forming the shell. This means phase 1 is highly connected and phase 2 is completely disconnected.

Effective medium models can incorporate any number of conductive phases by using weighted means. The parallel (longitudinal) and perpendicular (transverse) models make up the Wiener bounds [44]. A parallel model is made of layers of

Table 2.1: Summary of the main conductivity equations.

Name	Equation
Hashin-Shtrikman Bounds [40][41][42]	$\sigma^{+}_{bulk} = \sigma_2 \left(1 - \frac{3(1-\nu_2)(\sigma_2-\sigma_1)}{3\sigma_2-\nu_2(\sigma_2-\sigma_1)}\right)$ $\sigma^{-}_{bulk} = \sigma_2 \left(1 + \frac{3\nu_2(\sigma_2-\sigma_1)}{3\sigma_1+(1-\nu_2)(\sigma_2-\sigma_1)}\right)$ σ^{+}_{bulk} and σ^{-}_{bulk} are the upper and lower bound, σ_1 and σ_2 are phase 1 and 2 conductivities & ν_2 is a volume fraction of phase 2
Waff Model [43]	$\sigma_{bulk} = \frac{\sigma_2+(\sigma_1-\sigma_2)(1-(2\nu_2/3))}{1+(\nu_2/3)(\sigma_1/\sigma_2-1)}$ σ_1 and σ_2 are phase 1 and 2 conductivities & ν_2 is a volume fraction of phase 2
Parallel Model [44]	$\sigma_{bulk} = \sum_{i=1}^{N} \nu_i \sigma_i$ σ_i and ν_i are the ith phase conductivity & fractional volume, respectively
Perpendicular Model [44]	$\frac{1}{\sigma_{bulk}} = \sum_{i=1}^{N} \frac{\nu_i}{\sigma_i}$ σ_i and ν_i is the ith phase conductivities & fractional volume, respectively
Brick-layer Model [45] [46]	$\sigma_{bulk} = \frac{\sigma_2(\sigma_2(\nu_1^{2/3}-1)-\sigma_1\nu_1^{2/3})}{\sigma_1(\nu_1-\nu_1^{2/3})-\sigma_2(\nu_1^{2/3}-\nu_1-1)}$ $\sigma_1$and σ_2 are phase 1 and 2 conductivities & ν_1 is the volume fraction of phase 1
Random Model [47] [48]	$\sigma_{bulk} = \prod_{i=1}^{N} \sigma_i^{\nu_i}$ σ_i and ν_i are the ith phase conductivity & fractional volume respectively
Archie's Law [49]	$\frac{1}{\sigma_{bulk}} = aS^{-n_s}\phi^{-m_{cf}}\frac{1}{\sigma_{fluid}}$ σ_{fluid} is fluid conductivity, ϕ is porosity, m_{cf} is cementation factor, S is fraction saturation, n_s is the saturation exponent & a is the tortuosity factor
Arrhenius Relationship or Semi-conductor Equation [50]	$\sigma_{bulk} = \sigma_o e^{-a_e/k_c T}$ σ_o is the zero temperature conductivity, a_e is the activation energy, k_c is the Boltzmann's constant & T is absolute temperature

Note: for all equations σ_{bulk} is bulk conductivity.

different conducting phases with an applied parallel electric field. The bulk conductivity is then given by the arithmetic mean of each conductive phase, weighted by their fractional volume. Conversely, a perpendicular (transverse) model is the same except the electric field is applied perpendicular (transverse) to the layers and a harmonic mean is used. The brick-layer model assumes the phase configuration lies between the extreme parallel and perpendicular models and uses a combination of the two models [45] [46]. Finally, there is the random model that assumes a random distribution of phases with unknown connectivity [47] [48]. Here the bulk conductivity is given by the geometric mean, weighted by the volume fractions of each phase.

Conductivity relations have also been based on fitting experimental observations. The main empirical relationships are Archie's Law and the Arrhenius relationship, also known as the semi-conductor equation. Archie's Law is routinely used for sedimentary rocks and assumes that the rock matrix is an insulator so that the transmission of charge occurs only in the formation fluid. The bulk conductivity in Archie's Law is based on the fluid conductivity, porosity and a formation factor that accounts for the shape of the void space [49].

The Arrhenius relationship is used for mantle materials and relates bulk conductivity to temperature [50]. Constable *et al.* [56] used the Arrhenius relationship to model laboratory conductivity values of olivine. This was later updated to the SO3 model [57]. However, conductivity of mantle material depends on magnesium content, oxygen fugacity, pressure, hydration and connection of conducting phases as well as temperature [58]. The Arrhenius relationship can accommodate these factors. Hirsch *et al.* [59] incorporated iron content into an olivine model and Constable [57] considered oxygen fugacity in conductivity measurements of olivine.

2.1.3 Magnetotelluric Summary

Magnetotellurics is a passive electromagnetic technique sensitive to resistivity. The magnetic and electric fields behave diffusively in the subsurface for the source frequencies used by MT. The depth of penetration of the magnetic and electric field in a homogeneous half space is given by the skin depth equation (Equation 2.20). Surface

measurements of the orthogonal components of the horizontal electric and magnetic field at different frequencies are related to the subsurface resistivity through an impedance tensor (Equation 2.28), from which the apparent resistivity and phase values can be calculated (Equations 2.29 and 2.30). There is a non-linear relationship between the subsurface resistivity and the MT response. For a 2D Earth, the MT response can be split into two differently polarised modes, the TE and TM modes.

Bulk conductivity can be quantified in terms of different constituent conductivities for Earth materials or empirical relationships (Table 2.1). This will be used in Section 5.2 when determining the equation to use in the petrophysical joint inversion.

2.2 Gravity

Gravity is a popular and simple passive geophysical technique that yields information on the subsurface density distribution [60] [61]. The first gravity survey was conducted on Lake Balaton in 1901 [62]. It is now routinely used for crustal research as well as being a key technique in both mineral and petroleum exploration. For the latter, its use is mainly restricted to determining broad regional structure and thickness of sedimentary basins. In this section the basic theory of the gravity technique and the density equations that will be used by the petrophysical joint inversion (Chapter 6) are summarised.

2.2.1 Basic Gravity Theory

Gravity Principles

Gravity is a fundamental force in nature. Its importance was first discovered in the late 15th century by Sir Isaac Newton who developed the famous law of universal gravitation, which states [63],

"Every particle in the universe attracts every other particle with a force that is proportional to the product of their masses and inversely proportional to the square of the distance between them. This force acts along the line joining the two particles."

The gravitational force is expressed by

$$\mathbf{F}_g = G_c \left(\frac{M_1 M_2}{r^2} \right) \widehat{\mathbf{r}} \quad , \tag{2.37}$$

where $\mathbf{F}_g$ is the gravitational force in N, G_c is the gravitational constant of 6.67×10^{-11} $\text{Nm}^2\text{kg}^{-2}$, M_1 and M_2 are the masses of the two particles in kg, r is the distance between the two particles with units of m and $\widehat{\mathbf{r}}$ is the unit vector that points from particle 1 to particle 2. The gravitational force is an attractive force which acts at a distance. Linearity applies, such that if a mass has one or more gravity forces acting on it then the net force is the sum of the individual forces [35].

Equation 2.37 can be applied to a mass at the Earth's surface. Here, $M_1 = M_e$, the mass of the Earth, M_2 is the mass of the object at the Earth's surface and r_e is the radius of the Earth. The gravitational force becomes

$$\mathbf{F}_g = G_c \left(\frac{M_e M_2}{r_e^2} \right) \widehat{\mathbf{r}} \quad . \tag{2.38}$$

Gravitational acceleration due to the Earth can be derived from Equation 2.38. Force equals mass multiplied by acceleration ($\mathbf{F}_g = M\mathbf{a}$), therefore the gravitation acceleration vector ($\mathbf{g}$) can be expressed as

$$\mathbf{g} = \frac{\mathbf{F}_g}{M_2} \quad . \tag{2.39}$$

The SI unit of acceleration is ms^{-2}. In the CGS system gravitational acceleration is given in cms^{-2}, and this unit is known as a Gal (named after Galileo). However, gravity values are normally expressed as mGals which is 10^{-3} cms^{-2} = 10^{-5} ms^{-2}. Substituting Equation 2.38 into Equation 2.39 it follows that $\mathbf{g} = g_z \widehat{\mathbf{z}}$ with

$$g_z = G_c \frac{M_e}{r_e^2} \quad , \tag{2.40}$$

where the direction of acceleration is directed vertically towards the Earth.

The gravitational force produces a conservative field. This means the work done by a moving mass is only dependent on its starting and end point, it is independent of the path taken between the points. As a result the gravitational force and acceleration can be expressed in terms of a gravitational potential U_g,

$$\nabla U_g(r) = -\frac{\mathbf{F}_g(r)}{M_2} = -\mathbf{g}(r) \quad , \tag{2.41}$$

or alternatively,

$$U_g(r) = -\int_{\infty}^{r} \mathbf{g}(r)\, dr \quad . \tag{2.42}$$

This scalar potential describes the ability for a mass to do work at a particular location in a gravity field.

When determining the gravitational acceleration due to an arbitrary mass it is often easier to determine the scalar potential and then relate this back to the gravitational acceleration via Equation 2.41. To calculate either the scalar potential or the acceleration of an arbitrary mass, the mass is divided into small elements and the response of each is calculated. The total response is then the sum of the individual element responses. An example of calculating the gravity response of an arbitrary 3D body, as shown in Figure 2.3, starts by combining Equations 2.40 and 2.42, which gives

$$U_g(r) = -G_c \int_{\infty}^{r} \frac{M}{r^2} dr = G_c \frac{M}{r} \quad . \tag{2.43}$$

Therefore, the potential dU_g, at $\mathbf{P}(0,0,0)$ from a small element of the 3D body at point (x, y, z) with mass dM is

$$dU_g = -G_c \frac{dM}{r} = G_c \rho dx dy dz / r \quad , \tag{2.44}$$

where ρ is the density of the element in kgm^{-3} and $r^2 = x^2 + y^2 + z^2$ is the distance from $\mathbf{P}$ to the element. The total potential of the 3D body is the sum or integral of the potential of the individual elements and is given by

$$U_g = -G_c \int_x \int_y \int_z \frac{\rho}{r} dx dy dz \quad . \tag{2.45}$$

Note that ρ is a function of x, y, z, so the integral cannot be evaluated unless the functional form of $\rho(x, y, z)$ is given. The gravitational acceleration from Equa-

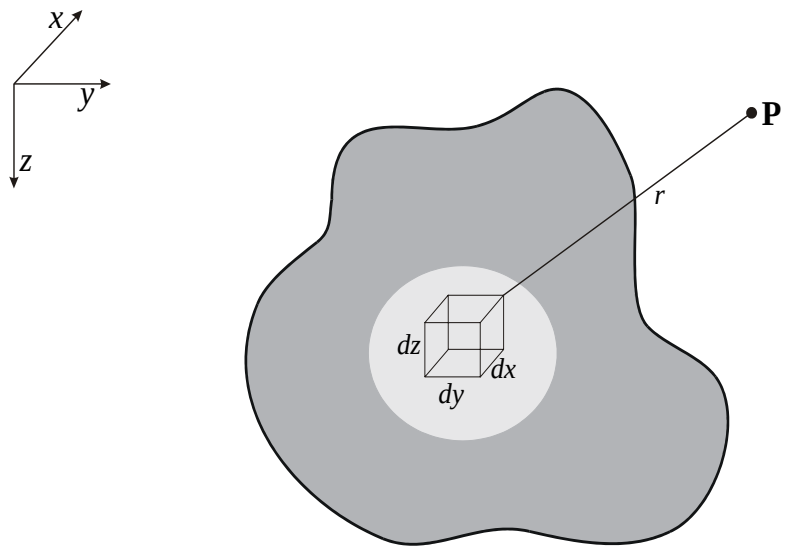

Figure 2.3: The configuration for calculating the potential at point **P** of a 3D mass, which involves dividing the mass into smaller elements.

tion 2.42 in the vertical (z) direction is

$$g_z = -\frac{\partial U_g}{\partial z} \quad . \tag{2.46}$$

Substituting Equation 2.45 into Equation 2.46 and assuming constant ρ gives an expression for the vertical gravitational acceleration,

$$g_z = -\frac{\partial U_g}{\partial z} = G_c \rho \int_x \int_y \int_z \frac{z}{r^3} dx dy dz \quad . \tag{2.47}$$

Equation 2.47 shows gravity expressed in the form of the Fredholm integral equation of the first order and shows the linear relationship between vertical gravitational acceleration and the density of a body.

An alternate expression for the scalar potential can be derived using Gauss' divergence theorem,

$$\int_\nu \nabla \cdot \mathbf{g} d\nu = \int_{s_f} \mathbf{g}\widehat{\mathbf{n}} ds_f \quad , \tag{2.48}$$

where ν is a volume, s_f is a surface and $\widehat{\mathbf{n}}$ is the unit normal to the surface element ds_f. Equation 2.48 states that the integral of the divergence of the gravity vector

$(\nabla \cdot \mathbf{g})$ over a volume, is equal to the surface integral of the component of the field that is normal to the surface, provided the surface encloses the volume. If there is no mass inside the volume, then $\nabla \cdot \mathbf{g} = 0$, which leads to

$$-\nabla \cdot \mathbf{g} = \nabla \cdot \nabla U_g = \nabla^2 U_g = 0 \quad . \tag{2.49}$$

However if there is mass at the centre of a sphere with radius r then

$$\int_{s_f} \mathbf{g}\widehat{\mathbf{n}} ds_f = -\left(G_c \frac{M}{r^2} \right) (4\pi r^2) = -4\pi G_c M \quad . \tag{2.50}$$

This can be shown to be true regardless of the shape of the surface and the position of the mass [6]. In Equation 2.48, if the volume is very small and enclosing only a point mass the integral can be removed, giving

$$\nabla \cdot \mathbf{g} = -4\pi G_c \rho \quad , \tag{2.51}$$

where ρ is the density of the point mass. It then follows that

$$\nabla^2 U_g = 4\pi G_c \rho \quad . \tag{2.52}$$

Equations 2.49 and 2.52 are the Laplace and Poisson equations respectively. The gravitational potential adheres to the Laplace equation in free space and the Poisson equation in regions containing mass. There is no time dependency in the Laplace or Poisson equations, which means the potential field is static.

Gravity is inherently non-unique as there are multiple density distributions that can produce the same potential over a surface. There is no explicit depth resolution as the potential, or acceleration, is only dependent on the distance from a mass, irrespective of direction. The simplest density distribution from which to reconstruct the potential or gravitational acceleration is an infinitely thin layer at the surface, having lateral variations [64].

Gravity of the Earth

Average gravitational acceleration values at the Earth's surface is approximately 981 Gals. To measure absolute gravity value a pendulum or a free falling mass are needed. Generally, relative gravity values are measured using gravity meters, such as the LaCoste and Romberg gravity meters. Current instrumentation has an accuracy of $0.03-0.06$ mGals [6]. Whichever type of gravity meter is used, corrections need to be made to account for instrument drift and the platform on which the measurement was made (e.g. the Eötvös correction for surveys made on a moving platform).

The magnitude of the gravity reading depends on five factors: latitude, elevation, surrounding topography, Earth-tides and variations in the subsurface density [6], of which only the last factor is of significance for exploration and crustal research. However, the response of the subsurface density variation is significantly smaller than that of the other factors combined. Therefore, the other four factors need to be corrected for, or removed, to be able to isolate the response of the subsurface density distribution. The Bouguer gravity anomaly term is used to refer to data which have undergone these corrections.

The latitude correction accounts for the variations in gravity values due to the non-spherical shape of the Earth, resulting from centrifugal force caused by the Earth's rotation. The free-air correction reduces the gravity values to a common reference elevation datum, which is typically mean sea level. However, the free air correction does not account for the mass between these different elevations, which is corrected for by the Bouguer correction. Terrain corrections allow for the changes in mass due to topographical variations. Earth-tides corrections account for the movement of the Moon and Sun. Correcting for the Earth-tide is generally combined with correcting for instrument drift and requires returning to a base station to make a measurement at regular intervals. Isostasy and the isostatic correction allow for the isostasy variations in the crust, and are of secondary importance.

Bouguer gravity data become Bouguer anomaly gravity data if a gravity reference model is subtracted from it [6]. There are two gravity reference models: the reference spheroid and the geoid, which generate theoretical gravity values for the whole Earth. The reference spheroid derives gravity values based on an oblate ellipsoid of mean

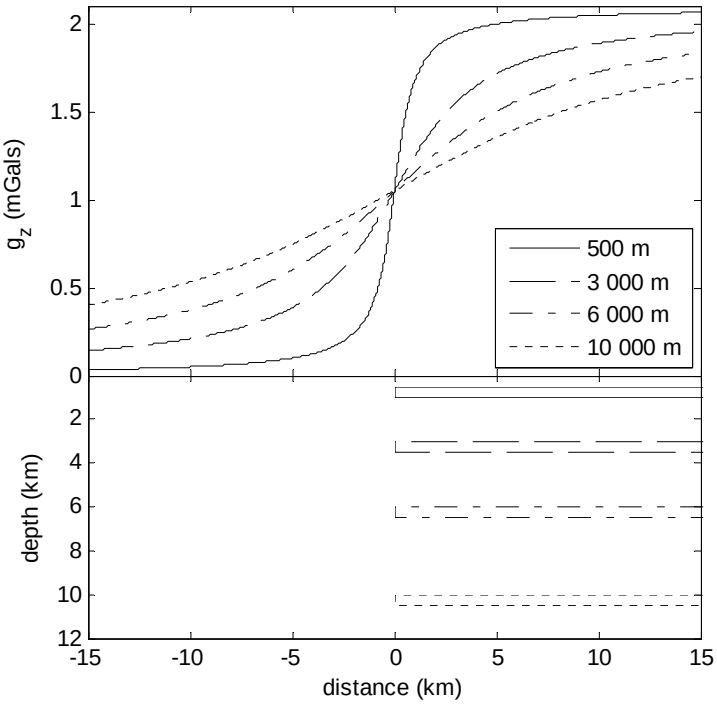

Figure 2.4: The gravitational response of a horizontal sheet at different depths of burial. The wavelength of the gravity response increases with increasing depth of burial.

sea level and can be used to make the latitude correction. The geoid is the average sea level surface for oceans and for the continents, assuming all mass above mean sea level is removed. Bouguer anomaly gravity can be tied in to national networks through the use of land calibration stations, such as the Australian Fundamental Gravity Network [65].

The nature of Bouguer anomaly data mean they only contain information about the density contrast of the subsurface relative to an unknown background density. A reference density point, such as data collected in wells, can be used to determine the background density and therefore the absolute density of the subsurface [66]. Bouguer anomaly data are only sensitive to lateral variations in density, since a 1D density distribution does not produce a gravity anomaly. In a situation where there are no lateral variations in density, Bouguer anomaly data of adjacent stations are identical.

The spatial wavelengths in a Bouguer anomaly pattern can give an indication of

the depth of burial of the anomalous mass (Figure 2.4), with deeper bodies yielding longer wavelength anomalies. There are numerous methods for estimating the depth of burial of causative bodies from the wavelength in potential field data, with a popular method being Euler decomposition [67]. The spatial wavelengths in a gravity response can be decomposed into a regional and residual component [68]. The regional response is usually the unwanted long wavelengths from large scale deep structures. Short wavelength residual responses, due to shallow density variations, are superimposed on this. The scale of the survey dictates what are the regional and what are the residual components.

2.2.2 Density Equations

Only a few equations have been used to quantify the behaviour of density, independent of elastic and seismic parameters (Table 2.2). The porosity-density relationship is an analytical expression for the bulk density of sedimentary rocks. It assumes rock is composed of two phases, fluid and solid. The void space or porosity between the rock matrix is assumed to be saturated with fluid. The bulk density is the sum of the fluid density and matrix density, appropriately weighted by porosity. Lee [69] calculated the bulk density of the mantle mineral peridotite. Lee [69] first determined the mineral composition, then the density of each mineral was calculated based on a function of the mineral compositional molar volumes. Finally, the mineral densities were weighted by their fractional volume and summed to give the bulk density. The density of mantle minerals at high temperatures can be linked to temperature through the High Temperature Model [70]. Through laboratory analysis of mantle minerals Jordan [71] found a linear relationship between the bulk density and the magnesium number (Mg#). The magnesium number is the ratio of magnesium and the magnesium plus iron content (note the iron number, Fe#, is the ratio of iron and iron plus magnesium content).

2.2.3 Gravity Summary

Gravity is sensitive to density variations in the subsurface and is an inherently non-unique technique with limited depth resolution. The gravitational potential satisfies

Table 2.2: Summary of the density equations.

Name	Equation
Porosity-Density Relationship	$\rho_{bulk} = \phi\rho_{fluid} + (1-\phi)\rho_{matrix}$ where ρ_{bulk} is the bulk density, ϕ is porosity, ρ_{fluid} is the pore fluid density & ρ_{matrix} is the matrix density
Mg# Density Model [69][71]	$\rho_{bulk} = c_1\text{Mg\#}+c_2$ where c_1 and c_2 are constants of density specific to mantle minerals & Mg# is the magnesium number
High Temperature Model [70]	$\rho_{bulk} = \rho_o e^{-\int_{T_o}^{T}\alpha_e(T')dT'}$ where T_o is the reference temperature, ρ_o its density & α_e is the expansion coefficient
Summation Model [69]	$\rho_{bulk} = \sum_{i=1}^{N}\rho_i\nu_i$ where ρ_i and ν_i are the density and fractional volume of the ith phase

Note: for all equations ρ_{bulk} is bulk density.

the Laplace equation in free space and the Poisson equation in regions containing mass. There is a linear relationship between the subsurface density and the gravity response. The total response of a body can be calculated by dividing the body into small elements and summing their responses. The gravity response is expressed as Bouguer anomaly data, which only contain information about the variation in subsurface density and not the absolute density values.

Bulk density can be quantified in terms of different constituent densities for Earth properties. These will be used in Section 5.2 to determine the equations to be used in the petrophysical joint inversion.

2.3 Conclusions

This chapter has provided the governing equations for the MT and gravity techniques. Gravity satisfies the Laplace and Poisson equations which produce a static field. However, the electric and magnetic fields in MT satisfy the diffusion equation, which is frequency dependent. The MT technique has depth resolving capabili-

ties whereas gravity is inherently non-unique and only responds to lateral variations. There is a simple linear relationship between density and its gravity response, whereas the relationship between the MT response and resistivity is highly non-linear.

Chapter 3

Magnetotelluric and Gravity Inversions

Mathematically, an inversion is a type of non-linear optimisation scheme which seeks to estimate the model parameters that provide the best fit between the computed model response and the observed data. Inversions are routinely applied in geophysics to measured field quantities in order to produce a model representation of the subsurface. Based on these idealised physical models, knowledge is gained about the subsurface and geological inferences and interpretations can be made. Therefore, the reliability and characteristics of an inversion are important in successfully delineating the subsurface geology. This chapter outlines the theory behind the different inversion schemes and reviews common approaches used for MT and gravity techniques. The most appropriate optimisation scheme for the joint inversion is then selected and described in some detail.

3.1 Inversions

Inversions are commonly applied to MT data but to a lesser extent on gravity data. The reason for this is the higher degree of non-uniqueness when working with potential field data [6]. The type of inversion scheme normally used is a local minimisation search approach, in which an initial guess model is progressively refined until a best fit is obtained. The global solvers, such as the Monte Carlo method,

simulated annealing and genetic algorithms, which explore the entire model space, can only cope with a limited number of model parameters and are computationally very expensive, especially for 3D models. Therefore, in this section only the basic theory of local minimisation approaches are covered; this is followed by a review of the single MT and gravity inversion methods.

3.1.1 Inversion Theory

For continuous data, the geophysical response can be expressed as a Fredholm integral equation of the first kind [72],

$$d(x) = \int_I G(x,y)m(y)dy \quad . \tag{3.1}$$

Here G is the kernel that describes the physics of the process, d is the continuous data and m are the model parameters. When discretised, the relationship for sampled data can be expressed as a system of equations, or in matrix form as

$$\mathbf{F}[\mathbf{m}] = \mathbf{d} \quad , \tag{3.2}$$

where $\mathbf{d} = (d_1, d_2, ..., d_q)$ is the data vector consisting of q observed data points, $\mathbf{m} = (m_1, m_2, ..., m_n)$ is a model vector of n model parameters and $\mathbf{F}$ is the $q \times n$ forward model operator that predicts (computes) the geophysical data for a particular model. The forward model operator or kernel provides the link between the data and the model spaces. Together the model parameters and the forward model operator ($\mathbf{F}[\mathbf{m}]$) give the model response, which ideally equals the observed data. The forward model operator for each geophysical technique is based on the governing or defining physics of the problem. Depending on the technique under consideration, the forward model operator can be expressed as either a linear (e.g., straight ray tomography) or non-linear relationship (e.g. curvilinear tomography) between the model parameters and the model response. Hereafter, these will be referred to as linear or non-linear forward model operators.

An inversion seeks to determine the model parameters $\mathbf{m}$, which are a solution to Equation 3.2 and are representative of the true geological model, $\mathbf{m}_{true}$. Concep-

tually, the corresponding inverse operator $\mathbf{F}^{-1}$ can be used to estimate the model parameters $\mathbf{m}^{est}$ from the observed data $\mathbf{d}^{obs}$,

$$\mathbf{m}^{est} = \mathbf{F}^{-1}(\mathbf{d}^{obs}) \quad . \tag{3.3}$$

However, in most geophysical techniques there is not enough information in Equation 3.2 to uniquely define all model parameters.

By its very nature, geophysical data are discrete, incomplete and subject to error (i.e. contain noise). Having discrete data, but more importantly noisy data, means that there are multiple models that can equally replicate or match the data to a given tolerance level [73]. Furthermore, these models may not resemble the true nature of the Earth [72]. Data errors can be incorporated into the inversion process through the maximum likelihood method and use of a weighting matrix. If the errors are independent and normally distributed, Equation 3.2 becomes

$$\mathbf{W}_d\mathbf{F}[\mathbf{m}] = \mathbf{W}_d\mathbf{d} \quad , \tag{3.4}$$

where $\mathbf{W}_d = diag\left(\frac{1}{\sigma_1^*}, \frac{1}{\sigma_2^*}, \ldots, \frac{1}{\sigma_m^*}\right)$ is the weighting matrix and the σ^* values denote the estimated standard deviations of each point [74]. If a standard deviation (estimated error) is large, then the reliability of that measurement is low and it is down-weighted in the inversion. Conversely, if the estimated error or uncertainty is small, the reliability is high and those data points get greater emphasis or weighting in the inversion.

Obtaining a solution to the geophysical inverse problem (Equation 3.4) depends on the nature of the forward model operator, $\mathbf{F}$. If matrix $\mathbf{F}$ is small, linear and non-singular (well conditioned), then the model parameters can be obtained by calculating the inverse of $\mathbf{F}$, using an approach such as singular value decomposition (SVD) [74]. If the condition number (i.e. ratio of largest to smallest eigenvalues) of $\mathbf{F}$ is large, then the inverse $\mathbf{F}^{-1}$ cannot be taken without first stabilising it through the introduction of some damping or regularisation; this involves adding values to the diagonal elements of $\mathbf{F}$ [74]. Alternative approaches that can be applied to both linear and non-linear forward model operators are based on selecting the 'best'

model that minimises the fit between the observed data and the model response. The measure of fit is determined by the norm. The most commonly used norms are the l_p-norms (e.g. $p = 1, 2, \infty$). The l_1-norm (sum of the absolute values) is robust to outliers, however, it is not continuously differentiable and is complex to minimise. The l_2-norm or the Euclidean norm has more desirable characteristics and is the most widely used in geophysics [75]. In this thesis only the l_2-norm will be considered. For the fit between the observed data and model response the l_2-norm is given by

$$U_d(m) = ||\mathbf{W}_d(\mathbf{d} - \mathbf{F}[\mathbf{m}])||^2 = \sqrt{\sum_{i=1}^{m} W_{d_i}\{d_i - \mathbf{F}[\mathbf{m}]_i\}^2} \quad , \tag{3.5}$$

where $U_d(m)$ is the data norm, $\mathbf{F}[\mathbf{m}]$ is the model response and $\mathbf{W}_d$ is a symmetric data weighting matrix.

The $\mathbf{W}_d$ matrix can have many forms. In Equation 3.4, $\mathbf{W}_d = C_d^{-1}$, the inverse covariance matrix, where the covariance matrix is a diagonal matrix of the data uncertainty. If such a $\mathbf{W}_d$ matrix is used in Equation 3.5 then the problem is referred to as generalised least squares. Alternatively, if $\mathbf{W}_d = \mathbf{I}$ (the identity matrix) the problem is referred to as common least squares [76]. The least square solution to Equation 3.5 can be expressed as $\mathbf{m} = (\mathbf{F}^T\mathbf{W}_d\mathbf{F})^{-1}\mathbf{F}^T\mathbf{W}_d\mathbf{F}\mathbf{d}$ if the forward model operator is linear [74]. However, schemes such as the Marquardt method [77] or creeping methods [78] [79] can be used to find a solution if $\mathbf{F}$ is non-linear. All solutions of the data norm are characteristically very rough.

There exist multiple and potentially different models that fit the data norm (Equation 3.5) equally well. A further complication is with the presence of noise, as it may be noise as well as signal being fitted. To counteract these problems, and to help stabilise the solution, optimisation algorithms can use a model regularisation term or have certain constraints applied. This is where a solution is sought that fits the data subject to a model criteria. The model criteria is expressed in the regularisation term or model norm,

$$U_m(m) = ||\mathbf{W}_m(\mathbf{m} - \mathbf{m}_0)||^2 = \sqrt{\sum_{i=1}^{n} W_{m_i}(m_i - m_{0i})^2} \quad , \tag{3.6}$$

where $U_m(m)$ is the model norm, $\mathbf{W}_m$ is the symmetric model weighting matrix, $\mathbf{m}_0$ is the reference or starting model parameters and $\mathbf{m}$ is the model parameters to be determined. The $\mathbf{W}_m$ matrix encapsulates the type of model desired by the inversion or incorporates *a priori* information. Generally, a model closest to some preferred model or a smooth or minimum roughness model is sought. To obtain information on model roughness, a first or second order differential operator can be used, such as $\mathbf{W}_m = \underline{\partial}^T\underline{\partial}$ where $\underline{\partial}$ is a difference operator [80] or for a 2D model $\mathbf{W}_m = \varpi_0\mathbf{I} + \varpi_y\underline{\partial}_y^T\underline{\partial}_y + \varpi_z\underline{\partial}_z^T\underline{\partial}_z$ where ϖ_0, ϖ_y and ϖ_z are constants and y and z are spatial directions (an extra term can be added for a 3D model) [81].

In general, the data and model norms are combined in the objective function $U(m)$, which is also known as the misfit or cost function. A model solution is then sought that minimises this function. Adding these terms together, after appropriate weighting, ensures that the "fit" of the model is evaluated in both the data space and the model space. When the data and model spaces are linear, the units of the data space are that of the measured data and the units of the model space are that of the model parameters. Data and model spaces can also be transformed, such as taking the logarithm of the model parameters. Transforms are used to better accommodate characteristics of the data or model parameters, and to maintain a relationship between the data and model parameters.

The addition of the model norm in the objective function introduces a bias into the optimisation scheme, as it will only produce models of the type described in the model norm. This means that unless the true model has the same model characteristics as the model norm, the inversion will not be able to faithfully reconstruct the true model. The bias also has an ill-effect on categorising the model parameter confidence intervals, which is not attempted in this thesis and therefore will not be discussed further.

The aim of an optimisation scheme is to find the model that minimises the objective function. The minimising model must be a stationary (minimum) point of the objective function. Stationary points occur when the objective function is differentiated with respect to the model parameters and found to be equal to zero,

$$\frac{\partial U(m)}{\partial m} = 0 \quad . \tag{3.7}$$

Finding a model solution directly from Equation 3.7 can be difficult if $\mathbf{F}$ is non-linear, because the derivative can only be evaluated for a single set of model parameters [75]. As a result, iterative schemes are used to obtain a model solution.

Iterative schemes search the model space by updating the model parameters based on the previous model and the Fréchet derivatives (Figure 3.1). The Fréchet derivatives are important as they are used to determine by how much each model parameter should be updated. The updated model should minimise the objective function more than the previous model. Updating the model parameters continues until the iterative scheme converges to a minimum or until no further improvement occurs. The minimum is global if the model gives the absolute minimum of the objective function. As shown in Figure 3.1, a local minimum can also occur, causing the iterative scheme to converge to an undesirable solution that is not the absolute minimum. A convex model space will guarantee there exists only one minimum which is global [74].

The objective function can contain different combinations of the data and model norms. Here two popular approaches will be discussed: the Tikhonov Regularisation and the Occam inversion.

Tikhonov Regularisation

The objective function of the Tikhonov Regularisation is given by

$$U_{Tik}(m) = U_d(m) + \lambda U_m(m) \quad , \tag{3.8}$$

where λ is the regularisation parameter, also known as the trade off or damping parameter [30]. The regularisation parameter controls the balance between fitting the data and the model criteria. When λ is large, U_{Tik} is dominated by fitting the model criteria. However when λ is small, U_{Tik} is dominated by fitting the data. The λ value is fixed to an arbitrary value prior to the inversion. It does have an optimal value which is unknown, since it depends on noise in the observed data and

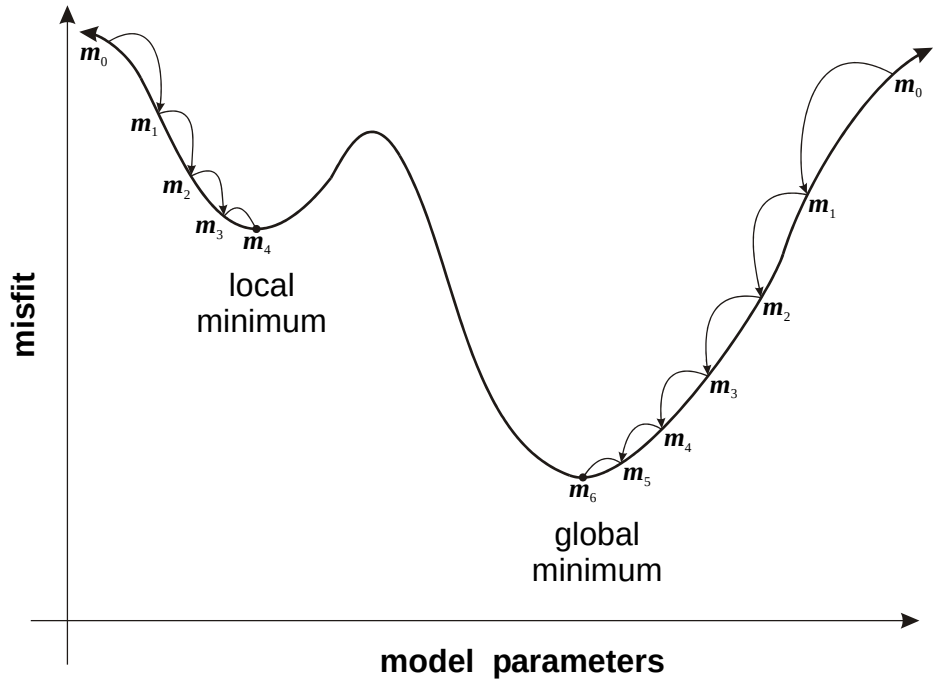

Figure 3.1: A schematic of an iterative search of the model space. The search on the right converges to the global minimum, whereas the search on the left gets trapped in a local minimum.

the bounds of the exact solution [82].

The Tikhonov Regularisation solution is found by taking the derivative of U_{Tik} with respect to the model parameters and setting the resulting expression equal to zero. From the definitions of the data and model norms (Equations 3.5 and 3.6, respectively) this is possible and yields

$$\lambda \mathbf{W}_m(\mathbf{m} - \mathbf{m}_0) = \mathbf{J}^T \mathbf{W}_d(\mathbf{d} - \mathbf{F}\mathbf{m}) \quad , \tag{3.9}$$

where $\mathbf{J} = \frac{\partial Fm}{\partial m}$ is the $q \times n$ Jacobian or sensitivity matrix, which comprises the Fréchet derivatives of the model response with respect to the model parameters. The Jacobian contains information on the perturbation (i.e. likely change) of the data for a given perturbation of each model parameter.

There are different iterative methods available to solve Equation 3.9. Of interest are the general iterative scheme, the iteratively linearised scheme and the conjugate gradient solvers [75]. The general iterative scheme is obtained by adding

$\left(\frac{\partial d}{\partial m}\right)^T \mathbf{W}_d \left(\frac{\partial d}{\partial m}\right) (\mathbf{m} - \mathbf{m}_0)$ to both sides of Equation 3.9 and, provided $\mathbf{W}_m$ is invertible, this yields [75]

$$\begin{aligned} & \left[\mathbf{W}_m^{-1}\mathbf{J}^T\mathbf{W}_d\mathbf{J}_0 + \lambda\mathbf{I}\right](\mathbf{m} - \mathbf{m}_0) \\ = \; & \mathbf{W}_m^{-1}\mathbf{J}_0^T\mathbf{W}_d\left\{(\mathbf{d} - \mathbf{F}\mathbf{m}_0) + \mathbf{J}_0(\mathbf{m} - \mathbf{m}_0)\right\} \quad . \end{aligned} \tag{3.10}$$

Isolating $\mathbf{m}$ on the left hand side, the following iterative scheme is suggested,

$$\begin{aligned} \mathbf{m}_{k+1} \; = \; & \mathbf{m}_k + \left[\mathbf{W}_m^{-1}\mathbf{J}_k^T\mathbf{W}_d\mathbf{J}_k + \lambda\mathbf{I}\right]^{-1} \\ & \times\mathbf{W}_m^{-1}\mathbf{J}_k^T\mathbf{W}_d(\mathbf{d} - \mathbf{F}\mathbf{m}_0) + \lambda(\mathbf{m}_0 - \mathbf{m}_k) \quad . \end{aligned} \tag{3.11}$$

The iteratively linearised scheme is based on linearising the forward model operator and then applying linear algebra to develop an iterative scheme [75] [80]. A Taylor series expansion is one method used to linearise the forward model operator, and is given to first order by

$$\mathbf{F}[\mathbf{m}] = \mathbf{F}(\mathbf{m}_0) + \mathbf{J}_0(\mathbf{m} - \mathbf{m}_0) \quad , \tag{3.12}$$

where $\mathbf{m}_0$ is the model about which the model response is linearised. When the Taylor series expansion is substituted into Equation 3.9, it follows that

$$\left[\mathbf{J}^T\mathbf{W}_d\mathbf{J}_0 + \lambda\mathbf{W}_m\right](\mathbf{m} - \mathbf{m}_0) = \mathbf{J}_0^T\mathbf{W}_d(\mathbf{d} - \mathbf{F}\mathbf{m}_0) \quad . \tag{3.13}$$

Isolating $\mathbf{m}$ on the left hand side, the following iterative scheme is suggested,

$$\begin{aligned} \mathbf{m}_{k+1} \; = \; & \mathbf{m}_k + \left[\mathbf{W}_m^{-1}\mathbf{J}_k^T\mathbf{W}_d\mathbf{J}_k + \lambda\mathbf{I}\right]^{-1} \\ & \times\mathbf{W}_m^{-1}\mathbf{J}_k^T\mathbf{W}_d(\mathbf{d} - \mathbf{F}\mathbf{m}_0) \quad . \end{aligned} \tag{3.14}$$

When identity weighting matrices are used, $\mathbf{W}_d = \mathbf{I}$ and $\mathbf{W}_m = \mathbf{I}$, in the iteratively linearised scheme, this becomes the Levenberg-Marquardt method [75].

Both iterative schemes in Equation 3.11 and Equation 3.14 are dependent on being able to obtain the inverse of a matrix $[\cdot]^{-1}$. Generally, the inverse will exist provided an appropriately large and positive value of the damping parameter λ is chosen [75].

The term $\lambda(\mathbf{m}_0 - \mathbf{m}_k)$ is the only difference between the general iterative scheme (Equation 3.11) and the iteratively linearised scheme (Equation 3.14). However, this results in each method searching the model space differently [75]. The iteratively linearised scheme keeps variations between $\mathbf{m}_{k+1}$ and $\mathbf{m}_k$ as small as possible at each iteration for a given λ value. On the other hand, the general iterative formula keeps the variations between $\mathbf{m}_{k+1}$ and $\mathbf{m}_0$ as small as possible at each iteration for a given λ value. The general iterative scheme yields a sequence of models close to the initial model $\mathbf{m}_0$, and produces significantly smoother results than the iteratively linearised scheme.

The general iterative scheme (Equation 3.11) and the iteratively linearised scheme (Equation 3.14) are forms of the steepest descent method. The steepest descent method updates the model according to

$$\mathbf{m}_{k+1} = \mathbf{m}_k - \widehat{\zeta}_k \cdot \widehat{o}_k \quad , \tag{3.15}$$

where $\widehat{o}_k$ is the vector of the direction of maximum decent and $\widehat{\zeta}_k$ is the scale of the step length [74] [75]. In the case of the general iterative scheme $\widehat{o}_k = \mathbf{W}_m^{-1}\mathbf{J}^T\mathbf{W}_d(\mathbf{d} - \mathbf{F}\mathbf{m}_0) + \lambda(\mathbf{m}_0 - \mathbf{m}_k)$ and $\widehat{\zeta}_k = \left[\mathbf{W}_m^{-1}\mathbf{J}^T\mathbf{W}_d\mathbf{J} + \lambda\mathbf{I}\right]^{-1}$. The updated search direction in the steepest descent method is orthogonal to the previous direction and results in a zig zag search path to the minimum of the model space.

Conjugate gradient (CG) methods can be used to solve the Tikhonov Regularisation problem and have better convergence properties than the steepest decent scheme [73]. Essentially, the CG methods are based on $n - 1$ conjugate search directions and it takes a step length in each direction so that by the last step it will line up exactly with the minimum in the model space [83]. The CG methods are implemented in a similar fashion to the steepest descent method, updating a model based on a search direction and an optimal step length. However, the updated search direction is in a conjugate direction to the last.

Occam or Smooth Model Inversion

The Occam or smooth model inversion seeks the smoothest model subject to fitting the data to some specified tolerance level χ [80],

$$\min(U_m(m)) \tag{3.16a}$$

$$U_d(m) = \chi_* \quad , \tag{3.16b}$$

where U_m describes smooth models through the $\mathbf{W}_m$ matrix. Smooth model inversion only allows sufficient structure required to fit the data into the model. Therefore, it avoids producing artifacts that can lead to misinterpretation. The unconstrained Occam problem (Equation 3.16), can be turned into a constrained optimisation problem using a Lagrange multiplier μ. The resulting objective function is

$$U(m) = U_m(m) + \mu^{-1}[U_d(m) - \chi_*] \quad . \tag{3.17}$$

A solution to the constrained problem (Equation 3.17) must satisfy the stationary conditions

$$\frac{\partial U}{\partial m} = \frac{\partial U_m}{\partial m} + \mu^{-1}\frac{\partial U_d}{\partial m} = 0 \tag{3.18a}$$

$$\frac{\partial U}{\partial \mu^{-1}} = U_d - \chi_* = 0 \quad . \tag{3.18b}$$

This is equal to

$$\mu^{-1}\mathbf{W}_m(\mathbf{m} - \mathbf{m}_0) = \mathbf{J}^T\mathbf{W}_d(\mathbf{d} - \mathbf{Fm}) \tag{3.19a}$$

$$(\mathbf{d} - \mathbf{Fm})^T\mathbf{W}_d(\mathbf{d} - \mathbf{Fm}) = \chi_* \quad . \tag{3.19b}$$

From Equation 3.17, μ can be likened to the Tikhonov Regularisation parameter λ, because they both control the balance between minimising the data and

model norms. Unlike λ, the quantity μ must satisfy both Equation 3.19a and Equation 3.19b. The non-linear nature of $\mathbf{F}$ makes finding an exact form or value for μ difficult.

A two-part sequence is used to find the solution to the Occam inversion problem. Firstly, it is noted that Equation 3.19a and the Tikhonov Regularisation (Equation 3.9) are the same for a fixed μ value. Therefore, a scheme used to solve the Tikhonov Regularisation, such as the iteratively linearised scheme, can be used to update the model. Secondly, an optimal value of μ is found that minimises the data norm. The optimal μ value depends on the data error level, model weighting, parameterisation used and the true model variation. It can be determined using methods such as the golden section search, L-curve or cross-validation [84].

Data space methods are becoming increasingly popular in determining a solution to inverse problems. All solutions presented until now have involved calculating $\mathbf{J}^T\mathbf{W}_d\mathbf{J}$, which is the $n \times n$ 'model space cross product' or weighted pseudo-Hessian matrix. However, the problem can be reformulated to find a solution based on the data space. Parker [79] showed that an iterative solution to Equation 3.8 can be expressed in terms of the rows of the Jacobian,

$$\mathbf{m}_{k+1} - \mathbf{m}_0 = \mathbf{W}_m\mathbf{J}_k^T\eta_{k+1} \quad , \tag{3.20}$$

where $\mathbf{W}_m\mathbf{J}^T$ is the basis function and η_{k+1} are the expansion coefficients. An expression for the coefficients can be obtained by substituting Equation 3.20 into Equation 3.9,

$$\eta_{k+1} = (\lambda\mathbf{W}_d + \mathbf{J}_k\mathbf{W}_m\mathbf{J}_k^T)^{-1}\widehat{\mathbf{d}}_k \quad , \tag{3.21}$$

where $\widehat{\mathbf{d}} = \mathbf{d} - \mathbf{F}[\mathbf{m}] + \mathbf{J}(\mathbf{m} - \mathbf{m}_0)$.

The solution is now in terms of $\mathbf{J}_k\mathbf{W}_m\mathbf{J}_k^T$, the $q \times q$ 'data space cross product'. The solutions derived from the model space and data space approaches are theoretically identical [85]. However, the number of equations solved to obtain a solution can be significantly different depending on the size of the model and data vectors. The dimensions of the 'data space cross product', $q \times q$, is usually much smaller in

practice than the 'model space cross product', $n \times n$, resulting in reduced computational cost. Data space methods can be applied to both the Tikhonov Regularisation inversion and the Occam inversion, depending on whether the λ value is fixed or calculated at each iteration.

When implementing any inversion there are three important factors to consider: solution existence, solution uniqueness and stability of the solution process [72]. In reality there always exists a solution to the inverse problem - the geological subsurface that generated the data. However, the validity of the physical assumptions made, the presence of noise and the mathematical model used may preclude generating a solution and this is generally reflected by a large misfit value [86]. Non-uniqueness was discussed previously and observed to stem from data error and the physics underlying the technique. Unstable inversions are referred to as ill-posed or ill-conditioned and occur when small changes to the data result in large changes in the model parameters. The resulting iterative scheme may exhibit wild oscillations in the model space. Constraints can be used to stabilise an inversion, as well as to reduce model non-uniqueness [72].

3.1.2 MT Inversion Review

The 1D MT inverse problem is one of the few geophysical problems where an analytical least squares solution exists. It is referred to as Parker's D^+ [86]. The inversion produces a model with a finite number of infinitely thin layers of specific conductance at different depths. Although there is no geological interpretation to the D^+ models, they can be used as an estimation of the maximum depth of resolution of a data set [9]. A geologically reasonable 1D model can be achieved by inverting for a discrete layered Earth. This was done by Wu [87] and Jupp and Vozoff [88] using non-linear least squares. Layered Earth inversions are generally unstable and to increase stability the number of layers needs to be restricted [9]. However, restricting or using the wrong number of layers can lead to a mis-representation of the subsurface structure. A more stable inversion that only produces structure required by the data is the 1D Occam inversion introduced by Constable *et al.* [80]. This 1D inversion seeks a smooth model that has a minimum difference between adjacent

layers. The 1D inversion approach of Smith and Booker [89] also sought a smooth model based on a model depth weighting function.

Inversions that generate smooth models have been extended to 2D. The 2D Occam inversion was developed by deGroot-Hedlin and Constable [90] and is a stable algorithm with good convergence properties. It was later reformulated by Siripunvaraporn and Egbert [91] as a data space method known as REBOCC. Smith and Booker [92] produced the rapid relaxation inversion (RRI) that uses a computationally economical approximation for the Jacobian matrix. Although it is fast, the method often fails to converge without user intervention [91]. Rodi and Mackie [93] developed an inversion scheme that produces a smooth model using a conjugate gradient method to solve the Tikhonov Regularisation.

Attempts have been made to produce sharp boundary 2D MT inversions. These types of inversions do not use a measure of roughness (smoothness constraint) in the regularisation term or, if they do, they require a decoupling of the regularisation term across any sharp boundary. A 2D MT sharp boundary inversion was first done by Jupp and Vozoff [94] who extended their 1D layered Earth inversion. Smith *et al.* [95] determined the boundary depths below individual stations and then interpolated them laterally, whereas deGroot-Hedlin and Constable [96] produced a variation of the Occam inversion to solve for sharp boundaries in a 2D cross section. Most recently, Farquharson [97] modified a typical smooth inversion algorithm to generate blocky, piecewise constant Earth models.

Increasing effort is being devoted to tackle the 3D MT inversion problem, primarily still working with smooth models [85] [93] [98]. The difficulty with 3D algorithms is the size of the model space and the computational time required to compute the Jacobian matrix. The currently published 3D inversion schemes are the Newman and Alumbaugh algorithm [98], which uses non-linear conjugant gradients, and the Siripunvaraporn *et al.* algorithm [85], which is an extension of their 2D data space inversion approach. There is also a commercially available 3D inversion software package (WinGLink), which is an extension of the Rodi and Mackie [93] 2D algorithm. For an extensive review of 3D inversion, the reader is referred to Avdeev [99].

Standard MT inversion, as practised today, is still predominately 2D, with the most common being the Occam inversion [90] and the Rodi and Mackie inversion [93], distributed in the commercial WinGLink package. Although 3D inversions are becoming increasingly popular, particularly Siripunvaraporn *et al.* [85], the actual algorithms are still being evaluated and verified by the EM community.

3.1.3 Gravity Inversion and Forward Modelling Review

The inversion of gravity data poses a problem because, being a potential field technique, it is inherently non-unique. There are an infinite number of density distributions that can fit the data equally well. One such distribution is an infinitely thin layer at the surface of laterally varying density [64], although such a solution can be rejected on geological grounds as totally implausible. Therefore, all gravity inversions must involve constraints or additional assumptions to reduce the number of acceptable models and make them geologically meaningful.

There are two common approaches to gravity inversion. The first accounts for a gravity anomaly by varying the geometry of the anomalous body and keeping a fixed density contrast with the surrounds. This gives a non-linear relationship between the gravity response and model parameters. Making assumptions about the geometry (shape, size) reduces the number of acceptable models. However, if the assumed geometry is wrong then the inversion can be misleading. Examples of regular geometric shapes to approximate a buried geologic structure include prisms, cylinders, spheres, and polygons, with the most common being the prism, from which more complicated bodies can be constructed by superposition. Bott [100] altered the depths to the base of a series of vertical prisms and through a trial and error process was able to determine the depth profile of a sedimentary basin. Formal inverse theory was applied by Oldenburg [101] to determine the thickness variations of an uneven 2D layer. Various other studies have extended the depth function idea [102] [103] [104]. As a slight variant on this approach, the unknown geometry of an isolated 2D or 3D causative body can be obtained by inverting for the location of polynomial vertices [105] [106].

The second approach to gravity inversion is to derive the subsurface density con-

trasts for a structure of fixed geometry. Generally, this is in the form of prisms that form a grid. Such a scheme yields a linear relationship between the gravity response and the density contrast model parameters. Green [107] applied the Backus-Gilbert approach and found models, that either minimised the departure from an initial model or used a variable weighting function. The constraint used by Last and Kubik [108] was to minimise compactness, and was the first weighting function to be based on the model parameters themselves. Guillen and Menichetti [109] extended this approach by also minimising the moments of inertia with respect to the centre of the body. These inversions have very specific constraints placed on the model and in many cases can only recover a single body. More complicated models can be recovered from a smooth 3D gravity inversion with a depth weighting function, as developed by Li and Oldenburg [64].

Since it is difficult to produce geologically meaningful results from an automatic gravity inversion, a common alternative is to simply carry out interactive forward modelling [6]. Such forward modelling entails a user defined model, which incorporates information from geology and other geophysical techniques, and then compares the model response to the actual observed data. The model can be adjusted on a trial and error basis to bring about a match between the computed and observed data. Analytical solutions to the forward problem exist for simple bodies such as spheres, cylinders and prisms. Such solutions can be readily incorporated into forward modelling programs for rapid calculation of the model response [6]. Talwani *et al.* [110] formulated the first computer-orientated gravity forward modelling equations that calculate the response of 2D bodies of polygonal cross sections. Initial 3D forward modelling by Talwani and Ewing [111] used thin irregular polygonal layers to build 3D bodies. However, the right rectangular prism [112] is now used to build complex 3D structures and is suited to finite difference grids. Finite element methods that use tetrahedral cells to construct 3D bodies were described by Barnett [113], whereas Okabe [114] used polygonal facets. Parker [115] offered an alternative to the spatial-domain approach. He performed the first gravity forward modelling using the Fourier transform, which was based on the convolution theorem and Green's functions.

3.1.4 Discussion

Consideration will now be given to pre-existing MT and gravity inversion approaches as reviewed above, with a view to determining the best scheme to be used in a joint inversion of MT and gravity data sets. In general, MT inversions use a smoothness constraint, which tends to smear boundaries and produce 'fuzzy images' of the subsurface. Yet, these smooth models can be justified since the MT technique is based on EM diffusion phenomena that naturally smears boundaries, being sensitive to the bulk resistivity and not so much to the actual discontinuities or boundaries in the subsurface resistivity distribution. The gravity inversions require strict constraints in the form of density contrasts, specific body geometries, minimising compactness or minimising the moments of inertia, and can generally only recover a single body. Constraints used for gravity inversions are specific to gravity and are not necessary for MT. Therefore, it is more desirable to base the joint inversion on an MT approach rather than a gravity approach. Further argument in support of an MT-based inversion approach is that gravity has a linear forward model operator that can exploit linear schemes. Such schemes can not be used for MT since its forward model operator is non-linear.

The MT inversions use either the Occam or the Tikhonov Regularisation formulations, such as the inversion approaches developed by deGroot-Hedlin and Constable [90] or Rodi and Mackie [93]. The Occam inversion is preferred because it determines the optimal trade off parameter (μ) value. For the Tikhonov Regularisation, which uses a fixed trade off (λ) value, multiple inversions with different λ values need to be executed to be able to determine the best value. The 2D Occam inversion [90] is favoured over the 1D Occam inversion [80] because a 1D model will not produce a Bouguer gravitational anomaly (lateral changes in density are required).

To summarise, the non-linear MT 2D Occam inversion developed by deGroot-Hedlin and Constable [90] will provide the basis for the joint inversion herein. This inversion method is a stable and rapidly converging scheme that is well accepted by the EM geophysical community. The specific details of the MT 2D Occam inversion are provided in the following section.

3.2 The Occam Inversion

The Occam inversion was first introduced by Constable *et al.* [80] to perform a 1D MT inversion. It was subsequently extended to 2D by deGroot-Hedlin and Constable [90]. The name Occam comes from Occam's Razor: "it is vain to do with more what can be done with fewer" [116]. In terms of geophysics, of all of the models capable of fitting the data, the simplest model, or model that requires the least spurious features not required by the data should be accepted. The Occam inversion achieves this by seeking a minimum structure or smooth model, subject to fitting the data to an acceptable tolerance. Smooth models only have features that depart from the simplest case (half space), as far as is necessary to fit the data. Therefore, only structure absolutely required by the data will appear, and the model cannot be over interpreted [80].

In this section the general aspects of the MT Occam scheme are discussed, followed by a discussion on those aspects specific for MT. This discussion forms the basis of the methodologies for the gravity and joint inversion schemes given in Chapters 4 and 6. This section is strongly based on the paper by deGroot-Hedlin and Constable and further details can be obtained from the original Occam papers [80] [90].

3.2.1 General Aspects

In Section 3.1.1 the general Occam inversion scheme was discussed. For the MT Occam inversion, the objective function is

$$U[\mathbf{m}] = \left\|\underline{\partial}_y \mathbf{m}\right\|^2 + \left\|\underline{\partial}_z \mathbf{m}\right\|^2 + \mu^{-1}\left\{\left\|\mathbf{W}_d\mathbf{d} - \mathbf{W}_d\mathbf{F}[\mathbf{m}]\right\|^2 - \chi_*^2\right\} \quad . \tag{3.22}$$

An iteratively linearised scheme is used to find a solution to this objective function and results in the model parameters being updated according to

$$\mathbf{m}_{k+1}(\mu) = \left[\mu\left(\underline{\partial}_y^T\partial_y + \underline{\partial}_z^T\underline{\partial}_z\right) + \left(\mathbf{W}_d\mathbf{J}_k\right)^T\left(\mathbf{W}_d\mathbf{J}_k\right)\right]^{-1}\left(\mathbf{W}_d\mathbf{J}_k\right)^T\left(\mathbf{W}_d\widehat{\mathbf{d}}_k\right) \quad . \tag{3.23}$$

In this section the general aspects of the MT Occam inversion are discussed and include the model parameterisation, data norm, model norm and searching for the Lagrange multiplier.

Model Parameterisation

The Occam inversion uses an over-parameterised 2D model, which means there are more model cells than degrees of freedom in the data (the number of independent data measurements). Under-parameterising the model has less cells than the degrees of freedom in the data and can cause structure to be suppressed, whereas over-parameterising the model can allow superfluous structure to appear [79]. In a normal least-squares sense, over-parameterisation of the model can result in an unstable inversion. However, the introduction of a smoothness constraint acts to stabilise the inversion, and the over-parameterisation then allows for smooth variation between different model cells.

The 2D model used by the Occam inversion is parameterised in terms of two grids, the regularisation grid and the finite element mesh, which remain fixed at each iteration. The two grids depicted in Figure 3.2 are described in Cartesian coordinates with the x-direction along strike, the y-direction across strike and the z-direction being depth (positive downwards).

The forward modelling is conducted on the finite element mesh. The structured finite element code used to calculate the MT response [117], requires the mesh to have a fine regular array of rectangular nodes to maintain its accuracy. Node spacing is also designed to aid the accuracy of the forward modelling code. The horizontal spacing is intended to be one-third of the skin depth and, since the EM fields decrease exponentially with depth, it has been found that a logarithmic depth scale is ideal [89]. There must be a node at the location of every MT station.

The model parameters correspond to the regularisation grid, which is made up of rectangular prisms of constant resistivity. The grid is terminated by an elongated prism at the bottom, to mimic a half space, and uniform layers laterally that extend to infinity. The regularisation cells are smaller than the data resolution length of MT, so their boundary locations do not affect the final inverted model. The cell size

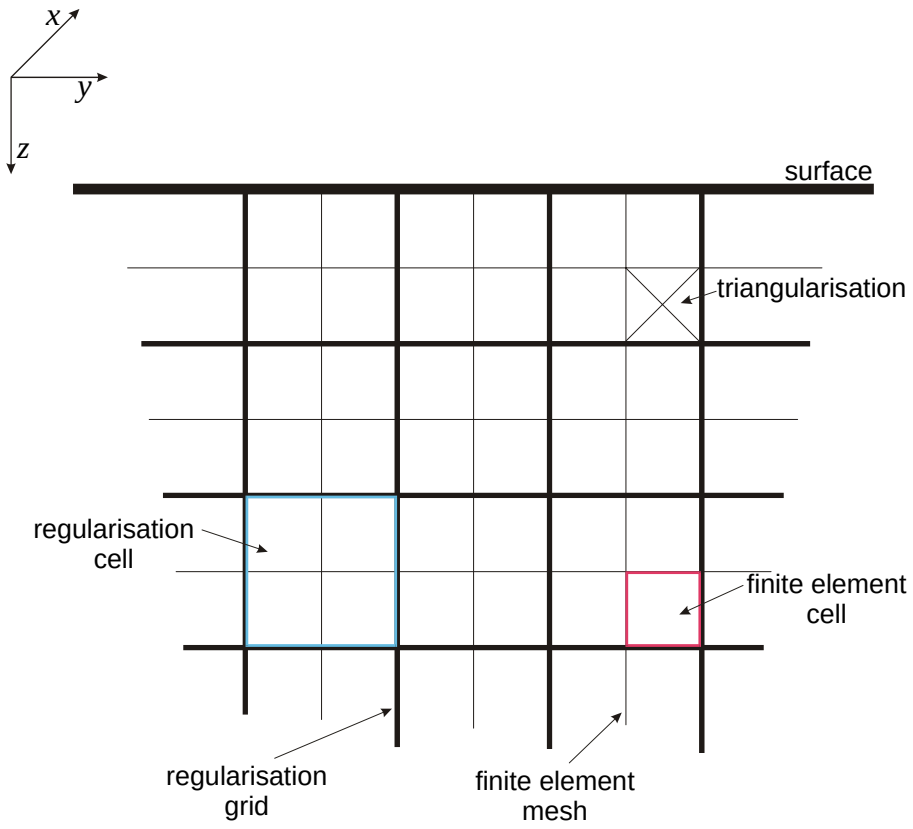

Figure 3.2: Configuration of the 2D grid system used by the Occam inversion. The regularisation grid is marked by the bold lines and the finite element mesh by the regular lines. The triangularisation configuration is indicated.

can increase with depth to account for the loss of resolution with depth.

The regularisation grid must be a subset of the finite element mesh, so that there is a node at every resistive regularisation cell boundary. The reason behind the two grid system is to be able to accurately calculate the MT response, which needs many nodes across a resistivity boundary, and still maintain computational efficiency by having a reduced number of model parameters in the regularisation grid.

Data Norm

The data norm is given in Equation 3.5. In this inversion, the data weighting matrix, $\mathbf{W}_d$, is the diagonal matrix of the data errors. The Occam scheme assumes the data errors are independent and have a zero mean Gaussian distribution. This confers on the data norm, U_d, the well known chi-squared distribution χ^2 with q degrees

of freedom. The expected value for the χ^2 distribution is q, the number of data points, and corresponds to an RMS $\left(\frac{\chi^2}{q}\right)^{\frac{1}{2}}$ of 1. Although this seems like a bold assumption about the data errors, they are generally poorly known and categorised. More refined statistical analysis would most likely yield little extra information.

Model Norm

The model norm, also referred to as the roughness term or smoothness constraint, is defined as

$$U_m = \left\|\underline{\partial}_y \mathbf{m}\right\|^2 + \left\|\underline{\partial}_z \mathbf{m}\right\|^2 \quad , \tag{3.24}$$

where $\|\cdot\|^2$ is the l_2-norm, $\underline{\partial}_y$ is the horizontal roughness matrix and $\underline{\partial}_z$ is the vertical roughness matrix. The model roughness is defined as the first spatial derivative of the model, such that smooth models have small derivatives. Essentially, the $\underline{\partial}_y$ and $\underline{\partial}_z$ matrices take the horizontal and vertical differences between adjacent cells in the grid. Minimising them results in a smooth model, which has minimal variation between adjacent cells.

Consider a regularisation grid comprising n cells with w_y elements in the y-direction and w_z elements in the z-direction [90]. Each cell has width ϑ and vertical length v_i where $i = 1, 2, ..., w_z$. Starting in the top left of the grid and numbering the elements from left to right, the $n \times n$ vertical roughness matrix is given by

$$\underline{\partial}_z = \begin{bmatrix} -1 & 0 & \cdots & 0 & 1 & 0 & & \cdots \\ 0 & -1 & 0 & \cdots & 0 & 1 & 0 & \cdots \\ & & \ddots & & & & \ddots & \\ & & & -1 & & \cdots & & 1 \\ & & & & \mathbf{0} & & & \end{bmatrix} \quad , \tag{3.25}$$

where there are $w_y - 1$ zeros between entries and $\mathbf{0}$ is a $w_y \times n$ matrix of zeros.

The horizontal roughness matrix can be expressed in an equivalent manner to the vertical roughness matrix through a series of 0 and ± 1. However, if the model cells are elongated with depth, then it is equivalent to increasing the roughness penalty with depth. To counteract this, a horizontal damping factor can be used

to weight the horizontal roughness matrix, and penalise against different depth-to-width ratios, so that the structure does not become elongated. The $n \times n$ horizontal roughness is given by

$$\underline{\partial}_y = \begin{bmatrix} \underline{\partial}_{y1} & & & \mathbf{0} \\ & \underline{\partial}_{y2} & & \\ & & \ddots & \\ \mathbf{0} & & & \underline{\partial}_{yk} \end{bmatrix} , \tag{3.26}$$

where $\underline{\partial}_{yi}$ is a $w_y \times w_y$ horizontal roughness matrix for layer i and is

$$\underline{\partial}_{yi} = \begin{bmatrix} -v_i/\vartheta & v_i/\vartheta & & & \mathbf{0} \\ & -v_i/\vartheta & v_i/\vartheta & & \\ & & \ddots & \ddots & \\ \mathbf{0} & & & -v_i/\vartheta & -v_i/\vartheta \\ & & & \mathbf{0} & \end{bmatrix} . \tag{3.27}$$

Searching for the Lagrange Multiplier

The μ value controls the balance between creating a smooth model and fitting the data. Larger μ values will result in a smooth model, however this happens at the expense of fitting the data. Smaller μ values result in an improved data fit but will produce a rougher model. There is an unknown optimal μ value that depends on the data error level, the model weighting, the parameterisation used and the true model variation.

Instead of using an arbitrary fixed value of μ, the Occam inversion calculates the optimal value. The μ value is found at each iteration by minimising the true non-linear data norm,

$$U_{dk+1}(\mu) = \|\mathbf{W}_d\mathbf{d} - \mathbf{W}_d\mathbf{F}[\mathbf{m}_{k+1}(\mu)]\|^2 \quad . \tag{3.28}$$

The true non-linear data norm is used instead of the data norm containing the Taylor series expansion, since this linear approximation is inaccurate unless the current model is close to the true solution.

The 1D optimisation problem for determining the optimal μ value is solved using the 'golden section search' [118]. The 'golden section search' sweeps through μ values from 0 (least squares solution) to ∞ (smoothest model) until the minimum of Equation 3.28 is found. If two μ values produce the same minimum value of Equation 3.28, then the larger one is chosen because it corresponds to the smoothest model.

3.2.2 Specific MT Aspects

The features of the Occam inversion that make it specific to MT are the data type, model parameters, the forward model operator and the Jacobian. The model parameterisation described in Section 3.2.1 has also been specifically designed for MT.

The data vector, $\mathbf{d}$, used in the MT Occam inversion contains the 2D MT response. Each element in the vector corresponds to a TE or TM mode apparent resistivity or phase for a particular station and frequency. The model parameter vector, $\mathbf{m}$, used in an inversion can be any monotonic function of the physical property in question. In the MT case, rather than using resistivity ϱ directly in a linear space, the transformation to logarithmic values $log(\varrho)$ is used. This forces the resistivities to be positive and better accommodates the large range of possible resistivity values of Earth materials, thus compressing the scale. Furthermore, the data space is most often specified as the logarithm of the apparent resistivity values, thus giving the same transformation (and units) to the data space and the model space. Each element in the MT model parameter vector is the $log(\varrho)$ of a corresponding cell in the regularisation grid.

The forward model operator, $\mathbf{F}$, in the MT Occam inversion converts the $log(\varrho)$ to a 2D MT response and is calculated using the code from Wannamaker *et al.* [117]. The Jacobian matrix, $\mathbf{J}$, has as its elements the Fréchet derivatives of the 2D MT model response with respect to the model parameters in $log(\varrho)$ form. It was initially calculated using a method outlined in Oristaglio and Worthington [119], then updated to the method from de Lugao and Wannamaker [120].

Since the data type, model parameters, the forward model operator and the

Jacobian make the inversion specific to MT, these are the features that need to be changed when applying this inversion algorithm to data from another geophysical technique.

3.2.3 The MT Occam Program

The 2D MT Occam program is freely available, courtesy of Professor Steven Constable from the Scripps Institute of Oceanography, and can be downloaded from his website ($http://marineemlab.ucsd.edu$).

The program underwent a major rewrite in 2006, when it was updated to Fortran 90 and allowed for dynamic memory allocation. This version is known as OCCAM2DMT v3.0 and is the version used in this thesis.

Figure 3.3, taken from deGroot-Hedlin and Constable [90], is a flow chart of the steps involved in the Occam inversion scheme. The scheme is normally well behaved and converges to a solution that is independent of the starting model. The final model will have the smallest roughness for a specified misfit level, and can be shown to be a solution of the original non-linear optimisation problem. There are instances when the updated model does not have a smaller misfit than the previous model, as well as instances when the desired misfit has been reached and the updated model is not smoother than the previous model. Such behaviour is due to a breakdown in the linear assumption, or errors in calculating the model response and the Jacobian. In such cases, the step length in the original search direction is changed to 1/2 (or 1/4, 1/8 etc.) of its earlier value in the following way

$$\mathbf{F}_{new}(\mu) = (1-c)\mathbf{m}_k + c\mathbf{F}(\mu) \quad . \tag{3.29}$$

Here $\mathbf{F}_{new}(\mu)$ is a set of new models, $\mathbf{m}_k$ is the current model, $\mathbf{F}(\mu)$ is the failed model and c is successively halved until an improved model is found.

The OCCAM2DMT v3.0 program has special features that allow users to adapt the inversion to their problem. The important features are model limits, topography or bathymetry, fixed values, triangularisation, sharp boundaries, structure in the starting model, a prejudiced model and static shift. These are explained below.

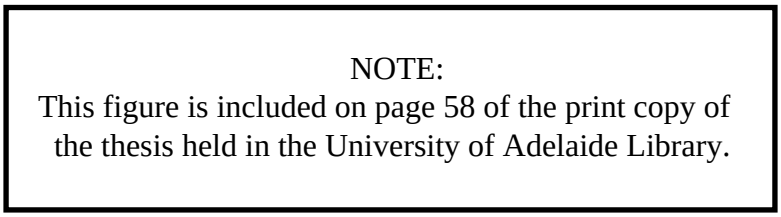

Figure 3.3: Outline of the steps taken by the 2D MT Occam inversion (reproduced from deGroot-Hedlin and Constable [90]).

i. Model limits, or hard bounds, can be placed on the resistivity values. They are applied by re-assigning any updated model parameters that go outside the acceptable limits by clamping them to the upper or lower bounds (whichever is appropriate).

ii. Surface topography or bathymetry of the sea floor can be applied by assigning the appropriate near-surface cells, in the regularisation grid or finite element mesh, respectively, to be air or water. The station location will then be placed on the topography or bathymetric surface.

iii. Fixed values can be assigned to certain parts of the model. If all finite element cells, which are aggregated to form the regularisation cells, are not fixed, then the inversion will only solve for the model parameter corresponding to the free finite element cells.

iv. Each cell in the finite element mesh can get subdivided into 4 triangles, referred to as triangularisation. For the configuration of the 4 triangles see Figure 3.2. Each triangle can be assigned a different resistivity to better mimic topography or the boundary of fixed value structures.

v. Sharp boundaries (or zonal decoupling) can be placed between cells in the regularisation grid, breaking the smoothness constraint between the two cells and allowing a discontinuity to exist.

vi. The initial or start-up model of the inversion does not have to be a homogeneous half space and can contain structure.

vii. A prejudiced or preferred model, containing suggested resistivity values, and weighted for certain cells, can be used to influence an inversion.

viii. The inversion can correct for static shift effects at individual stations.

3.3 Linear Occam

Unlike the MT techniques, the gravity technique has a linear forward model operator. This means the objective function can be differentiated with respect to the model

parameters and linear algebra can be used to ascertain the model parameters. The linear equivalent of the non-linear Occam scheme has the objective function,

$$U[\mathbf{m}] = \left\|\underline{\partial}_y \mathbf{m}\right\|^2 + \left\|\underline{\partial}_z \mathbf{m}\right\|^2 + \mu^{-1}\left\{\left\|\mathbf{W}_d\mathbf{d} - \mathbf{W}_d\mathbf{G}[\mathbf{m}]\right\|^2 - \chi_*^2\right\} \quad , \tag{3.30}$$

where $\mathbf{G}$ will be used to represent the linear forward model operator. When the objective function is differentiated with respect to the model parameters it yields

$$\left(\underline{\partial}_y^T\underline{\partial}_y + \underline{\partial}_z^T\underline{\partial}_z\right)\mathbf{m} + \mu^{-1}\left(\mathbf{W}_d\mathbf{G}\right)^T\left(\mathbf{W}_d\mathbf{G}\right)\mathbf{m} - \mu^{-1}\left(\mathbf{W}_d\mathbf{G}\right)^T\left(\mathbf{W}_d\mathbf{d}\right) = 0 \quad . \tag{3.31}$$

It then follows that the model parameters are updated according to

$$\mathbf{m}(\mu) = \left[\mu\left(\underline{\partial}_y^T\underline{\partial}_y + \underline{\partial}_z^T\underline{\partial}_z\right) + \left(\mathbf{W}_d\mathbf{G}\right)^T\left(\mathbf{W}_d\mathbf{G}\right)\right]^{-1}\left(\mathbf{W}_d\mathbf{G}\right)^T\left(\mathbf{W}_d\mathbf{d}\right) \quad . \tag{3.32}$$

The model parameters are dependent on the μ value that can be found by a similar method discussed in Section 3.2.1. Equation 3.32 does not outline an iterative scheme, rather the model parameters are found in one step, which incorporates searching for the optimal μ value. For more details on deriving the linear Occam inversion see Constable *et al.* [80].

3.4 Conclusions

In this chapter inversion theory is discussed and approaches used for MT and gravity data are reviewed. It was determined that the 2D MT Occam inversion was the best scheme for the joint inversion of disparate data sets. An account of the non-linear 2D MT Occam inversion was then given to provide the basic information needed to understand the methodology for the gravity inversion and joint inversion that is developed in Chapters 4 and 6. In the next chapter, the non-linear 2D Occam approach will be applied to the gravity technique before using it in combination with MT in a joint inversion.

Chapter 4

Occam Gravity Inversion

In this chapter an Occam-based gravity inversion approach is developed and forms the basis of the gravity component of the joint inversion. As explained in Section 3.1.4, the non-linear 2D Occam algorithm has been selected for the joint inversion. Therefore, the gravity inversion should also take this form for consistency and ease of integration and comparison with the single MT Occam inversion as well as the combined approach.

In the past, gravity inversion has not been formulated in this equivalent MT Occam fashion. However, there does exist the closely related 3D algorithm devised by Li and Oldenburg [64]. The similarities between the two schemes are that they both define 'structural roughness' in terms of the first order derivative of the model parameters and both construct the objective function using Lagrange multipliers. The difference between the two algorithms is the dimensionality (2D vs. 3D) and, more importantly, the scheme used to solve the objective function. The Occam inversion uses a non-linear iterative scheme whereas Li and Oldenburg [64] apply a subspace method designed for linear inverse problems.

This chapter is structured as follows. First, applying the non-linear optimisation technique to the linear gravity inversion technique is justified and reconciled. The methodology of the Occam gravity inversion is then explained. Finally, the inversion algorithm is tested using synthetic models.

4.1 Linear vs. Non-Linear Schemes

A primary aim of developing the new gravity inversion scheme is to have an approach that can be readily combined with MT in a joint inversion. The format of the joint inversion will be the non-linear 2D Occam inversion. Therefore, even though gravity is a linear technique and could be applied to the linear Occam approach, it will be applied to the non-linear 2D Occam inversion. It was shown in Section 3.2 that, in the non-linear scheme, the model parameters are updated according to the equation,

$$\begin{aligned} \mathbf{m}_{k+1}(\mu) &= \left[\mu\left(\underline{\partial}_y^T\underline{\partial}_y + \underline{\partial}_z^T\underline{\partial}_z\right) + \left(\mathbf{W}_d\mathbf{J}_k\right)^T\left(\mathbf{W}_d\mathbf{J}_k\right)\right]^{-1} \\ &\quad \left(\mathbf{W}_d\mathbf{J}_k\right)^T\left(\mathbf{W}_d\mathbf{d} - \mathbf{F}[\mathbf{m}_k] + \mathbf{J}_k\mathbf{m}_k\right) \quad . \end{aligned} \tag{4.1}$$

A prominent feature of discrete, linear inversion techniques (proven in Section 4.2.1) is that the linear forward model operator is equal to the Jacobian matrix ($\mathbf{G} = \mathbf{J}$). Substituting this into Equation 4.1 gives

$$\begin{aligned} \mathbf{m}_{k+1}(\mu) &= \left[\mu\left(\underline{\partial}_y^T\underline{\partial}_y + \underline{\partial}_z^T\underline{\partial}_z\right) + \left(\mathbf{W}_d\mathbf{G}_k\right)^T\left(\mathbf{W}_d\mathbf{G}_k\right)\right]^{-1} \\ &\quad \left(\mathbf{W}_d\mathbf{G}_k\right)^T\left(\mathbf{W}_d\mathbf{d} - \mathbf{G}_k\mathbf{m}_k + \mathbf{G}_k\mathbf{m}_k\right) \quad , \end{aligned} \tag{4.2}$$

which simplifies to

$$\mathbf{m}_{k+1}(\mu) = \left[\mu\left(\underline{\partial}_y^T\underline{\partial}_y + \underline{\partial}_z^T\underline{\partial}_z\right) + \left(\mathbf{W}_d\mathbf{G}_k\right)^T\left(\mathbf{W}_d\mathbf{G}_k\right)\right]^{-1}\left(\mathbf{W}_d\mathbf{G}_k\right)^T\left(\mathbf{W}_d\mathbf{d}\right) \quad . \tag{4.3}$$

In Section 4.2.1 the gravity forward model operator will be shown to be dependent only on the grid configuration and is fixed at each iteration. Therefore, the scheme is no longer iterative and Equation 4.3 no longer needs the k iteration subscript, becoming

$$\mathbf{m}(\mu) = \left[\mu\left(\underline{\partial}_y^T\underline{\partial}_y + \underline{\partial}_z^T\underline{\partial}_z\right) + \left(\mathbf{W}_d\mathbf{G}\right)^T\left(\mathbf{W}_d\mathbf{G}\right)\right]^{-1}\left(\mathbf{W}_d\mathbf{G}\right)^T\left(\mathbf{W}_d\mathbf{d}\right) \quad . \tag{4.4}$$

This expression for obtaining the model parameters is the same as that obtained from the linear Occam approach given in Section 3.3. Therefore, when applying the non-linear Occam scheme to gravity data, it reduces to the linear Occam scheme. The gravity inversion can be programmed in a format compatible with the MT inversion and yet, as a stand alone inversion scheme, be executed as the linear Occam approach.

4.2 Methodology

In this section the 2D Occam scheme outlined in Section 3.2 will be applied to the gravity technique. This is done by redefining the relevant parameters, then describing the implementation details.

4.2.1 Parameter Descriptions

The parameters of the MT inversion, as stated in Section 3.2, which make it specific to MT are the data type (apparent resistivity and phase), model parameters (resistivity), the forward model operator, the Jacobian matrix and the model parameterisation. Therefore, these are the quantities that need to be redefined so as to adapt the algorithm for gravity inversion.

Model Parameterisation

The model parameterisation used by the gravity inversion is the same as that used by the MT inversion (Section 3.2.1) namely rectangular cells, each of constant physical property (density in the case of gravity and resistivity in the case of MT). Having the same model parameterisation maintains compatibility between the gravity and MT inversion and means that they are in the same format for the joint inversion.

Data Type

The data type used by the Occam gravity inversion is the vertical component of the gravity response, expressed as Bouguer anomaly values in units of mGals. The data vector $\mathbf{d}$ is written as

$$\mathbf{d} = (d_1, d_2, ..., d_s) \quad , \tag{4.5}$$

where s is the number of data points and each datum corresponds to the Bouguer anomaly values at various stations along the 2D survey line. Accompanying every data point is an estimated error or uncertainty, expressed as a standard deviation (σ^*) and used in the data weighting matrix $\mathbf{W}_d$.

Model Value

Bouguer gravity anomaly data yield models in terms of subsurface density contrasts relative to an unknown background density. The actual density values of the rocks are the sum of the density contrast and the (unknown) background density (Section 2.2.1). Therefore, in specifying the density contrast model, the relative density values can be either positive or negative, depending on whether they are larger or smaller than the background. The model parameter vector $\mathbf{m}$ is written as

$$\mathbf{m} = (\rho_1, \rho_2, ..., \rho_n) \quad , \tag{4.6}$$

where n is the number of model parameters and ρ_i is the density of ith cell in the regularisation grid, in units of kgm^{-3}. Note that actual discrete density values are used as the model parameters rather than some monotonic function of density. This is to maintain the linear relationship between density and the model response.

Forward Model Operator

The forward model operator takes model parameters and the grid configuration to produce a theoretical model response. In Section 3.1.3 the various methods for calculating the gravity response of different shaped bodies were discussed. In the Occam inversion, the forward model operator acts on the finite element mesh, which consists of a regular array of rectangular cells. Therefore, methods that utilise a rectangular configuration are preferred. The 2D right angle prism configuration is detailed by Telford *et al.* [6] and used here.

Figure 4.1 shows the configuration of a right-angled rectangular prism of width

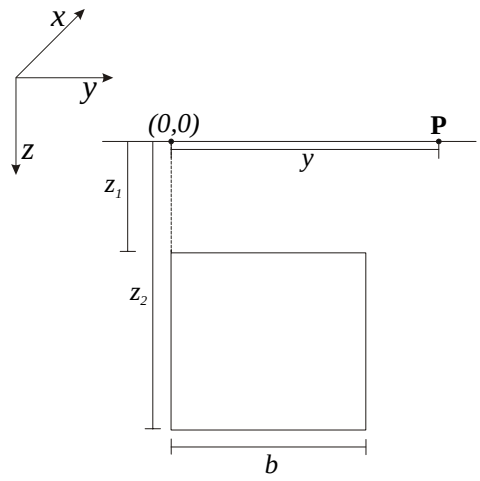

Figure 4.1: Configuration of a 2D right angled prism.

b, buried at a depth of z_1 and having a depth to its base of z_2. For the 2D situation, the model is assumed to extend infinitely in the x-direction. The profile (along the y axis) is perpendicular to strike. The vertical gravity response (g_z), in mGals, of the 2D prism body at point **P** on the surface is given by [6]

$$\begin{aligned} g_z &= 2\times 10^5 G_c\rho \left[\frac{b}{2}\log\left\{\frac{z_2^2+(y-b)^2}{z_1^2+(y-b)^2}\right\}\right. \\ &\quad +\frac{y}{2}\log\left\{\frac{z_2^2+y^2}{z_1^2+y^2} * \frac{z_1^2+(y-b)^2}{z_2^2+(y-b)^2}\right\} \\ &\quad -z_2\left\{\tan^{-1}\left(\frac{y-b}{z_2}\right)-\tan^{-1}\left(\frac{y}{z_2}\right)\right\} \\ &\quad \left.+z_1\left\{\tan^{-1}\left(\frac{y-b}{z_1}\right)-\tan^{-1}\left(\frac{y}{z_1}\right)\right\}\right] \quad , \end{aligned} \tag{4.7}$$

where ρ is the density of the prism and G_c is the universal gravitational constant, 6.67×10^{-11} $\mathrm{Nm^2kg^{-2}}$.

For a given station, the model response of each prism is calculated using Equation 4.7. The total model response at that station due to all prisms, is obtained by superposition, namely, simply adding together the gravity responses of each elementary prism. Mathematically, the model response is expressed as $\mathbf{F}[\mathbf{m}]$, with the density term ρ in Equation 4.7 being representative of the $\mathbf{m}$ term and the remain-

der of Equation 4.7 forming the basis of the **F** term. This means that the gravity forward model operator, **F**, is only dependent on the configuration of the grid.

Boundary Conditions of the Forward Model Operator

To maintain accuracy of the forward model calculations, the boundary conditions at the sides and bottom of the grid need to be addressed. The gravity inversion does not have a bottom boundary condition. The gravity kernel decreases according to distance squared. Therefore, provided the grid extends deep enough, the influence of the deep grid cells is negligible and has minimal effect on the overall gravity response. The depth termination of the grid will thus have minimal effect on the response.

A similar approach to the bottom boundaries could be taken for the side boundaries. If the gravity data at the edges of a profile are zero, a model response that is also zero is desired. This is achieved by the density values of the boundary cells being set to zero. However, if the gravity data are not zero at the edges of the profile, there is a need to extend the side boundary cells to infinity, which is done here using a 2D horizontal sheet [6]. Figure 4.2 shows the configuration of the 2D horizontal sheet used to terminate the rows at the right of the grid. It is a right angled rectangle that extends to infinity in the strike (x-directions) and positive y-direction. The vertical gravity response (g_{zRHS}), in mGals, of the horizontal sheet at point **P** is given by [6]

$$\begin{aligned} g_{zRHS} &= 2 \times 10^5 G_c \rho \left[\frac{\pi}{2} (z_2 - z_2) + \frac{y}{2} \log \left\{ \frac{z_2^2 + y^2}{z_1^2 + y^2} \right\} \right. \\ &\quad \left. + z_2 \tan^{-1} \left(\frac{y}{z_2} \right) - z_1 \tan^{-1} \left(\frac{y}{z_1} \right) \right] \quad . \end{aligned} \tag{4.8}$$

A similar formulation is used for the termination of the grid on the left hand side.

Jacobian

The Jacobian is an $s \times n$ matrix which determines how each model parameter affects the model response. The elements of the Jacobian are

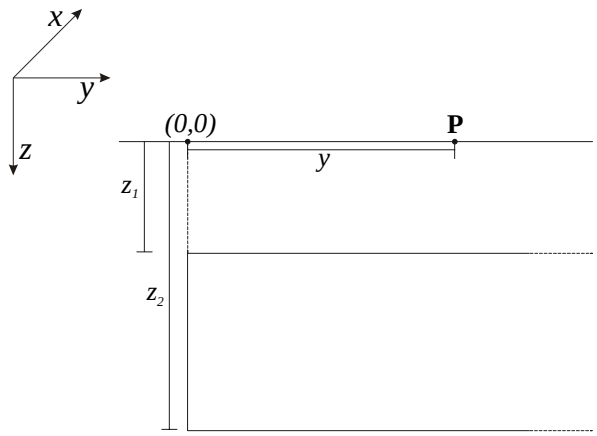

Figure 4.2: Configuration of a horizontal sheet used to terminate rows on the right hand side of the grid.

$$J_{ij} = \frac{\partial d_i}{\partial m_j} \quad , \tag{4.9}$$

where $i = 1, 2, ..., s$ corresponds to the gravity data points and $j = 1, 2, ..., n$ corresponds to the model parameters. This is equivalent to

$$\mathbf{J} = \frac{\partial \mathbf{F}\left[\mathbf{m}\right]}{\partial m} \quad , \tag{4.10}$$

and since there is a linear relationship between $\mathbf{F}$ and $\mathbf{m}$, taking the derivative in Equation 4.10 will result in $\mathbf{J} = \mathbf{F}$. The Jacobian and the forward model operator are equal. They are both independent of the model parameters and solely dependent on the grid configuration.

For a 2D prism, using Equation 4.7 the Jacobian is given by

$$\begin{aligned} J \;=\; & 2 \times 10^5 G_c \left[\frac{b}{2} \log \left\{ \frac{z_2^2 + (y-b)^2}{z_1^2 + (y-b)^2} \right\} \right. \\ & + \frac{y}{2} \log \left\{ \frac{z_2^2 + y^2}{z_1^2 + y^2} * \frac{z_1^2 + (y-b)^2}{z_2^2 + (y-b)^2} \right\} \\ & - z_2 \left\{ \tan^{-1}\left(\frac{y-b}{z_2} \right) - \tan^{-1}\left(\frac{y}{z_2} \right) \right\} \\ & \left. + z_1 \left\{ \tan^{-1}\left(\frac{y-b}{z_1} \right) - \tan^{-1}\left(\frac{y}{z_1} \right) \right\} \right] \quad . \end{aligned} \tag{4.11}$$

For the model parameters at the edge of the grid, the response was calculated using the horizontal sheet expression (Equation 4.8), the Jacobian is

$$\begin{aligned} J &= 2 \times 10^5 G_c \left[\frac{\pi}{2} (z_2 - z_2) + \frac{y}{2} \log \left\{ \frac{z_2^2 + y^2}{z_1^2 + y^2} \right\} \right. \\ &\quad \left. + z_2 \tan^{-1} \left(\frac{y}{z_2} \right) - z_1 \tan^{-1} \left(\frac{y}{z_1} \right) \right] \quad . \end{aligned} \tag{4.12}$$

4.2.2 The Computer Program and its Implementation

The above definitions of data type, model values, forward model operator, boundary conditions and Jacobian matrix were implemented to produce the Occam gravity inversion program. Figure 4.3 shows the steps involved in the gravity inversion; it is based on similar steps taken by the MT inversion. The changes in steps between the two versions reflect the fact that, in the gravity case, the forward model operator and Jacobian are equal, and so only one needs to be calculated. Also, the non-linear gravity inversion in Section 4.1 was shown to be equivalent to the linear scheme. Therefore it only requires one iteration to find the model parameters, followed by a search for the optimal μ value.

In the Occam gravity inversion program, the inverted model parameters (Equation 4.4) are only dependent on the data, the forward model operator and the μ value. However, it was shown that the forward model operator is only dependent on the grid configuration, which means that it and the data are pre-determined before the inversion is executed. As a result, finding a model that meets the desired tolerance is solely dependent on the μ value.

A user manual for conducting the gravity inversion is given in Appendix A. The program that performs the Occam gravity inversion has the same features as the MT program that was discussed in Section 3.2.3. These include model limits, topography or bathymetry, fixed values, sharp boundaries, structure in the start-up model and a prejudice or preferred model. The triangularisation feature is available but the response of each triangle is approximated as being one quarter the response of the total cell.

Figure 4.3: Flow chart of the steps taken by the Occam gravity inversion (adapted from the flow chart produced by deGroot-Hedlin and Constable [90]).

4.2.3 Methodology Summary

The Occam gravity inversion program takes the input Bouguer anomaly data in units of mGals and returns a density contrast model in units of kgm^{-3}. The forward model operator and the Jacobian are equal and only depend on the grid configuration. They are calculated using the analytical expression for a 2D prism. A 2D horizontal sheet is used as the side boundary condition, to effectively extend the sides of the grid to infinity.

4.3 Behavioural Characteristics

Convergence and stability are two important features of an inversion program that need to be considered in the context of the Occam gravity inversion development. It is desirable that the inversion program produces the same final model, regardless of

the starting model used. Unlike an iterative scheme, the gravity model parameters (Equation 4.4) are independent of the starting model and, for a given grid and data set, they are only dependent on the μ value. However, changing the starting model will result in the same μ value, because the μ value is found by minimising the data norm, which is also independent of the starting model. The stability of the inversion depends on being able to calculate the inverse matrix needed to obtain the model parameter values (Equation 4.4). The success of the inverse calculation requires that the μ value be large and positive [75]. For the inversions discussed in the next section, extremely small values of μ cause the inverse matrix calculation to fail. However, when the μ values are close to the value of the final solution the matrix inversion succeeds.

A key aspect of the inversion is the determination of the unknown optimal μ value. This is done using a golden section search method [118]. During the μ search, values of μ can be found that give an RMS value smaller than one, and in many cases an RMS value approaching zero. The data fit should not be to a level better than the expected uncertainty or error of the measurements. If so, then such models are essentially over-fitting the data and correspond to rough models. The μ search normally continues until a value is found that corresponds to an RMS of 1, which is a data fit equal to the standard deviation of each measurement. These models adhere to the Occam philosophy of producing the smoothest possible model that only contains structure essential to explain the observations.

Every model discussed in the following section on synthetic testing has a different optimal μ value. Therefore, it would be inappropriate and unsatisfactory to run this type of inversion with a fixed μ value. A fixed μ value is equivalent to a Tikhonov Regularisation inversion (Section 3.1.1), which finds the appropriate μ value through a trial and error approach. Although the optimum μ value is unpredictable, there are some general trends which can be observed. When the misfit level increases, the inversion generally needs to produce a rougher model to bring the calculated and observed data closer together. As a result, the optimal μ value decreases. Increasing the density contrast will produce a larger roughness term in the regularisation and so the μ value will increase in an attempt to produce a smoother model. There is one

situation where multiple inversions will produce the same μ value, and this is when the separate data sets are offset from each other by a fixed (constant) amount. This demonstrates that the μ value is sensitive to the relative variations in the response (and subsequent model), rather than the absolute values.

4.4 Synthetic Testing

In this section a number of synthetic models are used to test the newly developed Occam gravity inversion program. The objectives are to demonstrate that the inversion works and to determine how well the synthetic models are reconstructed.

4.4.1 Synthetic Models and Data

Four 2D density contrast models were used for the synthetic testing of the gravity Occam inversion. They are shown in Figure 4.4. These models are referred to as one box, two box, horizontal sheet and horizon models. The one box model is a 3×3 km square body with its top boundary located at a depth of 1 km. The two box model has two 3×3 km square bodies separated by 4.3 km, with their top boundary also at a depth of 1 km. The horizontal sheet model is a 1 km thick rectangle with its top boundary at a depth of 0.5 km. The left boundary of the horizontal sheet is located in the middle of the model and the right boundary extends to infinity. The horizon model is a vertical step model, in which the horizon on the left steps down from a depth of 3 km to a depth of 4 km for a distance of 4.5 km, before stepping back up to 3 km depth for a distance of 4.3 km. This is followed by a second step up to 1.5 km depth for a distance of 4 km. Eventually, the horizon returns to the 3 km depth. Both left and right edges of the horizon, at the 3 km depth level, extend to infinity.

The density contrast models have a background density of zero and seven different densities were assigned to the anomalous bodies enclosed in the models: 10, 25, 50, 100, 250, 500 and 1000 kgm^{-3}. The bodies in the horizontal sheet and horizon models were only assigned positive density contrast values, whereas the body in the one box model was assigned both a positive and a negative density contrast value.

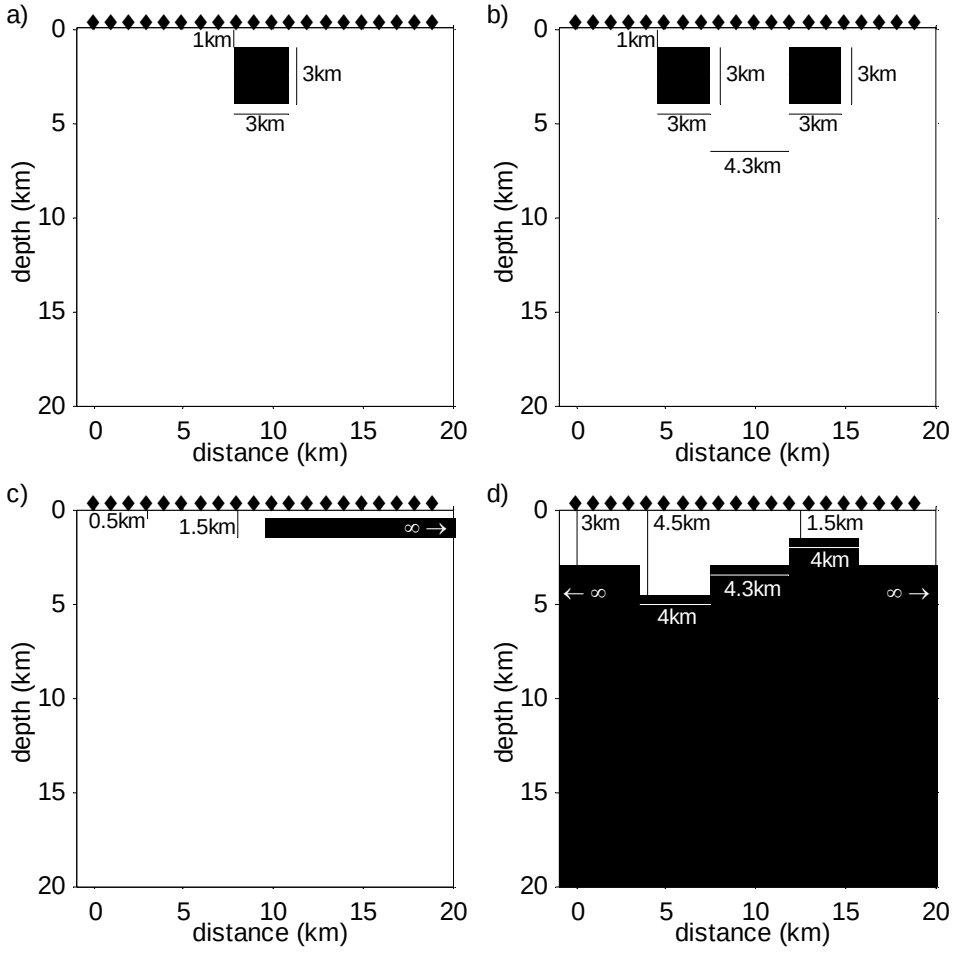

Figure 4.4: Synthetic models used to test the Occam gravity inversion. These are refered to as a) one box, b) two box, c) horizontal sheet and d) horizon models.

The two box model assigned the left box a negative density value and the right box a positive density value.

The data generated from these contrast models are already in Bouguer anomaly values. Along the profile, synthetic gravity values were computed for each model at 20 discrete locations separated by 1 km as simulated stations (see Figure 4.4). A combination of the analytical expressions for a 2D prism and a horizontal sheet as discussed in Section 4.2.1 were used to generate the synthetic data. The body in the horizon model does not have a defined lower limit. When calculating its response, changing the lower depth limit will offset the synthetic data by a constant value. Since the investigation with this model is only concerned with the contrast in the response caused by the steps, the data generated for the horizontal sheet model

Table 4.1: The synthetic response amplitudes and the error levels used to investigate the effects of errors on the Occam gravity inversion.

	one box	two box	horizontal sheet	horizon
synthetic amplitude	2.15	4.11	1.96	2.16
percentage of amplitude	error level (mGal)	error level (mGal)	error level (mGal)	error level (mGal)
1%A	0.02	0.04	0.02	0.02
3%A	0.06	0.12	0.06	0.06
5%A	0.11	0.21	0.10	0.11
8%A	0.17	0.33	0.16	0.17
10%A	0.22	0.41	0.20	0.22
15%A	0.32	0.62	0.29	0.32
25%A	0.54	1.03	0.49	0.54
50%A	1.08	2.06	0.98	1.08
75%A	1.61	3.08	1.47	1.61
100%A	2.15	4.11	1.96	2.16

are offset by a constant value in such a way that, at the mid point between the maximum and minimum gravity values, the data point is set to zero.

Noise was added to every synthetic data point in the form of an absolute random error having a zero mean Gaussian distribution. The maximum error levels used were either 0.03 or 0.06 mGals, which correspond to the precision range of current gravimeters [6]. The effect of the error level on the gravity inversion will be investigated. The various model types and density contrasts produce significantly different amplitudes in the synthetic data and applying the same fixed error level to all of them would make evaluating the effect of the error level difficult. Therefore a fixed error was still used, but the value is assigned to be a percentage of the maximum synthetic data amplitude. An example of the fixed error allocation based on the data amplitude is given in Table 4.1 for a density contrast of 50 kgm^{-3}. After the percentage value, used to calculate the fixed error, the symbol %A follows. This symbol is used throughout this thesis to delineate this style of gravity error allocation.

4.4.2 Inversion Grid

The same grid was used for each model and is shown in Figure 4.5. The top 5 km has a row spacing of 100 m and a column spacing of 333 m. Between depths of 5

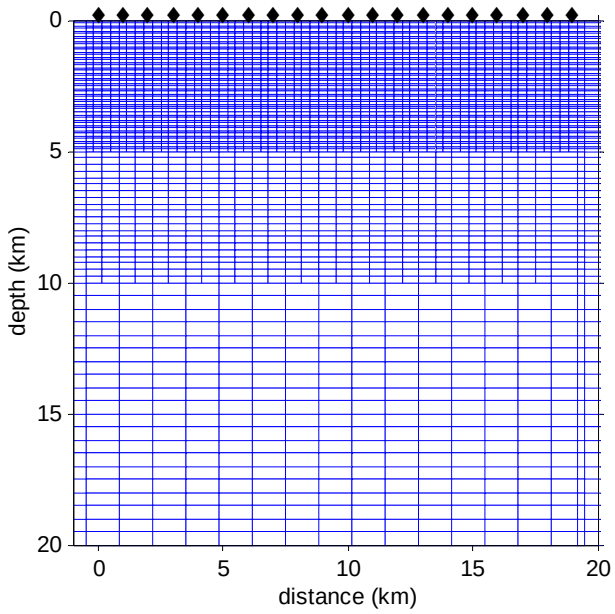

Figure 4.5: The regularisation grid used by all Occam gravity inversions.

and 10 km, the row and column spacings are 250 and 666 m, respectively. Below 10 km depth and extending to the termination of the grid at 20 km, the row spacing is 500 m and the column spacing is 1333 m. Further consideration is given to the grid configuration in Section 4.5.1.

4.4.3 Inverted Model Results

All models produced by the Occam gravity inversion have an RMS of 1. Selected results from the inversions of the one box, two box, horizontal sheet and horizon models are shown in Figures 4.6, 4.7, 4.8 and 4.9, respectively. All the synthetic data have an error of 0.03 mGal and respective density contrasts of 10, 100, 500 and 1000 kgm^{-3}. Due to the large number of inversions undertaken, not all results from the different contrasts and error levels are shown. However, all models have the same general characteristics and are consistent with the findings reported.

The Occam gravity inversion program produces models which have a similar appearance. Anomalous density values are placed at the surface because the gravity method has limited depth resolution capability [64]. The smoothness constraint then smears the surface anomalies vertically and laterally into the model. The lateral

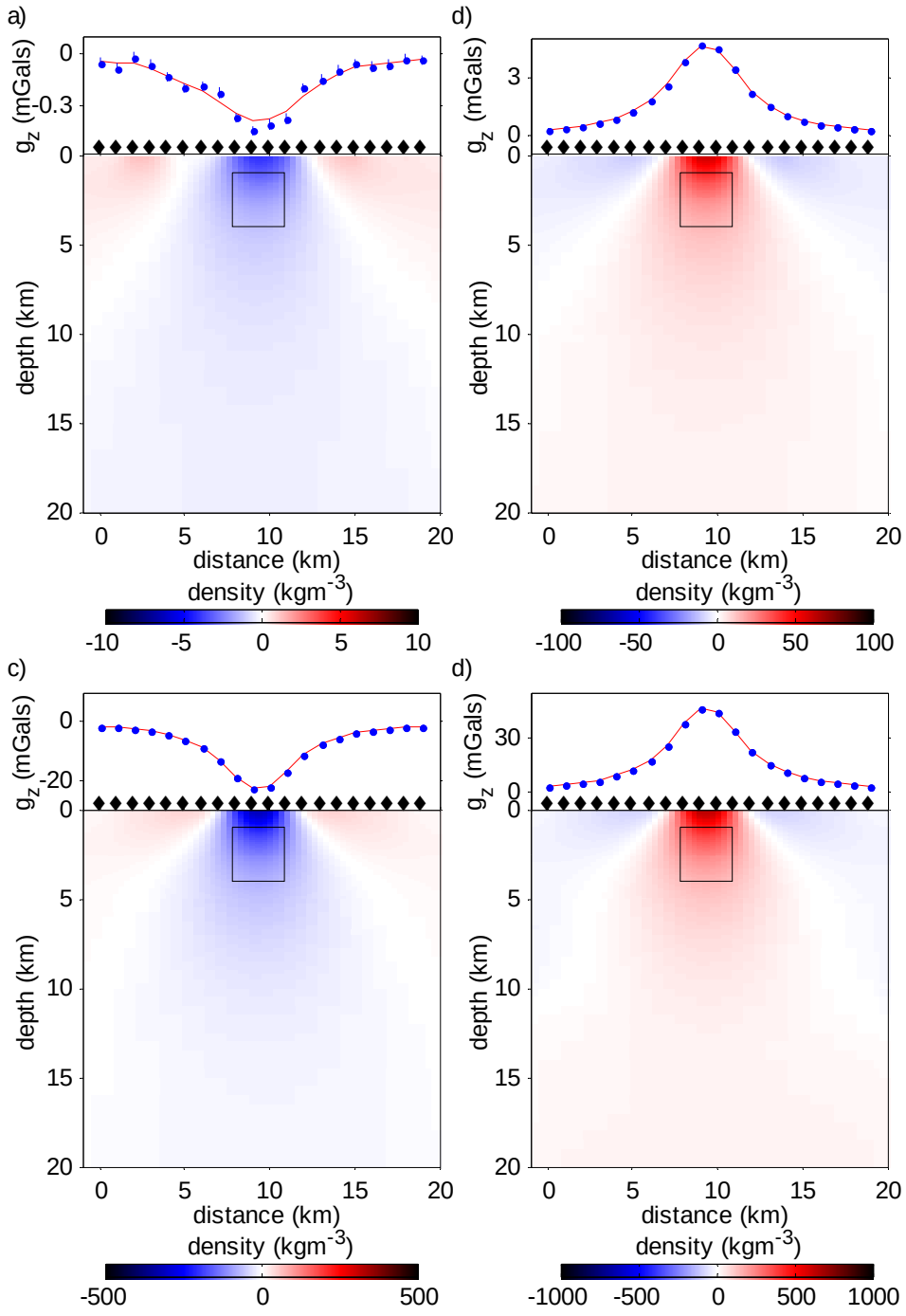

Figure 4.6: The results from the Occam gravity inversion for the one box synthetic model with an error of 0.03 mGals and a contrast of a) 10 kgm^{-3}, b) 100 kgm^{-3}, c) 500 kgm^{-3} and d) 1000 kgm^{-3}.

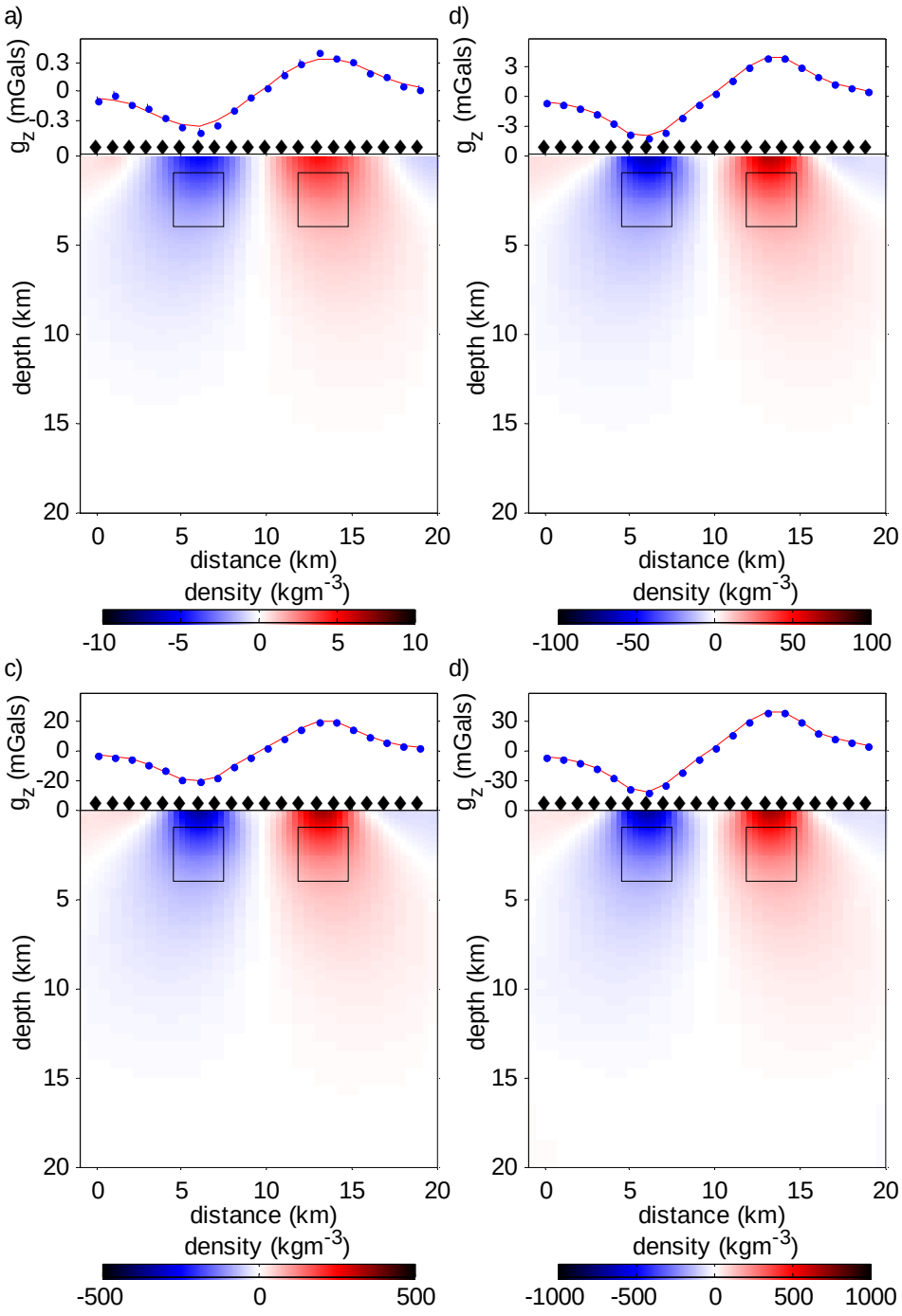

Figure 4.7: The results from the Occam gravity inversion for the two box synthetic model with an error of 0.03 mGals and a contrast of a) 10 kgm^{-3}, b) 100 kgm^{-3}, c) 500 kgm^{-3} and d) 1000 kgm^{-3}.

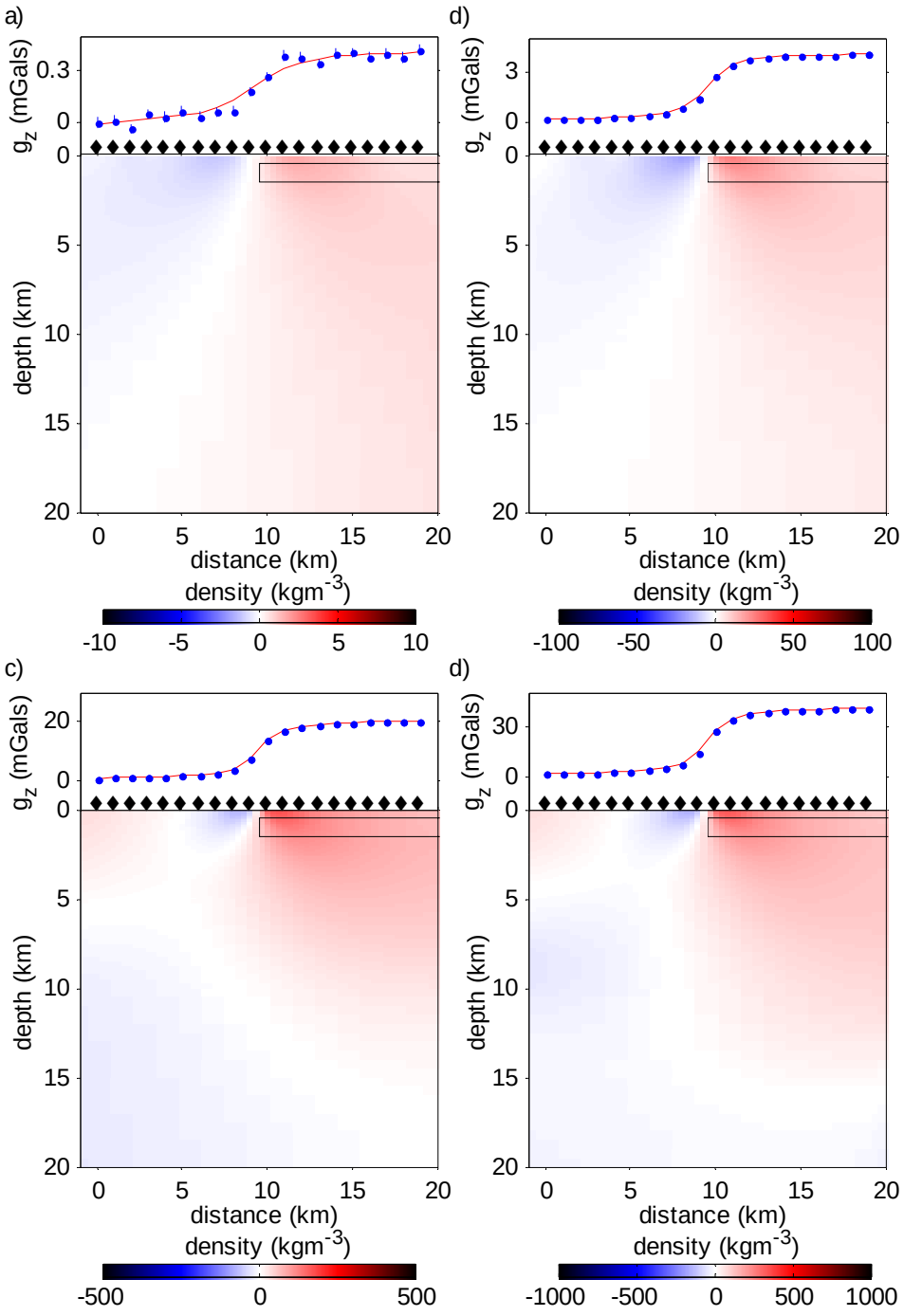

Figure 4.8: The results from the Occam gravity inversion for the horizontal sheet synthetic model with an error of 0.03 mGals and a contrast of a) 10 kgm^{-3}, b) 100 kgm^{-3}, c) 500 kgm^{-3} and d) 1000 kgm^{-3}.

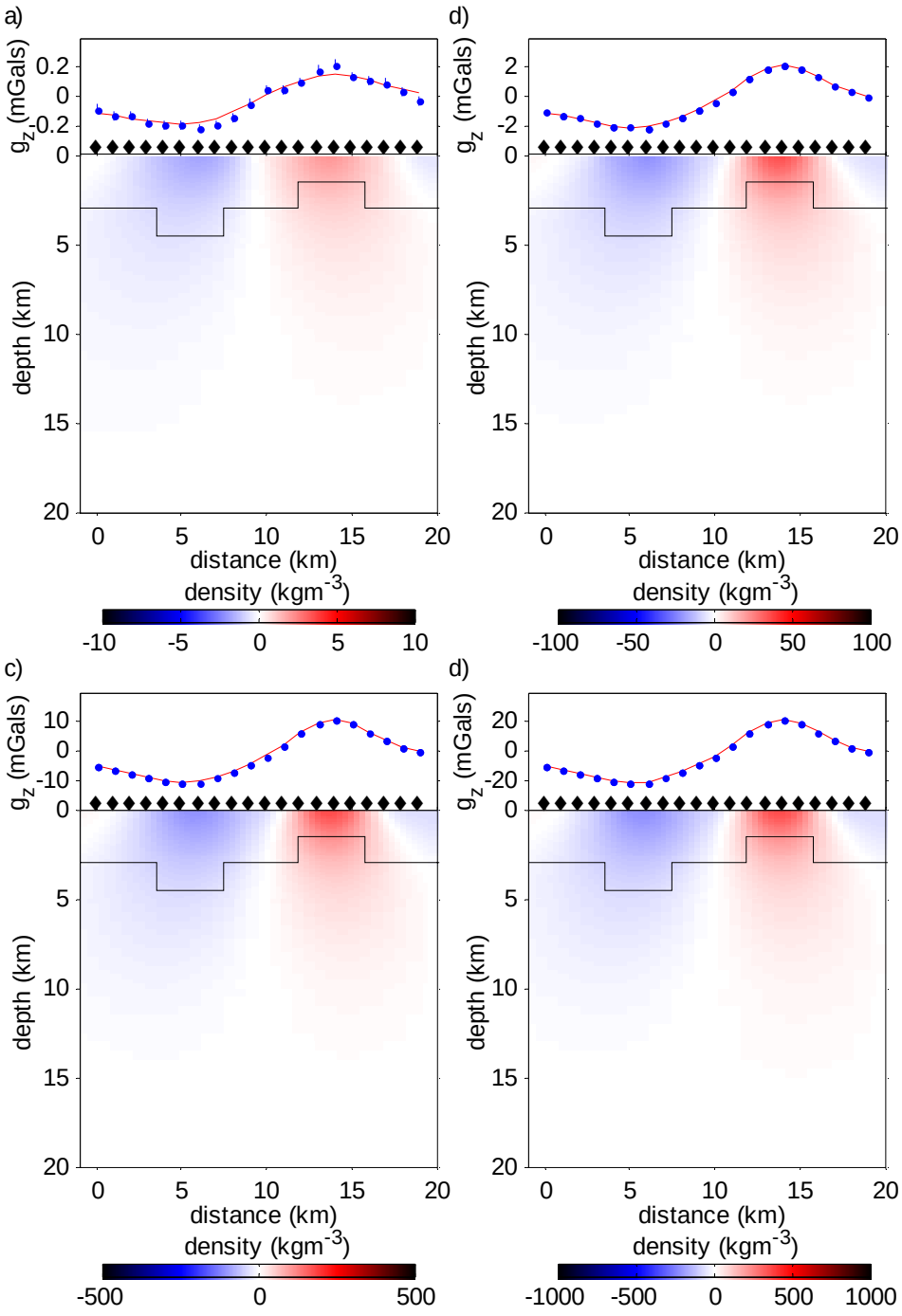

Figure 4.9: The results from the Occam gravity inversion for the horizon synthetic model with an error of 0.03 mGals and a contrast of a) 10 kgm^{-3}, b) 100 kgm^{-3}, c) 500 kgm^{-3} and d) 1000 kgm^{-3}.

positioning of the anomalous density values are controlled by the spatial gradients in the synthetic data. For all models, the edges of the anomalous densities at the surface coincide with the locations of the lateral boundaries in the synthetic models.

The lateral boundaries of the anomalous densities do not plunge vertically, but are inclined. The inclination is for two reasons. Firstly, the smoothness constraint endeavours to produce circular features, as they correspond to a small roughness value (Figure 4.6). Secondly, if the model feature has a positive contrast with its surrounds then the inclination is in the same direction as the decrease in the synthetic data (Figure 4.6b), or if the model feature has a negative contrast the inclination is in the opposite direction to the decrease in the synthetic data (Figure 4.6c). Therefore, the inclination of the boundary reflects the gradient of the synthetic data and it is this gradient which is being fitted in the inversion.

The magnitudes of the contrasts obtained by inverting the gravity data are always less than the true contrasts of the synthetic model. The total mass in the final model (the volume sum of all absolute density values of each cell) is the same as the synthetic model. The horizon model is excluded from this statement because the synthetic data were artificially altered (as discussed earlier), which cause a variation in the total mass of the final model. Since the total mass is the same for the other models, the smoothness constraint not only smears the boundaries of the model features but also redistributes the mass in the model. The redistribution of mass causes the contrast to be incorrect. This is compensated by the overshooting of the density values at the sides of the anomalous bodies to allow for a better fit of the synthetic data. A clear example of this is the one box model in Figure 4.6b. It shows a central positive feature but towards the model edges the density values overshoot, producing negative side lobes.

Varying the magnitude of the density contrasts in the synthetic model changes the actual density values and the resulting contrast of the model, but it does not change the overall appearance, shape and location of the reconstructed anomalies. An increased contrast causes the models to have larger roughness values because the variation between each cell needs to be larger to accommodate the greater contrast. In these synthetic experiments even a small contrast of 10 kgm^{-3} produces coherent

and plausible models when the error is at its smallest value of 0.03 mGals. For larger errors of measurement, such small contrast bodies would be difficult to detect and delineate.

The recovered model features are best when the errors are small (Figure 4.10a). As the error increases slightly, the model features are still evident but a smoother model with a decrease in contrast is reconstructed, with its boundaries less pronounced. The increased errors allow for a smoother model because the model response under-estimates the 'observed' synthetic data over a positive density contrast and over-estimates the synthetic data at the sides (Figure 4.10b). The RMS is a global average measure of data fit which does not identify individual data point agreements. As expected, when the errors are large, they hinder the inversion from correctly locating the boundaries. They can lead to erratic structure, which is used by the inversion program to fit the errors rather than the true signal (Figure 4.10c). Finally, the errors can be so large that they result in a very smooth inverted model which does not resemble the true (synthetic) model at all (Figure 4.10d).

4.4.4 Synthetic Testing Summary

The Occam gravity inversion has proven to be stable and always produces models with an RMS of 1. It was found that all density contrast distributions recovered by the inversion have a similar appearance. The main density anomalies are located at the surface and smeared laterally and vertically into the model. The surface boundary of the density anomalies corresponds to the lateral boundaries or edges of the anomalous features in the synthetic models, demonstrating the sensitivity of the gravity method to lateral changes in density. The recovered density contrast from the inversion is always less than that of the true (synthetic) model and is due to the smoothness constraint which redistributes the anomalous mass throughout the model. Increasing the error slightly allows for a smoother model to be obtained. However, large errors ($> 25\%$A) produce models having erratic structure.

The synthetic testing has validated the Occam gravity inversion program, established that it yields useful results, but due to the inherent non-uniqueness of the gravity method it is unable to reproduce the true synthetic model. This highlights

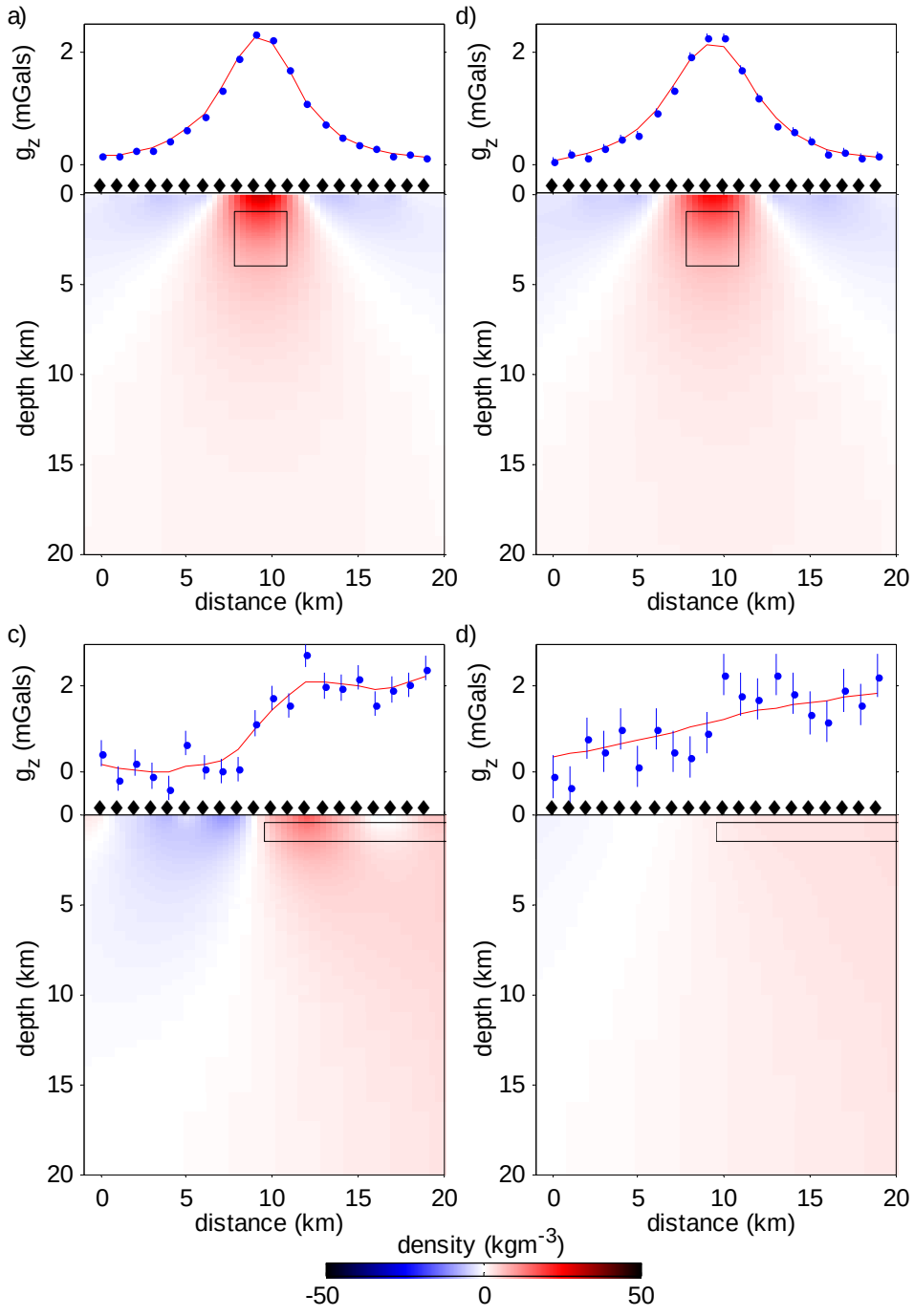

Figure 4.10: The results from the Occam gravity inversion for the one box and horizontal sheet synthetic models with a contrast of 50 kgm^{-3} and an error of a) 1 %A, b) 3 %A, c) 15 %A and d) 25 %A of the amplitude of their synthetic data.

the need for external constraints to aid the inversion in reconstructing the subsurface structure. Next, ways of improving the depth resolution of gravity data are investigated, as well as how to use additional geological information to constrain the inversion.

4.5 Depth Resolution

The models produced by the Occam gravity inversion are dominated by features located at or near the surface. In this section, two methods are examined which can aid the inversion in correctly locating the model features with depth. The two methods are altering the grid configuration and using a depth weighting function.

4.5.1 Grid Configuration

The EM fields decrease exponentially with depth in a homogeneous half space. In an MT inversion using a logarithmically depth scale, which has a grid thickness that increases in equal logarithmic intervals (exponentially), improves the structure location and data fit [80] [89]. Here, a similar approach is applied to gravity inversion. The gravity anomaly was expressed in Equation 2.47 as a Fredholm integral. The kernel of the integral embodies the physics of the gravity technique and encapsulates Newton's Law of Gravitation. The kernel (or Green's function) decreases inversely with the distance squared. To counteract this decay of the kernel, a new grid can be introduced which increases the row thickness in proportion to the depth squared. Since gravity data will ultimately be combined with MT data in a joint inversion, the effect of using an equal logarithmic grid spacing with depth (designed for MT) is also investigated. The results from the gravity and MT designed grids are then compared to the uniform grid discussed in Section 4.4.2.

The three grids, referred to as squared, logarithmic and uniform, have 90 layers and are terminated at 20 km. The row thickness increases as the depth squared and exponentially (equal logarithmic intervals) for the squared and logarithmic grids, respectively. The uniform grid has an equal spacing with depth, and was described in Section 4.4.2. The column thickness for all models is 333 m from the surface to

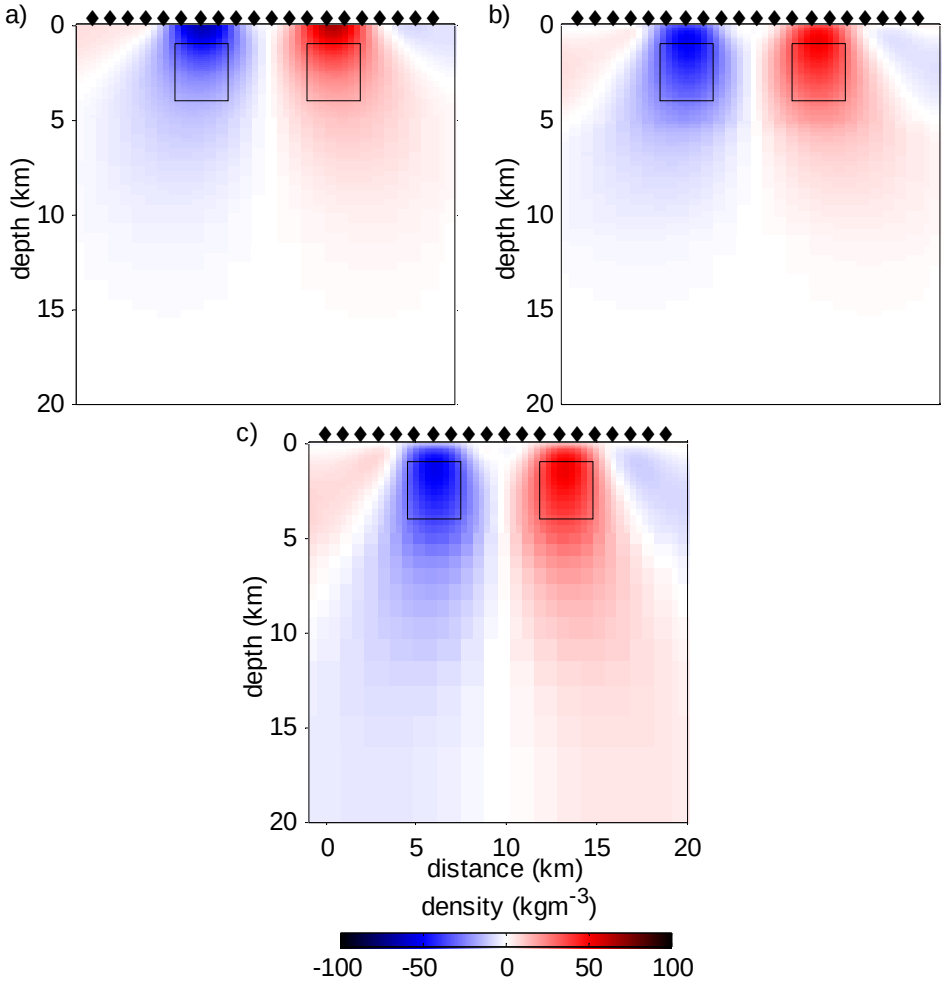

Figure 4.11: The results from the Occam gravity inversion with no horizontal damping factor for the two box synthetic model with an error of 0.03 mGals and contrast of 100 kgm^{-3}. The grid configurations are a) uniform grid, b) squared grid and c) logarithmic grid.

a depth of 5 km. Between 5 and 10 km depth, it is expanded to 666 m and below 10 km depth it is set at 1333 m. The different grid configurations were tested on the two box model and the horizon model, each for a density contrast of 100 kgm^{-3} and a measurement error of 0.03 mGals. The Occam inversion scheme normally uses a horizontal damping factor applied to the horizontal roughness term to stop structure becoming elongated with depth (Section 3.2.1). The Occam gravity inversion was run with and without the damping factor applied.

Figure 4.11 shows the results of the different grid configurations for the two box model. When the horizontal damping factor was not applied the models produced

by the squared and logarithmic grids are very similar in the shallow section and produce a better representation of the synthetic model than the equal grid. The squared and logarithmic grids have caused the surface structure to be elongated with depth and yield anomalous density values in the true box positions. However, neither grid can map the top of the boxes, since the structure starts at the surface and continues vertically downwards. Although smeared, the side boundaries of the anomalous density values are consistent with the known box boundaries. The bottom boundaries of the two boxes are better defined using the squared grid than the logarithmic grid, as the large thickness of the logarithmic grid cells continues to extend structure to the very base of the grid.

The results of the horizon model using the different grid configurations are given in Figure 4.12. In similar fashion to the two box model, when the horizontal damping factor was not applied, the squared and logarithmic grids produced features starting at the surface that are elongated with depth. For both grids, the side boundaries of the feature representing the 'high' in the horizon are hard to delineate but are in general agreement with the true (synthetic) model. At the centre of this feature there appears to be a slight anomalous density high, which coincides with the top of the horizon high. For the squared and logarithmic grids, the feature that represents the low in the horizon have become very smeared and the lateral boundaries are almost indistinguishable. The use of grids has not been able to aid in correctly locating this feature.

When the horizontal damping factor was applied (not shown here), the models produced by the three grids are almost identical with the anomalous density values placed at the surface. This is because the horizontal damping factor is designed to counteract the increase in row thickness with depth and not allow features to elongate with depth. The uniform grid has minimal variation in row thickness and the two models produced with and without the horizontal damping factor are similar, except the model produced with the horizontal damping factor has slight elongation. The anomalous density region produced when the horizontal damping factor is applied is concentrated at the surface. It therefore has a slightly higher density value than the model produced with no horizontal damping factor applied,

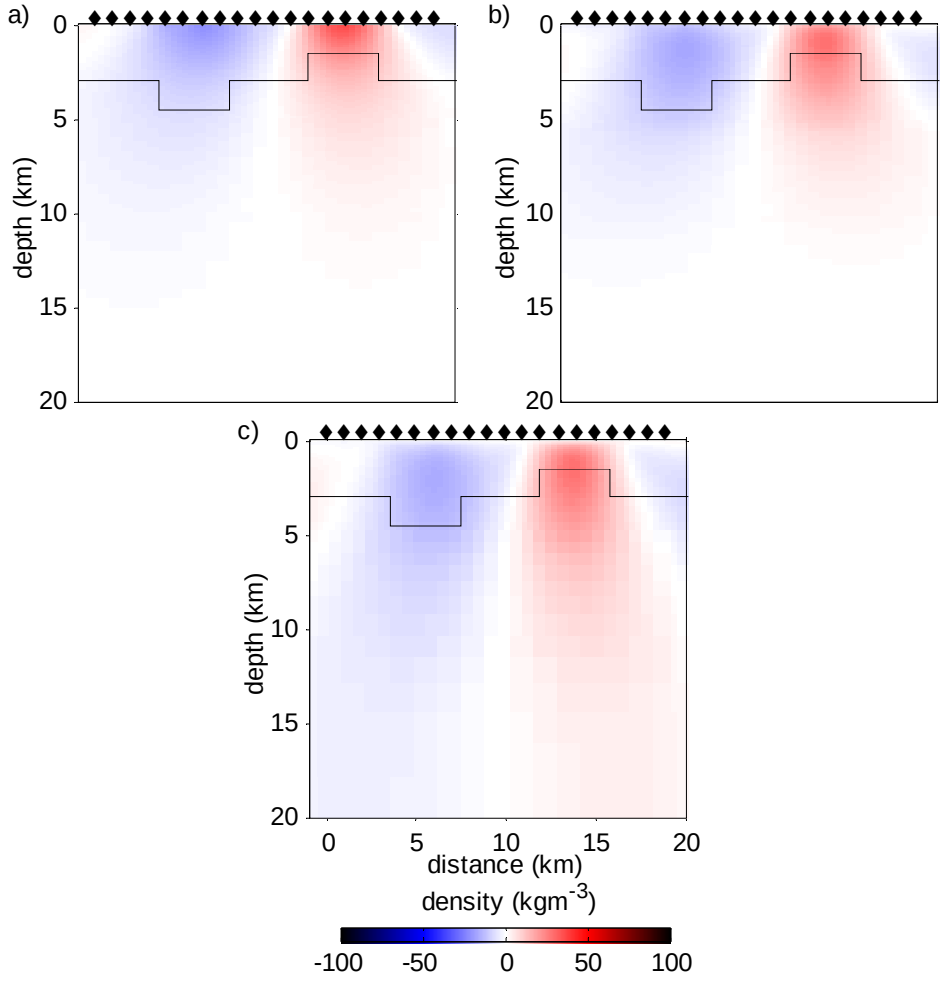

Figure 4.12: The results from the Occam gravity inversion with no horizontal damping factor for the horizon synthetic model with an error of 0.03 mGals and contrast of 100 kgm^{-3}. The grid configurations are a) uniform grid, b) squared grid and c) logarithmic grid.

which yields a larger volume (but lower density) anomalous region of equivalent total mass.

4.5.2 Depth Weighting Function

The idea of a depth weighting function is to counteract the natural decay of the gravity kernel with depth, which contributes to the lack of depth resolution. Its inclusion gives every cell at different depths an equal probability to enter the model solution with a non-zero value [64]. Li and Oldenburg [64] found that a function of the form $(z + z_0)^{-2}$ closely approximates the kernel's natural depth decay beneath

Table 4.2: The optimal weighting factor values used in Li and Oldenburg's depth weighting function for the synthetic models.

Model	β_*	z_0
one box (positive anomaly)	2	50
two box	2	50
horizontal sheet	1.5	50
horizon	2	100

a given station. The exponent 2 is appropriate, indicating the inverse square law, as the gravity kernel decays at a rate of inverse distance squared. They developed the following depth weighting function,

$$w(z) = \frac{1}{(z + z_0)^{\beta_*/2}} \quad , \tag{4.13}$$

where z is depth, and β_* and z_0 are weighting factors, with β_* varying between 1.5 and 2.0. The larger the β_* and z_0 values, the deeper the structure will be placed. Li and Oldenburg's depth function was incorporated into the gravity inversion by weighting the roughness matrix, with each element having its weight determined by the depth of the corresponding cell.

A depth weighted inversion was performed for each synthetic model, and used a density contrast of 100 kgm^{-3} and an error of 0.03 mGals. Through a process of trial and error, the best values of β_* and z_0 were determined for each model. These values are given in Table 4.2. The inverted model results are shown in Figure 4.13. Other combinations of the two weighting parameters produced similar results. As expected, it was found that the correct placement of the structure was most sensitive to β_*, whereas changing z_0 had little effect.

The optimal β_* and z_0 values for all models (see Table 4.2) are consistent with larger β_* and z_0 values being needed for deeper structures. The same β_* and z_0 values are used for the one box and two box synthetic models to correctly locate the top of the box boundaries. The values are the same because the two models have similar features at the same depth. For the horizontal sheet model, the depth weighting function correctly locates its top boundary close to its lateral boundary in the middle of the model. However, at positions away from the middle of the model, the top boundary has a steep inclination and continues to depths far greater than

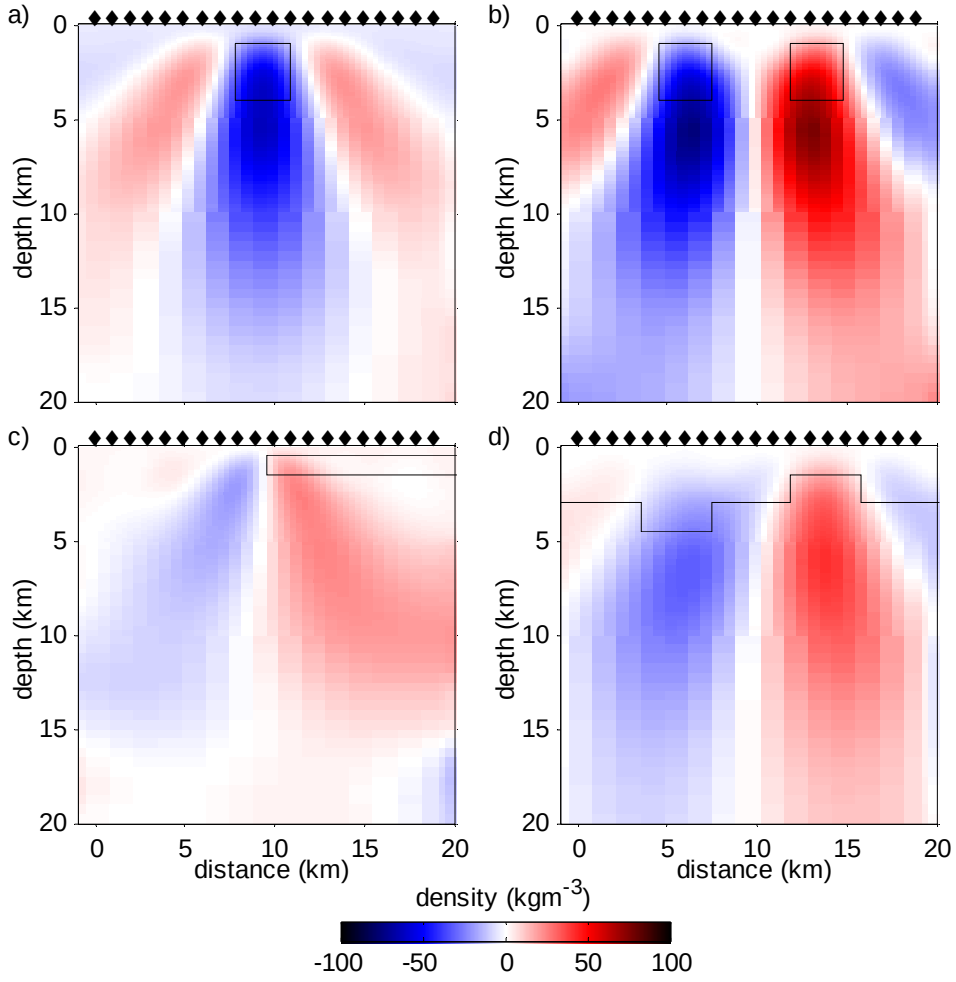

Figure 4.13: The results from the Occam gravity inversion with a depth weighting function for the a) one box, b) two box, c) horizontal sheet and d) horizon synthetic models with an error of 0.03 mGals and a contrast 100 kgm^{-3}. The associated β_* and z_0 values are given in Table 4.2.

the actual depth of the top boundary. In the horizon model, which has two features at different depths, the depth weighting function can only correctly locate the top of the 'high' in the horizon and fails to locate the 'low'.

Although the depth weighting function can be of benefit in correctly locating the top of the model's features, it occurs at the cost of losing all other boundaries. The bottom boundaries are indeterminate, due to the elongation of the features. The lateral boundaries are difficult to determine as they change with depth. The depth weighting has also caused a fictitious widening of the features with depth. This is particularly evident in the box models (Figures 4.13a and 4.13b). The inverted

density contrast for the models produced using the depth weighting function is larger than for the models without, and is a better representation of the true value. However, the main anomalous density values occur at depths lower than the bodies they actually represent.

4.5.3 Depth Resolution Summary

A depth weighting function or an appropriate grid configuration transformation (e.g. squared or logarithmic grids) can marginally aid the Occam gravity inversion to correctly locate structure with depth. The depth weighting function can find the top boundary of the synthetic model's features but this is at the expense of not being able to determine the lateral and bottom boundaries.

The squared, logarithmic and uniform grids return similar results if a horizontal damping factor is applied to the smoothing, but then the grid configuration is of secondary importance. Without a horizontal damping factor, grids where row thickness increases in proportion to the depth squared or exponentially, will produce similar models. The anomalous buried bodies have a surface expression and are elongated with depth. Neither grid was able to reconstruct the top boundary of a feature, but the lateral boundaries were consistent with the true models. A benefit of the transformed non-linear grids is that each produced similar results. Therefore, for joint inversion of MT and gravity data, the logarithmic grid (commonplace in MT) can be used without any adverse effect on the gravity component of the inversion.

4.6 Constraining the Inversion

The Occam features discussed in Section 4.2.2 can be used to incorporate *a priori* information into the inversion. *A priori* information can be in the form of geological information such as the location of different formation units, faults, unconformities or rock type boundaries. This information is introduced to the inversion by using sharp boundaries, fixing density values and assigning a prejudice (preferred) model.

The two box model, having a density contrast of 100 kgm^{-3} and an error of 0.03 mGal, was used to demonstrate the Occam features. Inversions were carried

out with sharp boundaries or regularisation decoupling at the side boundaries of the boxes only, the top boundary only, and along all boundaries. Inversions were also run with the density contrast of the boxes or the inner part of the boxes fixed at the correct value and with a prejudice model, with a prejudice weighting of 50, 75 or 100%, that contained the correct density values at the location of the two boxes.

When a sharp boundary is placed at the top boundary of the boxes (Figure 4.14b) there is no improvement in the inversion result (Figure 4.14a). The model features are still placed at the surface and smoothed over the sharp boundary. The reason for this is that gravity is sensitive to lateral changes and not horizontal features. Placing sharp boundaries vertically at the box side boundaries results in the two boxes being better defined and the main density anomaly located in the box areas (Figure 4.14c). However, the smoothness constraint and the inversion inability to locate structure with depth cause the density anomaly to be extended in the vertical direction. Placing sharp boundaries at all box boundaries ensures that the inversion estimates the location of the boxes accurately; the resulting density contrast inversion result is almost identical to the original true model (Figure 4.14d).

When only the inner part of the boxes' density was fixed, rather than placing the required extra density within the boxes on each side, it was placed at the surface, independent of the boxes (Figure 4.14e). Using a prejudice model with a low prejudice weighting enables the inversion to correctly locate the two boxes (Figure 4.14f). However, it causes an overshooting of density values for the boxes and spurious features around each box. These spurious features diminish as the weighting of the prejudice model increases. At the point at which the prejudice weighting is 100%, the inversion produces a model that is almost identical to the original.

4.7 Conclusions

The Occam gravity inversion program developed in this chapter is implemented as a non-linear 2D scheme, in the same format as the MT inversion, for ease of incorporation into a joint inversion approach. However, the non-linear scheme reduces to the linear Occam scheme when it is applied to a geophysical technique such as

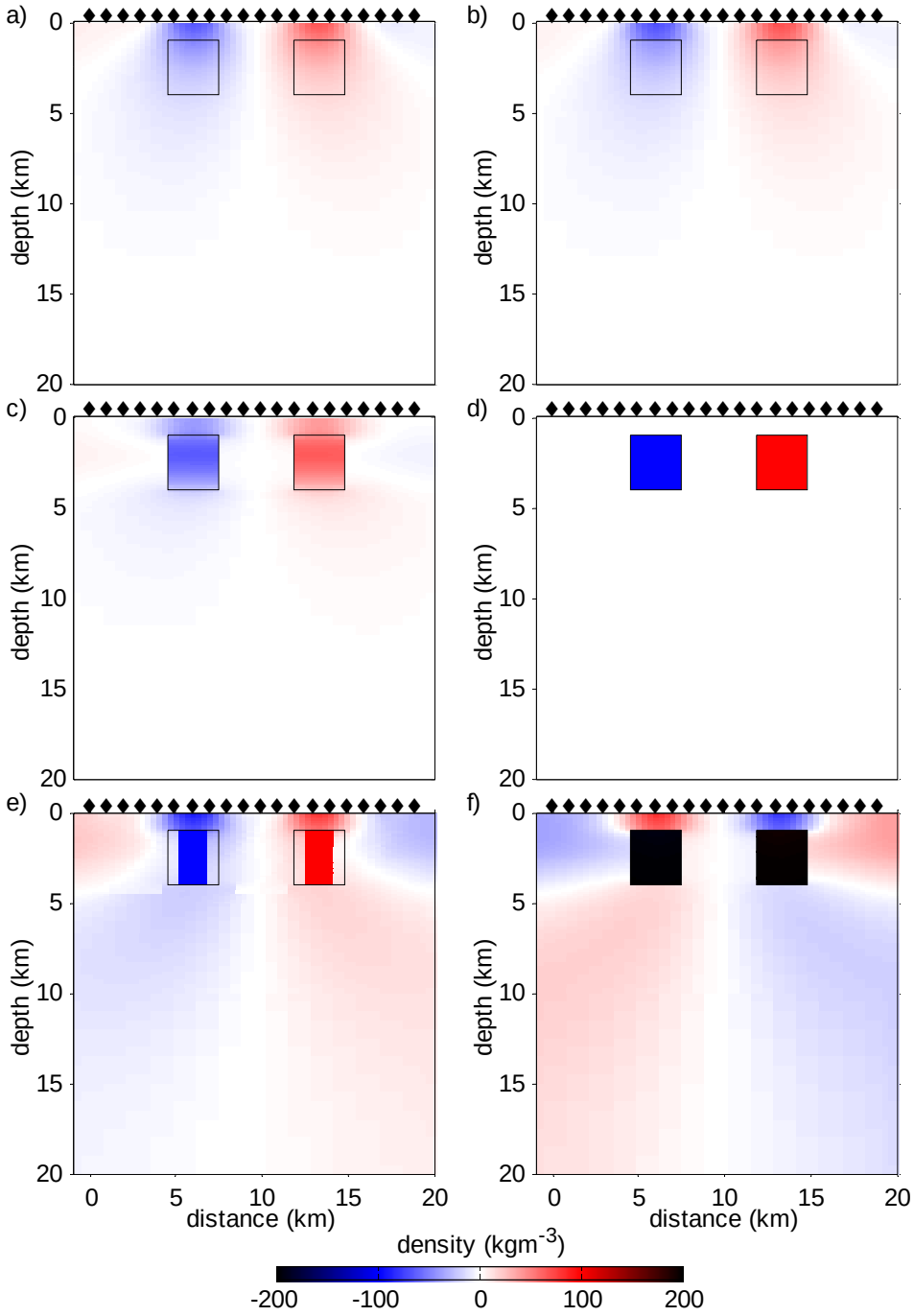

Figure 4.14: The results from the Occam gravity inversion for the two box synthetic model with an error of 0.03 mGals and a contrast of 100 kgm^{-3}. The constraints imposed are a) no constraints, b) sharp boundaries along the top, c) sharp boundaries along the sides, d) sharp boundaries at all boundaries, e) fixed density of 100 kgm^{-3} in the inner part of the boxes and f) prejudice model with the each box having a density of 100 kgm^{-3} and a 50 % weighting.

gravity, which has a linear forward model formulation. The Occam gravity inversion is stable and always produces models with an RMS of 1. The inverted models have anomalous density values placed primarily at the surface, but because of smoothing get smeared vertically and laterally into the model.

Chapter 5

Linking the Gravity and Magnetotelluric Techniques

Gravity and MT are two fundamentally different techniques that will be combined in a petrophysical joint inversion. The benefits of combining these two techniques and establishing how density and conductivity should be linked in the joint inversion form the subject matter of this chapter. Also, the equations used to link density and conductivity are critically examined.

5.1 Why Gravity and Magnetotellurics?

Individual inversions of gravity data or MT data produce highly varied models that can fit the data equally well. Gravity inversions are inherently non-unique and have little intrinsic depth resolution, while MT inversions are vulnerable to distortions (noise) in the MT data. MT inversions are also less sensitive to resistive (low conductivity) structures. These facts suggest that the gravity and MT techniques could benefit from some form of joint inversion. In this section the theoretical and logistical benefits specific to combining these two techniques will be discussed.

Theoretically, gravity and MT are fundamentally different techniques. In Section 2.2.1 it was shown that the gravity technique satisfies the Laplace and Poisson equations, whereas in Section 2.1.1 it was shown that the MT technique satisfies the diffusion equation. Having two techniques which satisfy different governing

equations can be beneficial to a joint inversion because each technique can provide different information about the subsurface. The MT technique can provide depth resolution, for which the gravity technique is limited, although gravity data can help constrain lateral variations in the subsurface. A diffusion-based technique, involving a first order time derivative (quasi-static case) will contain more information about the subsurface than a potential field method which has no time-dependency (static case). Therefore, in the joint inversion, the MT technique is expected to play the dominant role in the reconstruction of the subsurface, whereas the gravity technique aids in refining these results.

In Section 2.1.1 it was shown when working with a poor conductor or for a specific (fixed) instance in time, the diffusion equation which governs the MT technique reduces to the Laplace equation (away from a source) or the Poisson equation (in the presence of a source). This means that the MT field quantities satisfy the potential field equations which govern gravity. Therefore, on a comparable scale it would be expected that both techniques behave in a similar manner. Similar behaviour of the two techniques when combined in a joint inversion is desirable, as there is an increased likelihood that they will detect the same subsurface features and exhibit similar variations in their responses over a given distance. The similar spatial patterns of the gravity and MT responses have previously been observed on a large scales [121] [122] [123]. In the Fowler domain in South Australia, the structural boundaries in the Bouguer anomaly map align with the 2D MT responses and these correspond to adjacent blocks having different chemical, temperature and fluid properties [121].

Comparable spatial variations in the MT and gravity responses mean they have similar acquisition trends. It is often beneficial for the two techniques in a joint inversion to have similar station spacing as the number of stations and the station spacing influences the size and shape of the inversion grid. If two techniques are jointly inverted while having a significantly different number of stations or an irregular station density in relation to the other technique, then this can cause the joint inversion to favour fitting one technique at the expense of the other (Section 7.3).

The gravity and MT techniques are well suited in terms of field acquisition.

They are both relatively cheap techniques by which to acquire data, and this has led to a large volume of freely accessible data. In Australia, there exists the Australian National Gravity Database [65] which contains open-file information about all gravity surveys conducted in Australia. Internationally, experiments such as the Gravity Recovery and Climate Experiment (GRACE), have yielded open-file gravity data for the globe [124]. There is also an increase in MT data acquisition being achieved; one example is the AuScope program, an initiative of the Australian Federal Government [125]. Gravity and MT data sets are also starting to be acquired during the same geological investigations, predominately for petroleum and geothermal exploration in sedimentary basins [126] [127] [128]. Joint acquisitions and easily accessible data have created many opportunities for gravity and MT joint inversions to be undertaken, contributing further to geophysical research.

Finally, as shown in Chapter 6, gravity and MT provide an opportunity to develop a new implementation of a petrophysical joint inversion. However, the link between conductivity and density (which will be used in the joint inversion) must first be established and validated.

5.2 Choice of Defining Equations

The choice of suitable and applicable defining equations used to link the two techniques in a petrophysical joint inversion is the key to its success. These defining equations determine how robust the joint inversion will be and to what geological environments it can be applied. In the case of gravity and MT, there is no analytical equation that directly links density and conductivity, however, the individual behaviour of both conductivity and density were previously described in Sections 2.1.2 and 2.2.2. Based on these equations an indirect link between density and conductivity can be determined.

Effective medium conductivity models give the bulk conductivity of multiple conducting phases with different shapes and geometries, such models include the Hashin-Shtrikman Bounds, Waff model, parallel model, perpendicular model, bricklayer model and the random model [40] [41] [42] [43] [44] [45] [46] [47] [48]. These

conductivity models and the summation density model [69] are analogous; they are all functions of the conductivity or density of each constituent phase and their volume fractions. Using these models to developing a link between density and conductivity is practically impossible as they are functions of their own properties. The only similarity between the models is that they all involve fractional volumes. Therefore, if there exists prior knowledge on the conductivity and density of each phase then one can try to ascertain the fractional volumes of the different phases. However, fractional volumes are simply a reflection of rock composition and do not clearly describe a joint behaviour between conductivity and density. Another drawback of using effective medium models as a link in a joint inversion is that they are not representative of the true conductivity of the Earth, as they only apply to simple geometric distributions of conductivity phases and give bounds between which the true conductivity lies.

In the case of mantle minerals, the Arrhenius relationship [50] can be used to describe conductivity values, while the High Temperature density model and Mg# density model [69] [70] [71] can be used to describe density values. The Arrhenius relationship and the High Temperature density models describe both conductivity and density in terms of temperature. An increase in temperature will cause an increase in conductivity, and a decrease in density. The Hirsch variation [59] of the Arrhenius relationship and the Mg# density models describe mantle mineral density and conductivity in terms of the magnesium number. Iron and magnesium are important, since iron can be chemically substituted for magnesium in the lattice [129], giving rise to an increase in both conductivity and density. Using these equations could result in temperature or the magnesium number providing a link between density and conductivity, with the final joint inversion having applications in mantle investigations but hardly for sedimentary basin and upper crustal investigations.

One problem associated with using a density and conductivity link based on mantle minerals is that mantle conductivity processes are not fully understood. Temperature and Mg# dominate mantle mineral conductivity, but oxygen fugacity, hydration, pressure and grain size also have an effect [58]. The lack of understanding of mantle conductivity processes is highlighted by the mismatch in conductivity

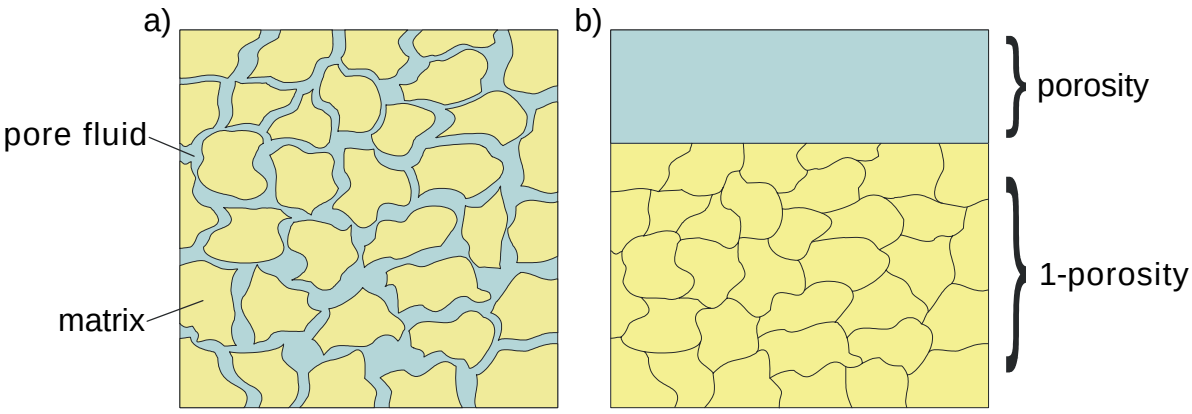

Figure 5.1: Schematic representation of a sedimentary rock showing a) the two different phases, matrix and pores, and b) their relative proportions based on porosity.

of mantle minerals obtained from laboratory estimations and values extracted from field data. Also, the Arrhenius relationship and Hirsch model, which model laboratory conductivity measurements, only allow for a single mantle mineral and this makes applying these equations to the true Earth difficult.

For exploration purposes, the most relevant equations are the porosity-density relationship for density, and Archie's Law for conductivity. These are both well established and accepted empirical equations that describe the bulk properties of sedimentary rocks in term of porosity. Archie's Law and the porosity-density relationship offer a link between density and conductivity through porosity and will thus form the basis for the gravity and MT petrophysical joint inversion. The following section discusses the validity of the porosity-density relation, Archie's Law and the joint behaviour of density, conductivity and porosity.

5.3 Porosity-Density Relationships

The porosity-density relationship describes the bulk density of sedimentary rock [130]. As shown in Figure 5.1a, the two primary phases used to describe sedimentary rocks are the rock matrix (or skeleton of mineral grains) and the pore fluid which fills the voids. Porosity is a measure of void space, being the ratio of the volume of voids to the total volume. Porosity values vary between zero, which corresponds to only matrix with no void space, and a value of one, which has only void space with

no matrix. Based on porosity, the two components can be redistributed as depicted in Figure 5.1b and the porosity-density relationship can then be written as

$$\rho_{bulk} = \phi\rho_{fluid} + (1-\phi)\rho_{matrix} \quad , \tag{5.1}$$

where ρ_{bulk} is the bulk density, ϕ is porosity, ρ_{fluid} is the pore fluid density and ρ_{matrix} is the matrix (grain) density. The density of the rock matrix is dependent on the rock type and composition. The matrix density of sandstone, limestone and dolomite are roughly fixed at 2650, 2710 and 2870 kgm^{-3}, respectively, while shale densities can vary on average over the range 2650 kgm^{-3} to 2700 kgm^{-3} [130].

The pore fluid is most often water or hydrocarbons, with the densities of gas and oil being approximately 0.7 kgm^{-3} and 850 kgm^{-3}, respectively [130]. The density of the formation water is dependent on temperature, pressure and salinity. Water salinity can vary considerably from fresh water, with salinity of < 10000 ppm, to hyper-saline fluid with a salinity > 300000 ppm. The salinity of sea water is ~ 35000 ppm and formation fluids are typically saline with the salinity generally increasing with depth [131]. Attempts to quantify the relationship between fluid density, temperature, pressure and salinity have been primarily based on laboratory observations and are summarised by Adams and Bachu [132]. The best fluid density model was developed by Batzle and Wang [133] as it can be used for a wide range of salinities (≤ 320000 ppm), temperatures ($20-350$ °C) and pressures ($5-100$ MPa). The Batzle and Wang model initially calculates the density of fresh water then adjusts it to account for salinity, and can be stated as follows

$$\begin{aligned} \rho_w &= 1 + 1\times10^{-6}(-80T - 3.3T^2 + 0.00175T^3 + 489P \\ &\quad -2TP + 0.016T^2P - 1.3\times10^{-5}T^3P \\ &\quad -0.333P^2 - 0.002TP^2) \end{aligned} \tag{5.2a}$$

$$\begin{aligned} \rho_{fluid} &= \rho_w + Sal\{0.668 + 0.44Sal + 1\times10^{-6}[300P \\ &\quad -2400PSal + T(80 + 3T - 3300Sal \\ &\quad -13P + 47PSal)]\} \end{aligned} \tag{5.2b}$$

.

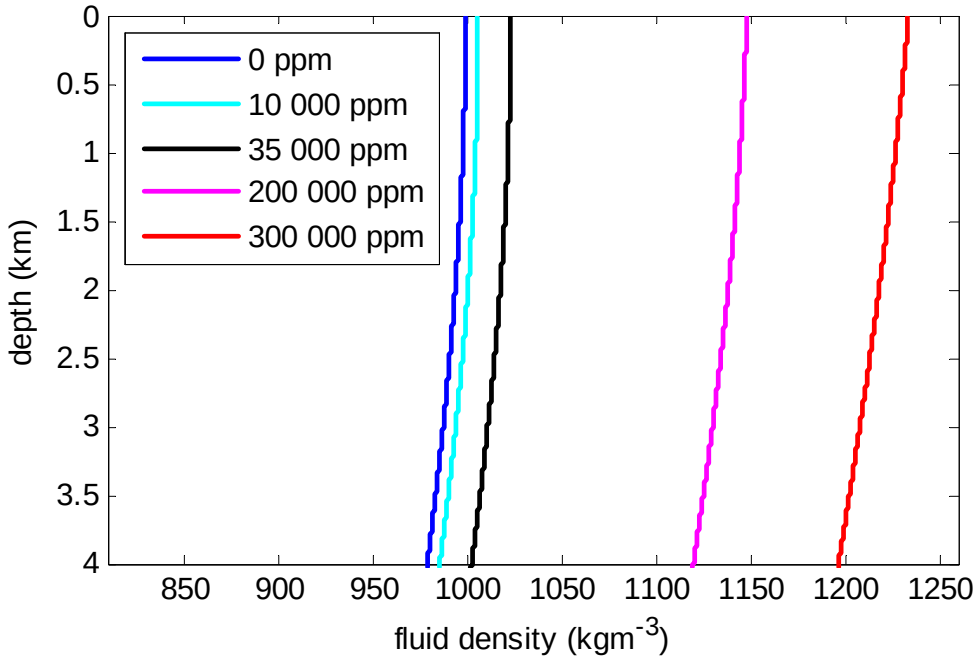

Figure 5.2: An example of a fluid density vs. depth profile for different salinities based on the Batzle and Wang model [133], using a pressure gradient of 9.9 MPakm^{-1} and a temperature gradient of 20 °Ckm^{-1}.

Here ρ_w is the density of fresh water, T is temperature in °C, P is pressure in MPa and Sal is the salinity represented by the sodium chloride (NaCl) mass fraction in ppm10^{-6}.

The Batzle and Wang model (Equation 5.2) is graphically depicted in Figure 5.2, using a pressure gradient of 9.9 MPakm^{-1} and a temperature gradient of 20 °Ckm^{-1}. These are typical gradients for sedimentary basins. The plot shows minimal variation in the density values with depth for a given salinity, but the effect of increased salinity causes an offset to higher densities. If the temperature gradient is increased it would cause a decrease of density with depth, whereas a pressure increase would cause an increase in density. Except for extreme temperature gradients, the fluid density variation with depth remains relatively constant. Due to the lack of variation in fluid density with depth, it is generally assumed to be constant for a given salinity. The density of fresh water is $\sim$ 1000 kgm^{-3}, that of sea water is $\sim$ 1030 kgm^{-3}, while hyper-saline fluid can achieve densities greater than 1200 kgm^{-3}.

Figure 5.3 shows several plots of the porosity-bulk density relationship for changes

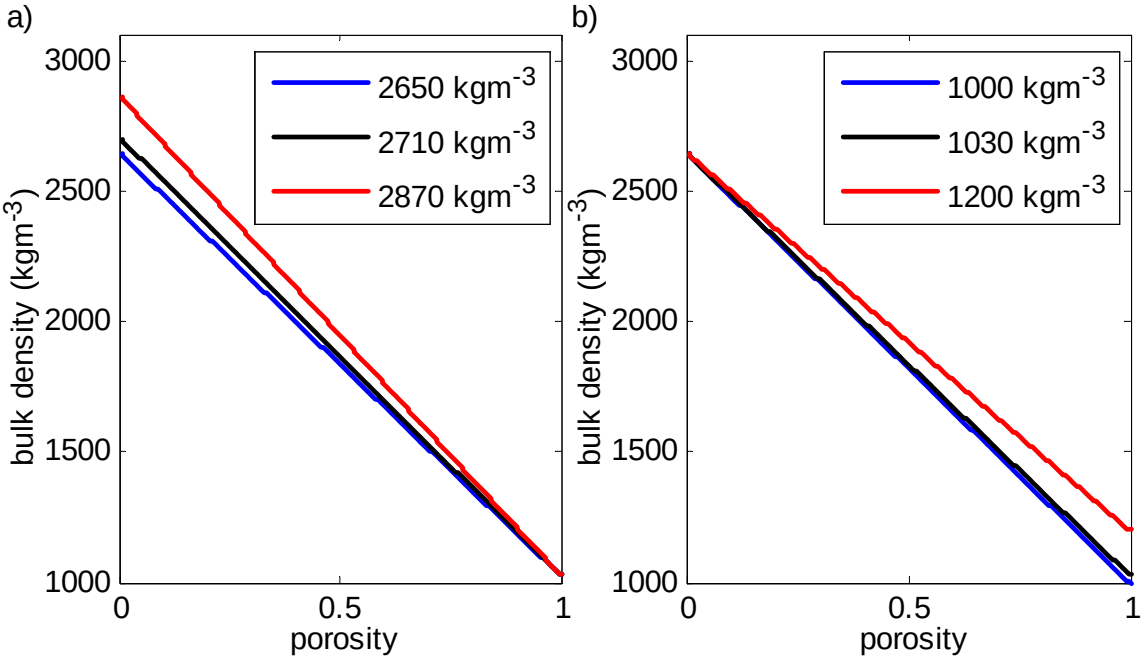

Figure 5.3: An example of the porosity-density relationship for a) fixed fluid density of sea water (1030 kgm^{-3}) and the matrix densities corresponding to sandstone (2650 kgm^{-3}), limestone (2710 kgm^{-3}) and dolomite (2870 kgm^{-3}) and b) fixed matrix density of sandstone (2650 kgm^{-3}) and the fluid densities corresponding to fresh water (1000 kgm^{-3}), sea water (1030 kgm^{-3}) and hypersaline fluids (1200 kgm^{-3}).

in the matrix and fluid densities. The upper bound on the bulk density is the matrix density and the lower bound is the fluid density, which corresponds to porosity values of zero and one, respectively. Between these two end point values, there is a linear relationship between porosity and bulk density. Variation in the matrix density has the greatest effect on the bulk property when the porosity approaches zero. Conversely, the fluid density has the greatest effect on the bulk property when porosity approaches one.

If assumptions are made about the matrix and fluid densities then porosity values can be directly obtained from the bulk density values using the porosity-density relationship. This is common practice when interpreting wireline logs [105]. Using the porosity-density relationship to determine the correct porosity value leads to erroneous results when the assumed matrix and fluid densities are incorrect. Confusing fresh water with sea water, or even oil, will only return a small error ($\sim 1\%$) in porosity, as their densities are closely related with typical values of 1000 kgm^{-3},

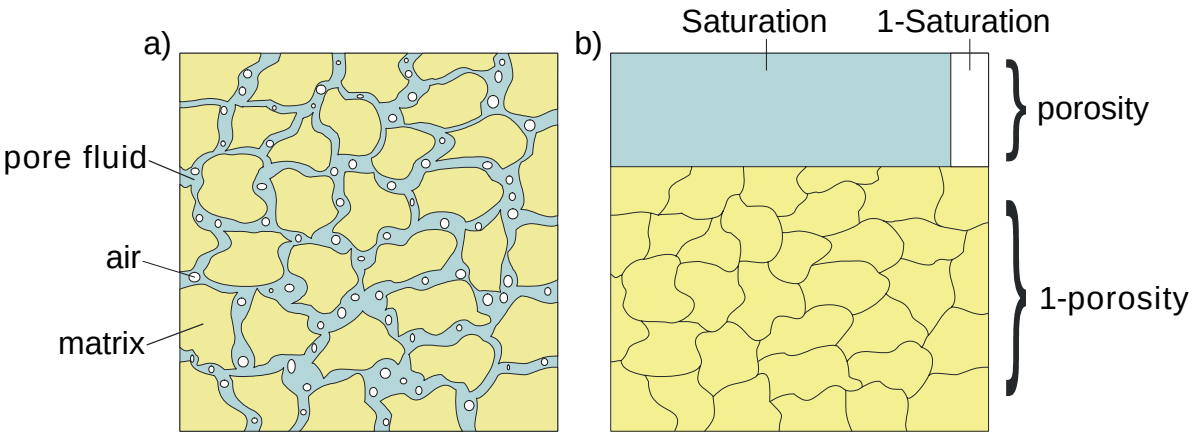

Figure 5.4: Schematic representation of a partially-saturated sedimentary rock with a) the different components – matrix, air and fluid and b) their dependence on the porosity and saturation terms.

1030 kgm^{-3} and 850 kgm^{-3}, respectively. However gas has a markedly different density of $\sim$ 0.7 kgm^{-3} and if incorrectly identified will cause unrealistic porosity values. Matrix density variations are due to impurities, where sandstones can contain felspars ($2520 - 2630$ kgm^{-3}), micas ($2650 - 3100$ kgm^{-3}), lignite fragments ($500 - 1800$ kgm^{-3}) and even heavy minerals ($2700 - 5000$ kgm^{-3}). Variations in the shale matrix density are generally due to composition, with an increase in carbonate content causing an increase in the density. The presence of organic matter ($500 - 1800$ kgm^{-3}) can also drastically decrease the shale density. Changes in grain densities and consequently matrix densities are generally small, gradual and often occur in a predictable way [130].

So far the bulk density as a function of two components, namely the matrix and pore fluid, has been considered. However, the bulk density can be described as the sum of any number of components, weighted by their fractional volumes. One such variation is to allow fractional degrees of saturation, as shown in Figure 5.4. This schematic diagram allows one to express the porosity-density relationship in the following way

$$\rho_{bulk} = S\phi\rho_{fluid} + (1 - S)\phi\rho_{air} + (1 - \phi)\rho_{matrix} \quad , \tag{5.3}$$

where ρ_{air} is the density of air, which normally has a value of zero, and S is the

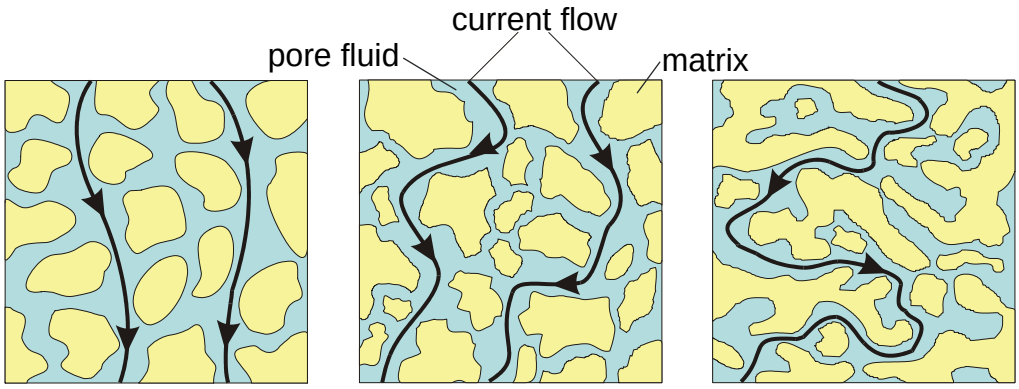

Figure 5.5: Examples of the electric current flow paths in the pore fluid and its dependence on the rock matrix.

degree of saturation ($0 < S < 1$). Allowing for saturation means that the overall bulk density is lower than in the fully saturated case, where the lower bound is now the fluid density weighted by the fractional saturation. The addition of saturation terms allows the porosity-density relationship to have wider applicability and is more closely connected with Archie's Law.

5.4 Archie's Law

Archie's Law is a well known and well established empirical equation that describes the bulk conductivity of sedimentary rocks [49]. In such rocks the dominant mode of conduction is ionic, involving flow of current through the pore fluid. The mineral matrix itself acts as an electrical insulator and does not contribute to the bulk conductivity. However, it does play an indirect role, with the texture of the rock dictating the size, geometry (shape) and inter-connectedness of the pore space (tortuosity). The texture of the rock and pore throat size is important in relation to the type and radius of ions and controls the paths of the ions through the rock. Poor connections and narrow openings inhibit current flow, whereas good connections and large openings promote current flow, as shown in Figure 5.5. Archie's law is normally written in terms of resistivity $\left(\frac{1}{\sigma}\right)$ but for consistency with Chapter 2 it will be written in terms of conductivity and assumes the form

Table 5.1: The tortuosity factor and cementation factor values for different lithologies.

Description of rock	a	m_{cf}
Weakly cemented detrital rocks, such as sand, sandstone and some limestones, with a porosity range from 25 to 45%, usually Tertiary in age	0.88	1.37
Moderately well cemented sedimentary rocks, including sandstones and limestones, with a porosity range from 18 to 35%, usually Mesozoic in age	0.62	1.72
Well-cemented sedimentary rocks with a porosity range from 5 to 25%, usually Paleozoic in age	0.62	1.95
Highly porous volcanic rocks, such as tuff, pahoehoe and aa, with porosity in the range 20 to 80%	3.50	1.44
Rocks with less than 4% porosity, including dense igneous rocks and metamorphosed sedimentary rocks	1.40	1.58

$$\frac{1}{\sigma_{bulk}} = aS^{-n_s}\phi^{-m_{cf}}\frac{1}{\sigma_{fluid}} \quad , \tag{5.4}$$

where σ_{bulk} is the bulk rock conductivity, σ_{fluid} is the pore fluid conductivity, ϕ is porosity, m_{cf} is the cementation factor ($1.3 < m_{cf} < 3$), S is the degree of saturation, n_s is the saturation exponent (~ 2) and a is the tortuosity factor ($0.6 < a < 1.5$) [134].

The variables (a, m_{cf}, S, n_s) in Archie's Law make it environmentally specific. The terms a and m_{cf} characterise the rock texture. The tortuosity factor a was introduced by Winsauer *et al.* [135] to account for the tortuosity of current paths due to pore geometry, while the m_{cf} value accounts for the pore geometry and connections. Typical values of a and m_{cf}, taken from Keller [136], are given in Table 5.1. Archie's Law has been generalised to allow for partial saturation through S and n_s. However, their introduction has not been completely established [137] and will be assumed to be 1, unless otherwise stated.

The fluid electrical conductivity of a rock controls the amount of current (charge per unit time) that can be transmitted. The pore fluid can be either water or hydrocarbons, the latter having high resistivity and being essentially an insulator

Figure 5.6: Variations in resistivity due to temperature, pressure and KCl concentration taken from Nesbitt [138]. There is an inverse relationship between resistivity and conductivity.

[130]. The conductivity of water varies greatly and similar to fluid density, it is dependent on temperature, pressure and salinity [138] [139]. Figure 5.6, taken from Nesbitt [138], summarises these combined effects. Pressure has a minimal effect on the fluid conductivity except at high temperatures (> 300 °C) where the low pressures cause an uncharacteristic lowering of the conductivity. Temperatures $<$ 300 °C cause a sharp increase in the fluid conductivity, which then stabilises between $200-300$ °C, while temperatures > 300 °C show increased conductivity values. The unusual behaviour exhibited by conductivity at temperatures > 300 °C is caused by a change in viscosity and a decrease in fluid density, which causes an increase in the extent of ion pairing, lowering the concentration of free ions and consequently the conductivity [138] [139]. The dominant dissolved salt in subsurface fluids is NaCl, and with increasing salinity, the conductivity increases. However, as the concentration approaches saturation level, the electrical conductivity tends towards the value for molten salt [140].

For shallow temperature distributions (< 300 °C) a linear relationship between temperature and fluid conductivity of water has been assumed by many researchers

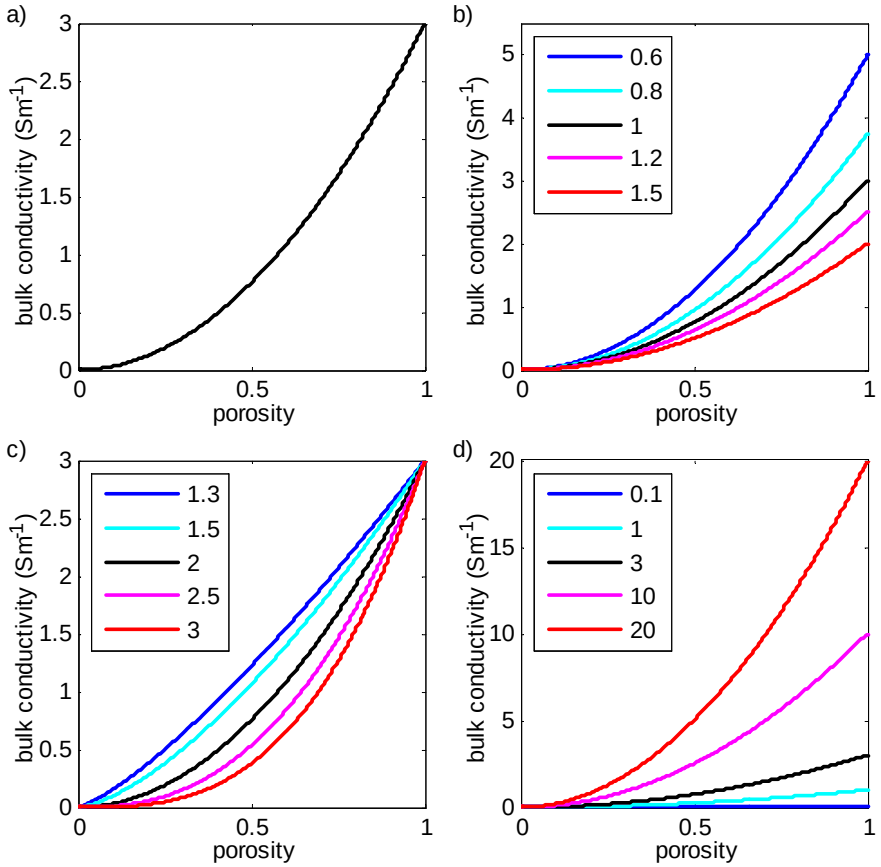

Figure 5.7: Archie's Law in graphical form, where $m_{cf} = 2$, $a = 1$ and $\sigma_{fluid} = 3$ Sm^{-1} unless otherwise indicated a) general behaviour, b) changes in the a-value, c) changes in the m_{cf}-value and d) changes in the fluid conductivities.

[122] [141]. In its most general form, it can be written as

$$\sigma_w(T) = \sigma_{w_o} + \frac{T}{10} \quad , \tag{5.5}$$

where σ_w is the conductivity of water, T is temperature in °C and σ_{w_o} is the conductivity of water at zero temperature and fixed salinity. For sea water, σ_{w_o} is 3 Sm^{-1} [142].

A general version of Archie's Law is shown graphically in Figure 5.7a. When porosity approaches zero the insulating rock matrix becomes dominant and the bulk conductivity approaches zero. At a porosity of one, there is no rock matrix and the bulk conductivity equals the fluid conductivity. Between these two end points there is a power law relation between the bulk conductivity and the porosity, controlled by

the exponent value m_{cf}. As the m_{cf}-value increases, the bulk conductivity decreases (Figure 5.7c), which corresponds to the rock particles moving away from being spherical and becoming more platy and jagged. Other textural elements, such as particle size and spread, have minimal effect on the m_{cf}-value when compared to the shape [143]. The a term is a scaling factor which Keller and Frischknecht [144] suggests has values of $a < 1.0$ for rocks with intergranular porosity and $a > 1.0$ for those with fracture porosity [143]. As the a-value increases, the bulk conductivity decreases, with the maximum variation in the bulk conductivity due to the a-value occurring at large porosities (Figure 5.7b). The inclusion of the a-value means that the bulk conductivity will no longer equal the fluid conductivity at 100% porosity. This is undesirable because physically it makes no sense.

Figure 5.7d shows Archie's Law in graphical form for varying fluid conductivity values. The curves corresponding to values of 0.1, 1 and 3 Sm^{-1} are representative of hydrocarbons, fresh water and sea water, respectively. The fluid conductivities of 10 Sm^{-1} and 20 Sm^{-1} are indicative of high salinity or high temperatures. Increasing the fluid conductivity will increase the bulk conductivity. A considerable difference in the bulk conductivity can result from variations in the fluid conductivity at large porosities. For small porosities, when the rock matrix is dominant, the effect of the fluid conductivity variations is reduced. Fluid conductivities of 0.1 Sm^{-1} give almost no variation in the bulk conductivity with changing porosity. Duba *et al.* [145] have questioned the validity of Archie's Law, based on laboratory observations, when fluid conductivity is < 1 Sm^{-1}. Although fluid conductivities can cause significant variations in the bulk conductivity, for most sedimentary geological situations the fluid conductivity behaves in a predictable way according to Equation 5.5.

As is evident in Figure 5.7b-5.7d, for changes in either a, m_{cf} or the fluid conductivity, the resulting variations in bulk conductivity are not as significant as those for porosity. Archie himself found porosity has the greatest control on the bulk conductivity [49]. So when the rock type (represented by the a and m_{cf} values) and fluid conductivity are known, the bulk conductivity can be used to determine porosity from Archie's Law.

Archie's Law is very useful at determining porosity when used in the right envi-

ronment, but it breaks down when the assumed matrix insulator becomes a conductor. This occurs when there is either mineralisation or clays present. Mineralisation, in particular graphite and sulphides, behave as electronic (ohmic) conductors and will contribute to the bulk conductivity. As a result, Archie's law will drastically under-estimate the bulk conductivity of the rock, the magnitude dependent on the amount and inter-connectedness of the mineralisation. A clay matrix will cause additional conduction due to an electrical double layer that forms on the particle surface in the presence of water. The electrical double layer effect, referred to as surface conductivity, allows ions to move through the system with less resistance than in the fluid phase [146]. The conductivity of clays depends on the clay species, surface area and the nature of the pore fluid. In some situations the clay surface conductivity can exceed that of the pore fluid and can cause oil-saturated shaly-sands to have unexpectedly high conductivities. In such instances, modifications can be made to Archie's Law to allow for a matrix conductor [147] [148] [149].

Archie's Law was developed for a porous medium with an emphasis on sedimentary rocks. However, it can also be used in any environment where the dominant conduction is a fluid phase and the matrix is an insulator that controls the fluid distribution. Archie's Law has been applied to partial melts where the melt takes on the role of the pore fluid [150] as well as having been successfully applied to oceanic [151] and continental basement rocks [152].

5.5 Joint Behaviour

Porosity is the main controlling factor of density and conductivity in sedimentary rocks. There are two main types of porosity - primary and secondary. The primary porosity is the porosity in a rock originating from its deposition and is connected with the original rock fabric or texture. Secondary porosity is a subsequent porosity generated in the rock due to fracturing (fracture porosity), jointing and chemical leaching or dissolving of minerals (vuggy porosity). It often enhances the overall porosity. Primary and secondary porosity can either coexist (dual porosity), or secondary porosity can dominate and override the primary porosity. Archie's Law

was developed for primary porosity and this will be the main focus in this thesis.

Porosity is an important quantity in geoscience and particularly in sedimentary basin analysis. It can be used to evaluate the volume of hydrocarbons or water and can provide an indication of the flow rate, path and pressure of formation fluids. Porosity is also used to determine basin history as it is dependent on depositional environments and is affected by rate and depth of burial. Changes in porosity can also be a diagnostic for changes in rock type, with the greatest change occurring at the boundary between sedimentary rocks and the basement.

In sedimentary basins the porosity generally decreases with depth due to compaction. This causes an irreversible loss of porosity from the three dimensional strain of burial (self-compression). Therefore, porosity values are related to the maximum depth of burial and not the present day depth at which the rock is found. Giles *et al.* [153] collated available porosity-depth trends and found that there is a broad range of porosity trends and values, but there is always a smooth decrease in porosity with depth. They found that sandstones having initial porosities between $35-50\%$ steadily decrease to $2-10\%$ at depths of $4-6$ km. Carbonates have a similar trend, however initial porosities are between $25-70\%$. Shales have initial surface porosities of $\sim 70\%$, which decrease sharply over the top few kilometres before a gradual decrease to final porosities values which are also between $2-10\%$. The main exception to porosity decreasing with depth is in regions of overpressure [154]. In such regions, the fluid becomes trapped during compaction and starts to support the load, which results in the preservation of the porosity. Porosity values can also be lower than expected through constant burial in areas of uplift.

Compaction, which controls the porosity-depth trend and actual values, is dependent on rock age, composition, initial porosity, geothermal gradient, tectonic history and the general make-up of the sedimentary basin environment [155] [156] [157] [158] [159]. In general, porosity will be preserved at depth in areas which are young, have a low geothermal gradient and rapid rates of sedimentation [153]. Although porosity-depth trends due to compaction are varied, there have still been attempts to create porosity-depth models. A linear model can be used to represent the porosity-depth trend for sandstones over a small range; however at some point

this will result in negative porosities. Baldwin and Butler [160] used a power law to model the porosity-depth trend, whereas Falvey and Middleton [161] proposed an inverse model based on changes in porosity being proportional to changes in load. The most common porosity-depth model is an exponential relationship given by Athy [162],

$$\phi = \phi_o e^{-\lambda_c z} \quad , \tag{5.6}$$

where ϕ_o is the surface porosity, λ_c is the compaction coefficient and z is the depth. The porosity value obtained from each of these models can vary up to 20% for a given depth, highlighting the need to calibrate any model with data from the area in question [153].

A typical sandstone porosity-depth trend, shown in Figure 5.8a, was used in the porosity-density relationship and Archie's Law to generate the density and conductivity-depth trend shown in Figure 5.8b and 5.8c. The porosity-depth trend was generated using Athy's model (Equation 5.6) with $\phi_o = 0.49$ and $\lambda_c = 270$ m [163]. The matrix density of sandstone (2650 kgm^{-3}) and a fluid density of sea water (1030 kgm^{-3}) were used in the porosity-density relationship. The a- and m_{cf}-values in Archie's law were set at 0.62 and 1.72, respectively, taken from Table 5.1. The fluid conductivity of sea water used in Archie's Law was given by Equation 5.5 with a temperature gradient of 30 °C.

Figure 5.8b shows density increasing as the porosity decreases due to effects of compaction. The primary loss of porosity is in the top 3 km and corresponds to the greatest loss of density. Conductivity increases down to a depth of 1 km because the temperature gradient in Equation 5.5 causes the fluid conductivity to increase at a greater rate than the compaction of porosity. Below 1 km depth the compaction of porosity becomes the dominant mechanism and the conductivity starts to decrease. Below 6 km depth the low porosity values means that the density approaches the matrix density and the conductivity approaches zero. Conductivity, across all rock types, has a larger range than density. However, in the sedimentary environment described in Figure 5.8, density varies between 1850 kgm^{-3} and 2595 kgm^{-3}, whereas conductivity varies between 0.15 Sm^{-1} and 1.8 Sm^{-1}.

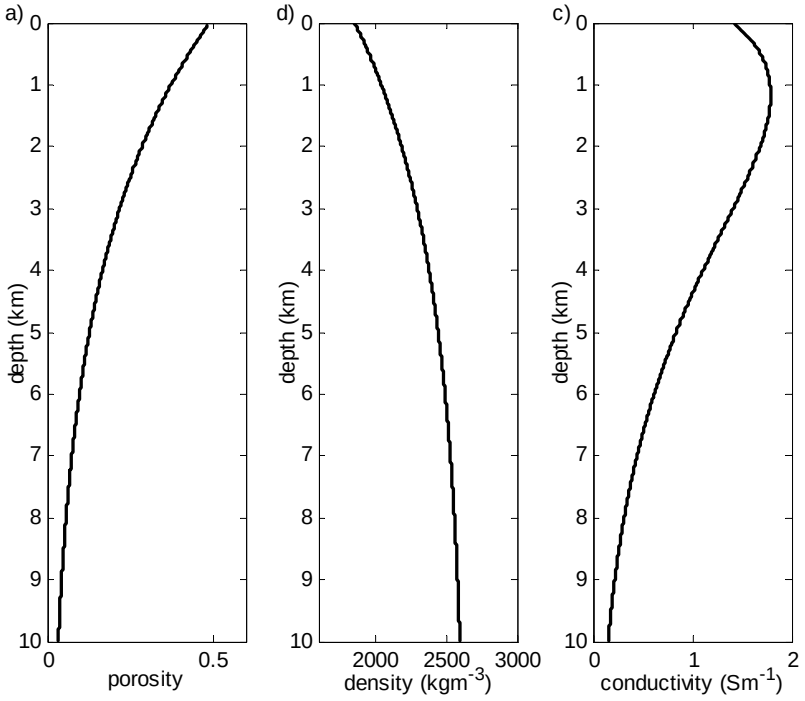

Figure 5.8: Examples of the porosity-, density- and conductivity-depth trends for sandstone. a) is the porosity-depth trend generated using Athy's model with $\phi_o = 0.49$ and $\lambda_c = 270$ m. b) is the density-depth trend generated using the porosity-density relationship with the porosity values from Athy's model and the matrix and fluid densities fixed at 2650 kgm^{-3} and 1030 kgm^{-3}, respectively. c) is the conductivity-depth profile generated using Archie's Law with the porosity values from Athy's model, $a = 0.62$ and $m_{cf} = 1.72$.

An alternative method to examine the joint behaviour of conductivity and density is to use porosity to develop an expression that directly relates them. This is achieved by rearranging Archie's Law and the porosity-density relationship to express porosity in terms of the other variables. The modified expressions of Archie's Law and the porosity-density relationship are then set equal to each other to yield

$$\rho_{bulk} = \left\{ \left(\frac{a\sigma_{bulk}}{S^{n_s}\sigma_{fluid}} \right)^{\frac{1}{m_{cf}}} * (S\rho_{fluid} - \rho_{matrix}) \right\} + \rho_{matrix} \quad (5.7a)$$

$$\sigma_{bulk} = \left(\frac{\rho_{bulk} - \rho_{matrix}}{S\rho_{fluid} - \rho_{matrix}} \right)^{m_{cf}} * \left(\frac{S^{n_s}}{a}\sigma_{fluid} \right) \quad . \quad (5.7b)$$

The explicit relationship between density and conductivity for sandstone is shown in Figure 5.9. The general behaviour is that as conductivity increases, density

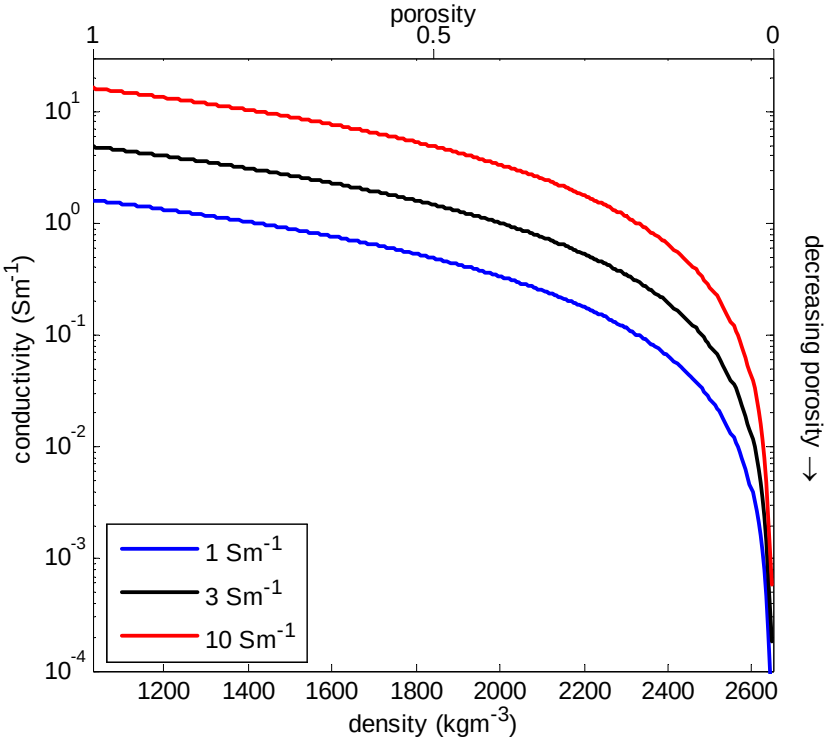

Figure 5.9: An example of the explicit relationship between conductivity and density for sandstone. In the equation $\rho_{matrix} = 2650$ kgm^{-3}, $\rho_{fluid} = 1030$ kgm^{-3}, $a = 0.62$, $m_{cf} = 1.72$ and fluid conductivity varies.

decreases. In Figure 5.9, the largest conductivity value is that of the fluid and occurs at the minimum density value, which is the fluid density (equivalent to $\phi = 1$). The maximum density value, which is the matrix density, corresponds to conductivity approaching zero (equivalent to $\phi = 0$). At high densities (small ϕ), a small change in density will cause a large change in bulk conductivity, whereas at low densities (large ϕ) a small change in density will result in a small change in conductivity.

The fluid and matrix densities constitute the upper and lower bounds on bulk density, so changing these values will result in the shortening or elongation of the relationship. The nature of the curve is relatively unaffected as the porosity-density relationship is linear and only changes to the parameters in Archie's Law will significantly change the curve. The main effect on the shape of the curve is the value of m_{cf}, whereas the a-value and fluid conductivity values are scaling factors. Fluid conductivity will have the greatest effect on the density-conductivity relationship because it has a large range of values by which to scale the relationship.

5.6 Conclusions

It is beneficial to combine gravity and MT data in an inversion as they have similar spatial characteristics and are both widely accessible; this allows for multiple applications of the joint inversion. By looking at the individual behaviour of both conductivity and density, it was found that Archie's Law and the porosity-density relationship both describe conductivity or density in terms of porosity. It was thus deemed that porosity is the strongest and most robust link on which to base the joint inversion.

In sedimentary basins, as the porosity increases the system is dominated by the fluid properties and the conductivity will increase, whereas density will decrease. When porosity decreases the system is dominated by the rock matrix and the conductivity decreases and the density increases. The other variables in Archie's Law describe the texture of the rock and are environmentally specific, while the other variables in the porosity-density relationship reflect the composition of the rock and are also environmentally specific.

Chapter 6

Joint Inversion Methodology

The new joint inversion scheme developed as part of this research is outlined in this chapter. The joint inversion combines MT and gravity data in a petrophysical approach using Archie's Law and the porosity-density relationship, as was described in Chapter 5. The general idea behind the joint inversion is introduced at the start of this chapter, then the actual methodology is described and this is then followed by the outline of some behavioural characteristics. The mathematical reasons why joint inversions can be beneficial are enunciated. The discussions contained in Chapter 5 were mainly in terms of conductivity, and this is how the literature generally presents petrophysical equations. However, when discussing MT inversion results, resistivity models are normally used. Therefore this chapter will reflect this shift and is thus written in terms of resistivity.

6.1 The Basic Idea

An MT and gravity petrophysical joint inversion requires a link between the two techniques. In Chapter 5, porosity was established as the crucial link between resistivity and density through Archie's Law and the porosity-density relationship. This dependency on porosity is exploited by the implementation of the petrophysical joint inversion which inverts directly for a porosity model. This model is constrained using both the MT and gravity data, in that the computed responses for the final model must fit the observed data sets.

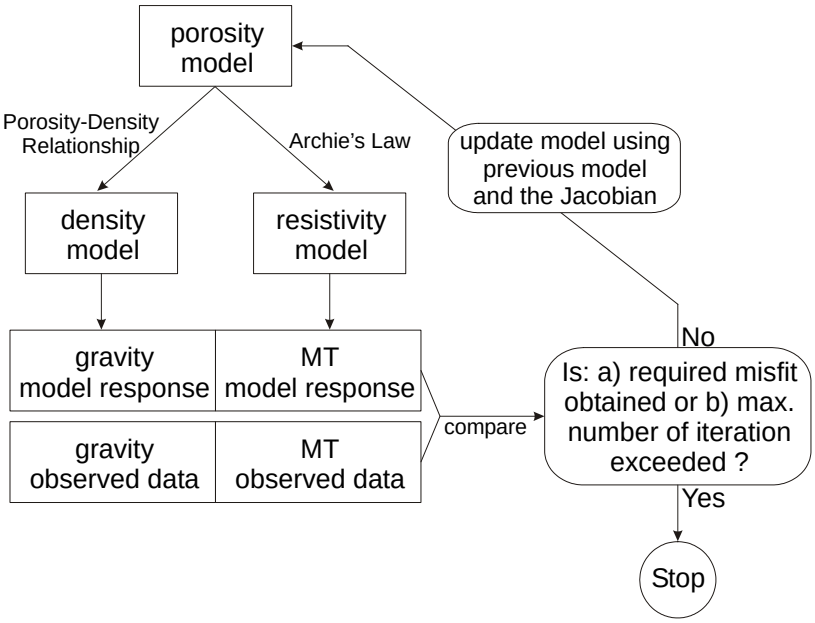

Figure 6.1: A simplified flow chart of the general steps taken by the gravity and MT joint inversion.

A flow chart for the joint inversion is shown in Figure 6.1. It illustrates how the porosity model at each iteration is converted to a resistivity and density model using Archie's Law and the porosity-density relationship. The response of the resistivity and density models is then computed and compared to the observed MT and gravity data. Based on both techniques, through their sensitivities (Fréchet derivatives) and the previous model, the porosity model is progressively updated. This process is repeated until a porosity model is found that satisfies both data sets.

A difficulty arises in the joint inversion formulation due to an inherent limitation of the gravity technique itself. The Bouguer anomaly data only contain information about the density contrast (relative densities) of the subsurface, whereas the porosity-density relationship yields absolute density values from the porosity values. If ignored, this will lead to an inconsistency in the joint inversion, causing it to fail. Such an inconsistency may be reconciled by the introduction of a gravity offset term. This is a constant value which must be added to all Bouguer anomaly data points to make them correspond to an absolute density model. In most situations the exact value of the gravity offset is unknown, and must be found as an additional parameter in the inversion itself.

6.2 Methodology

The aim of the joint inversion is to produce a single porosity model that satisfies both the MT and gravity data. The optimisation scheme used by the joint inversion is the 2D non-linear Occam scheme, which was outlined in Section 3.2. The main differences between the single technique Occam scheme and the requirements for the joint inversion are that the joint inversion involves two very different types of data and the model response is not directly calculated from the model parameters. At each iteration the joint inversion requires the current porosity model, which is being optimised, to be converted to a resistivity and density model and then their theoretical model responses are compared to the observed MT and gravity data sets.

In order to maintain the integrity of the Occam scheme, whilst still accommodating the extra requirements of the joint inversion, changes must be made to some of the inversion parameter definitions. In the following section the inversion parameters are redefined and their implementation discussed.

6.2.1 Parameter Description

Converting the single technique Occam scheme to a two technique joint inversion scheme requires the different inversion parameters to be redefined. Here, changes to the model parameterisation, data vector, model parameters, forward model operator, boundary conditions, and the Jacobian matrix are discussed and the gravity offset term defined.

Model Parameterisation

The original model parameterisation of the MT Occam inversion was designed to maintain accuracy of the MT forward model operator. The horizontal spacing should be one third of the skin depth of the highest frequency and the vertical spacing is at equal logarithmic increments to counteract the natural decay of the MT kernel [90]. The gravity forward model operator is based on an analytical expression and places no requirement on the computational mesh to maintain accuracy. It was shown in Section 4.5.1 that a logarithmic grid does not limit the ability of the gravity inversion

to reconstruct the subsurface density. Therefore, the model parameterisation is kept the same as in the original MT inversion (Section 3.2.1).

Another consideration is that the MT and gravity stations do not have to coincide and so they can be at different locations along the profile. Since the MT and gravity forward model operators are independent of each other, using different station locations has no effect on the accuracy or computation of either model response. The only requirement is that every station, regardless of type, must be at the same location as one of the surface node points within the finite element mesh.

Data

The MT data vector of length p can be written as $\mathbf{d}_{MT} = (d_{MT1}, d_{MT2}, ..., d_{MTp})$, where each element corresponds to a TE or TM apparent resistivity or phase for a particular station and frequency. The gravity data vector consists of a Bouguer anomaly data point for each station and can be written as $\mathbf{d}_{GV} = (d_{GV1}, d_{GV2}, ..., d_{GVs})$, where s is the number of gravity data stations. For the joint inversion, both the MT and gravity data are contained in the same data vector $\mathbf{d}$, which has MT data followed by the gravity data. It is given by

$$\mathbf{d} = (d_{MT1}, d_{MT2}, ..., d_{MTp}, d_{GVp+1}, d_{GVp+2}, ..., d_{GVp+s}) \quad , \tag{6.1}$$

where $q = p + s$ is the total number of data points. The $q \times q$ data weighting matrix $\mathbf{W}_d$ contains the standard deviations (σ^*) for every data point. Due to the split in the joint inversion data vector, $\mathbf{W}_d$ takes the form

$$\mathbf{W}_d = diag\left(\frac{1}{\sigma^*_{MT1}}, \frac{1}{\sigma^*_{MT2}}, ..., \frac{1}{\sigma^*_{MTp}}, \frac{1}{\sigma^*_{GVp+1}}, \frac{1}{\sigma^*_{GVp+2}}, ..., \frac{1}{\sigma^*_{GVp+s}}\right) \quad . \tag{6.2}$$

The 2D MT response at each station contains data points from different modes and frequencies, whereas gravity has only a single data point for each station. Therefore, there will always be considerably more MT data than gravity data for a given joint inversion ($p \gg s$).

The location or measurement datum for the MT and gravity stations does not

have to be the same. The MT data always relate to measurements made on the Earth's surface and the joint inversion will place the stations on the topographic surface. By contrast, gravity data are corrected to a single datum (elevation) and the joint inversion will place the stations at the top of the grid, regardless of whether there is variable topography or not.

Model Values

In the joint inversion the model parameter inverted for is porosity, therefore the model parameter vector $\mathbf{m}$ is given by

$$\mathbf{m} = (\phi_1, \phi_2, ..., \phi_n) \quad , \tag{6.3}$$

where n is the number of model parameters. Each model parameter corresponds to the porosity value of a specific cell (element) in the regularisation grid. The porosity can only vary between 0 and 1, and anything outside this range is not physically possible.

Gravity Offset Term

The Bouguer anomaly data used by the joint inversion will only produce a density contrast model (Section 2.2.1). However, converting porosity to density using the porosity-density relationship will yield absolute density values. Unless adjusted, the joint inversion would encounter an inconsistency between the observed data and model response.

Correcting the inconsistency between the Bouguer anomaly data and the model response produced from the absolute density model can be achieved by taking advantage of the linear nature of the gravity technique. That is, the net gravitational response is the algebraic sum of the responses of individual subsurface masses. The absolute density model can be made into a density contrast model by subtracting a constant background density value. This is equivalent to subtracting a constant value from the model response of the absolute density model. By doing so makes the response of the absolute density model compatible with the Bouguer anomaly data. This can be expressed in the following way

$$\mathbf{d}_{GV} = \mathbf{F}_{GV}(\mathbf{m}) + \Delta\mathrm{g} \quad , \tag{6.4}$$

where $\mathbf{F}_{GV}$ is the gravity forward model operator, and Δg is the unknown (negative) constant value and is referred to as the gravity offset term.

Initially the correct value of the gravity offset term is unknown; however, the inversion can be used to determine its value. By treating the gravity offset term as an additional model parameter, the inversion can solve for the optimal value. This means that the gravity offset term is included in the model parameter vector, which becomes

$$\mathbf{m} = (\phi_1, \phi_2, ..., \phi_n, \Delta\mathrm{g}) \quad , \tag{6.5}$$

and now has a length of $n+1$. Unless explicitly stated otherwise, the model parameters denoted by m_ϕ will hereafter only refer to the porosity component of the $\mathbf{m}$ vector.

Forward Model Operator

In the joint inversion the porosity model is converted to a resistivity model and a density model and then the theoretical MT and gravity model responses are calculated. The model responses are computed using the same forward model operators as in the single MT ($\mathbf{F}_{MT}$) and gravity ($\mathbf{F}_{GV}$) inversions, described in earlier chapters. The observed data vector in the joint inversion has the MT data followed by the gravity data; the forward model operations are executed to produce an equivalent model response.

The forward model operator of the joint inversion refers to the whole process of producing MT and gravity responses from the porosity model. This includes converting the porosity model to a resistivity and density model and the addition of the gravity offset term to the gravity response. The joint inversion forward model operator can be thought of as having two components, an MT component followed by a gravity component,

$$\mathbf{F}[\mathbf{m}] = \{\mathbf{F}_{MT}[\mathbf{m}_\phi] \ , \quad \mathbf{F}_{GV}(\mathbf{m}_\phi) + \Delta \mathrm{g}\} \quad . \tag{6.6}$$

Boundary Conditions

The forward model operator of the joint inversion is made up of the single MT and single gravity forward model operators. As a result, the boundary conditions of the individual MT and gravity forward model operators are the same as in the original single method formulations. This involves having the MT bottom boundary condition as the deepest row of cells in the regularisation grid, which are considerably elongated in depth to mimic a half space. However, the gravity bottom boundary condition requires the cells to be extended to such a depth that their response is negligible (Section 4.2.1). The elongated cells required by the MT forward model operator are not used in the gravity component of the inversion because the cells are unrealistically large and can have a major unwanted effect on the gravity response. Not including these cells in the gravity boundary condition means that they are only constrained by the MT data. Since the elongated cells are still contained in the smoothness constraint, the joint inversion cannot use these cells to improve the MT data fit without affecting the gravity data fit.

Jacobian Matrix

The elements of the joint inversion Jacobian matrix are given by

$$J_{ij} = \frac{\partial d_i}{\partial m_j} \quad , \tag{6.7}$$

where $j = 1, 2, ..., n, n+1$ corresponds to the model parameters and i corresponds to the number of data points of length q. For the joint inversion the data vector contains the MT data followed by the gravity data and the model parameters are porosity ϕ and the gravity offset Δg. Therefore the joint inversion Jacobian comprises the changes in MT or gravity data due to changes in porosity and the gravity offset and is expressed by

$$\mathbf{J} = \begin{bmatrix} \frac{\partial d_{MT1}}{\partial \phi_1} & \frac{\partial d_{MT1}}{\partial \phi_2} & \dots & \frac{\partial d_{MT1}}{\partial \phi_n} & \frac{\partial d_{MT1}}{\partial \Delta \mathrm{g}} \\ \frac{\partial d_{MT2}}{\partial \phi_1} & \frac{\partial d_{MT2}}{\partial \phi_2} & \dots & \frac{\partial d_{MT2}}{\partial \phi_n} & \frac{\partial d_{MT2}}{\partial \Delta \mathrm{g}} \\ \vdots & \vdots & & \vdots & \vdots \\ \frac{\partial d_{MTp}}{\partial \phi_1} & \frac{\partial d_{MTp}}{\partial \phi_2} & \dots & \frac{\partial d_{MTp}}{\partial \phi_n} & \frac{\partial d_{MTp}}{\partial \Delta \mathrm{g}} \\ \frac{\partial d_{GV1}}{\partial \phi_1} & \frac{\partial d_{GV1}}{\partial \phi_2} & \dots & \frac{\partial d_{GV1}}{\partial \phi_n} & \frac{\partial d_{GV1}}{\partial \Delta \mathrm{g}} \\ \frac{\partial d_{GV2}}{\partial \phi_1} & \frac{\partial d_{GV2}}{\partial \phi_2} & \dots & \frac{\partial d_{GV2}}{\partial \phi_n} & \frac{\partial d_{GV2}}{\partial \Delta \mathrm{g}} \\ \vdots & \vdots & & \vdots & \vdots \\ \frac{\partial d_{GVs}}{\partial \phi_1} & \frac{\partial d_{GVs}}{\partial \phi_2} & \dots & \frac{\partial d_{GVs}}{\partial \phi_n} & \frac{\partial d_{GVs}}{\partial \Delta \mathrm{g}} \end{bmatrix} . \tag{6.8}$$

The differential chain rule is used to ascertain the MT elements of the joint inversion Jacobian from the Jacobian produced from the single MT inversion. The chain rule can be stated as

$$J_{MTij} = \frac{\partial d_{MTi}}{\partial \phi_j} = \frac{\partial d_{MTi}}{\partial (\log(\varrho)_j)} \frac{\partial (\log(\varrho)_j)}{\partial (\varrho_j)} \frac{\partial (\varrho_j)}{\partial \phi_j} \quad , \tag{6.9}$$

where $\frac{\partial d_{MTi}}{\partial (\log(\varrho)_j)}$ is derived from the single MT inversion, while $\frac{\partial (\log(\varrho)_j)}{\partial (\varrho_j)} = \frac{1}{\varrho_j} \log(e)$ and $\frac{\partial (\varrho_j)}{\partial \phi_j}$ can be found by differentiating Archie's Law with respect to porosity. It is given as

$$\frac{\partial (\varrho_j)}{\partial \phi_j} = -m_{cf} a S^{-n_s} \phi^{-m_{cf}-1} \varrho_{fluid} \quad . \tag{6.10}$$

A similar approach is taken to derive the gravity elements of the joint inversion Jacobian from the Jacobian produced from the single gravity inversion,

$$J_{GVij} = \frac{\partial d_{GVi}}{\partial \phi_j} = \frac{\partial d_{GVi}}{\partial (\rho_j)} \frac{\partial (\rho_j)}{\partial \phi_j} \quad , \tag{6.11}$$

where $\frac{\partial d_{GVi}}{\partial (\rho_j)}$ is derived from the single gravity inversion and $\frac{\partial (\varrho_j)}{\partial \phi_j}$ can be found by differentiating the porosity-density relationship. The latter term is given by

$$\frac{\partial (\rho_j)}{\partial \phi_j} = S \rho_{fluid} + (1 - S) \rho_{air} - \rho_{matrix} \quad . \tag{6.12}$$

The final column in the Jacobian relates to the gravity offset term. Since there is no relationship between the gravity offset term and the MT data, these partial

derivatives can be set to zero,

$$\frac{\partial d_{MTi}}{\partial \Delta \mathrm{g}} = 0 \quad . \tag{6.13}$$

For the gravity elements of the Jacobian Equation 6.4 is used. This gives the change in gravity data due to the gravity offset term as

$$\frac{\partial d_{GV}}{\partial \Delta \mathrm{g}} = \frac{\partial}{\partial \Delta \mathrm{g}} \left(\mathbf{F}_{GV}(\mathbf{m}) + \Delta \mathrm{g} \right) = 1 \quad . \tag{6.14}$$

All the terms in Equation 6.12, Equation 6.14 and $\frac{\partial d_{GVi}}{\partial (\rho_j)}$ are constant, which means the gravity elements of the joint inversion Jacobian remain constant at each iteration.

6.2.2 Implementation and Computer Program

The optimisation scheme used in the joint inversion is based on the 2D non-linear Occam scheme outlined in Section 3.2. The objective function for this scheme can be written as

$$U[\mathbf{m}] = \left\| \underline{\partial}_y \mathbf{m}_\phi \right\|^2 + \| \underline{\partial}_z \mathbf{m}_\phi \|^2 + \mu^{-1} \left\{ \| \mathbf{W}_d \mathbf{d} - \mathbf{W}_d \mathbf{F}[\mathbf{m}] \|^2 - \chi_*^2 \right\} \quad . \tag{6.15}$$

The joint inversion objective function can remain the same as Equation 6.15 using the above inversion parameter definitions. The model norm component of the objective function, $\left(\left\| \underline{\partial}_y \mathbf{m}_\phi \right\|^2 + \| \underline{\partial}_z \mathbf{m}_\phi \|^2 \right)$, is the smoothness constraint and only acts on the porosity values in the model parameter vector and not the gravity offset term. Therefore, the definition of $\underline{\partial}_y$ and $\underline{\partial}_z$ given in Section 3.2, remains the same. The redefined inversion parameters mean the matrix operations in the data norm component of the objective function, $\left(\| \mathbf{W}_d \mathbf{d} - \mathbf{W}_d \mathbf{F}[\mathbf{m}] \|^2 - \chi_*^2 \right)$, align the MT and gravity components to give an overall misfit value. The overall RMS calculation includes every data point and does not distinguish between MT or gravity data points. All data errors are assumed to be independent and have a zero mean Gaussian distribution. Therefore the data norm is still the chi-square distribution with an expected value of q, the total number of MT and gravity data points, which

corresponds to a relative RMS of 1.

There will always be more MT data points than gravity data points. This means if a large number of MT data points are fitted well by the model, then the small number of gravity points that are being fitted poorly can be obscured or overlooked. Therefore, there is the potential for the joint inversion to be biased towards fitting the MT data at the expense of fitting the gravity data. Such bias in the joint inversion can be mitigated by weighting each data set differently, and this will be investigated in Section 8.3.

The objective function of the joint inversion and the single technique Occam scheme are essentially the same, which means that determining the Lagrange multiplier μ and the approach to updating the model parameters are the same as was presented in Section 3.2. They are repeated below,

$$\begin{aligned} \mathbf{m}_{k+1}(\mu) &= \left[\mu\left(\underline{\partial}_y^T\underline{\partial}_y + \underline{\partial}_z^T\underline{\partial}_z\right) + \left(\mathbf{W}_d\mathbf{J}_k\right)^T\left(\mathbf{W}_d\mathbf{J}_k\right)\right]^{-1} \\ &\qquad \left(\mathbf{W}_d\mathbf{J}_k\right)^T\left(\mathbf{W}_d\widehat{\mathbf{d}}_k\right) \qquad (6.16a) \\ U_{dk+1}(\mu) &= \left\|\mathbf{W}_d\mathbf{d} - \mathbf{W}_d\mathbf{F}[\mathbf{m}_{k+1}(\mu)]\right\|^2 \quad . \qquad (6.16b) \end{aligned}$$

The expressions for the single and joint inversion model updates are the same. However, in the joint inversion the data vector, model response and Jacobian matrix contain information about both techniques. Therefore the porosity model parameters are updated in accordance with both techniques.

Figure 6.2 is the joint inversion update of the steps taken by the single method inversion in Figure 3.3. The steps taken in the joint inversion are essentially the same as for the single method inversion except the joint inversion forward model operator involves converting the porosity model to a resistivity and density model and then computing their response. A user manual for conducting the joint inversion, including the input and output file structures, is given in Appendix B.

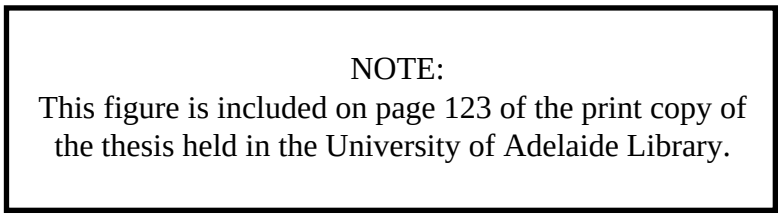

Figure 6.2: A flow chart reproduced from deGroot-Hedlin and Constable [90] of the steps taken by the 2D MT Occam inversion, which has been altered to accommodate the joint inversion steps.

Model Limits

A physical constraint can be placed on the joint inversion, since porosity can only vary between 0 and 1. There are two classifications of bounds or constraints, 'soft' and 'hard' [164]. 'Soft' bounds are where the model weighting matrix ($\mathbf{W}_m$) is used to influence the probability distribution of the model parameter values [164]. 'Hard' bounds will only allow the model values to vary between fixed upper and lower limits. Porosity model values can assume values in the range $0 \leq \mathbf{m} \leq 1$, where 0 is the lower limit and 1 is the upper limit. This makes the porosity constraint a 'hard' bound.

'Hard' bounds can be implemented in an inversion scheme using a method such as a truncation operator [165], a bound value least squares algorithm for linear problems [166] or the logarithmic barrier approach [167]. The joint inversion developed here applies the 'hard' bound using the pre-existing program feature model limits, discussed in Section 3.2.3. Model limits re-assign any updated model parameter outside the model limits to the appropriate upper or lower bound. The model limits feature was chosen for simplicity and more importantly it maintains the integrity of the Occam inversion because other implementations would mean altering the scheme. However, applying model limits means the Occam inversion might get trapped in a local minima that it might otherwise have been able to avoid [168].

Care needs to be taken when choosing the lower limit of the porosity value in the joint inversion. Although physically the lower limit of porosity is 0, this corresponds to an infinite resistivity (Section 5.4). Extremely high resistivities are not only geologically implausible but they also cause the MT forward model operator to fail. At what point the porosity values correspond to impractical resistivity values depends on the parameters (m_{cf}, S, n_s and ϱ_{fluid}) in Archie's Law. These variables will change value from inversion to inversion. The lower porosity limit has been set at 0.001 unless otherwise stated.

Occam Features

The program features of the MT Occam inversion were discussed in Section 3.2.3. They include topography or bathymetry, fixed values, sharp boundaries, structure in

the startup model, a prejudiced or preferred model and static shift removal. These are also available in the joint inversion program.

6.2.3 Discussion

An MT and gravity joint inversion has not been executed in this manner before, where the joint inversion inverts directly for a common linking factor. Similar petrophysical joint inversions by Hoversten *et al.*[27] and Tseng and Lee [28] invert for reservoir or hydrological parameters but produce multiple models. A benefit of the new implementation is that only a single model is produced and it contains information from both techniques. Also the model portrays the link between the two parameters rather than having it distributed between multiple models.

Applications of the joint inversion are restricted to scenarios where both Archie's Law and the porosity-density relationship can be used. Archie's Law can only be applied to porous environments [49], thereby limiting the joint inversion to porous rock environments. For this thesis the main focus is on sedimentary basins, although Archie's Law has been successfully applied to fractured hard rock environments as well (Section 5.4). The parameters in Archie's Law and the porosity-density relationship quantify the environmental setting of the porosity model. It is important to use the correct values of the parameters in these equations and to be sure that the parameters describe the same environment. For example, if the values of the cementation factor and tortuosity factor quantify a sandstone environment, then the matrix and fluid density should also reflect a sandstone environment. In Section 8.2 the ramifications on the joint inversion of using the incorrect parameter values in Archie's Law and the porosity-density relationship will be discussed.

6.2.4 Methodology Summary

The aim of the joint inversion is to produce a single porosity model that satisfies both the MT and gravity data. It uses the 2D non-linear Occam optimisation scheme. In order to use this scheme the model parameterisation, data vector, model parameters, forward model operator, boundary conditions and Jacobian matrix were redefined and the gravity offset term introduced. With such modifications, the steps taken in

the single method 2D non-linear Occam optimisation scheme can be retained.

6.3 Behavioural Characteristics

The 2D non-linear Occam optimisation scheme is very stable and exhibits good convergence [90]. These characteristics have also been observed in all the joint inversions undertaken for this research. This section will examine the effects of trying to fit two data sets and the convergence characteristics of the joint inversion.

6.3.1 Misfit Maps

The joint inversion must satisfy two data sets. The total RMS value quantity that the joint inversion seeks to minimise involves all data points and does not differentiate between the MT and gravity data. However, it is nevertheless instructive to scrutinise the individual MT and gravity fit, referred to as the RMS_{MT} and RMS_{GV}, respectively.

The simple porosity model, shown in Figure 6.3a, was used to examine the RMS values for different model parameter combinations. The true model consists of a vertical fault separating material on the left side with $\phi_1 = 0.1$ from material on the right side with porosity $\phi_2 = 0.3$. A horizontal interface at a depth of 5.3 km separates these two units from basement material, which has a very low porosity equal to 0.02. Model responses were calculated for various values of ϕ_1 and ϕ_2 in the range 0.01 to 1, at an increment of 0.01. The model responses were then compared to the true model response and subsequent RMS values calculated.

The total RMS, as well as the RMS_{MT} and RMS_{GV} values for different ϕ_1 and ϕ_2 values are shown in Figures 6.3b, 6.3c and 6.3d, respectively. The range of the RMS_{GV} values is approximately 14 times larger than the RMS_{MT} range. As discussed in Section 6.2.2 the RMS used by the joint inversion has a bias towards fitting the MT data and this can be seen in RMS maps.

The patterns of the RMS_{MT} and RMS_{GV} maps are different, as can be seen in Figure 6.3, because the two techniques are sensitive to different physical parameters and respond differently to the Earth model. The non-uniqueness of the gravity

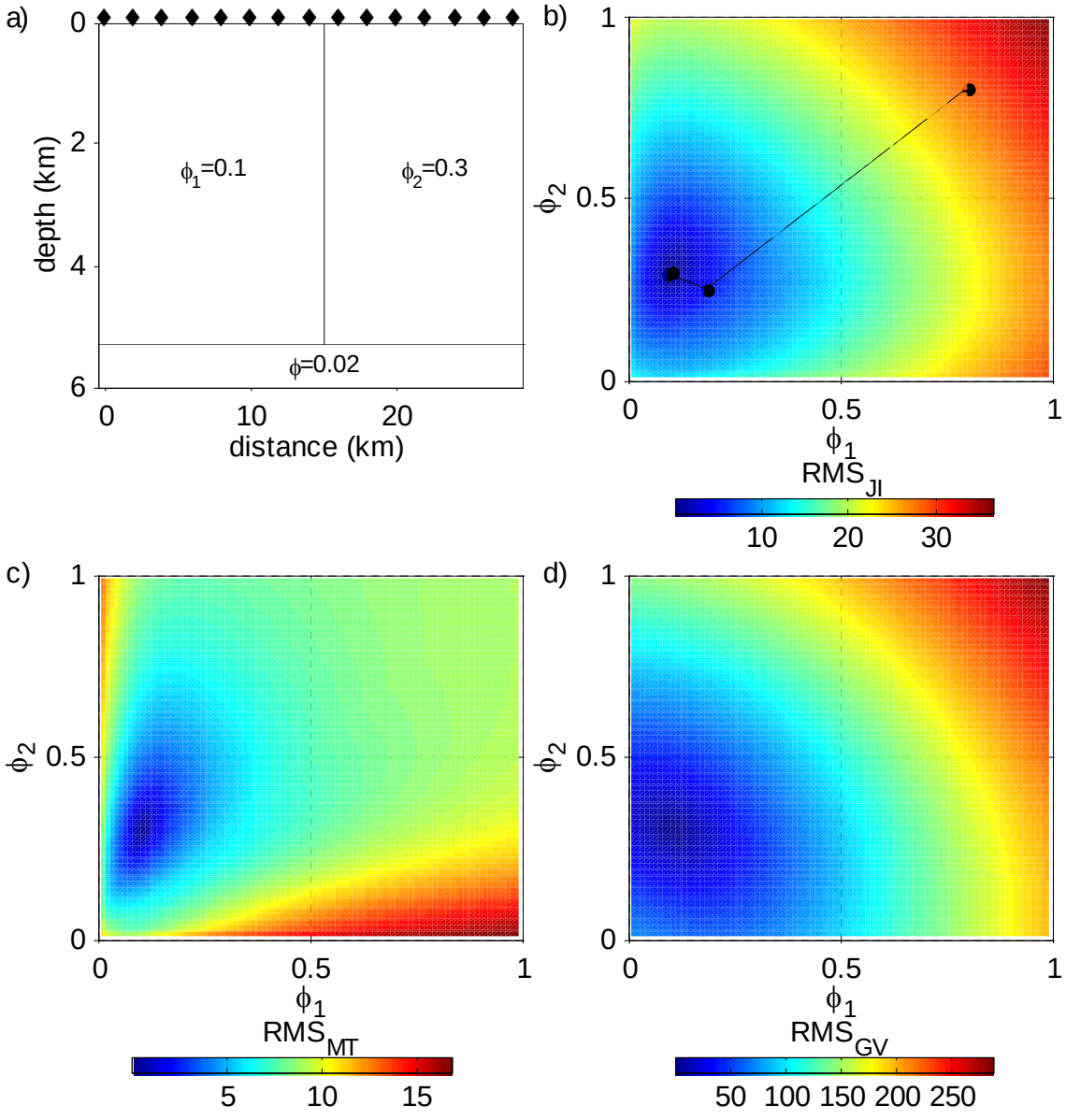

Figure 6.3: a) The simple porosity model with the true ϕ_1 and ϕ_2 values indicated. b) The RMS$_{JI}$ values, c) the RMS$_{MT}$ values and d) the RMS$_{GV}$ values, for different ϕ_1 and ϕ_2 combinations.

technique is reflected in the RMS_{GV} map, which has a broad local minimum equating to a large uncertainty in the true solution. However, the local minimum in the RMS_{MT} map is smaller and contains greater certainty in the true solution. It is only when the ϕ_1 and ϕ_2 values are close to their true porosity values that both techniques exhibit their minimum misfit values. In a pictorial sense, Figure 6.3 shows why joint inversions can be beneficial; the model parameters have to satisfy both data sets and this will only occur around the true model parameter values. Therefore, if a local minimum occurs in one technique, it is unlikely that a local minimum would occur at the same model parameter location in the other technique, and the joint inversion is less likely to get trapped in such local minima.

In Section 8.3, different weighting factors for the MT and gravity data sets are introduced in an attempt to improve the joint inversion result. Depending on the manner in which the weighting is applied, the RMS_{MT} and RMS_{GV} remain the same but the way they are combined to give the total RMS of the joint inversion is changed. Figure 6.3b would instead become a weighted sum of the individual RMS_{MT} and RMS_{GV} plots.

6.3.2 Convergence

The joint inversion converges to the same porosity model and RMS value, regardless of the starting model. This was tested by carrying out joint inversions on three different models (block, fault and trough models see Section 7.1.1), with porosity starting models of 0.0, 0.1, 0.2, 0.3, 0.4, 0.5, 0.6, 0.7, 0.8, 0.9, 1.0 and 1.5. If the starting porosity value lies outside the physical limits of 0 and 1 then the joint inversion fails to converge to the correct model, and returns an incorrect result. Also if the starting porosity value is 0 then the inversion fails for the reasons given in Section 6.2.2.

There are four stopping criteria that are used to terminate the Occam inversion,

i. Normal convergence — the inversion produces the smoothest possible model for the achieved target misfit.

ii. Maximum iterations — the number of user defined iterations has been reached.

iii. RMS not reducing — the RMS of the previous model cannot be bettered.

iv. Smoothness consideration — the smoothness of the previous model cannot be improved without increasing the RMS value.

A finding of the investigations reported in the next chapter is that the joint inversion avoids fitting the noise contained in either data set and never fits the data as well as the individual MT and gravity inversions. As a result, the joint inversion rarely reaches the target RMS of 1, and therefore cannot reach the requirements for normal convergence. In general, the joint inversion is terminated using either option ii or iii. During the first iteration of the joint inversion, the approximate gravity offset value is determined. Over the next $4-8$ iterations, depending on the error levels, model type and size, the RMS value is significantly reduced and is close to the final RMS value. Then the joint inversion continues until the maximum specified number of iterations is reached or until the RMS value cannot be improved. These later iterations only provide marginal improvement to the RMS value.

The joint inversion of the simple porosity model in the previous section was run with random Gaussian noise of 2% added to the MT data and 0.06 mGals added to the gravity data. The joint inversion reached an RMS of 1.6 after 35 iterations and had a conversion of type iii (RMS problems). The models produced by the joint inversion are smooth and every model parameter can have a different porosity value, whereas the RMS maps in Figure 6.3 only refer to the two porosity values either side of the fault. An approximation of the ϕ_1 and ϕ_2 values were produced from each iteration model of the joint inversion by averaging the porosity value either side of the fault. Figure 6.3b shows that after 4 iterations the joint inversion is close to the global minimum and the RMS has reduced from 38 to 2.4. Between iteration 5 and 9 the RMS is reduced by 0.4, but in the following 27 iteration the RMS is only reduced by a further 0.4.

6.3.3 Behavioural Characteristic Summary

The MT and gravity techniques are sensitive to different physical parameters and respond differently to the Earth. Therefore their RMS values differ, depending on

the model parameters. It is only when the model is close to the true model that both techniques have a low RMS values. The joint inversion is stable and converges to a single model regardless of the starting model. The main reduction of the RMS value occurs in the first $4-8$ iterations. Continued iterations will only provide marginal improvement to the RMS value.

6.4 Mathematical Considerations

In this section the mathematical aspects to conducting a joint inversion for two techniques which both have a linear forward model operator are considered. The MT technique does not have a linear forward model operator, which means that the following discussion cannot strictly apply to joint inversions involving the MT technique. Nevertheless, this section is important because it shows in a preliminary mathematical sense how the joint inversion can reduce the non-uniqueness of a geophysical problem. The linear inverse problem can be stated as

$$\mathbf{Gm} = \mathbf{d} \quad , \tag{6.17}$$

where $\mathbf{d} = (d_1, d_2, ..., d_q)$ is a vector consisting of q observed data points, $\mathbf{m} = (m_1, m_2, ..., m_n)$ is the vector of n model parameters and $\mathbf{G}$ is the $q \times n$ linear forward model operator. Equation 6.17 is essentially a system of q equations each containing information about the n model parameters. Contained in this system of equations are h linearly independent equations. These equations all contain different information about the model parameters. The remaining $q - h$ equations are linearly dependent and contain no additional information about the model parameters contained in the h linearly independent equations.

Figure 6.4 shows a schematic of the linear inversion problem. There exists a model space of dimension n and a data space of dimension q. These two spaces are related through the forward model operator which maps the model parameters contained in the model space to data values contained in the data space. For each specific inversion problem the model space contains a subspace, called the model solution subspace, which includes all possible model parameter combinations that

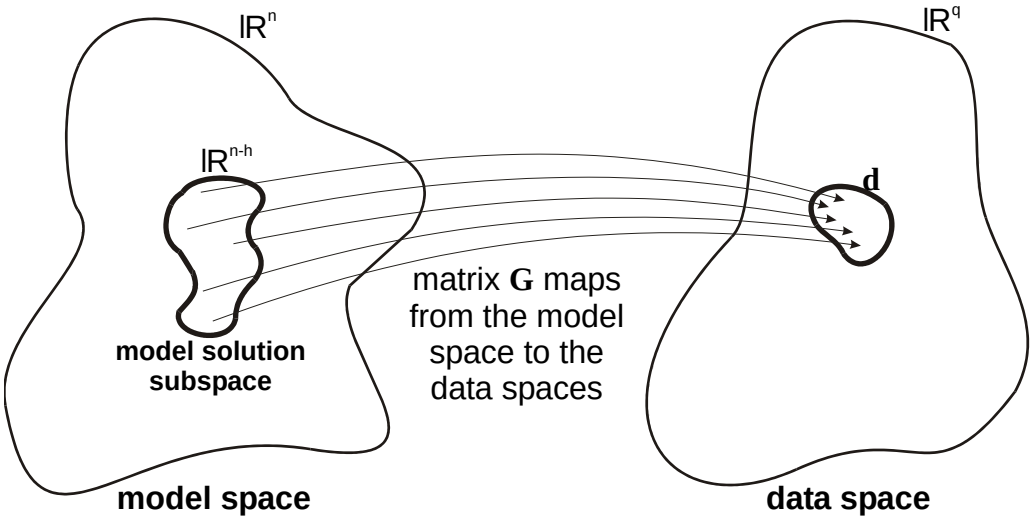

Figure 6.4: A schematic of the inverse problem, where the matrix **G** maps model parameters in the model space to data values in the data space. The model space contains a subspace called the model solution subspace which maps to the observed data.

can be mapped to the observed data. The dimension of the model solution subspace is $n - h$, the number of model parameters minus the number of linearly independent equations. In the case where $h = n$ there is a unique solution, where only one set of model parameters will map the observed data. If the model solution subspace is empty there are no model parameters that satisfy the observed data. The geophysical inverse problem normally lies in between these two extreme scenarios, with the model solution space neither empty nor containing enough information to uniquely define all model parameters. This leaves an infinite number of possible model parameter combinations that can be mapped to the observed data.

If there exists extra information (e.g. prior constraints) about the model parameters then it can be incorporated into the inverse problem, Equation 6.17. The dimension of the model solution subspace is $n-h$, therefore every linearly independent equation added to the inverse problem reduces the dimension of the model solution subspace by 1. Reducing the dimensions of the model solution subspace reduces the degrees of freedom of the model parameter, thus reducing the non-uniqueness of the inverse problem.

Different geophysical techniques are sensitive to different properties of the subsurface and are based on different physical phenomenon, therefore their information about the model parameters is assumed to be independent. The premise of the joint inversion presented in this thesis is that it uses two different geophysical techniques to solve for one set of model parameters. This type of joint inversion will therefore increase the number of linearly independent equations, while solving for the same number of model parameters. The increase in the number of linear independent equations will reduce the dimension of the model solution subspace compared to the single technique inverse problem. This decrease in model solution subspace dimensions corresponds to a reduction in the model non-uniqueness. There could exist a situation such that between the two techniques the number of linearly independent equations is equal to the number of model parameters and a unique solution is achieved, although this is unlikely.

Other joint inversion approaches, such as the structural approach, solve for two sets of model parameters which are linked in some way. Such approaches have a model space of dimension $2n$, which means the model solution subspace will be of dimension $2n - h$. Therefore, when the same two techniques are combined using this type of joint inversion, a larger model solution subspace will always occur than if the techniques were combined using a joint inversion which solves for only one set of model parameters.

6.5 Conclusions

The joint inversion approach discussed in this chapter inverts directly for a porosity model that is constrained by both gravity and MT data. In the joint inversion the porosity model is then converted to a resistivity and density model using Archie's Law and the porosity-density relationship. The resistivity and density model responses, with the aid of a gravity offset term for the Bouguer anomaly data, are compared to the observed data. Then, based on both techniques, the porosity model will be updated until a model is found that fits both data sets. The benefit of this method is that a single model is produced but it contains the information

from two techniques.

In this chapter, two possible benefits of joint inversions were discussed. Firstly, joint inversion reduces the likelihood of the inversion getting trapped in local minima, since the local minima of the different techniques are unlikely to occur at the same values of the model parameters. Secondly, the joint inversion implemented in this way reduces the degrees of freedom of the model parameters, thus reducing the non-uniqueness of the inverse problem.

Chapter 7

Synthetic Data Inversion Experiments

The objective of this chapter is to categorise and investigate the behaviour of the joint inversion in different scenarios, using synthetic models. The chapter is divided into four distinct sections, each looking at different aspects of the joint inversion. The sections and their objectives are as follows:

1. Proof of Concept – investigates the effectiveness of the joint inversion in reconstructing the subsurface and compares the results to those obtained by the single method gravity and MT inversion.

2. Effects of Data Errors – evaluates the effect of having different magnitude errors in the MT and gravity data on the joint inversion.

3. Station Configurations – examines how the different survey geometries (e.g. number and spacing of stations) for MT and gravity influences the inversion results.

4. Target Contrast and Resolution – looks at the minimum contrast and horizontal and vertical resolution of the joint inversions and compares them to the single MT inversions

7.1 Proof of Concept

Synthetic models are used to evaluate the effectiveness of the joint inversion approach. In this section, the results from the joint inversion are compared to the results of MT and gravity single inversions to determine if the joint inversion can produce a more accurate representation of the subsurface than can be achieved from single technique inversions alone.

7.1.1 Synthetic Models and Data

Three synthetic 2D porosity models were used to test the joint inversion. These models are shown in Figure 7.1, and are referred to as the block, fault and trough models. The block model (Figure 7.1a) has nine recording stations separated by 1 km, as shown by the diamond symbols. The top 500 m of the block model is an unconsolidated zone which has a high porosity value of 0.6. Below the unconsolidated zone the porosity-depth compaction trend is based on the lithostatic reduction in porosity for sandstone [153]. The sandstone compaction trend is determined from the Athy model (Equation 5.6), using a surface porosity of 0.49 and a compaction coefficient of 270 m [163]. The sandstone compaction trend is terminated at a depth of $\sim$ 7 km with a constant porosity of 0.03, which is representative of basement. In the centre of the block model there is an anomalous zone of width 2 km and thickness 3 km, located at a depth of 1 km below the surface. The anomalous zone has a constant porosity value of 0.1.

The fault model (Figure 7.1b) has fifteen recording stations, each separated by 2 km. It consists of a sandstone compaction depth trend and a shale compaction depth trend on the left and right of this figure, respectively. As is discussed in Section 5.4, Archie's Law should not be used for shales. However, a shale compaction trend is used in this fault model as it provides different porosity compaction behaviour and is in strong contrast to the sandstone trend. The sandstone compaction trend was generated in the same manner as for the block model. The shale compaction trend was determined from Athy's model using a surface porosity of 0.63 and a compaction coefficient of 510 m [163]. Both porosity trends are terminated at

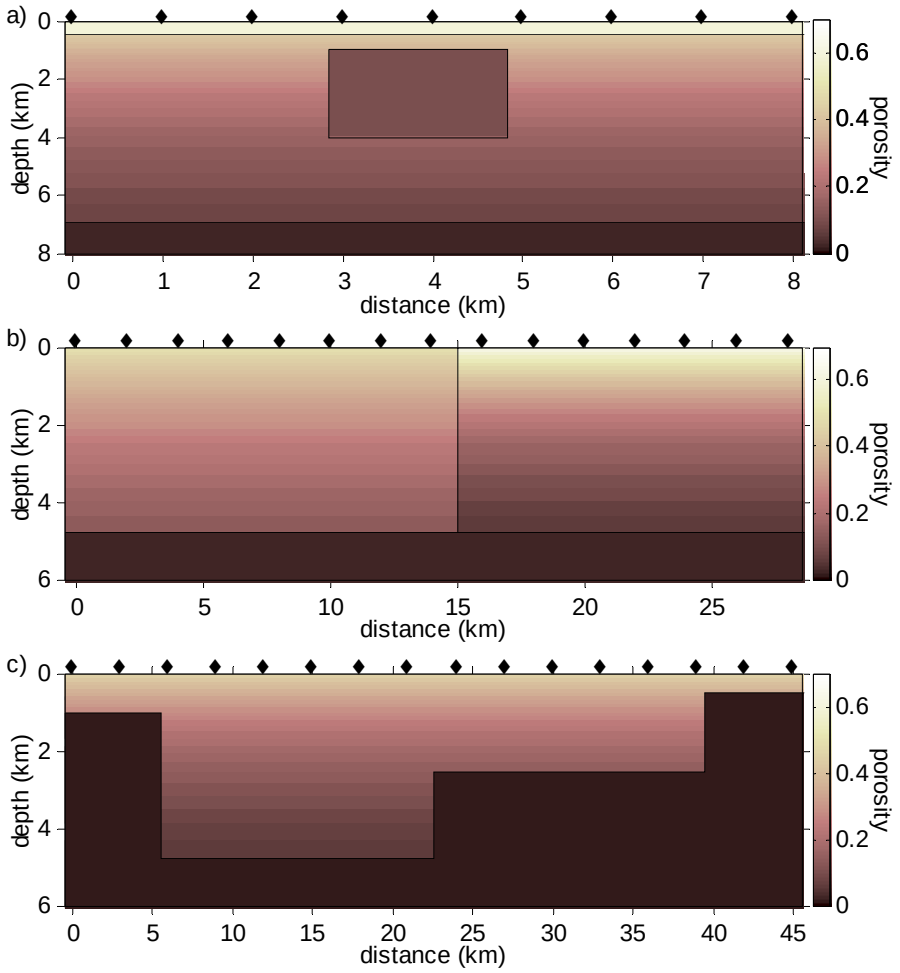

Figure 7.1: The synthetic porosity models referred to as a) the block model, b) the fault model and c) the trough model.

a depth of $\sim$ 4.8 km with a basement represented by a porosity value of 0.03.

Figure 7.1c shows the trough model, which includes sixteen recording stations, each separated by 3 km. As observed in this figure, the trough model is a step model where the basement starts on the left at a depth of 1 km before dropping to a depth of $\sim$ 4.8 km for a horizontal distance of 17 km. The basement then rises to a depth of $\sim$ 2.5 km for another horizontal distance of 17 km before rising again to a depth of 0.5 km at the right side of the model. A typical sandstone compaction trend was used to represent the sediments in the trough. It was generated from Athy's model using a surface porosity of 0.45 and a compaction coefficient of 450 m [153]. A porosity value of 0.02 was assigned to the basement.

The three synthetic models were designed to evaluate the ability of the joint

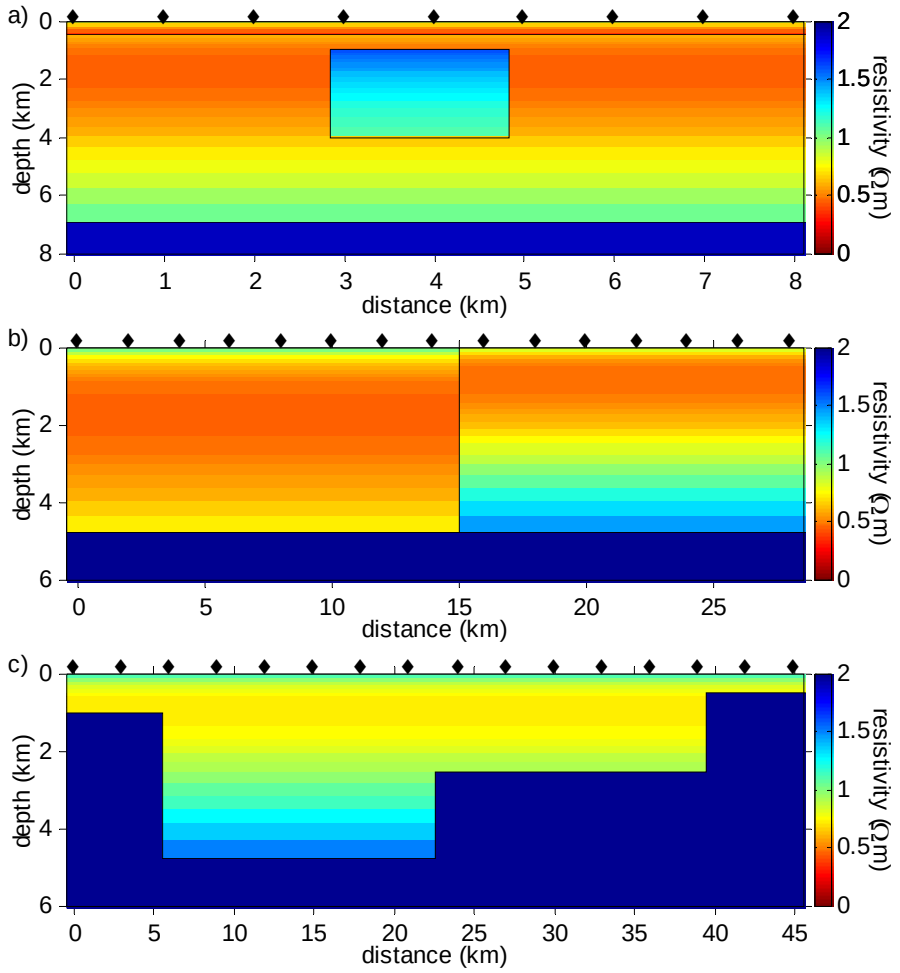

Figure 7.2: The synthetic porosity models in Figure 7.1 converted to resistivity models using Archie's Law.

inversion to resolve different subsurface structures. The block model is intended to examine the capability of the joint inversion to detect and delineate anomalous porosity values. The fault model is used to determine if the joint inversion can distinguish between variations in porosity-compaction trends. Finally, the trough model tests how the joint inversion can reconstruct topography in the basement.

Both MT and gravity synthetic data were generated at each station for each model. To generate synthetic MT data, the three porosity models were converted to resistivity models, as shown in Figure 7.2. This was achieved using parameter values of $a = 1$, $m_{cf} = 2$, $S = 1$ and $n_s = 2$ in Archie's Law (Equation 5.4). The fluid resistivity varied with depth and was calculated using Equation 5.5, with a surface resistivity of 0.3 Ωm and a temperature gradient of 20 ^{o}Ckm^{-1}. The fluid

resistivity was held constant below a depth of 4.8 km for both the fault and trough models and below a depth of 7 km for the block model. This was done because Equation 5.5 is only valid for temperatures below 300 °C.

The resistivity models corresponding to the porosity models are shown in Figure 7.2. These values correspond to a conductive sedimentary environment. The resistivity trends exhibited in these models are variations of the trend described in Section 5.5, except expressed in terms of resistivity and not its reciprocal, conductivity. In the block model the anomaly and consolidated zone have constant porosity but due to the variation in fluid resistivity with depth, these features do not have a constant resistivity value. A similar change in resistivity value due to the change in fluid resistivity occurs in the basement of the trough model.

The MT synthetic data were generated for each resistivity model using the finite element computer program of Wannamaker *et al.* [117]. The program uses the same grid as will be used in the inversion. Data were generated at 16 frequencies, which varied between 1000 Hz and 0.01 Hz, and is characteristic of broadband MT data.

The porosity models were also converted to a density model using the porosity-density relationship (Equation 5.1). For each model, the matrix density was assigned a value of 2650 kgm^{-3} and the fluid density was fixed with depth at 1030 kgm^{-3}. Figure 7.3 shows the density models which are given in terms of absolute density values. The gravity synthetic data were generated for these models using the forward model outlined in Section 4.2.1. Since the density models are absolute values, the response does not correspond to data in a Bouguer anomaly format. In order to mimic Bouguer anomaly data, a constant value was subtracted for each data point such that the smallest gravity data value point was 1 mGal.

Noise was added to every synthetic MT and gravity data point in the form of a random error with a zero mean Gaussian distribution. Initial testing of the joint inversion was conducted using an MT error of 2%, which corresponds to good quality field data [31]. Telford *et al.* [6] quotes the accuracy of a typical commercial exploration gravimeter as $0.03 - 0.06$ mGals. The upper limit of this range, 0.06 mGals, is used as the gravity error in the synthetic data inversion experiments. Low error levels were chosen as these will produce the best possible models from the single

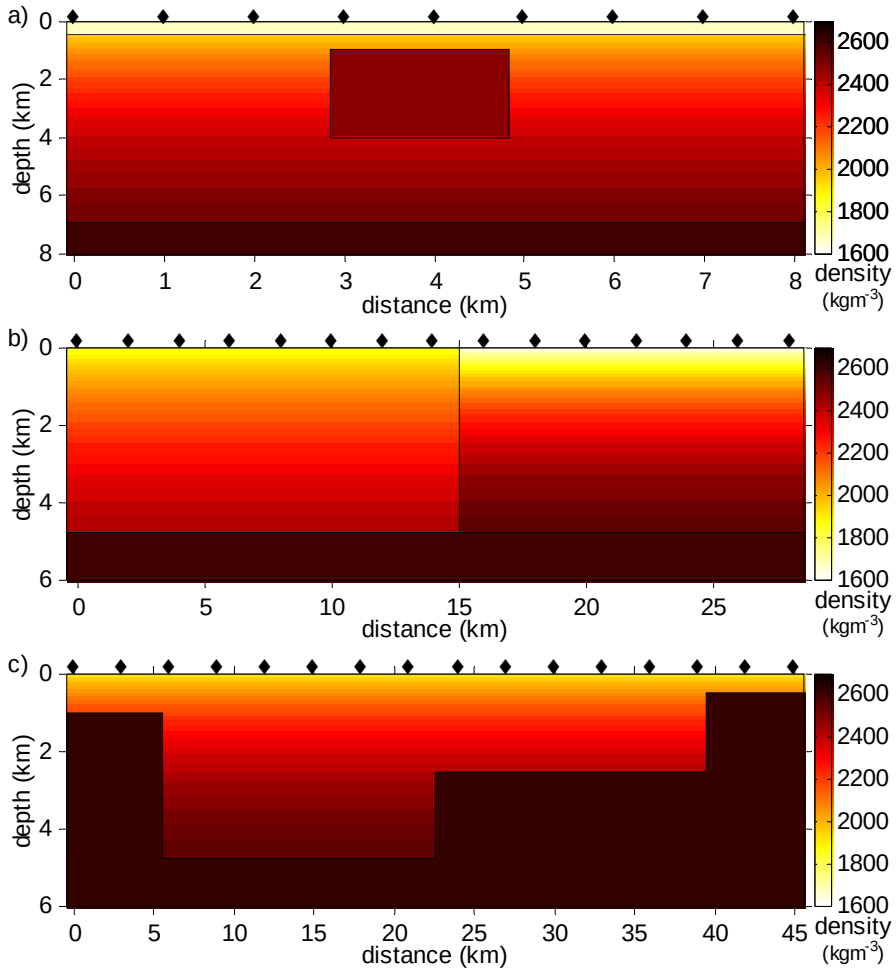

Figure 7.3: The synthetic porosity models in Figure 7.1 converted to density models using the porosity-density relationship.

technique MT or gravity inversions. Therefore, it can be readily established if the joint inversion produces a model that is better than the best possible MT and gravity models.

7.1.2 Single Technique Inversion Results

Magnetotellurics

The results of the 2D MT Occam inversions for the block, fault and trough models are shown in Figures 7.4, 7.5 and 7.6, respectively. The resistivity models from the MT inversion have been converted to a porosity model using Archie's Law. This allows for an easy comparison between the MT and the joint inversion results.

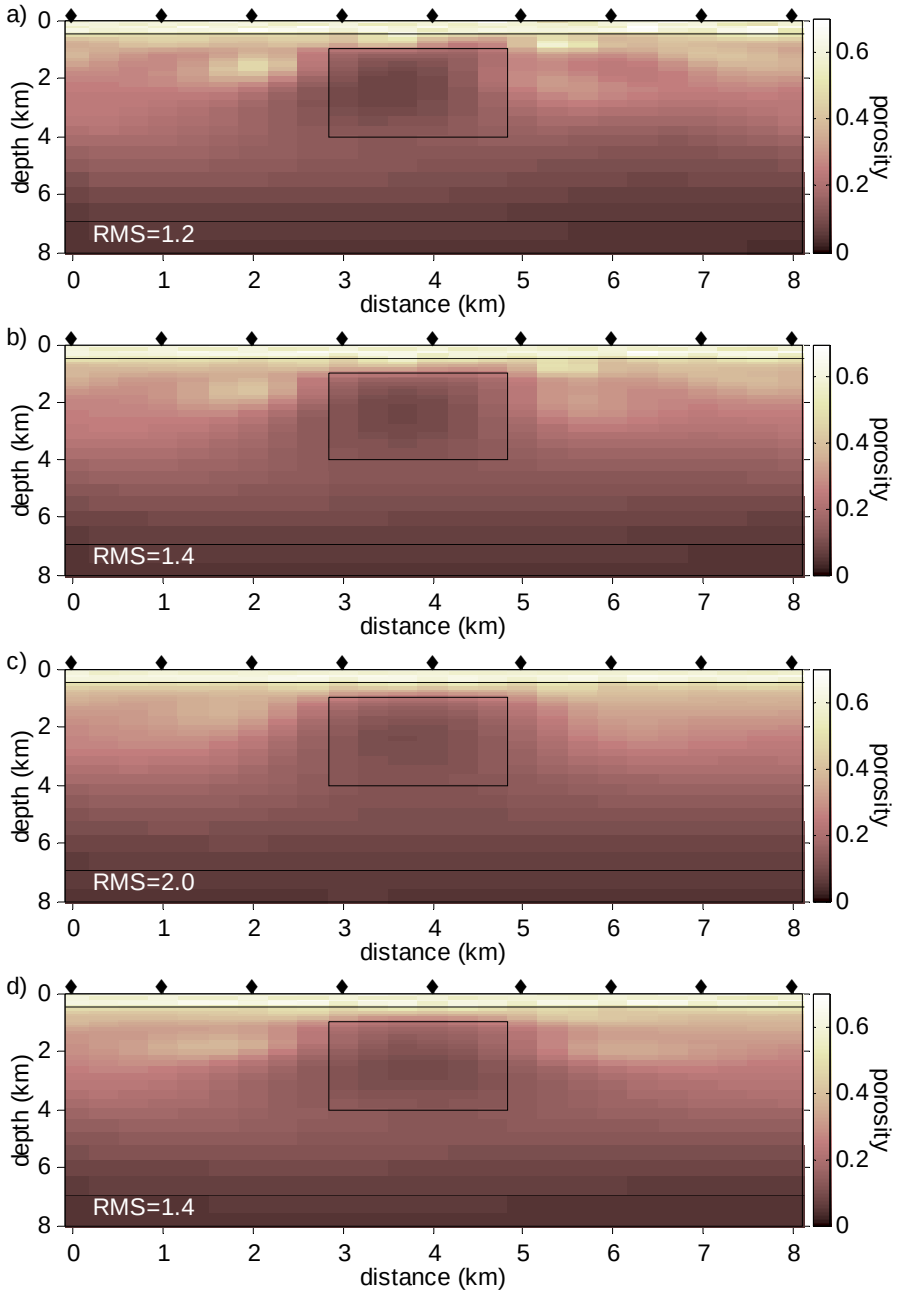

Figure 7.4: The models produced from an MT inversion of the block model synthetic data with an error of 2% and a target RMS of a) 1.2, b) 1.4, c) 2.0 and d) 1.4 with a horizontal smoothness weighting of 3. These models have been converted to a porosity model using Archie's Law.

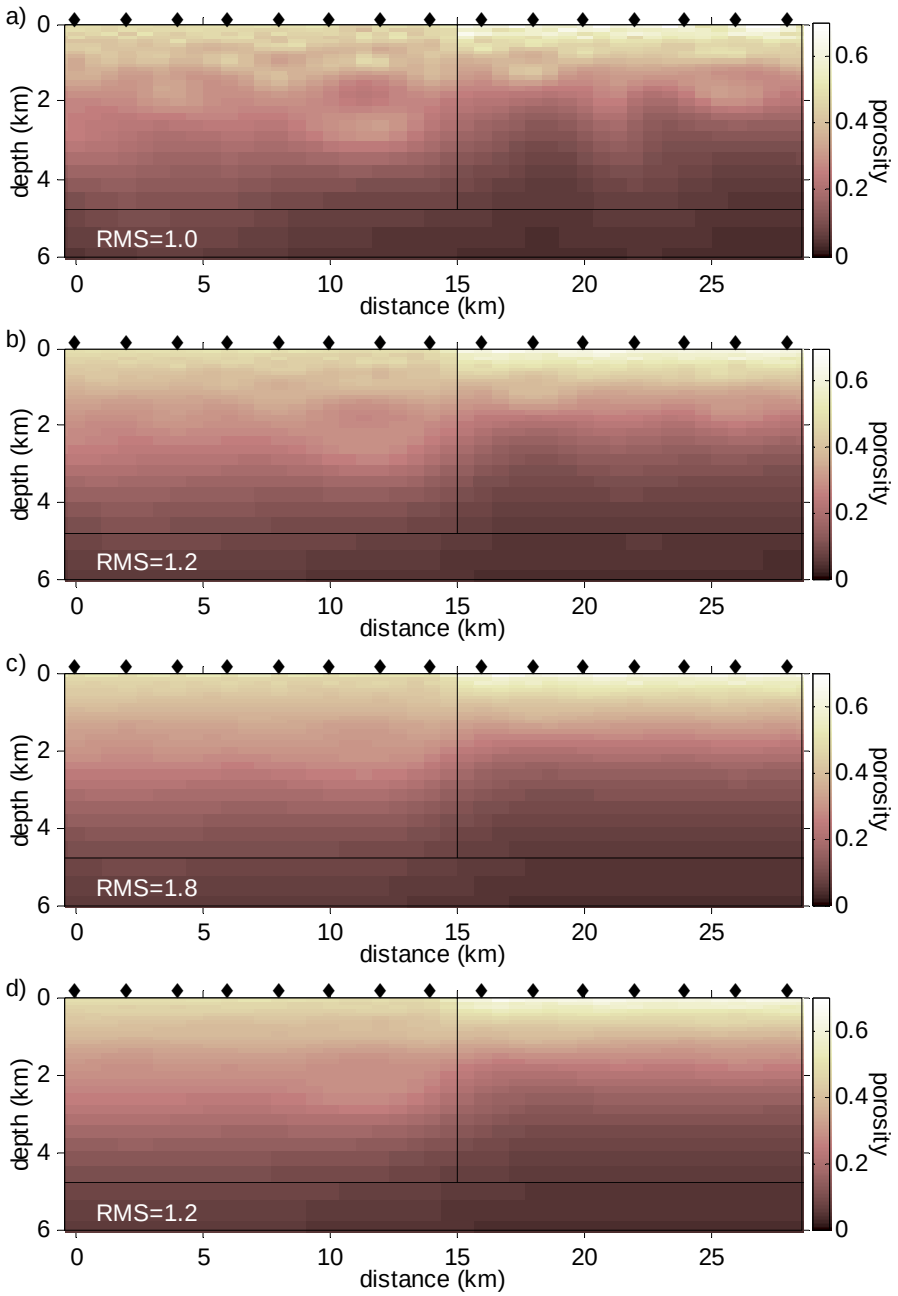

Figure 7.5: The models produced from an MT inversion of the fault model synthetic data with an error of 2% and a target RMS of a) 1.0, b) 1.2, c) 1.8 and d) 1.2 with a horizontal smoothness weighting of 3. These models have been converted to a porosity model using Archie's Law.

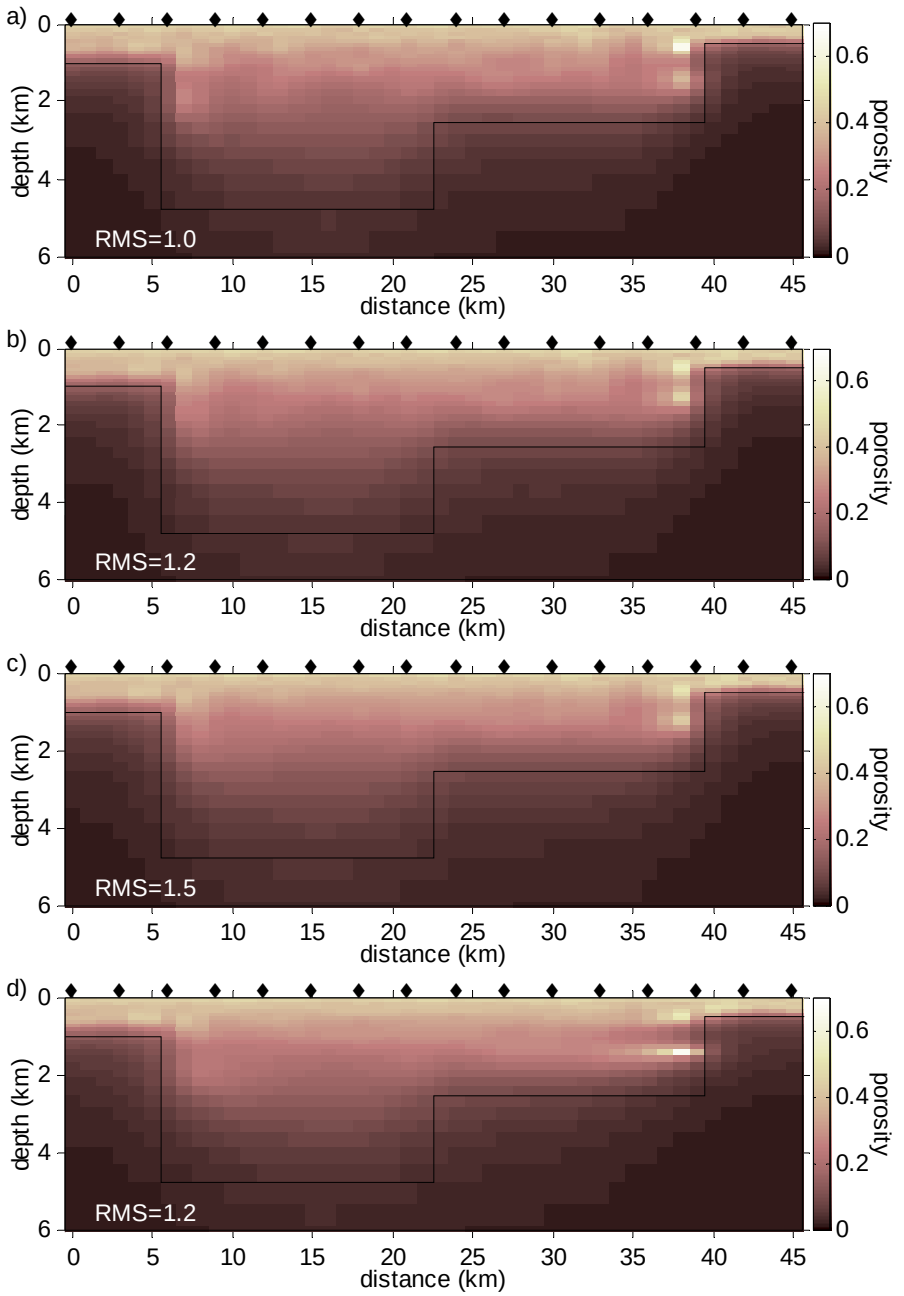

Figure 7.6: The models produced from an MT inversion of the trough model synthetic data with an error of 2% and a target RMS of a) 1.0, b) 1.2, c) 1.5 and d) 1.2 with a horizontal smoothness weighting of 2. These models have been converted to a porosity model using Archie's Law.

Figures 7.7, 7.8 and 7.9 show the misfit plots between every synthetic data point and the corresponding model response. These misfit plots were generated by subtracting the model response from the synthetic data and then normalising it by the estimated error of each data point.

Figures 7.4a, 7.5a and 7.6a show the results from an MT inversion with a target RMS of 1. A model with an RMS of 1 (or the smallest possible value) corresponds to the roughest possible model. These rough models result from more and more structure being needed to fit the subtle variations in the MT data. Since the MT data contain noise, fitting the data to a small RMS value mean 'structure' in the inverted model can arise by fitting the noise, as if it were signal. This type of behaviour is presented in Figures 7.4a, 7.5a and 7.6a which contain artifacts, especially in the shallower part of the section (depth $<$ 4 km). These artifacts (false features in the image) could be mistaken for real structure and they make determination of the porosity-depth compaction trend difficult. However, a benefit of the models in Figures 7.4a, 7.5a and 7.6a is that the fits between the synthetic MT data and the model responses are random across all data points (Figures 7.7a, 7.8a and 7.9a). This random fit of data points means that there is neither a systematic fitting nor misfitting of the different frequencies for the different modes and stations.

A relaxation can be applied to an inversion to reduce artifacts caused by fitting noise. A relaxation involves re-executing the MT inversion with an increased target misfit; normally an increase of 20% of the smallest achieved RMS is used. A 20% relaxation was applied to the block, fault and trough models with the results shown in Figures 7.4b, 7.5b and 7.6b. These models are smoother and show less artifacts. In general, their porosity values are a good representation of the original compaction trends. However, this 20% relaxation has not removed the larger artifacts, such as in the fault model at a depth of 2 km and at a distance of 12 km. In order to remove the larger artifacts, the RMS needs to be relaxed to 1.8 for the fault model and 2.0 for the body model, with results shown in Figure 7.4c and Figure 7.5c, respectively. Increasing the target RMS of the inversion allows for a systematic misfitting of the MT response. In Figures 7.7c and 7.8c, and to a lesser extent in Figure 7.7b and 7.8b, at high frequencies the TE mode is under estimated and the

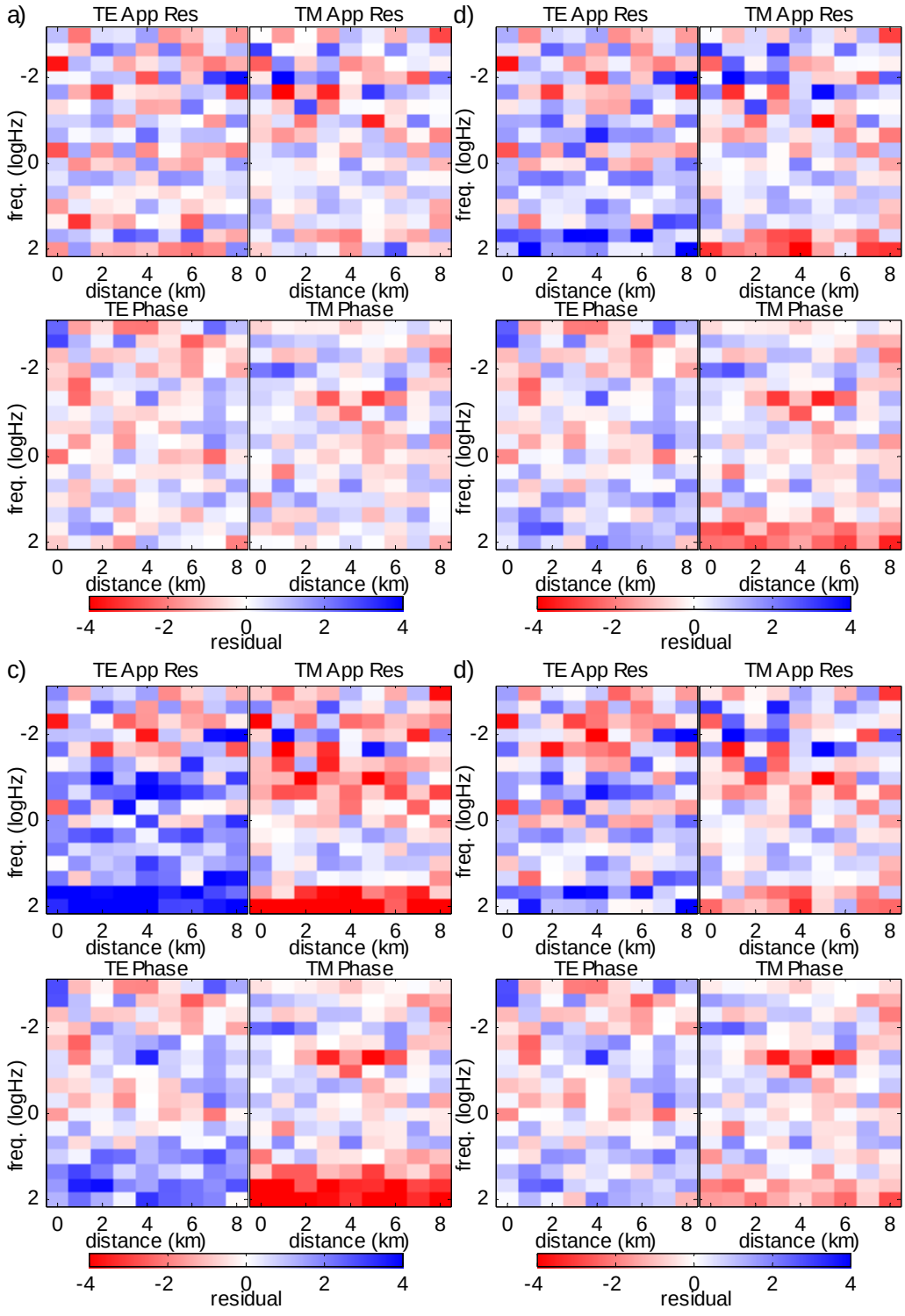

Figure 7.7: The MT misfit map from models produced in Figure 7.4, which are from an MT inversion of the block model synthetic data with a target RMS of a) 1.2, b) 1.4, c) 2.0 and d) 1.4, with a horizontal smoothness weighting of 3. For each data point the MT misfit map takes the difference between the data and the model response, normalised by the data error. Each data point is then plotted as station location vs. frequency.

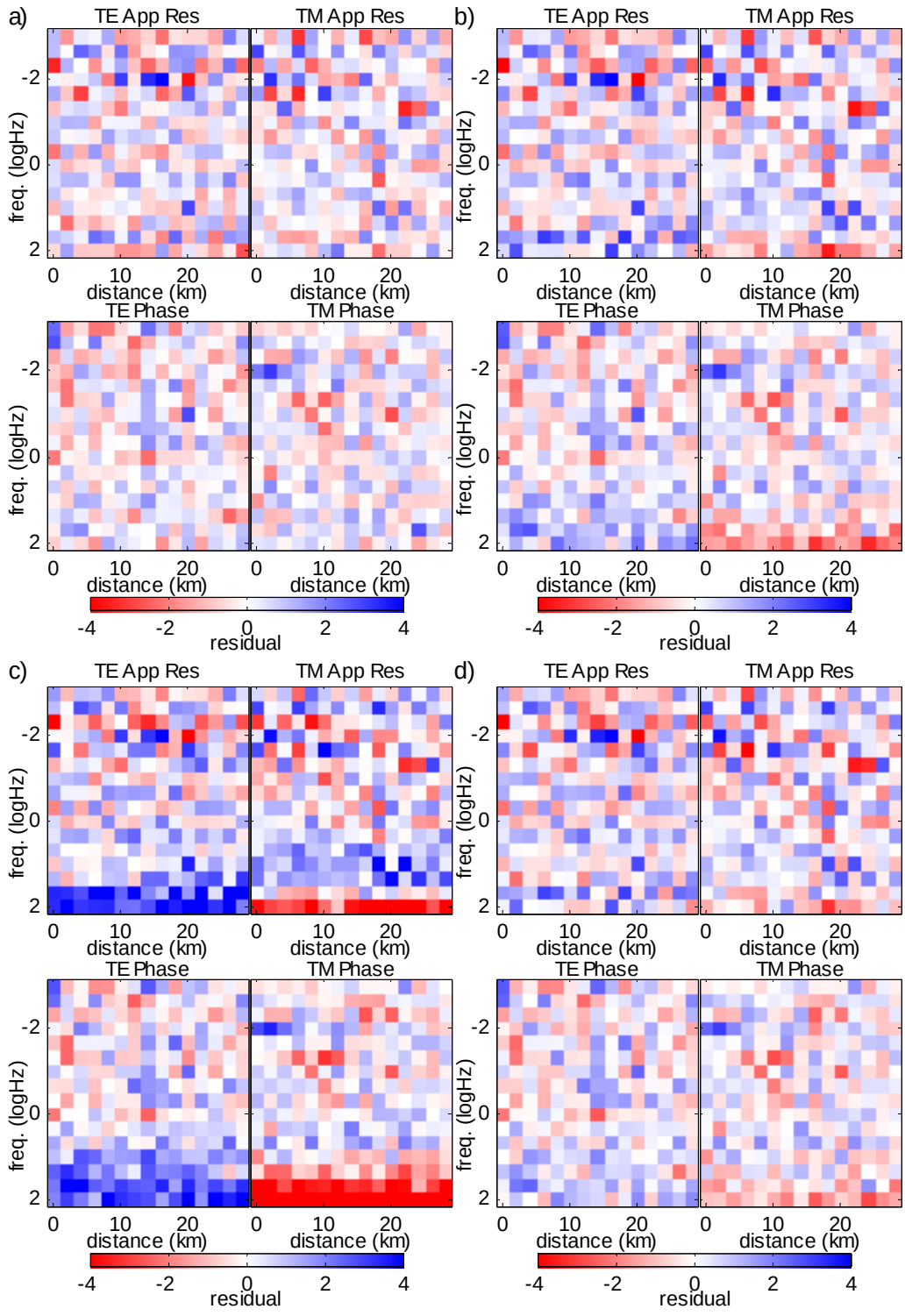

Figure 7.8: The MT misfit map from models produced in Figure 7.5, which are from an MT inversion of the fault synthetic data with a target RMS of a) 1.0, b) 1.2, c) 1.8 and d) 1.2, with a horizontal smoothness weighting of 3. For each data point the MT misfit map shows the difference between the data and the model response, normalised by the data error. Each data point is then plotted as station location vs. frequency.

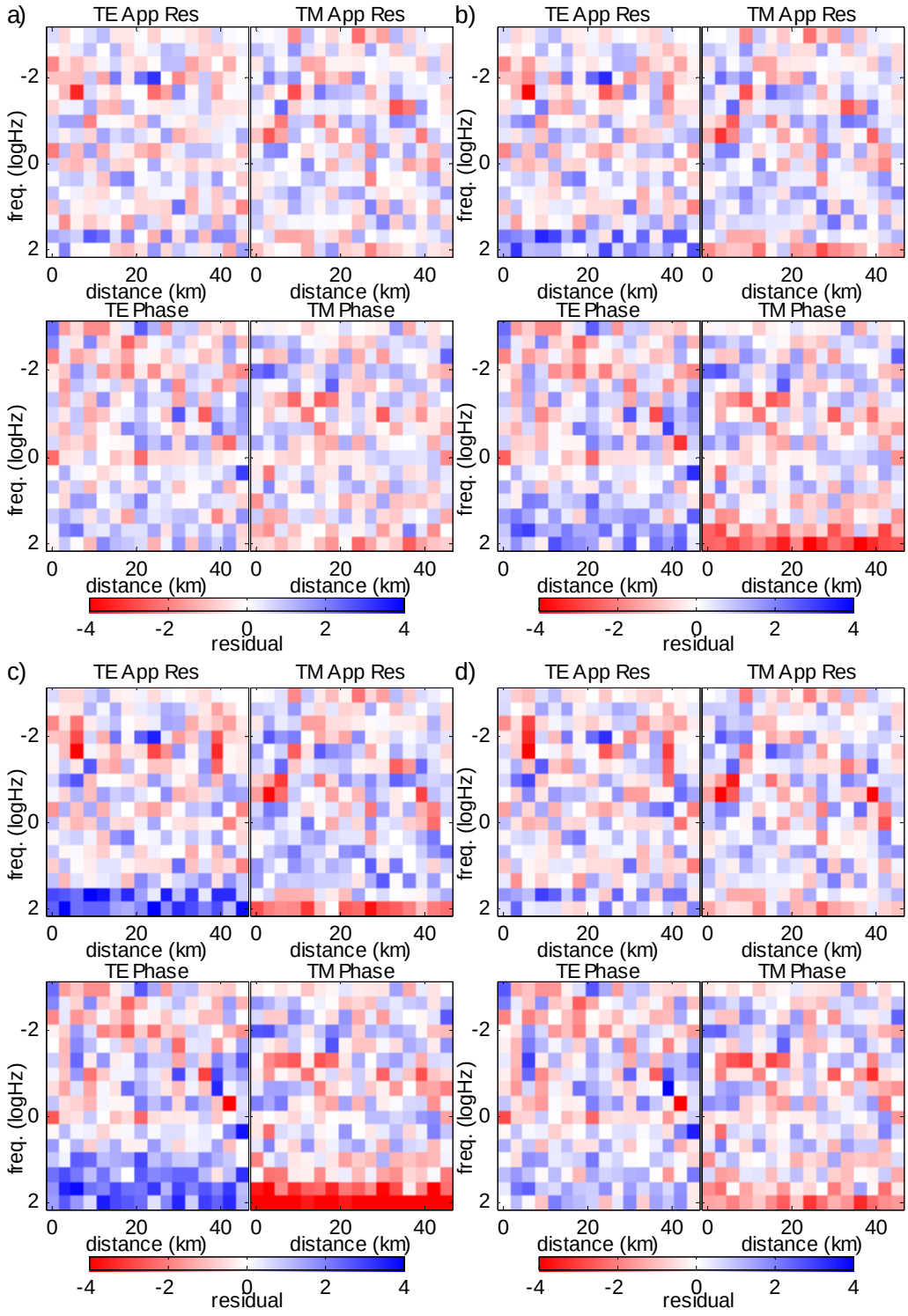

Figure 7.9: The MT misfit map from models produced in Figure 7.6, which are from an MT inversion of the trough model synthetic data with a target RMS of a) 1.0, b) 1.2, c) 1.5 and d) 1.2, with a horizontal smoothness weighting of 2. For each data point the MT misfit map takes the difference between the data and the model response, normalised by the data error. Each data point is then plotted as station location vs. frequency.

TM mode is overestimated. The larger the relaxation of the RMS value, the larger the systematic misfitting.

An alternate way to produce a smoother model without having to considerably increase the RMS is to use a higher weighting on the horizontal or vertical smoothing. A horizontal weighting was used in favour of a vertical weighting because the models are intrinsically more coherent horizontally. The results of using a horizontal smoothing weight of 3 and a 20% relaxation are shown in Figures 7.4d and 7.5d for the block and fault models, respectively. The trough model result, shown in Figure 7.6d, has a horizontal smoothing of 2 and a 20% relaxation. The models produced using a horizontal smoothing weighting are smoother than models without it. However, it does not remove the artifacts and they just become smeared into the model. This is particularly evident for the artifact in the trough model at a depth of 1.5 km and at a distance of 40 km. Horizontal weighting does reduce the systematic misfit of the MT response at low/high frequency; this can be seen in Figures 7.7d, 7.8d and 7.9d.

Once the artifacts are reduced, the MT models are adequate representations of the synthetic models. The fault model has two distinct compaction trends, although the boundary between them is blurred due to the smoothness contrast. The shallow flat basement boundaries in the trough model are well constrained, as are the vertical boundaries which have a large porosity contrast in the upper part of the section. However, when the contrast across the vertical boundaries becomes smaller they are more difficult to determine. In the block model, the unconsolidated region and the top of the embedded block anomaly are well defined. However, the side boundaries on the block are unclear and the bottom boundary, which has a small contrast across it, is indeterminate. The flat basement boundaries in the block and fault models, as well as the deep flat boundaries in the trough model, are not well defined.

Gravity

The 2D Occam gravity inversion developed in Chapter 4 was used to invert the synthetic Bouguer anomaly data for all three models. The inversions did not use a depth weighting function and were performed using the same grid as the MT and

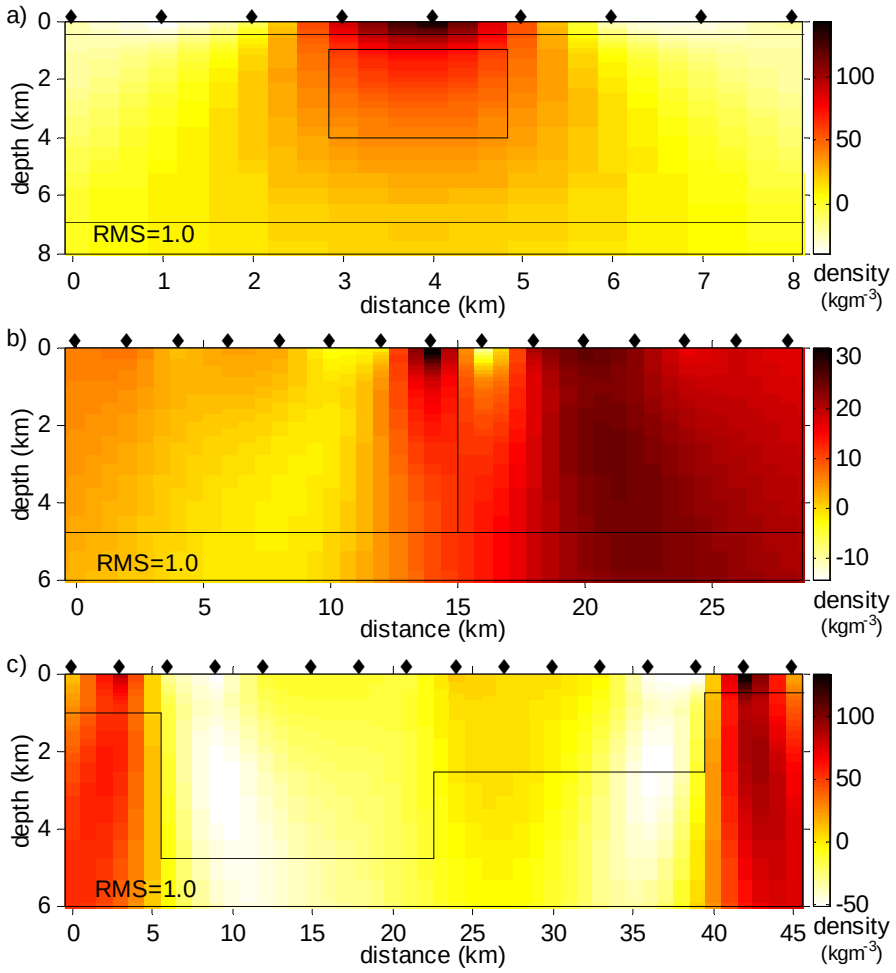

Figure 7.10: The Occam gravity inversion for the synthetic data, with a 0.06 mGal error, for the a) block, b) fault and c) trough models.

joint inversions, which increases at equal logarithmic depth increments. Figure 7.3 shows the original density models which are in absolute density values and Figure 7.10 shows the inversion results which are a density contrast model. In order to compare the different types of models, comparisons are made between the shape of structure and the variation in density between different structures.

In common with the observations and statements made in Chapter 4, the gravity inversions for all three models placed the structures at the surface and then smeared them with depth. The lateral changes in the density values at the surface are in general agreement with the vertical boundaries present in the block and trough models. The location of the fault in the fault model is hard to determine due to artifacts caused by noise in the data. Any horizontal boundary across the whole model, such

as the unconsolidated zone or the flat basement in the block and fault models, are not present in the gravity inversion images. These features have a constant gravity response for every station and therefore this signal would be removed when forming the Bouguer anomaly data.

As discussed in Section 4.4.3, the Occam gravity inversion will under- and overshoot the true density values in order to produce a tight fit of the synthetic data. This behaviour can be seen in these models as they have negative density contrast values, even though all synthetic data points are positive. The density variations in the inversion models are smaller than the original synthetic models. This has been attributed to the mass in the model being redistributed vertically due to the smoothness constraint and now occupying a greater area. Therefore, to produce the same gravity response the density values are reduced.

7.1.3 Joint Inversion Results

The joint inversions of the block, fault and trough models were conducted with the correct parameter values used in Archie's Law and the porosity-density relationship. The joint inversion results will be discussed in terms of three misfit values, RMS_{JI}, RMS_{MT} and RMS_{GV}. The total misfit, or RMS_{JI}, is the RMS value that is minimised in the joint inversion and does not distinguish between the MT and gravity data points. RMS_{MT} is the RMS of only the MT data points and RMS_{GV} is the RMS of the gravity data points alone. The RMS_{MT} and RMS_{GV} values have no influence on the joint inversion and were introduced in order to evaluate the fits of the MT and gravity data. The sum or average of RMS_{MT} and RMS_{GV} does not equal RMS_{JI}.

Figure 7.11 shows the final results of the block, fault and trough joint inversions. The fault model has a total RMS_{JI} of 1.2, RMS_{MT} of 1.2 and RMS_{GV} of 0.9. For the trough model, RMS_{JI} is 1.6, the RMS_{MT} is 1.5 and the RMS_{GV} is 5.0. The block model has a RMS_{JI} of 1.4, the RMS_{MT} is 1.4 and RMS_{GV} is 1.7. As discussed in Section 6.2.2, there is a bias in the joint inversion towards fitting the MT data and this is evident in the three RMS values. The total RMS_{JI} is very similar to the RMS_{MT} value, regardless of the RMS_{GV} value. Even though there is a preferential

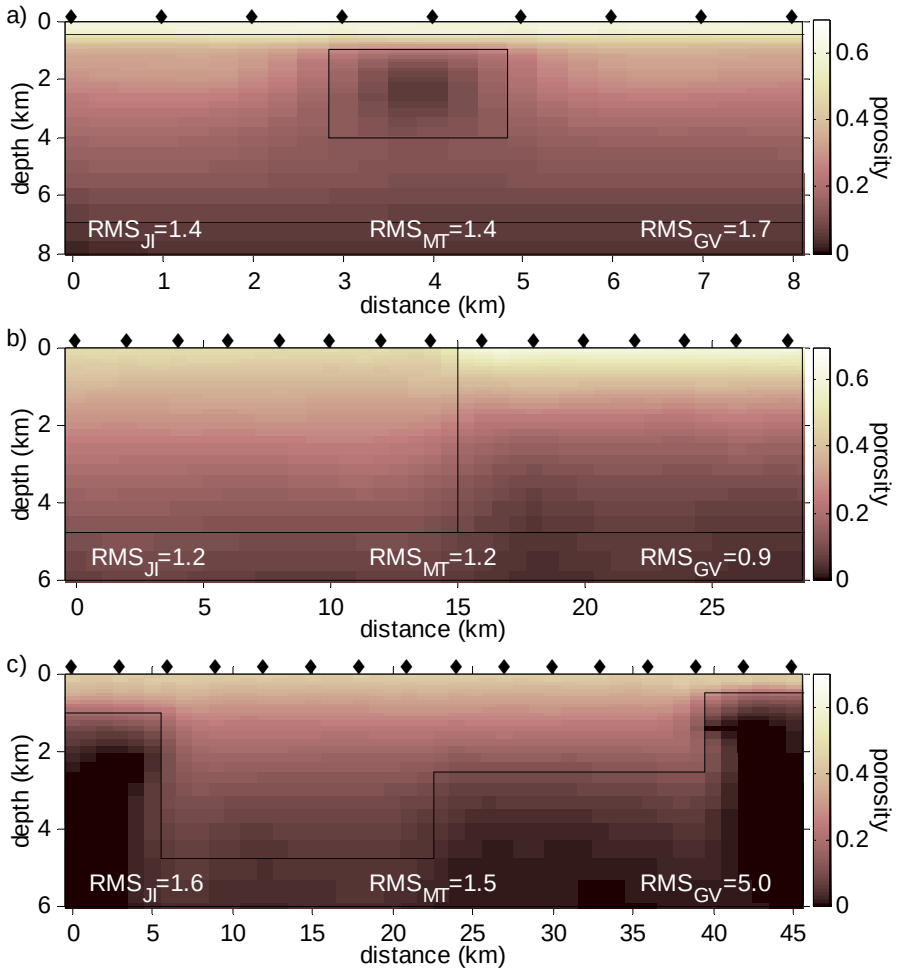

Figure 7.11: The joint inversion results for synthetic data with an MT error of 2% and a gravity error of 0.06 mGals, for the a) block, b) fault and c) trough models.

bias towards fitting the MT data, the block and fault models are both characterised by a good fit of the MT and gravity data, shown in Figure 7.12. The MT fits, shown in Figures 7.13a and 7.13b, have no systematic misfitting of the data at any frequency. The trough model has a larger gravity misfit than the block and fault models. Figure 7.13c shows how the inability to fit the gravity data allows a slight over- and under- estimation of the TE and TM modes in the MT data.

A prominent feature of all the joint inversion models is that they do not contain artifacts, enabling a clear porosity-compaction trend to be established. The sandstone and shale porosity-compaction trends in the fault model are almost identical to the synthetic model, however the boundary between them has been inevitably smeared. In the block model, the unconsolidated zone and the top of the embedded

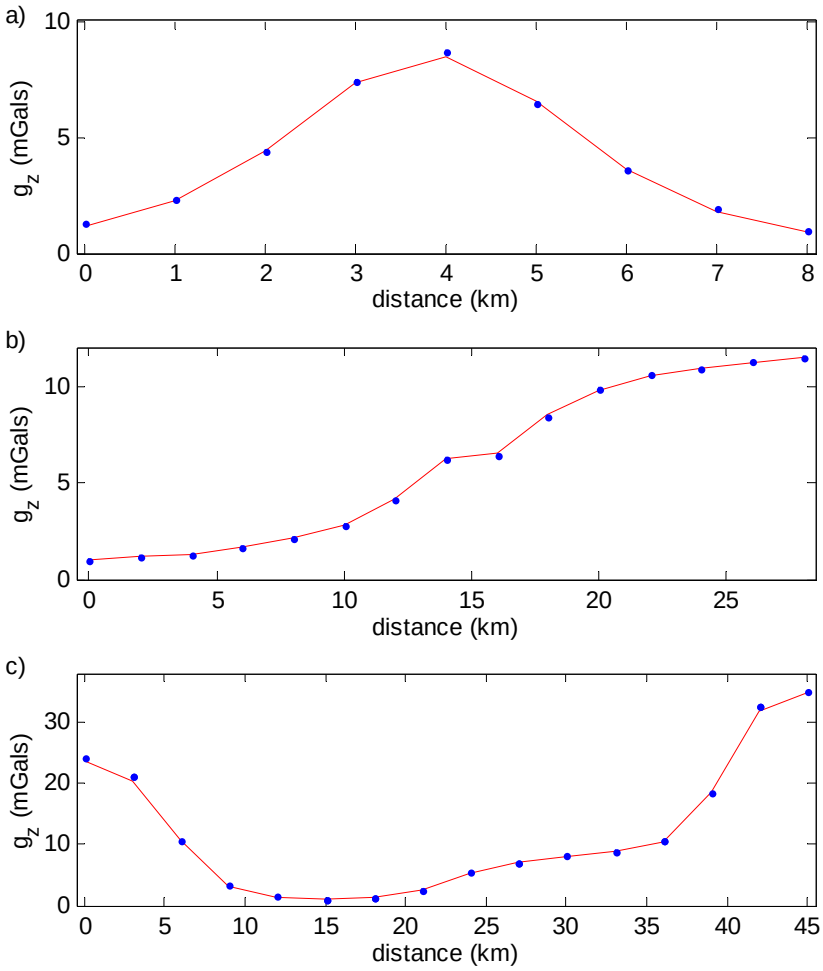

Figure 7.12: The gravity data (blue dots) and model responses (red lines) for the joint inversions of the synthetic data, with an MT error of 2% and a gravity error of 0.06 mGals, for the a) block, b) fault and c) trough models.

block are well mapped, however the exact location of the sides and bottom boundary of the block are hard to determine. The porosity-compaction trend away from the anomalous body is a true representation of the original, but the porosity value of the anomaly itself is slightly high. The trough model has a high gravity misfit which is investigated in greater detail in Section 8.1.3, while different weightings for the two data sets to reduce RMS_{GV} are tested in Section 8.3. Regardless of the high RMS_{GV} value, the shallow horizontal and vertical basement boundaries of the trough are well defined and again the porosity-compaction trend is also identical to the original.

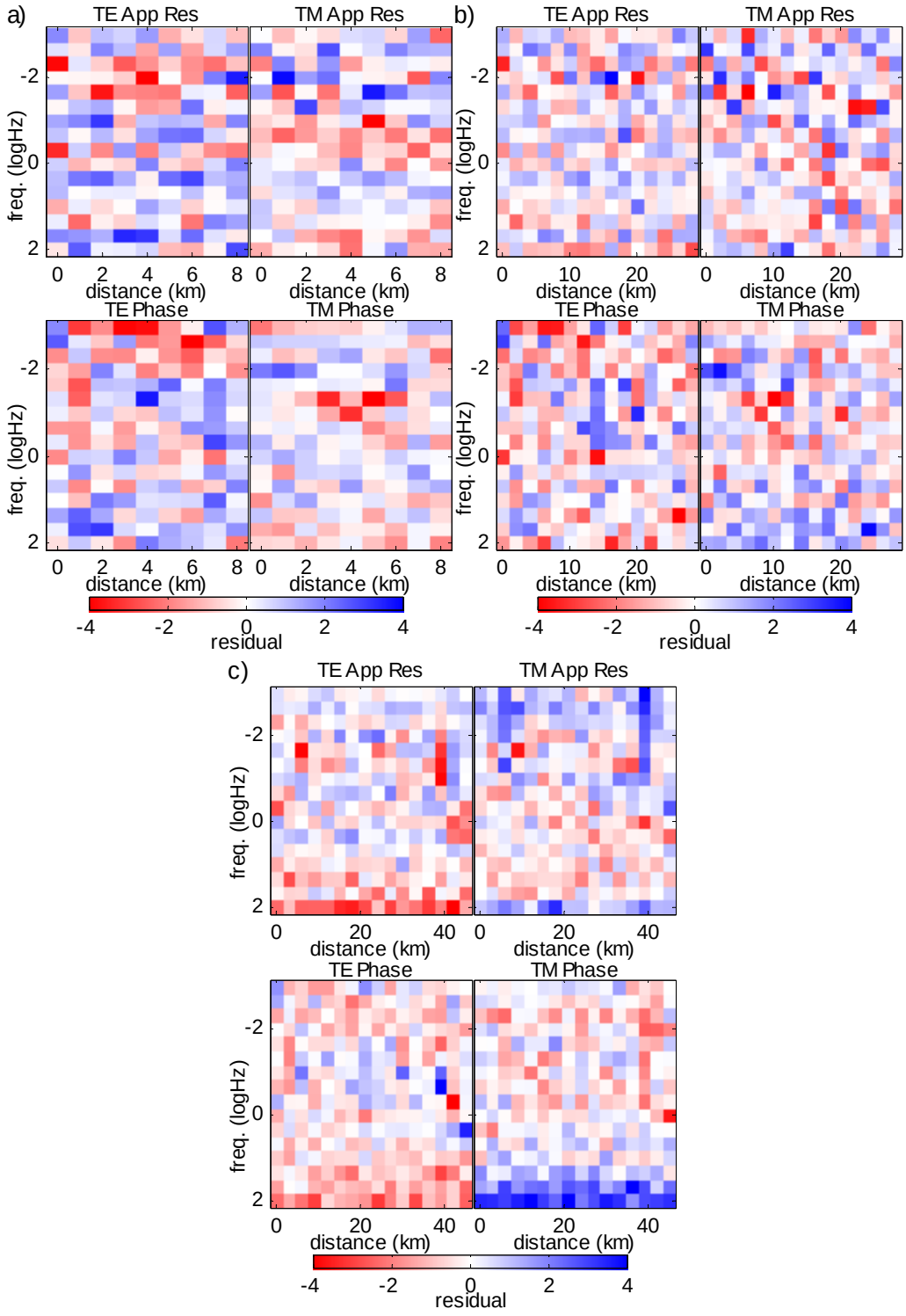

Figure 7.13: The MT misfit map from models produced in Figure 7.11, which are from the joint inversion of the a) block, b) fault and c) trough models. For each MT data point the MT misfit map takes the difference between the data and the model response, normalised by the data error. Each data point is then plotted as station location vs. frequency.

7.1.4 Discussion

From the findings reported in Chapter 4 and from Figure 7.10, it is clear that the joint inversion produces a more accurate representation of the subsurface than an individual gravity inversion. Therefore, for the remainder of this chapter the emphasis is placed on determining if the joint inversion can produce more accurate images of the subsurface than the single data set MT inversion.

The single MT data inversion will always produce a smaller RMS value than the RMS_{JI} and RMS_{MT} values for the joint inversion. The reason for this is that the MT inversion can fit all the subtle variations, including noise, contained in the data, whereas the joint inversion cannot as it also has to satisfy the gravity data. A similar situation arises for the gravity inversion. The RMS values of the MT and gravity inversions produce lower limits on the RMS_{MT} and RMS_{GV} values than can be achieved through joint inversion.

Similarities between the MT and joint inversion results are that they both struggle to reproduce the horizontal basement in the block and fault models, as well as the deep basement features of the tough model. In general, if structure does not appear in the MT model then there is no basis for such structure in the MT data. Therefore, the question arises as to whether or not the joint inversion can be expected to reconstruct structure to which the MT technique is insensitive.

A major difference between the MT and joint inversion models is that the MT models obtained with a target RMS of 1 contain artifacts. These artifacts do not appear in the joint inversion models, although they have higher values of misfit. For the fault and block models, the equivalent joint inversion RMS_{MT} value is achieved by an MT inversion with a 20% relaxation. However, the 20% relaxation MT models still contain artifacts, whereas the joint inversion gives a clearer image of the subsurface. Also the 20% relaxation in the MT inversion allows for a systematic misfit of the MT data, as revealed in Figures 7.7b and 7.8b. Such behaviour is not present in the joint inversion result of Figure 7.13.

The points at which all the artifacts are removed from the MT inversions occur at an RMS value of 2.0 and 1.8 for the block and the fault models, respectively. Although these models are comparable to the joint inversion in terms of clarity of

the compaction trend and the boundary locations, they have a larger RMS value than the joint inversion RMS_{MT}. Again, these MT models exhibit a systematic misfitting of the MT response, whereas the joint inversion does not.

The joint inversion is therefore favoured over single MT inversion as a way to reconstruct the subsurface structure. The joint inversion models do not contain the artifacts present in the MT inversions that have a target RMS of 1 and the joint inversion models have RMS_{MT} values smaller than any single MT inversion that attempts to remove the artifacts.

7.1.5 Proof of Concept Summary

The joint inversion produces coherent models and provides an effective means of reconstructing the subsurface. It was shown that the joint inversion can resolve density anomalies, differences in porosity-compaction trends and basement topography. The joint inversion was shown to produce a better representation of the subsurface than either the MT or gravity inversion alone.

7.2 Effects of Data Errors

All data points have an associated error or uncertainty, which must be estimated. In an inversion scheme, the error level defines the tolerance to which each data point is replicated. It makes no sense trying to fit the observed data with predicted data (for a given model) to a level better than the data errors. For the joint inversion, the MT and gravity data sets have their own error values, which give the tolerance to which each data set is to be matched. In this section the effect on the joint inversion of the magnitude of the MT and gravity errors is investigated and has been broken into two parts: the effect of increasing the gravity error, and the effect of increasing the MT error.

7.2.1 Gravity Data Errors

To investigate the effects of the gravity errors on the joint inversion, the inversion was executed with the MT errors held constant, and the gravity errors varied. In

keeping with the discussion of Section 4.4.1, the gravity error level was assigned a fixed value based on the amplitude of the synthetic data. The symbol %A is again used and differentiates this style of gravity error allocation. Figure 7.14 shows the joint inversion results for the block model with an MT error of 6% and gravity errors of 2, 15 and 50%A . The fault model inversion results, shown in Figure 7.15, have an MT error of 4% and the gravity errors are progressively set at 2, 15 and 50%A. Figure 7.16 shows the results for the trough model with an MT error of 10% and gravity errors of 2, 10 and 25%A.

The block and fault models (Figures 7.14 and 7.15), show the general trend which occurs as the gravity error is increased. When the gravity error is small, the joint inversion produces a good representation of the true synthetic model (Figures 7.14a and 7.15a). Here, the boundaries are well defined, the porosity-depth compaction trend is clear and the true porosity values are well recovered. As the gravity error increases (Figures 7.14b, 7.14c, 7.15b and 7.15c), the inverted models develop artifacts, blurred boundaries and incorrect porosity values. In general, the models produced by the joint inversions start to approach the model produced from a single MT inversion with a target RMS of 1 (Figures 7.14d and 7.15d).

Even when the gravity error is close to 100%A, and the data contain no reliable information about the subsurface, the joint inversion does not produce the same model as the MT inversion. A model is produced which has similar features but is smoother, and this is indicative of the RMS_{MT} value of the joint inversion never reaching the RMS of the single MT inversion. This is an extension of the behaviour seen in Section 4.4.3 where a single gravity Occam inversion with high gravity errors produced a very smooth or almost homogenous model.

The inclusion of gravity data with a small error mean that a slight variation away from the gravity data value will produce a large RMS_{GV}, and subsequently a large RMS_{JI} value. Therefore, a small gravity error encourages the joint inversion to fit the gravity data and produces a reliable image. However, as the gravity error is increased the preference of the joint inversion to fit the gravity data decreases. The joint inversion is then dominated by the MT data, thus producing models that resemble the single MT inversion results.

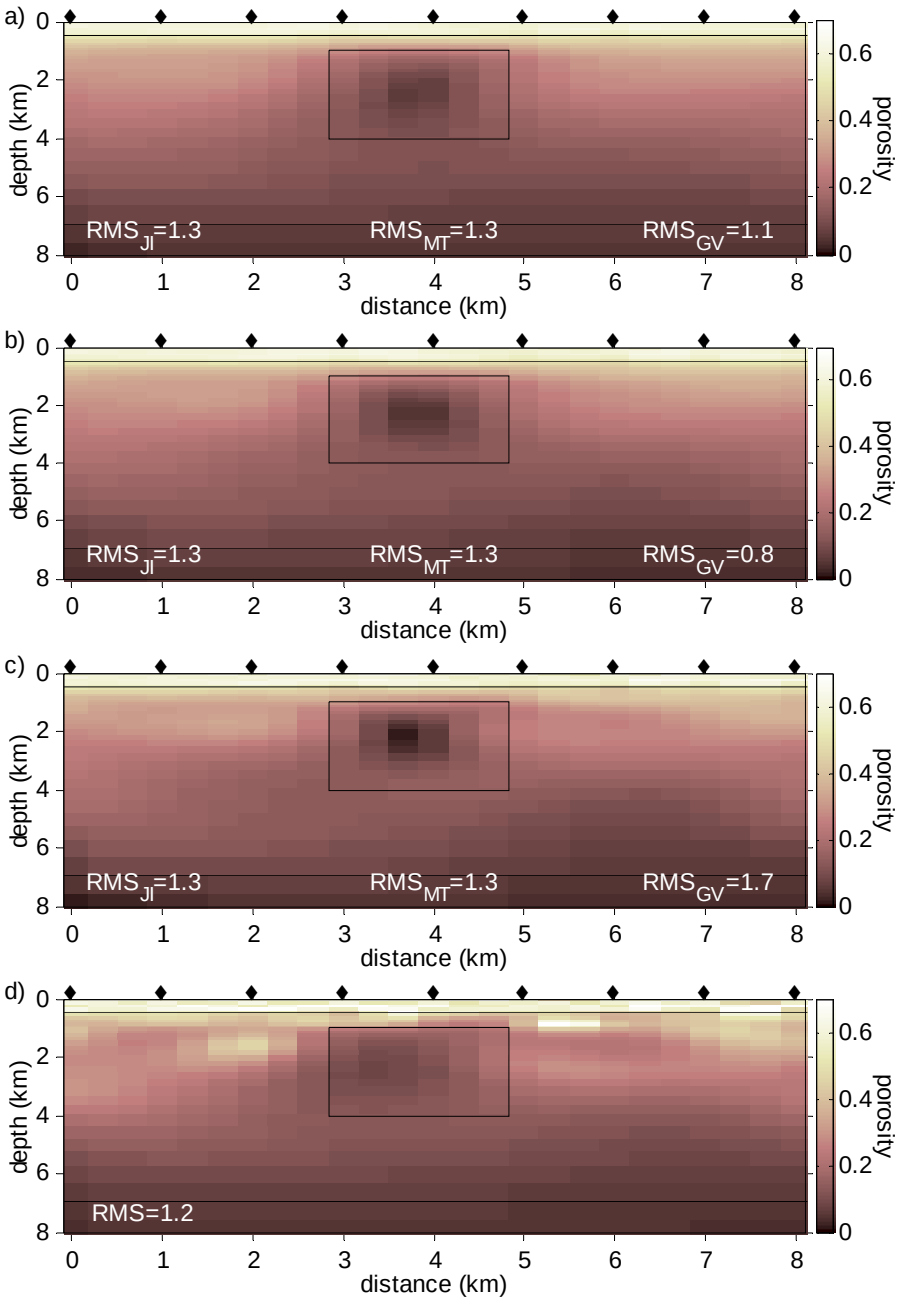

Figure 7.14: Joint inversion results using the block model synthetic data with an MT error of 6% and a gravity error of a) 2%A, b) 15%A and c) 50%A. d) MT inversion of the block model synthetic data with an error of 6% and converted to a porosity model using Archie's Law.

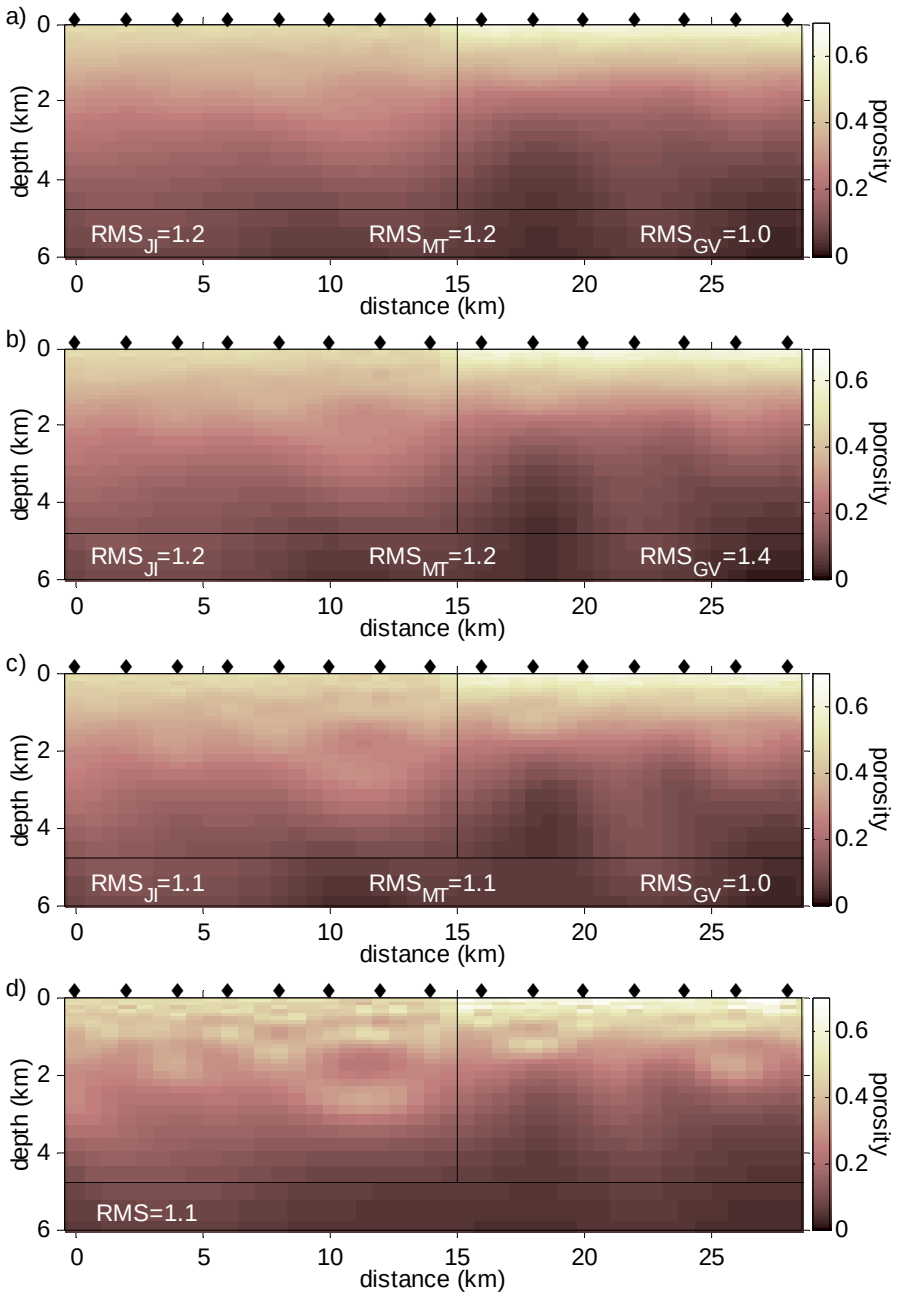

Figure 7.15: Joint inversion results using the fault model synthetic data with an MT error of 4% and gravity error of a) 2%A, b) 15%A and c) 50%A. d) MT inversion of the fault synthetic data with an error of 4% and converted to a porosity model using Archie's Law.

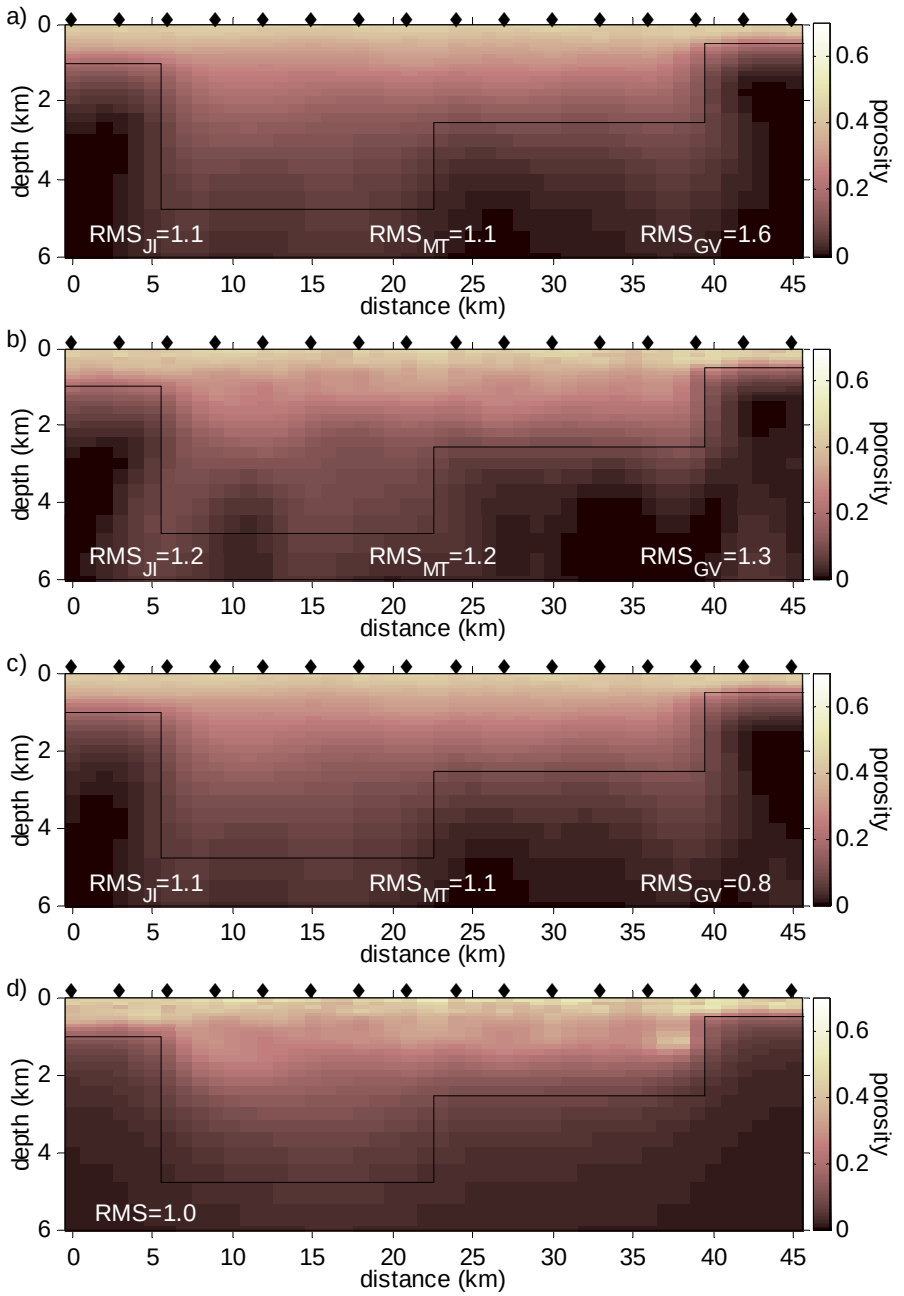

Figure 7.16: Joint inversion results using the trough model synthetic data with an MT error of 10% and gravity error of a) 2%A, b) 10%A and c) 25%A. d) MT inversion of the trough model synthetic data with an error of 10% and converted to a porosity model using Archie's Law.

The trough model results, shown in Figure 7.16, exhibit a slightly different trend to that of the previous block and fault examples. As with the fault and block examples, increasing the gravity error leads to artifacts developing in the joint inversion models (Figure 7.16b). However, if both the MT and gravity errors are significantly large, then the joint inversion can produce a smooth coherent model with no artifacts, as depicted in Figure 7.16c. The image in this figure has an MT error of 10% and a gravity error of 25%A. It is an adequate representation of the synthetic trough model, although it is smoother and a slight over-estimation of the porosity values. When data errors are high, the Occam inversion produces a smoother model and this is the joint inversion equivalent of such behaviour. However, the joint inversion must satisfy both the MT and gravity data sets, which do not contain coherent noise information, thus reducing the risk of artifacts and resulting in a model which resembles the original.

7.2.2 MT Data Errors

To investigate the effects of MT data errors on the joint inversion, the inversion was executed with the gravity error held constant and the MT error allowed to vary. Figure 7.17 shows the joint inversion results for the block model with a gravity error of 2%A and MT errors of 2, 4, 10 and 20%. The fault model results, shown in Figure 7.18, have a gravity error of 5%A and MT errors of 2, 5, 7 and 15%. For the trough model, shown in Figure 7.19, the gravity error is 0.06 mGals and the MT errors are 3, 7, 15 and 25%.

The trough model illustrates the changes in the joint inversion results when the gravity error is small and the MT error is increased (see Figure 7.19). There is a slight change in the basement boundary and the porosity value, but in general all models are smooth, contain no artifacts and are good representations of the synthetic trough model. The consistency in these models, regardless of MT error, is attributed to the gravity and MT data not having correlated noise information. Therefore, the gravity data do not support model artifacts, which arise when inverting the MT data alone. For the specific trough example given, the RMS_{GV} seems uncharacteristically high, although all RMS_{GV} errors are smaller than the RMS_{GV} values in Section 7.1.3.

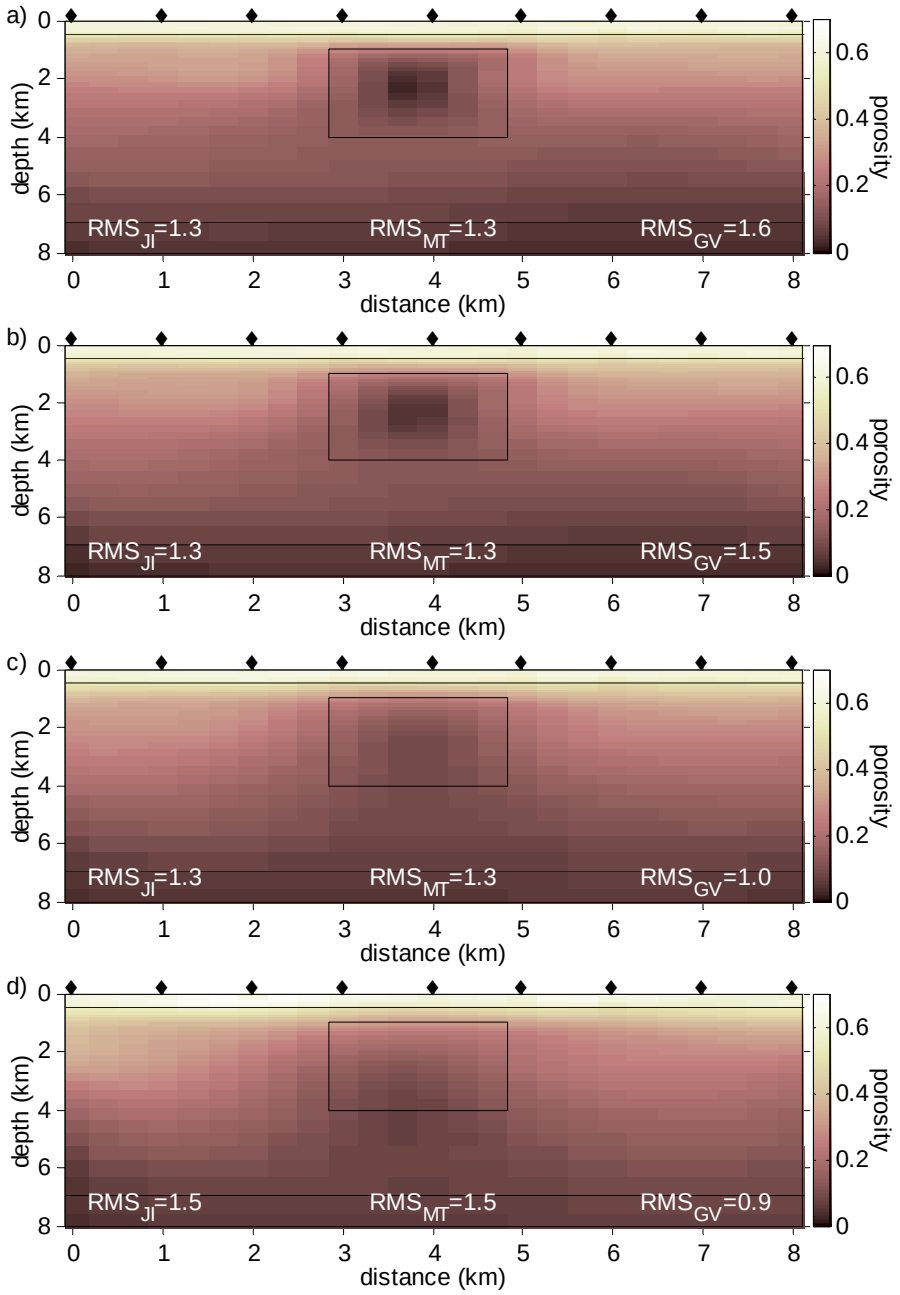

Figure 7.17: Joint inversion results using the block model synthetic data with a gravity error of 2%A of the data amplitude and an MT error of a) 2%, b) 4%, c) 10% and d) 20%.

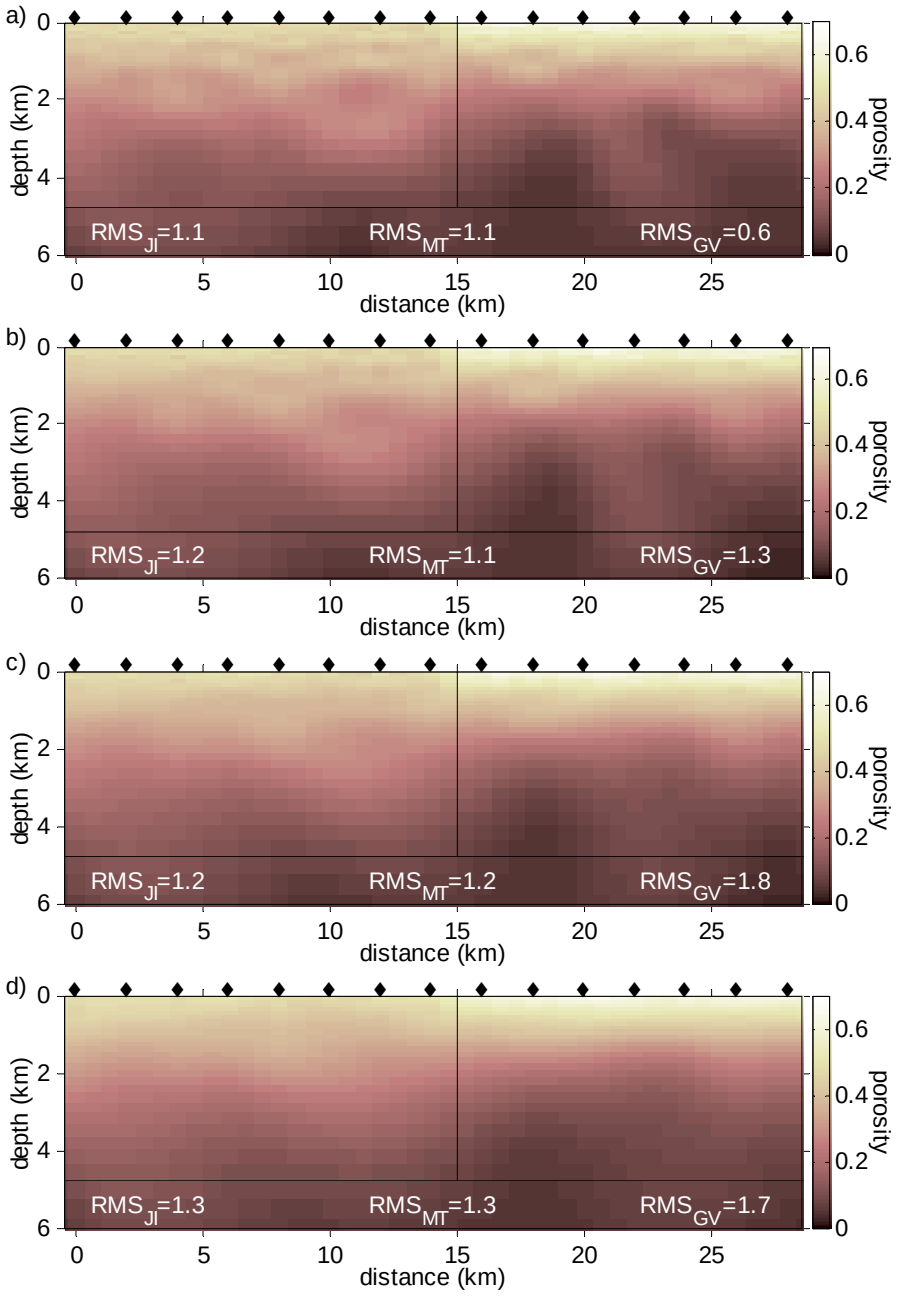

Figure 7.18: Joint inversion results using the fault model synthetic data with a gravity error of 5%A of the data amplitude and an MT error of a) 2%, b) 5%, c) 7% and d) 15%.

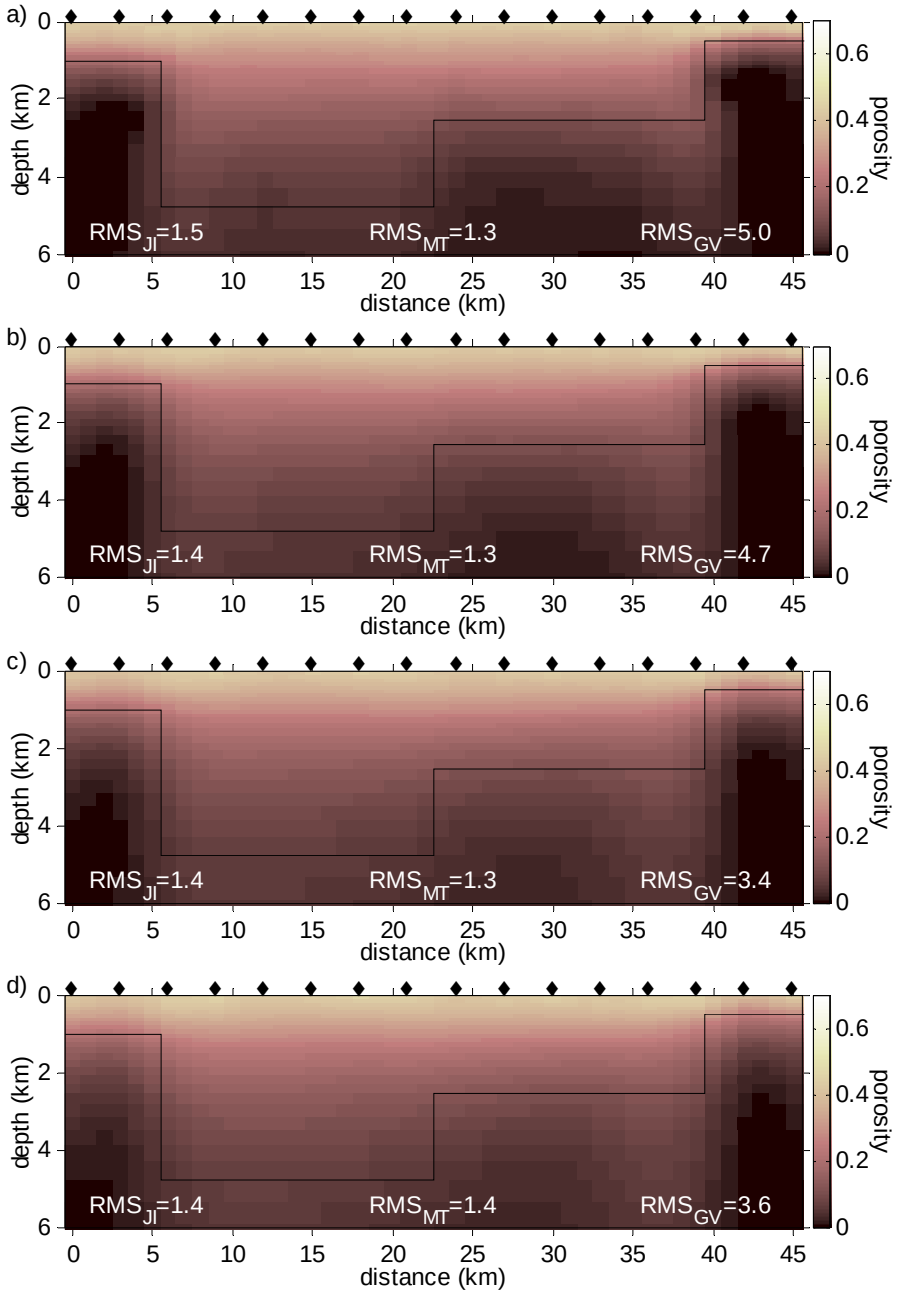

Figure 7.19: Joint inversion results using the trough model synthetic data with a gravity error of 0.06 mGals and an MT error of a) 3%, b) 7%, c) 15% and d) 25%.

Figure 7.17 shows the joint inversion results for the block model with a slightly higher gravity error than the previous trough example. This relaxes the ability of the gravity data to constrain the MT data in the joint inversion, and as a result there is no longer a consistency of models across the full range of MT errors. In Figure 7.17a, for which the MT error is low, the joint inversion still produces a good representation of the true synthetic model. However, at higher MT errors, as shown in Figure 7.17c, the joint inversion reconstructed models become smoother and the block anomaly feature is harder to recover.

The fault model results shown in Figure 7.18 have the highest gravity error of 5%A. As previously discussed, when the gravity errors are high and the MT errors are low, the joint inversion produces a model which resembles the single MT inversion. This is illustrated in Figure 7.18a. However, when both the MT and gravity errors are high, a smooth model is produced, as is evident in Figure 7.18d. This is similar to observations made for the trough example in Section 7.2.1. Figures 7.18b and 7.18c show the transition between these two extremes.

7.2.3 Data Error Summary

Low MT and gravity errors are highly desirable because low noise data produce the best possible representation of the subsurface. As the gravity error increases, the joint inversion model develops more artifacts and begins to resemble the model from a single MT inversion with a target RMS of 1. However, if both the MT and gravity errors are high, then a smooth model can still be produced. When a high MT error is combined with a low gravity error, the low error gravity data can constrain the noisy MT data. This will produce a model that is artifact free and a good representation of the original model. An implication of these findings is that coherent information can be obtained from noisy MT data by combining it with high quality (low noise) gravity data.

7.3 Station Configurations

There are several reasons why the gravity and MT station configurations may not coincide. This could be the result of surveys being conducted at different times or because of different survey requirements. Gravity data can be acquired at a higher speed than the MT technique, which requires careful station preparation and long recording times. Therefore the gravity and MT stations will generally not occupy the same locations, and so the joint inversion must allow for arbitrary locations in each case. This section investigates how different station configurations (and numbers of stations) affect the joint inversion results. It should be appreciated that changing the MT and gravity station configurations change the ratio of gravity to MT data points. This could potentially produce a bias against the MT data, because of the large difference between the number of stations in each case (gravity data are easier to collect and are therefore a potentially denser acquisition). However, this is offset to some extent by the increased data in MT (multiple frequencies for each station) and so the bias is most likely to be slight and deemed not to be an issue.

The first part of this section considers having more gravity than MT stations, whereas in the second part the reverse is true, with more MT than gravity stations. Having different numbers of MT and gravity stations means that the techniques could contain information about different potentially conflicting subsurface features. However, in this section, the gravity and MT data used are compatible and contain the signal from the same subsurface features.

7.3.1 Additional Gravity Stations

The aim is to determine if having extra gravity stations helps to 'fill in' information between the MT stations and aid resolving lateral boundaries. The MT station spacing of the block, fault and trough models were doubled to allow for the extra gravity stations. The new MT station spacings are 2, 4 and 6 km for the block, fault and trough models, respectively. Three gravity station configurations, shown in Figure 7.20, were used in conjunction with the new MT spacings; (1) a gravity station at every MT station, as a control, (2) one gravity station in between every

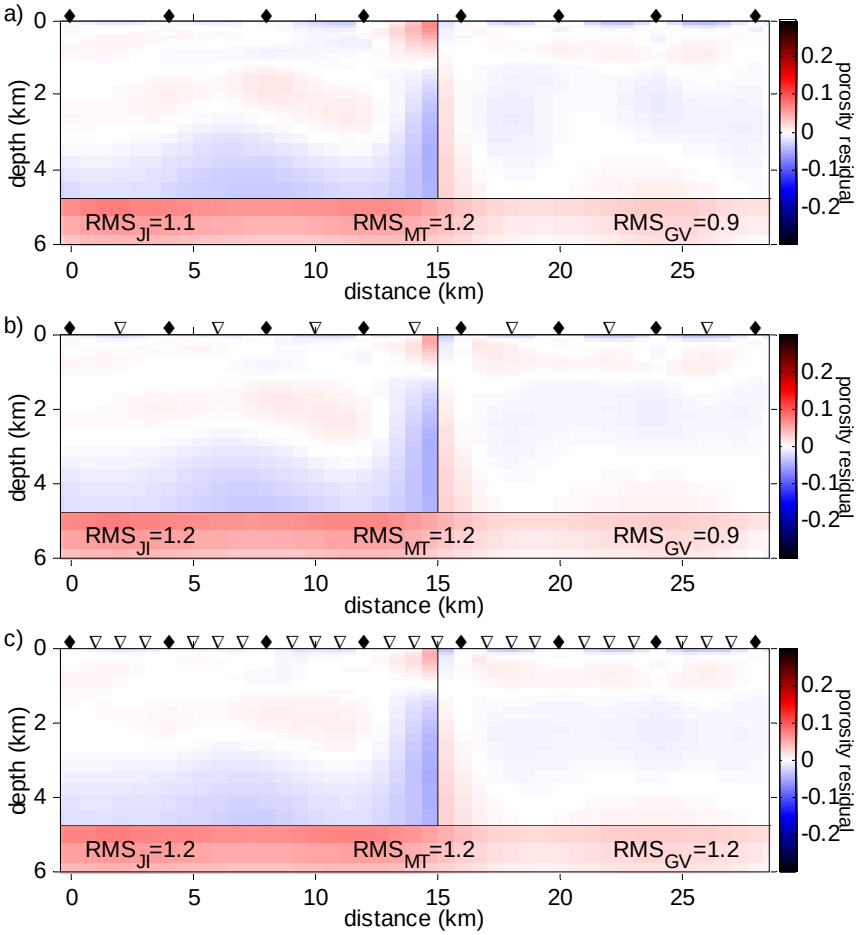

Figure 7.20: The residual porosity models for the joint inversion of the fault model synthetic data with an MT error of 2% and a gravity error of 0.06 mGals. Models a), b) and c) have different MT and gravity station configurations. A black diamond is a station where both MT and gravity data are recorded, whereas a white triangle is a station where just gravity data are recorded. The porosity residual models are generated by subtracting the synthetic (true) model from the joint inversion model.

other station which has both MT and gravity and (3) three gravity stations evenly spaced between every primary stations which has both MT and gravity stations.

The joint inversions were performed using a gravity error of 0.06 mGals, since a small gravity error encourages the joint inversion to fit the gravity data (Section 7.2). The MT errors were varied for each run, and included values of 2, 4, 6, 8 and 10%. Figure 7.20 shows the reconstructed porosity deviations for the fault model from a joint inversion using the different station configurations. The MT data error is 2% for this plot. The images in this figure are residual models which are obtained by subtracting the porosity values of the true synthetic model from the joint

inversion model. Therefore, positive residual values are where the joint inversion model over-estimates the true values and the negative residual values are where the joint inversion under- estimates the true values. Residual models are used in the display because they best exploit the available dynamic range and show the subtle variations between the models where the different station configurations are used.

The results depicted in Figure 7.20 show that there is only a very minor improvement in the ability of the joint inversion to reconstruct the original fault model as the number of gravity stations increases relative to the number of MT stations. At a distance of $\sim$ 16 km and depth of $\sim$ 1 km an artifact appears in the image as the number of gravity stations increases. In general, the addition of extra gravity stations provided minimal or no improvement to the ability of the joint inversion to reconstruct the synthetic models for all three models and error levels tested. By its nature, the gravity response is smooth and so sampling it at a higher density does not change the basic characteristics of the response curve. Therefore, there is minimal information gained by having additional gravity stations, when compared to the station configuration which has the gravity and MT stations at the same location.

7.3.2 Additional MT Stations

In this section the effect on the joint inversion results, when there are more MT than gravity stations, is investigated. For this investigation the block, fault and trough synthetic models were again used, with their original recording station spacing of 1, 2 and 3 km, respectively. Four gravity station configurations were used and are shown in Figure 7.21; (1) a gravity station at every MT station, as a control, (2) the removal of a gravity station at every second MT station location, (3) the removal of gravity stations to set up a sequence entailing both MT and gravity stations coincident, followed by two sites involving only MT stations and (4) only three gravity stations, one at each end site and one at the middle site. The joint inversions were run, using a gravity error of 0.06 mGals, and sequential MT errors of 2, 4, 6, 8 and 10%.

Figure 7.21 shows the residual models for the fault model, with an MT error of

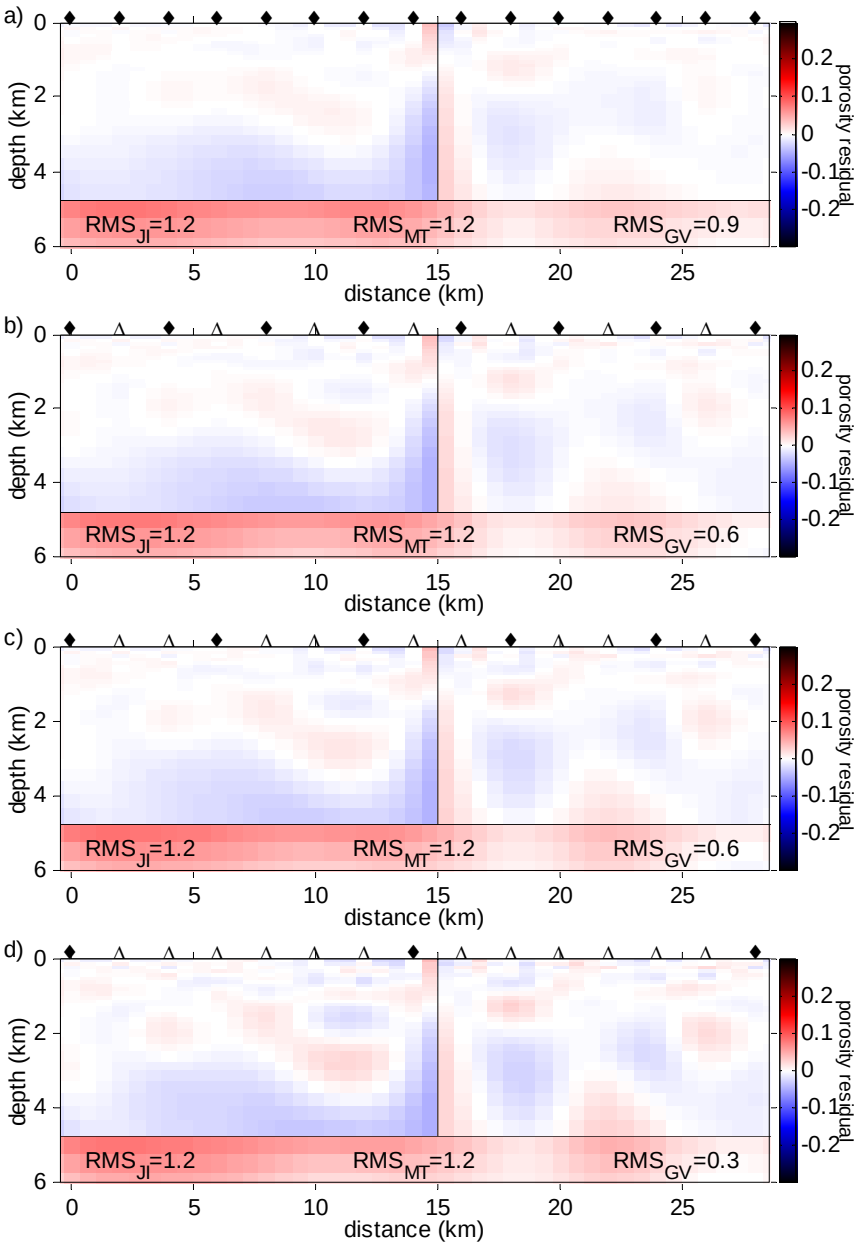

Figure 7.21: The residual porosity models for the joint inversion of the fault model synthetic data with an MT error of 2% and a gravity error of 0.06 mGals. Models a), b) and c) have different MT and gravity station configurations. A black diamond is a station where both MT and gravity data are recorded, whereas a white inverted triangle is a station where just MT data are recorded. The porosity residual models are generated by subtracting the synthetic (true) model from the joint inversion model.

2%. The different diagrams correspond to the four different station configurations. The fewer gravity stations there are, the less information the gravity response contains about the subsurface. Therefore, the capacity of the gravity data to constrain the MT data in the joint inversion is reduced. As a result, progressively more image artifacts appear in the joint inversion models as the number of gravity stations decrease. The models approach a similar appearance to an MT inversion with a target RMS of 1. However, even when there are only three gravity stations the joint inversion still produces a model with less artifacts than the single MT inversion. These findings are consistent for all synthetic model types and error levels tested, although only the results for the fault model and one MT data error (2%) are shown.

7.3.3 Station Configurations Summary

Additional gravity stations, except at every MT station along the profile, provide only minimal or no improvement in the ability of the joint inversion to reconstruct the subsurface. However, these extra gravity stations do not harm the results and should therefore be used in a joint inversion if available. More MT than gravity stations leads to artifacts in the joint inversion result, although using only three gravity stations still provides an improvement over an individual MT inversion.

7.4 Target Contrast and Resolution Observations

The aim of this section is to determine how the joint inversion reacts to different porosity contrasts and to study the resolving capacity of the joint inversion, and compare it to the MT inversion alone.

7.4.1 Target Contrast

In this section the effects of different porosity contrasts on the joint inversion is investigated and compares these results to the MT inversion. The synthetic model used in this numerical experiment is shown in Figure 7.22a. It comprises an 8 km by 4 km embedded box within a uniform background, having its top surface at a depth of 1 km below the surface. Since the MT technique has a greater sensitivity

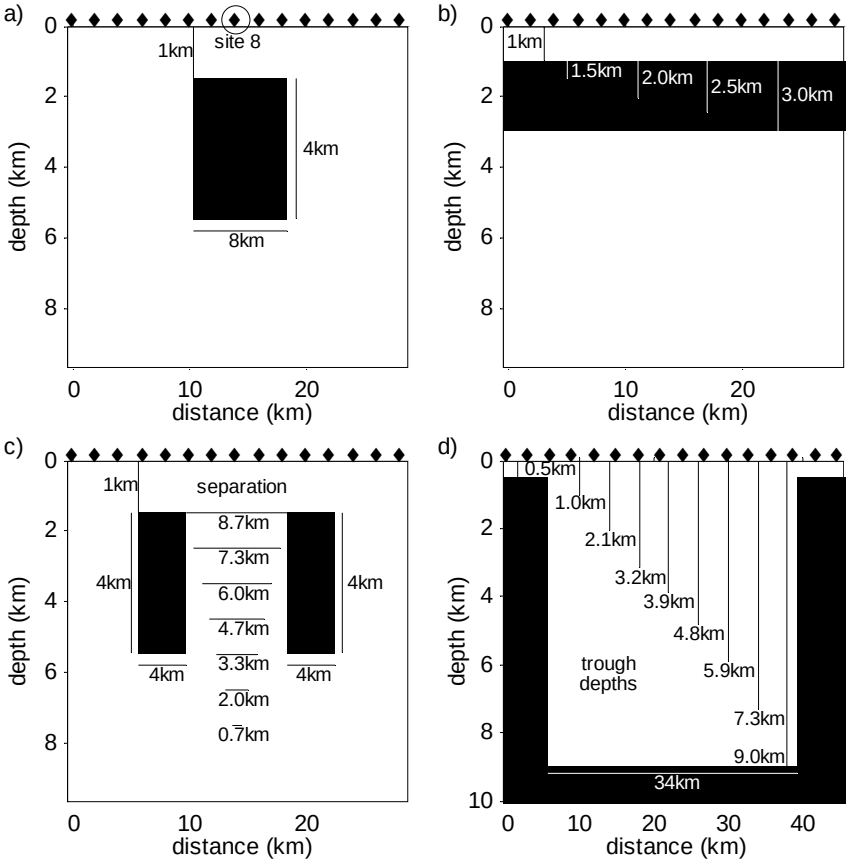

Figure 7.22: a) Synthetic box model. b) Synthetic layered model with different middle layer thicknesses, as indicated. c) Two box model with different separation distances, as indicated. d) Basement model with different trough depths, as indicated.

to resistivity structures than conductive structures [31] both positive and negative contrasts between the background and the box porosity values need to be investigated. Table 7.1 lists the porosity values assigned to the box and the background. The parameter values used in Archie's Law and the porosity-density relationship were $a = 1$, $m_{cf} = 2$, $S = 1$, $n_s = 2$, $\varrho_{fluid} = 0.33$ Ωm, $\rho_{matrix} = 2650$ kgm^{-3} and $\rho_{fluid} = 1030$ kgm^{-3}. These parameters are fixed with depth to allow for a constant resistivity and density contrast across the whole model. Using the above listed parameters of Archie's Law and the porosity-density relationship, the corresponding resistivity and density values of the background and the inclusion (box) are calculated and shown in Table 7.1.

For each of the porosity contrasts given in Table 7.1, the MT and gravity data

Table 7.1: The density, resistivity and porosity values used the inversion of the one box model for the negative and positive porosity contrasts.

negative contrast	background ϕ	box ϕ	background ϱ (Ωm)	box ϱ (Ωm)	background ρ (kgm^{-3})	box ρ (kgm^{-3})
1%	0.11	0.10	12.4	15.0	2471.8	2488.0
2%	0.12	0.10	10.4	15.0	2455.6	2488.0
3%	0.13	0.10	8.9	15.0	2439.4	2488.0
4%	0.14	0.10	7.7	15.0	2423.2	2488.0
5%	0.15	0.10	6.7	15.0	2407.0	2488.0
6%	0.16	0.10	5.9	15.0	2390.8	2488.0
7%	0.17	0.10	5.2	15.0	2374.6	2488.0
8%	0.18	0.10	4.6	15.0	2358.4	2488.0
10%	0.20	0.10	3.7	15.0	2326.0	2488.0
15%	0.25	0.10	2.4	15.0	2245.0	2488.0
20%	0.30	0.10	1.7	15.0	2164.0	2488.0
positive contrast	background ϕ	box ϕ	background ϱ (Ωm)	box ϱ (Ωm)	background ρ (kgm^{-3})	box ρ (kgm^{-3})
1%	0.10	0.11	15.0	12.4	2488.0	2471.8
2%	0.10	0.12	15.0	10.4	2488.0	2455.6
3%	0.10	0.13	15.0	8.9	2488.0	2439.4
4%	0.10	0.14	15.0	7.7	2488.0	2423.2
5%	0.10	0.15	15.0	6.7	2488.0	2407.0
6%	0.10	0.16	15.0	5.9	2488.0	2390.8
7%	0.10	0.17	15.0	5.2	2488.0	2374.6
8%	0.10	0.18	15.0	4.6	2488.0	2358.4
10%	0.10	0.20	15.0	3.7	2488.0	2326.0
15%	0.10	0.25	15.0	2.4	2488.0	2245.0
20%	0.10	0.30	15.0	1.7	2488.0	2164.0

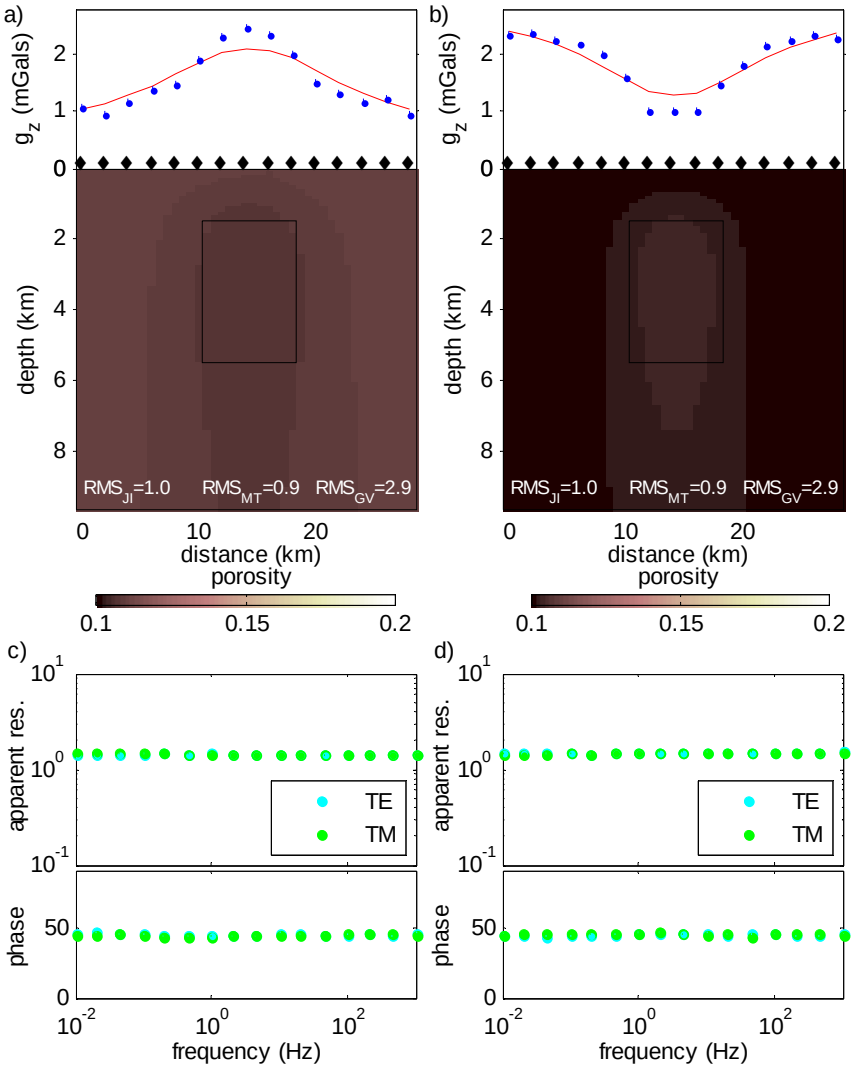

Figure 7.23: Joint inversion results for the box model synthetic data with a) a 1% negative porosity contrast and b) a 1% positive porosity contrast . The joint inversion used an MT error of 2% and a gravity error of 0.06 mGals. Also indicated are the gravity data (blue dots) and the model responses (red line). The MT synthetic data for station 8, indicated on Figure 7.22, for a) a 1% negative porosity contrast and b) a 1% positive porosity contrast.

were calculated at fifteen stations, with a station spacing of 2 km. It was demonstrated in Section 7.3 that there is only marginal, to no benefit, in employing more gravity stations than MT stations. Therefore, the MT and gravity data were calculated at the same station locations. It was shown in Section 7.2 that the joint inversion produces the most accurate representation of the subsurface when the gravity and MT errors are small. Therefore a gravity error of 0.06 mGals and an MT error of 2% were used.

Figures 7.23a and 7.23b show the gravity data for boxes having 1% positive and negative contrasts, respectively. The maximum amplitude of the gravity anomaly is 1.4 mGal in both cases. The MT data for station 8, which is indicated on Figure 7.22a as being directly above the top of the box, are shown in Figures 7.23c and 7.23d. The MT data show very little variation away from the half space response, which has a constant apparent resistivity of 10 Ωm and a phase of 45^{o} for all frequencies. When MT data are inverted alone, a practically smooth model is produced with an RMS of 1.

Unlike the MT inversion, the joint inversion of the MT and gravity data for the positive and negative 1% contrasts, yields models containing structure, as shown in Figure 7.23. For both contrast models the total RMS is 1.0, with an RMS_{MT} value of 0.9. However, the gravity RMS_{GV} is large at 2.9 for both contrasts. The gravity data contain a strong signal of the box structure and the joint inversion struggles to fit this signal, as it is not supported by an equivalent anomaly in the MT data. For this scenario it is questionable whether it can be concluded that the joint inversion produces a better representation of the subsurface than the MT inversion or if the joint inversion is producing structure that is only compatible with one of the data sets.

A positive or negative porosity contrast of 2% produces a similar inversion response to the 1% contrast situation. Contrasts above 2%, although small, have a clear indication (anomaly) of the box in the MT as well as the gravity data. Figures 7.24 and 7.25 show the recovered residual porosity models from the MT and joint inversions for positive and negative contrasts of 3% and 6%, respectively. All the residual models show an over- and under-estimation of the porosity values across

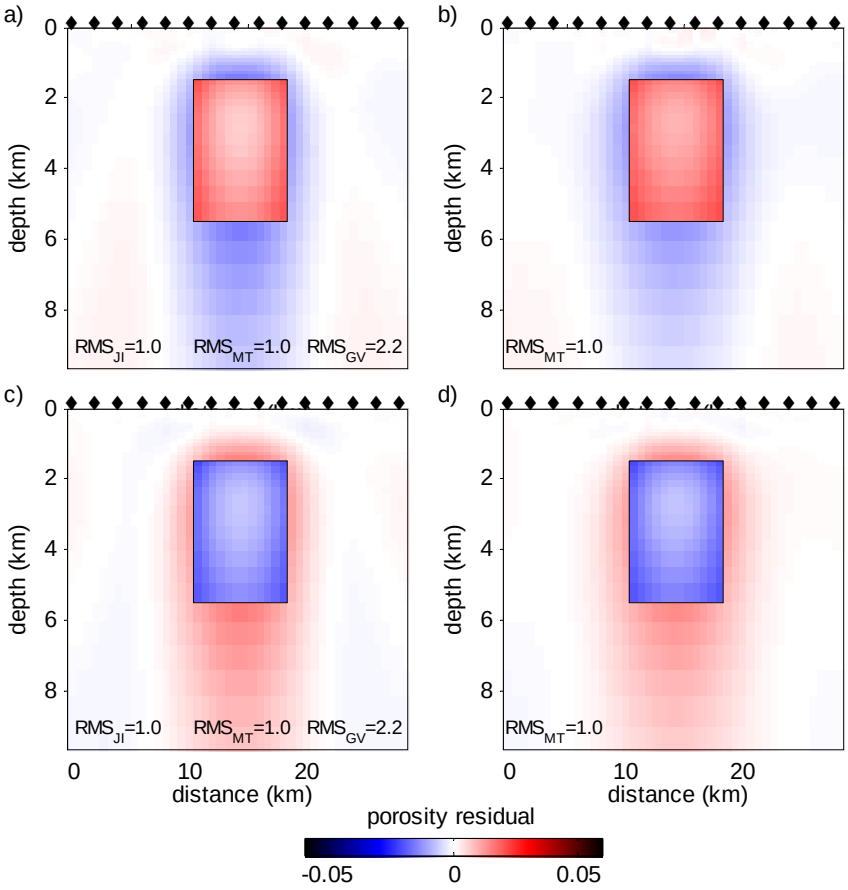

Figure 7.24: The porosity residual models for a joint inversion, with an MT error of 2% and gravity error of 0.06 mGals, for the one box model synthetic data with a) a 3% negative contrast and c) a 3% positive contrast. b) The porosity residual models of an MT inversion, with an error of 2%, for the one box model synthetic data with b) a 3% negative contrast and d) a 3% positive contrast. The porosity residual models are generated by subtracting the synthetic model from the joint inversion model or the MT model converted to a porosity model using Archie's Law.

the box boundary. This is expected and is due to the smoothness constraint not allowing a sharp boundary to occur. A 3% positive or negative contrast has little variation between the MT and joint inversion models, as shown in Figure 7.24. At a 6% contrast, the joint inversion provides a more accurate representation of the box porosity values than does the MT inversion, as evident in Figure 7.25. However, the joint inversion over- and under-shoots the background porosity values more than the MT inversion.

This over- and under-shooting of the background porosity is even more evident at higher porosity contrasts, for example a 15% contrast is shown in Figure 7.26. For

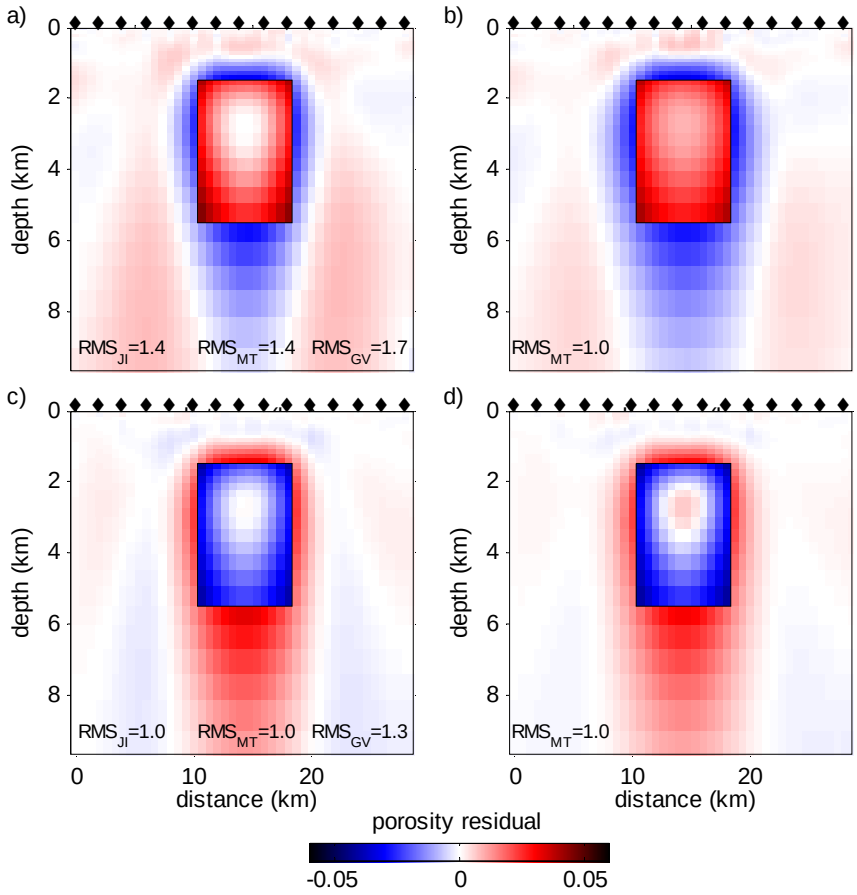

Figure 7.25: The porosity residual models for a joint inversion, with an MT error of 2% and gravity error of 0.06 mGals, for the one box model synthetic data with a) a 6% negative contrast and c) a 6% positive contrast. b) The porosity residual models of an MT inversion, with an error of 2%, for the box synthetic data with b) a 6% negative contrast and d) a 6% positive contrast. The porosity residual models are generated by subtracting the synthetic model from the joint inversion model or the MT model converted to a porosity model using Archie's Law.

a 15% negative contrast the joint inversion model under-estimates the box porosity value and overshoots the background porosity (Figure 7.26e). The corresponding MT inversion, (Figure 7.26a), has an RMS of 1.1 and it too under-estimates the box porosity value, but has significant artifacts. A 20% relaxation can be applied, (Figure 7.26b) and yields a smoother model with fewer artifacts. It does however slightly over-estimate the box porosity value and the box boundaries are not as well defined.

A positive contrast of 15% corresponds to a conductive body, to which the MT technique is more sensitive. Unlike the negative contrast case, the MT inversion

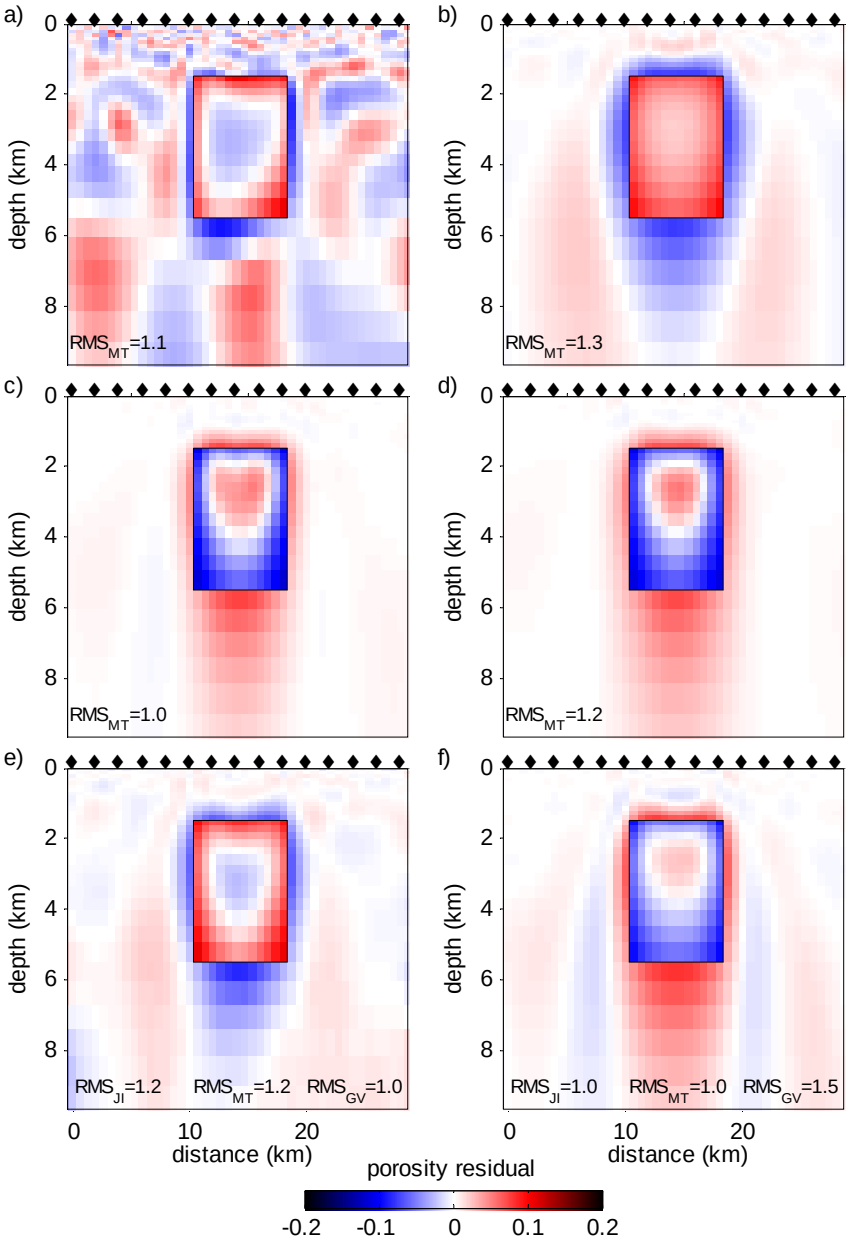

Figure 7.26: The porosity residual models for the one box model synthetic data with an MT error of 2% and gravity error of 0.06 mGals. a) MT inversion of a 15% negative contrast anomaly with a target RMS of 1. b) 20% relaxation of the model in a). c) MT inversion of a 15% positive contrast anomaly with a target RMS of 1. d) is a 20% relaxation of the model in c). e) is the joint inversion of a 15% negative contrast anomaly and f) is the joint inversion of a 15% negative contrast anomaly. The porosity residual models are generated by subtracting the synthetic model from the joint inversion model or the MT model converted to a porosity model using Archie's Law.

Table 7.2: The density, resistivity and porosity values used in the inversion of the layered model for different porosity distributions.

porosity configuration:	decreasing	increasing	negative anomaly	positive anomaly
top layer ϕ	0.30	0.10	0.30	0.10
middle layer ϕ	0.15	0.15	0.10	0.30
bottom layer ϕ	0.10	0.30	0.30	0.10
top layer ϱ (Ωm)	3.7	33.0	3.7	33.0
middle layer ϱ (Ωm)	14.7	14.7	33.0	3.7
bottom layer ϱ (Ωm)	33.0	3.7	3.7	33.0
top layer ρ (kgm^{-3})	2164.0	2488.0	2164.0	2488.0
middle layer ρ (kgm^{-3})	2407.0	2407.0	2488.0	2164.0
bottom layer ρ (kgm^{-3})	2488.0	2164.0	2164.0	2488.0

reaches an RMS of 1 and in so doing enables the inversion to seek the smoothest possible model with this RMS. Thus, the MT model does not contain significant artifacts (Figure 7.26c). However, it does over-estimate the box porosity value by a greater amount than does the joint inversion (Figure 7.26f).

The inversions were repeated using MT errors of 4, 6 and 8%. At higher MT errors, a stronger porosity contrast is required for the MT inversion to produce a model containing structure. Conversely, the joint inversion produces models containing structure at a smaller contrast than the MT inversion. These results also tie in with the findings of Section 7.2, where it was observed that a small gravity error aids a large MT error in reconstructing the synthetic model.

7.4.2 Resolution Observations

Vertical Resolution

A three layered model, shown in Figure 7.22b, is used to test and compare the vertical resolution of the joint inversion and MT models. The top of the middle layer is fixed at a depth of 1 km. The thickness was allowed to vary and fixed values of 1.5, 2.0, 2.5 and 3.0 km were assigned with separate inversions run for each thickness. The porosity values assigned to the three layers are given in Table 7.2. Four porosity distributions are considered and referred to as increasing, decreasing, positive anomaly and negative anomaly. The parameter values in Archie's Law and the porosity-density relationship were fixed with depth and are $a = 1$, $m_{cf} = 2$,

$S = 1$, $n_s = 2$, $\varrho_{fluid} = 0.33$ Ωm, $\rho_{matrix} = 2650$ kgm^{-3} and $\rho_{fluid} = 1030$ kgm^{-3}. Using these values, the corresponding resistivity and density values for the three layers are computed and also listed in Table 7.2.

For each porosity distribution, the MT and gravity synthetic data were calculated at fifteen stations along the surface of the model, at a station spacing of 2 km (see Figure 7.22b). As for the target contrast investigation (Section 7.4.1), the MT and gravity data were generated at the same station locations and the gravity error was set at 0.06 mGals, while the MT error was 2%. The gravity technique is sensitive to lateral changes, however the layered model has none. Therefore, the gravity response for all stations will be the same (no anomaly).

The increasing and positive anomaly porosity distributions have conductive features, to which the MT technique is more sensitive (than the resistive features) [31]. As a result, the MT inversions of these porosity configurations all reached an RMS of 1, which allows the MT inversion to seek the smoothest possible model with this RMS. Therefore these models do not contain artifacts and do not require a 20% relaxation (see Figures 7.27b and 7.27d). Conversely, the MT inversions of the decreasing and negative anomaly configurations, which contain resistive features, never have an RMS less than 1.1. These models are peppered with artifacts and require a 20% relaxation in the target RMS to produce a smooth artifact free model (Figures 7.28b and 7.28d).

Similar to the MT inversions, the joint inversions of the increasing and positive anomaly distributions always have an RMS of approximately 1. The joint inversions of the decreasing and negative anomaly distributions never reach an RMS_{JI} less than 1.2. All joint inversions, regardless of the porosity distribution or middle layer thickness, produced an RMS_{GV} value never greater than 0.7. This is an over fit of the gravity data and occurs as the joint inversion does not distinguish between data types, thus making it unaware that it is systematically over or under fitting one of the data sets.

Figure 7.28 shows an example of the decreasing and negative porosity anomaly distributions for middle layer thicknesses of 2.0 km and 3.0 km. The joint inversion results contain minimal artifacts, whereas the MT inversions alone exhibit significant

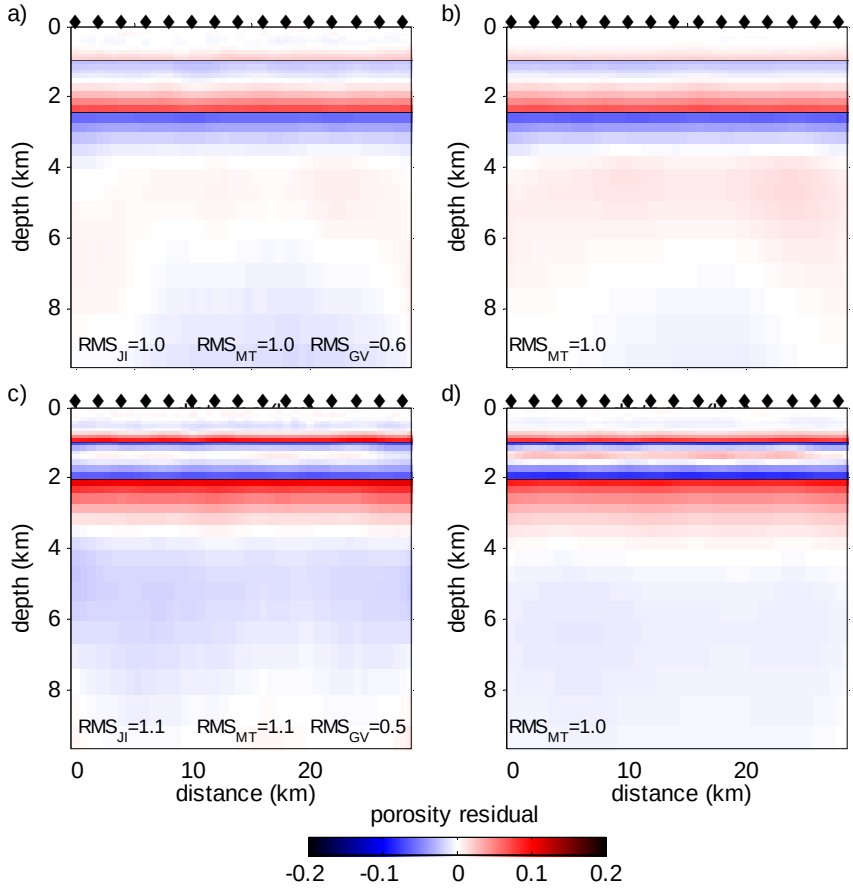

Figure 7.27: The porosity residual models for the layered model synthetic data with an MT error of 2% and gravity error of 0.06 mGals. a) joint inversion of an increasing porosity distribution and a middle layer thickness of 2.5 km. b) MT inversion of an increasing porosity distribution and a middle layer thickness of 2.5 km. c) joint inversion of a positive anomaly porosity distribution and a middle layer thickness of 2.0 km. d) MT inversion of a positive anomaly porosity distribution and a middle layer thickness of 2.0 km. The porosity residual models are generated by subtracting the synthetic model from the joint inversion model or the MT model converted to a porosity model using Archie's Law.

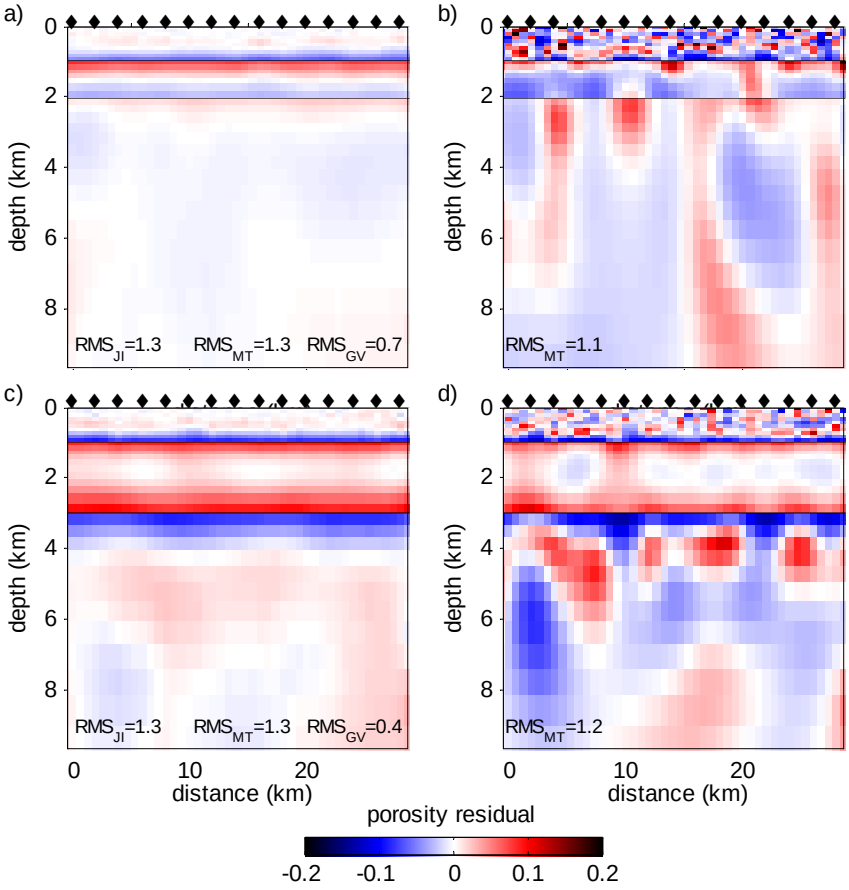

Figure 7.28: The porosity residual models of the layered model synthetic data with an MT error of 2% and gravity error of 0.06 mGals. a) joint inversion of a decreasing porosity distribution and a middle layer thickness of 2.0 km. b) MT inversion of a decreasing porosity distribution and a middle layer thickness of 2.0 km. c) joint inversion of a negative anomaly porosity distribution and a middle layer thickness of 3.0 km. d) MT inversion of a negative anomaly porosity distribution and a middle layer thickness of 3.0 km. The porosity residual models are generated by subtracting the synthetic model from the joint inversion model or the MT model converted to a porosity model using Archie's Law.

artifacts. The MT images have lateral boundaries, but the gravity response does not contain any information supporting any such lateral features. Therefore the presence of the gravity data in the joint inversion discourage against finding lateral boundaries.

Figure 7.27 shows inversion results for the increasing and positive anomaly porosity distributions for middle layer thicknesses of 2.5 km and 2.0 km. This figure shows that the models produced by the MT and joint inversions are smooth, artifact free and almost identical while having similar RMS values. The similarities are due to the gravity data discriminating against the artifacts in the joint inversion and the MT inversion reaching an RMS of 1, thus being able to produce the smoothest possible model with this RMS.

Since the MT and joint inversions produce very similar models, it can be concluded that the joint inversion does not aid in improving vertical resolution. The vertical resolving capacity of the MT and joint inversions is dependent on the signal contained in the MT data. A benefit of the joint inversion in a layered environment is that the gravity data discriminate against lateral features and aid in delineating resistivity structures.

Horizontal Resolution

A model comprising of two isolated boxes in a uniform background (see Figure 7.22c) was used to test and compare the horizontal resolution of the MT and joint inversions. The two boxes are of dimensions 4 km by 4 km, with their top boundary located at a depth of 1 km. A series of eight models were constructed by varying the horizontal separation between the two boxes. The first model has the two boxes situated next to each other (touching), the next one has them 0.7 km apart. Subsequent models increase the separation by increasing increments of 1.35 km until they are separated by 8.7 km.

Table 7.3 lists the porosity values used for the two boxes and the background and are based on a porosity contrast of 6% and 20%. There were three porosity distributions tested, referred to as positive anomaly, negative anomaly and opposite anomaly. Once again, the parameters in Archie's Law and the porosity-density

Table 7.3: The density, resistivity and porosity values used in the inversion of the two box model for different porosity distributions.

6% porosity configuration:	negative anomaly	positive anomaly	opposite anomaly	
			negative box	positive box
background ϕ	0.16	0.10	0.16	
box ϕ	0.10	0.16	0.10	0.22
background ϱ (Ωm)	12.9	33.0	12.9	
box ϱ (Ωm)	33.0	12.9	33.0	6.8
background ρ (kgm^{-3})	2390.8	2488.0	2390.8	
box ρ (kgm^{-3})	2488.0	2390.8	2488.0	2293.6
20% porosity configuration:	**negative anomaly**	**positive anomaly**	**opposite anomaly**	
			negative box	**positive box**
background ϕ	0.30	0.10	0.15	
box ϕ	0.10	0.30	0.10	0.30
background ϱ (Ωm)	3.7	33.0	14.7	
box ϱ (Ωm)	33.0	3.7	33.0	3.7
background ρ (kgm^{-3})	2164.0	2488.0	2407.0	
box ρ (kgm^{-3})	2488.0	2164.0	2488.0	2164.0

relationship were fixed with depth and were $a = 1$, $m_{cf} = 2$, $S = 1$, $n_s = 2$, $\varrho_{fluid} = 0.33$ Ωm, $\rho_{matrix} = 2650$ kgm^{-3} and $\rho_{fluid} = 1030$ kgm^{-3}. Using these values, the corresponding resistivity and density values for the two box models were calculated and are given in Table 7.3. For each porosity distribution, the MT and gravity data were calculated at fifteen stations with a station spacing of 2 km. As with the target contrast investigation (Section 7.4.1), the MT and gravity data were generated at the same stations, with the gravity error set at 0.06 mGals and the MT error 2%.

All the MT inversions which were based on a contrast of 6% had an RMS of 1, which allows the inversion to produce the smoothest possible model free of artifacts. The joint inversion models are also free of artifacts and have an RMS$_{JI}$ of 1. Figure 7.29 shows the joint inversion and MT residual models for a contrast of 6%, where the two boxes are 6.0 km apart. The recovered joint inversion and MT models are similar.

The MT and joint inversions for the models with a 20% contrast and having opposite and positive anomaly distributions all reach an RMS of 1. The negative anomaly porosity distribution contains resistive features to which the MT technique is less sensitive. The MT and joint inversions for these models never reach an RMS

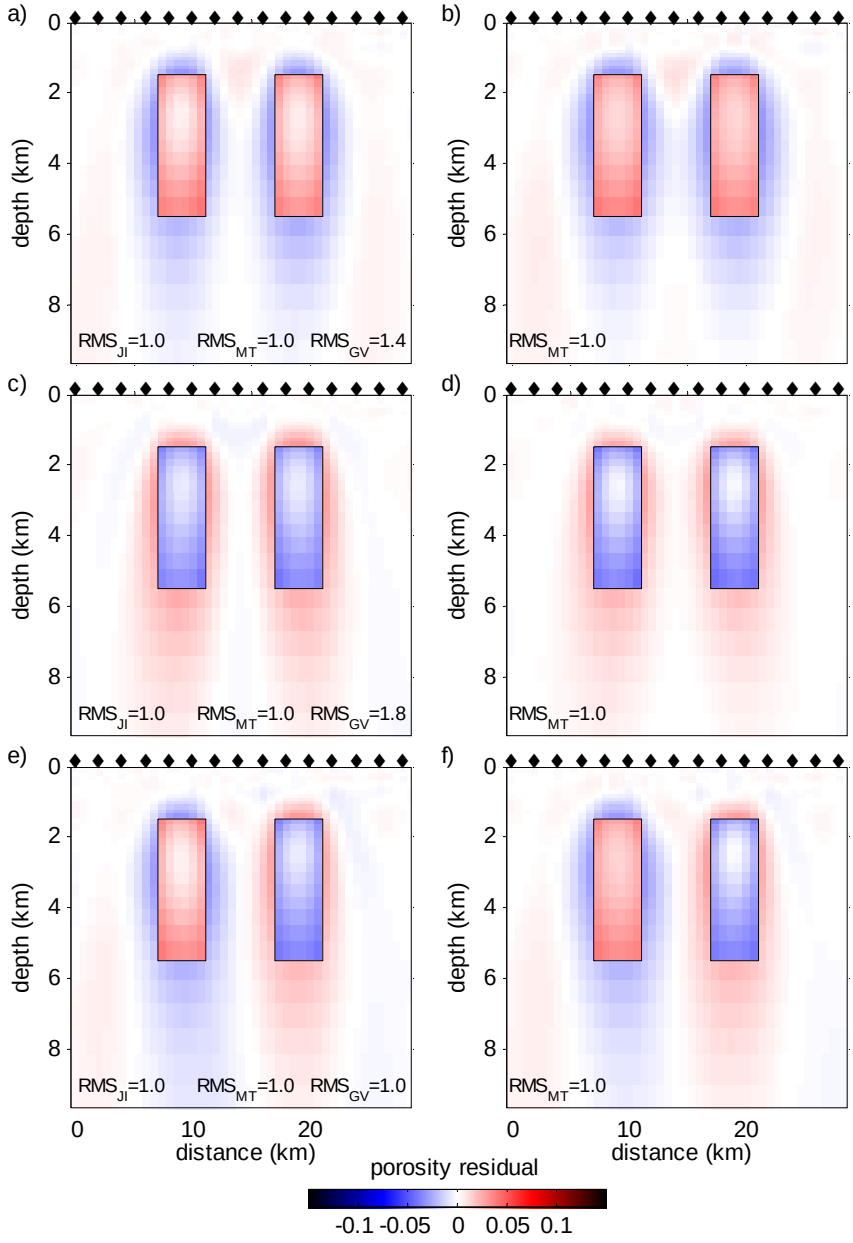

Figure 7.29: The porosity residual models for a joint inversion, with an MT error of 2% and gravity error of 0.06 mGals, for the two box model synthetic data with a) a 6% negative contrast, c) a 6% positive contrast and e) an opposite porosity distribution and a contrast of 6%. The porosity residual models of an MT inversion, with an error of 2%, for the two box model synthetic data with b) a 6% negative contrast, d) a 6% positive contrast and f) an opposite porosity distribution and a contrast of 6%. All models have the separation distance between the two boxes at 6.0 km. The porosity residual models are generated by subtracting the synthetic model from the joint inversion model or MT model converted to a porosity model using Archie's Law.

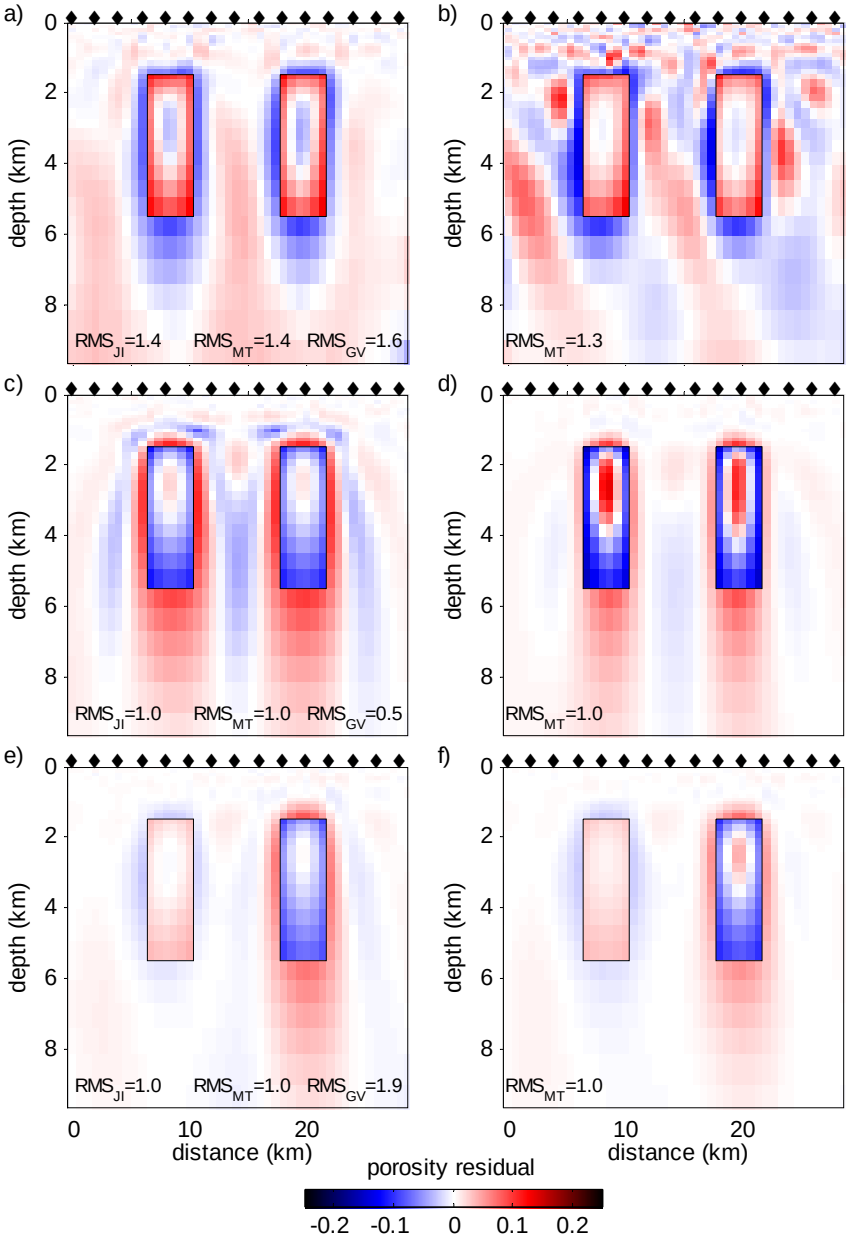

Figure 7.30: The porosity residual models for a joint inversion, with an MT error of 2% and gravity error of 0.06 mGals, for the two box model synthetic data with a) a 20% negative contrast, c) a 20% positive contrast and e) an opposite porosity distribution and a contrast of 20%. The porosity residual models of an MT inversion, with an error of 2%, for the two box model synthetic data with b) a 20% negative contrast, d) a 20% positive contrast and f) an opposite porosity distribution and a contrast of 20%. All models have the separation distance between the two boxes at 7.3 km. The porosity residual models are generated by subtracting the synthetic model from the joint inversion model or the MT model converted to a porosity model using Archie's Law.

less than 1.3. Figure 7.30 shows the MT and joint inversion results for the three porosity distributions when the two boxes are separated by 7.3 km.

The MT and joint inversion models for the opposite porosity distribution (Figures 7.30e and 7.30f) are very similar, except the MT model over-estimates the positive contrast box. The MT model of the positive configuration (Figure 7.30d) has tighter lateral boundaries than the joint inversion model (Figure 7.30c). However, the MT model over-estimates the box porosity values more than the joint inversion, but the joint inversion undershoots the background porosity values. For the negative porosity distribution, the MT inversion result (Figure 7.30b) is contaminated with artifacts, whereas the joint inversion image (Figure 7.30a) is smoother. The MT inversion results can be improved by performing a 20% relaxation but this will result in a model that has an RMS higher than the joint inversion.

In general the joint inversion and the MT inversion, with or without a 20% relaxation (depending on the model), produce similar results for the series of 8 synthetic models for a given contrast and porosity distribution. This is a similar result to the vertical resolution investigations and reinforces that joint inversions are dependent on the signal contained in the MT data and therefore have similar resolution characteristics to a single MT inversion.

7.4.3 Target Contrast and Resolution Summary

The joint inversion cannot recover a smaller contrast anomaly than the MT inversion, nor does it have better horizontal or vertical resolution. For optimum results, the joint inversion requires that there is a signal recognisable anomaly of the subsurface features in both the MT and gravity data sets. Therefore, if the anomaly is in the MT response, then the MT inversion will be able to represent the feature. However, where the joint inversion can be beneficial is in reducing artifacts, imaging resistive structures and improving the clarity of the subsurface features.

7.5 Conclusions

The joint inversion scheme is effective in reconstructing a reasonable image of the subsurface structure. It produces a more accurate image than an MT inversion alone with a target RMS of 1 and has a lower RMS than an MT inversion which tries to improve the image through relaxing the RMS value. However, the joint inversion cannot produce structure that is not reflected as signal (anomaly) in the MT or gravity data sets. Therefore, the minimum contrast and the resulting vertical and horizontal resolution that the joint inversion can achieve is very similar to that of the single technique MT inversion. For the best joint inversion results the MT and gravity errors should be small; however small gravity errors can aid in producing coherent models from very noisy MT data.

Chapter 8

Sensitivity and Related Issues

This chapter continues the investigation and discussion of synthetic data inversions but concentrates attention on the primary question of sensitivity. The aim is to examine the sensitivity functions for gravity and MT and determine how they differ in the subsurface. A critical issue to examine is the compatibility between the two techniques in a joint inversion. Also investigated are different weighting approaches to combining the two data sets and to understand the consequences on the joint inversion of using incorrect parameters in the petrophysical relationships that unite the two techniques. In this chapter the following issues are examined:

1. Compatibility and Sensitivity – determines when the MT and gravity techniques are compatible and what areas of the subsurface they are sensitive to; in doing so a new method for evaluating MT sensitivities is developed.

2. Validity of Petrophysical Relationships – looks at the ramifications of having incorrect parameters in Archie's Law and the porosity-density relationship.

3. Differential Weighting – evaluates two different weighting approaches and determines if they can improve the balance between fitting the MT and gravity data sets.

8.1 Compatibility and Sensitivity

The compatibilities and sensitivities of the MT and gravity techniques are investigated in this section. Firstly, the sensitivity analysis and evaluation of the compatibility between broadband MT and gravity data are explained. Secondly, the difference between using long period and broadband MT data in the joint inversion is examined. An investigation into the cause of the high RMS_{GV} value obtained for the trough model in Section 7.1 is then performed. Finally, incompatibilities between the MT and gravity data due to different subsurface structures are investigated.

8.1.1 Jacobian Matrix Analysis

The Jacobian or sensitivity matrix $\mathbf{J}$ is a $q \times n$ matrix, where q is the number of data points and n is the number of model parameters. The matrix elements are the Fréchet derivatives of the model response with respect to the model parameters. The Jacobian matrix was introduced through a Taylor series expansion of the differentiated objective function in Section 3.1.1 and is used to update the model parameters with each iteration. An alternate and complementary use for the Jacobian matrix is in a formal sensitivity analysis. The sensitivity analysis aims to determine what model features the data is most sensitive to and what is the depth of investigation. In this section the Jacobian is used in a sensitivity analysis to compare the MT and gravity sensitivities of the joint inversion.

The Jacobian matrix in a joint inversion contains information about both the MT and gravity techniques. It depends not only on the assumed (or current) subsurface model, but also on the station distribution and form of recorded data. The first p rows of the Jacobian correspond to the MT technique and the last s rows correspond to the gravity technique, where p is the number of MT data points and s is the number of gravity data points. In the joint inversion the Jacobian matrix is expressed in terms of porosity and not explicitly resistivity or density. In Section 6.2.1 the corrections that needed to be made to the original MT and gravity Jacobian matrices in order to produce a combined Jacobian in terms of porosity were outlined. These corrections involved multiplying the elements of the gravity Jacobian by a constant

value, whereas the MT correction was dependent on the corresponding porosity model. The corrections outlined in Section 6.2.1 were undone in order to remove the dependence of the Jacobian on the porosity model and the Jacobian matrices are once again expressed in their original form. For this analysis the MT Jacobian refers to the first p rows of the joint inversion Jacobian that have been uncorrected to give a change in the model response due to resistivity. The gravity Jacobian refers to the last s rows of the joint inversion Jacobian that have been uncorrected to the change in model response due to absolute density.

The MT Jacobian is a very large matrix which can make interpretation difficult. To help with interpretation, there are currently two methods used by the MT community for viewing the MT Jacobian. The first method uses the WinGLink program and computes the pseudo Hessian matrix $\mathbf{J}^T\mathbf{W}_d^{-1}\mathbf{J}$, where $\mathbf{W}_d$ is the data weighting matrix that contains the estimated individual data point standard deviations [169]. The second method, presented by Schwalenberg *et al.* [170], is a cumulative type of sensitivity for all measurements and is given by

$$SA_j = \frac{1}{A_j}\sum_{i}^{q}\left\|\frac{1}{\sigma_i^*}J_{ij}\right\| \quad , \tag{8.1}$$

where SA_j is the sensitivity of the jth model parameter, A_j is the cross-sectional area of the cell corresponding to the jth parameter, σ_i^* is the standard deviation of the ith data point and J_{ij} is the Fréchet derivative between the ith model response point and jth model parameter expressed as resistivity. The resulting vector contains the sensitivity information for each model parameter and can then be viewed on the same grid as the model. The Schwalenberg *et al.* method was chosen for this Jacobian analysis because it is computationally simple and accounts for the size of the model cells.

The individual elements of the MT Jacobian can be positive or negative, corresponding to positive or negative sensitivity. A negative sensitivity implies that a positive perturbation (small increase) in the model parameter leads to a decrease in the observed or measured value, or a small decrease in the model parameter causes an increase in the recorded quantity. Conversely, a positive sensitivity implies that a positive perturbation in the model parameter causes an increase in the measured

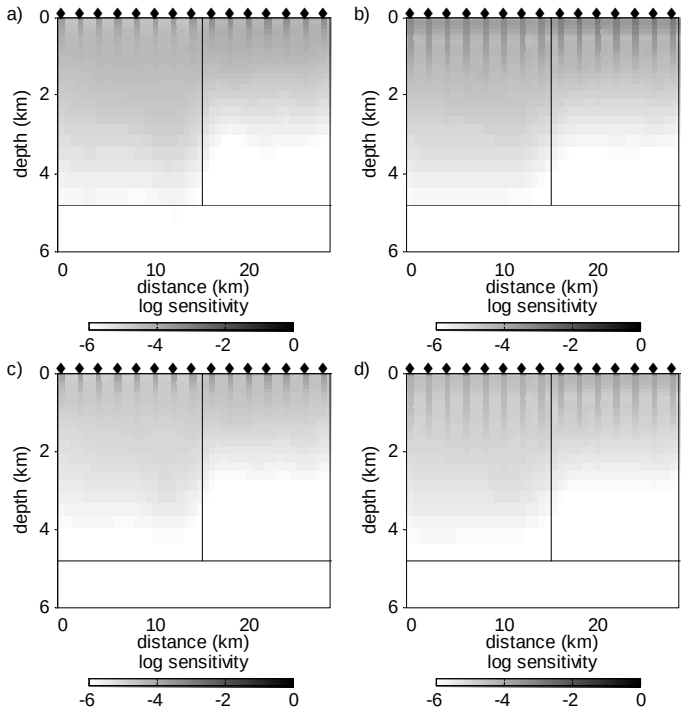

Figure 8.1: The MT sensitivity distribution broken into its components of a) TE apparent resistivity, b) TM apparent resistivity, c) TE phase and d) TM phase, for the joint inversion of the fault model synthetic data with an MT error of 2% and a gravity error of 0.06 mGals.

quantity, or a negative perturbation (small decrease) in the model parameter causes a decrease in the measured quantity. In the analysis given here, only the absolute values of each element in the Jacobian will be used, as changes in the model response, regardless of direction, are of concern. Secondly, the MT technique has a non-linear forward model operator. As a result, the first order Taylor series expansion is used to linearise the forward model operator about a particular model (Section 3.1.1). This a way of introducing and defining the Jacobian matrix and means that the MT Jacobian analysis only holds true for models in and around the model that has been used in the linearisation process. Even so, the Jacobian analysis can still provide valuable information, although its shortcomings should be kept in mind.

When evaluating Equation 8.1, different elements of the Jacobian matrix can be used and the sensitivity plot can be obtained for different frequencies, stations and the different MT modes. Figure 8.1 shows the sensitivity plots for the apparent resistivity and phase of the TE and TM modes, using the fault model of Figure 7.1.

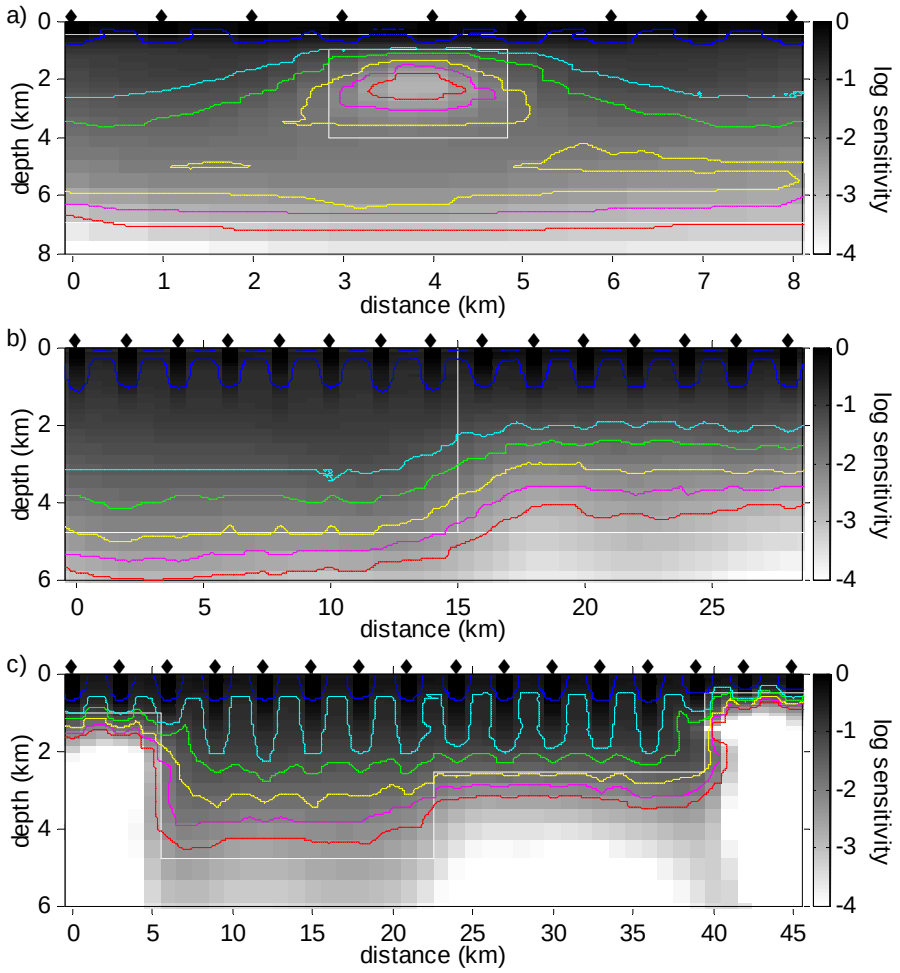

Figure 8.2: The MT sensitivity distribution for the a) block model, b) fault model and c) trough model, with data change isoclines drawn, where blue = 1 Ωm, cyan = 5 Ωm, green = 10 Ωm, yellow = 25 Ωm, magenta = 50 Ωm and red = 100 Ωm. All models are from a joint inversion of broadband MT data with an error of 2% and gravity error of 0.06 mGals.

The amplitude of the apparent resistivity sensitivity is approximately an order of magnitude larger than the phase sensitivity. Also, the TM mode has a greater sensitivity to the boundaries whereas the TE mode has a greater sensitivity to the resistivity value [171]. All the different components of the sensitivity contribute to the total sensitivity of the MT method, but due to differences in their magnitudes this might not be evident in the total sensitivity model [170]. Therefore, each of the components is normalised by its maximum value so that the values range between 0 and 1. The normalised components are then summed to give the total sensitivity model, as shown in Figure 8.2b. In this figure, parts a) and c) also display the

sensitivities for the block and trough models of Chapter 7.

It is difficult to place the sensitivity values into a context that is easily understood. There has been much conjecture as to what sensitivity value delineates the model parameter threshold for which the data are no longer sensitive. This problem is then compounded by the normalisation of the MT component. Schwalenberg *et al.* [170] used the 10^{-4} isoclines as the depth of investigation threshold. However, in this thesis a new method is presented based on the Taylor series expansion, to place the sensitivity values into a more readily digestible form. Formally, one can write out the Taylor series to the first order,

$$\mathbf{F}[\mathbf{m_1} + \Delta\mathbf{m}] = \mathbf{F}[\mathbf{m}_1] + \mathbf{J}_1\Delta\mathbf{m} \quad , \tag{8.2}$$

to obtain the expected data for a perturbation in the model space $\Delta\mathbf{m}$. Here $\mathbf{F}$ is the MT forward model operator, $\mathbf{m}_1$ is the model about which the forward model operator is linearised (for this analysis it is the final joint inversion porosity model which has been converted to a resistivity model), and $J_1 = \left(\frac{\partial F}{\partial m}\right)_{m_1}$ is the MT Jacobian that corresponds to $\mathbf{m}_1$. Equation 8.2 can then be rearranged to give

$$\mathbf{J_1}\Delta\mathbf{m} = \mathbf{F}[\mathbf{m}_1 + \Delta\mathbf{m}] - \mathbf{F}[\mathbf{m}_1] \quad . \tag{8.3}$$

Equation 8.3 shows that the Jacobian multiplied by a small perturbation in the model space equals the change in the model response due to this small perturbation.

The method presented here changes one of the model parameters by a small amount, δm, which corresponds to a $\Delta\mathbf{m}$ vector of all zeros except for the element which was changed by δm. The Jacobian and $\Delta\mathbf{m}$ are then multiplied to give the change in model response due to the small change in the model. The number of data points is then counted for which the change in the model response is greater than the data error. This is repeated for a change in each model parameter and a picture such as Figure 8.3 can be obtained. Figures 8.3a and 8.3d are actual counts for each parameter (model cell) of how many data points will change by an amount greater than their estimated error (uncertainty), if the parameter is changed by 10 Ωm and 100 Ωm, respectively. Strictly speaking the size of the perturbation

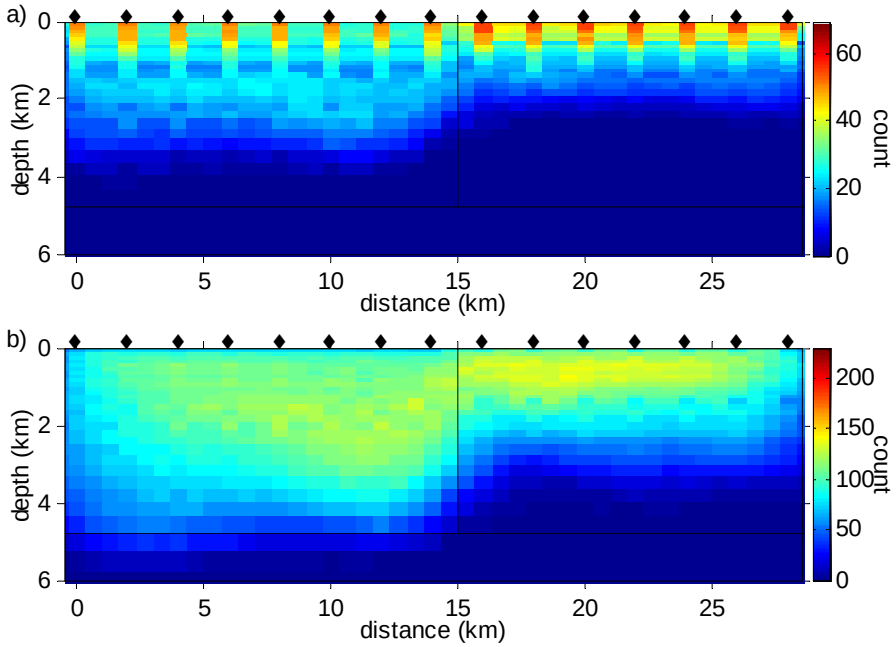

Figure 8.3: Data count distributions for the joint inversion of the fault model synthetic data with an MT error of 2% and gravity error of 0.06 mGals. Each subsurface cell is coloured according to the count, which represents the number of MT data points that would be increased above their error level if the model space parameter at this location is changed by a) 10 Ωm and b) 100 Ωm.

should be infinitesimally small, however an approximation is sought using larger values to obtain a greater understanding of the behaviour of the sensitivities.

Once a plot such as Figure 8.3 is produced, the isoclines for one data point change can be transferred to the sensitivity plot. The isoclines for a different number of data point changes can also be used. The process described above can be repeated for different small perturbation values. Here, the small perturbation values of 1, 5, 10, 25, 50 and 100 Ωm were used and are shown in Figure 8.2b for the fault model. By placing these isoclines on the sensitivity model it gives an indication of what level of change is required in the model to affect the data. Like the Jacobian, the isoclines of the data change can be generated for different frequencies, stations and MT modes by isolating the corresponding part of the Jacobian.

Figure 8.2 shows the block, fault and trough model MT sensitivity plots for the joint inversion with an MT error of 2% and gravity error of 0.06 mGals. From these figures it can be seen that the MT sensitivity plot is highly dependent on the

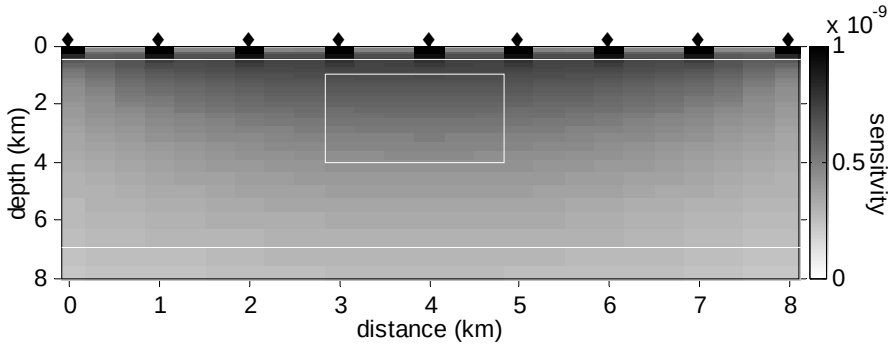

Figure 8.4: The gravity sensitivity distribution for the block model from a joint inversion of broadband MT data with an error of 2% and a gravity error of 0.06 mGals.

corresponding final joint inversion model. High sensitivity values occur in conductive zones (high porosity), such as the shallow features of the models. These areas also require less change in the resistivity value to cause a change in the data. The sensitivity values are low in zones of high resistivity (low porosity), such as the basement and the embedded block anomaly. They also require a far greater change in the resistivity value to produce a change in the data. The block, fault and trough models have a station spacing of 1, 2 and 3 km, respectively. Comparing the sensitivity plots, it can be observed that sensitivity between stations decreases as the station spacing increases. This should be considered when planning field surveys.

The gravity forward model operator is linear, which means that the Jacobian multiplied by density gives the model response. As explained in Section 4.2.1, the gravity Jacobian remains fixed for each iteration of the inversion. Figure 8.4 shows the gravity sensitivity plot for the block model. Like the MT sensitivity plots, it too was produced using the Schwalenberg *et al.* method [170]. Each gravity station has a sensitivity that reduces at a rate inversely proportional to the distance squared in all directions away from the station. Therefore, when all station sensitivity responses are summed, the result is Figure 8.4, which shows a central region of higher sensitivity due to the overlap of sensitivity from each station.

Since the values in the gravity sensitivity plot have been corrected for cell size, Figure 8.5 shows the reduction in sensitivity with depth for different sized cells or blocks. Figure 8.5a is a plot of the gravity sensitivity versus depth for rectangular

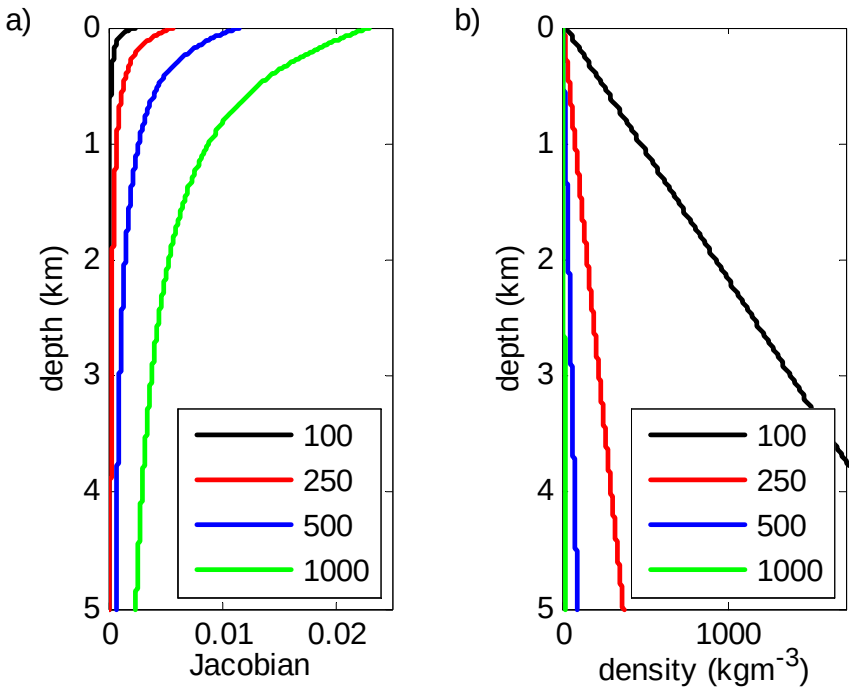

Figure 8.5: a) The gravity Jacobian values for 100×100, 250×250, 500×500 and 1000×1000 m rectangular blocks (sensitivity cells) as the top of the block increases with depth. b) The density contrast needed by the block at that depth in order to produce a change in the gravity data greater than 0.06 mGals. Note that the block extends infinitely in the strike direction.

blocks of dimension 100×100, 250×250, 500×500 and 1000×1000 m (note that for 2D models, the block extends to infinity in the strike direction). The Jacobian value is clearly dependent on the size of the block, where the larger the block the higher the sensitivity value. However, the behaviour of the sensitivity is similar for all sized blocks and reduces rapidly in the shallower part of the section (< 2 km) before starting to approach zero. Figure 8.5b shows the density perturbation (contrast) required in each block size as a function of depth to produce a model response greater than 0.06 mGals. For a block of size 100×100 m, the density values required at depth are unrealistically high. For the larger sized blocks, the change in density ranges from < 45 kgm^{-3} at 0.5 km to < 370 kgm^{-3} at 5 km.

The MT and gravity Jacobians, and the subsequent sensitivity plots, show a significantly different range of values. The gravity sensitivity values are approximately 2 orders of magnitude smaller than the MT sensitivity values. This is a reflection of

the differences in the actual physical quantities (resistivity versus density) and the type and range of the measured quantity (gravity varies by mGals whereas apparent resistivity can vary by an order of magnitude). A bias towards the MT technique can result from it having larger sensitivity values [172]. As discussed in Section 7.1, such a bias towards the MT technique has been observed. Until now, the bias towards fitting the MT data has been attributed to the greater number of MT rather than gravity data points, although the variations in Jacobian values would also be a contributor.

Aside from differing magnitudes for the MT and gravity sensitivity values, the MT and gravity sensitivity distributions appear to be compatible, and the main zones of enhanced sensitivity coincide. For the present investigation, the MT data correspond to a broadband frequency range. In the next section the effects of using only long period MT data in the joint inversion are examined.

8.1.2 Broadband vs. Long Period MT Data

Until now, all MT data have occupied the frequency range 1000 to 0.01 Hz. Instead of using broadband data, the long period data in the range 0.1 to 0.001 Hz is inverted in this section. Synthetic data are then generated in this range for all three models-block, fault and trough. Joint and MT inversions are then executed with the long period data. The joint inversion used the same gravity data as in the broadband joint inversions. The error levels used were various combinations of an MT error of either 2, 4 or 6% and a gravity error of 0.03, 0.06, 0.1, 0.3 or 0.5 mGals.

Figure 8.6 shows the results of the MT inversion with long period data having an error of 2% and using a 20% relaxation. These three diagrams correspond to the three different models and are comparable to the broadband inverted models in Figures 7.4b, 7.5b and 7.6b. The long period models have slightly higher RMS values than their broadband counterparts, but have fewer artifacts. The long period inverted block model does not delineate the unconsolidated zone and the porosity-compaction trend appears lower than the original. The top boundary of the block anomaly is indistinct and rather subjective, even though there is a fuzzy gradation, while the bottom boundary of the embedded block is indistinguishable from the

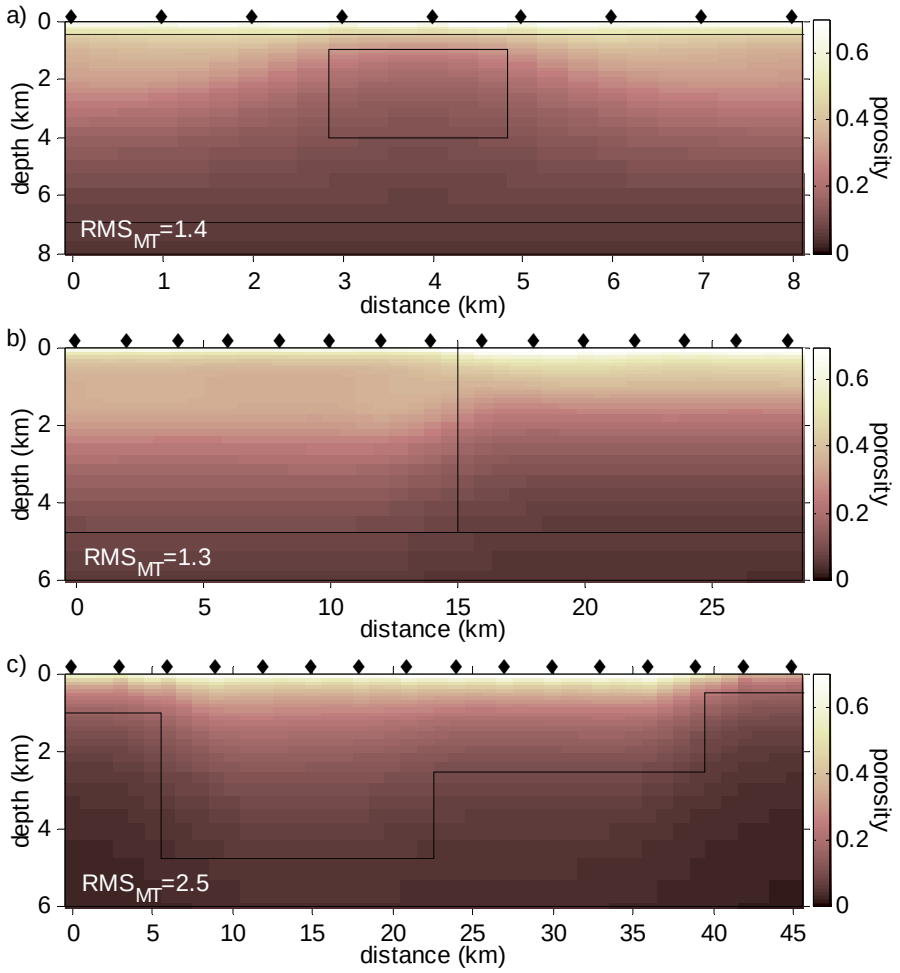

Figure 8.6: The models produced from an MT inversion of long period MT data with an error of 2% for synthetic data produced from the a) block, b) fault and c) trough models. These models have been converted to a porosity model using Archie's Law.

basement. The side boundaries of the block are hard to determine and appear to widen with increasing depth.

The long period fault inverted model shows an incorrect porosity-compaction trend. Instead of porosity values only increasing with depth, the porosity values are too low in the top 3 km of the model. However, the sharpness of the boundary between the two compaction trends is similar to the broadband inverted model. The long period inverted trough model is a very poor representation of the original synthetic model. The porosity-compaction trend is too low and the basement boundaries are difficult to delineate.

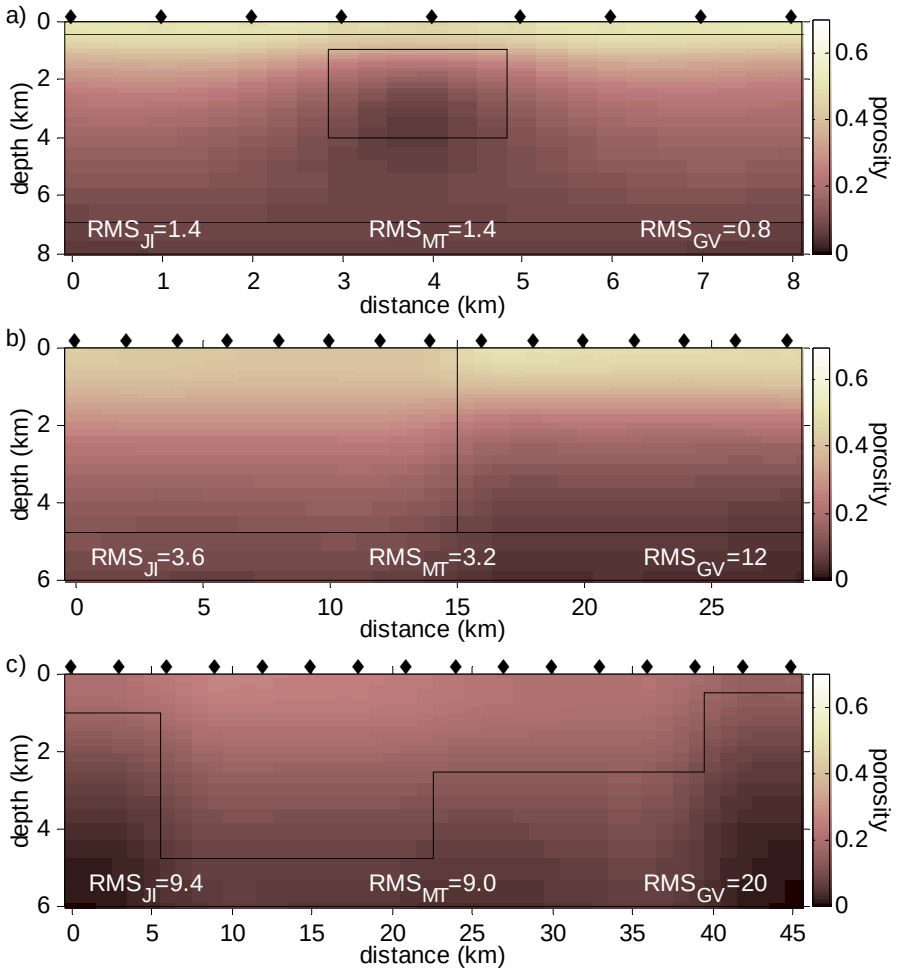

Figure 8.7: The models produced from a joint inversion of long period MT data with an error of 2% and the gravity data with an error of 0.06 mGals for synthetic data produced from the a) block, b) fault and c) trough models.

Combining the long period MT data with the gravity data in a joint inversion improves some of the drawbacks discussed above for the block and fault models. Figure 8.7 shows the joint inversion results for the block, fault and trough models in which the assumed MT data error is 2% and the gravity data error is 0.06 mGals. The unconsolidated zone in the block model is still not well defined but the porosity-compaction trend is clear below 2 km. The clarity of the top and side boundaries of the embedded block anomaly have improved, although the bottom boundary remains indistinct. The compaction trends in the inverted fault model now only increase with depth, although the upper 2 km shows incorrect porosity values. There is no improvement in the inverted trough model, which can be attributed to the model

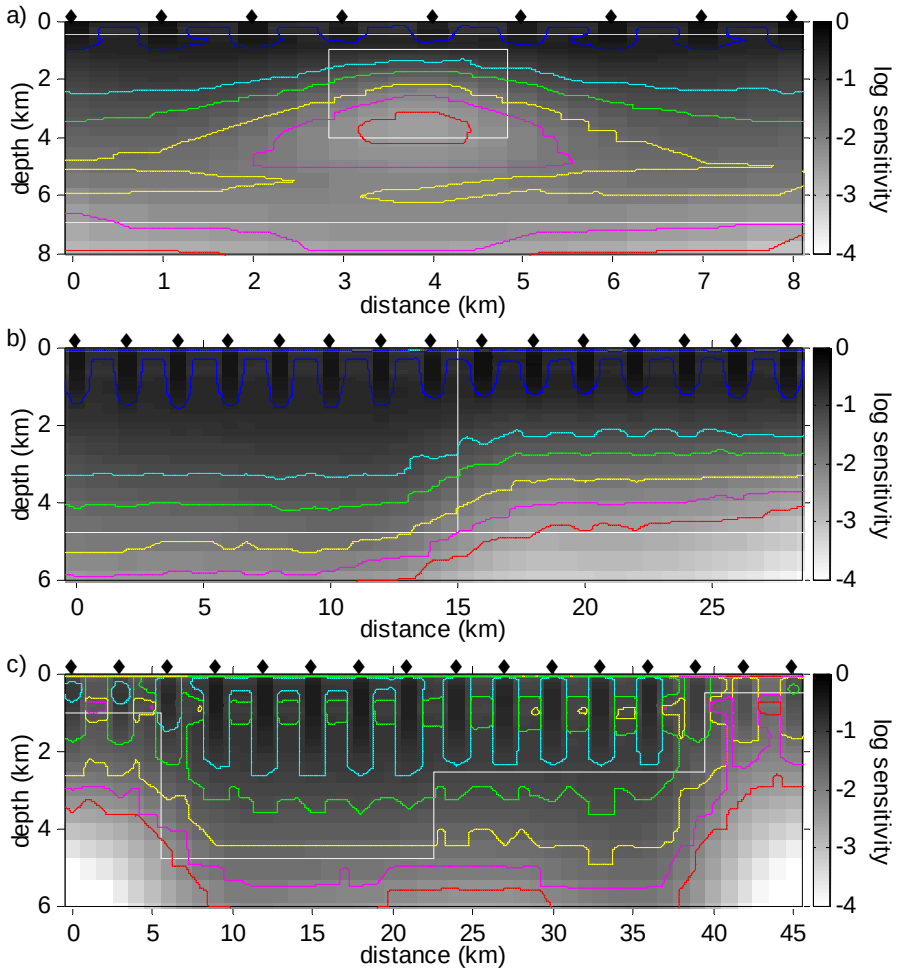

Figure 8.8: The MT sensitivity distribution for the a) block model, b) fault model and c) trough model, showing data change isoclines, where blue = 1 Ωm, cyan = 5 Ωm, green = 10 Ωm, yellow = 25 Ωm, magenta = 50 Ωm and red = 100 Ωm. All models are from a joint inversion of long period MT data with an error of 2% and gravity data with an error of 0.06 mGals.

only reaching an RMS_{JI} of 9.4. In general, the long period data inversions struggle to reproduce the correct porosity values and cannot reconstruct the upper 2 km.

Figure 8.8 shows the MT sensitivity plots for the long period joint inversions. The sensitivity plots were produced in an equivalent manner to the broadband plots, however the maximum value used to normalise each component has been taken from the broadband analysis. This was done so that the sensitivity magnitudes in each case are comparable. Before comparing the broadband and long period sensitivity plots, it is important to remember that the MT Jacobian is dependent on the final joint inversion model. As a result, the block model which does not define

the embedded anomaly, yields a sensitivity which is not insignificant in this region. Also, the trough model which is inaccurately reconstructed produces a sensitivity plot which reflects this.

There are two main conclusions to draw in comparing the joint inversion MT sensitivity plots of the different MT data types (Figures 8.2 and 8.8). Firstly, as expected the long period data are sensitive to greater depths. Secondly, the long period data produce models that are incorrect in the top 2 km. The long period sensitivity plot shows high sensitivity in this zone, thus demonstrating that the simplified Jacobian analysis only shows what the data are sensitive to, and not what can be resolved. This means that the Jacobian analysis cannot be used to determine what each technique is resolving.

Long period MT data are sensitive to greater depths and have an inability to resolve features in the shallower part of the section. However, gravity data contain a strong signal of shallow features. When the long period MT and gravity data are combined in a joint inversion it results in an improved reconstruction of the shallow features. This suggests a potential benefit of joint inversion is that one technique could compensate where the other technique is poor. Although in this case, gravity is inherently non-unique and struggles to fully delineate the shallow features without the assistance of the MT data. Therefore, for optimal MT and gravity joint inversion results, broadband MT data are preferred over long period MT data.

8.1.3 Basement Imaging

In Section 7.1.3 it was found that the joint inversion for the trough model had a high misfit of the gravity data. This section investigates the potential cause of this problem and if it is related to a mismatch in the sensitivities of the MT and gravity techniques. For this investigation the trough model was simplified to no longer contain a step in its bottom boundary and the horizontal shallow side boundaries are at a depth of 0.5 km (see Figure 7.22d). Joint inversions were sequentially run with the bottom boundary of the trough at varying depths of 1.0, 2.1, 3.2, 3.9, 4.8, 5.9, 7.3 and 9.0 km, as indicated in Figure 7.22d. An MT error of 2% and gravity error of 0.06 mGals were used on each inversion.

Table 8.1: The density, resistivity and porosity values used in the inversion of the basement model for different porosity contrasts.

contrast	sediment ϕ	basement ϕ	sediment ϱ (Ωm)	basement ϱ (Ωm)	sediment ρ (kgm^{-3})	basement ρ (kgm^{-3})
5%	0.07	0.02	67.3	825.0	2536.6	2617.6
10%	0.12	0.02	22.9	825.0	2455.6	2617.6
20%	0.22	0.02	6.8	825.0	2293.6	2617.6
30%	0.32	0.02	3.2	825.0	2131.6	2617.6

A fixed porosity contrast with depth was used rather than a porosity-compaction trend. This was done to maintain the same porosity contrast between the sediments and the basement for all trough depths. Four porosity contrasts (5, 10, 20 and 30%) between the basement and sediments were tested and are listed in Table 8.1. The parameters used in Archie's Law and the porosity-density relationship were also fixed with depth and were set to $a = 1$, $m_{cf} = 2$, $S = 1$, $n_s = 2$, $\varrho_{fluid} = 0.33$ Ωm, $\rho_{matrix} = 2650$ kgm^{-3} and $\rho_{fluid} = 1030$ kgm^{-3}. This gives rise to the resistivity and density values for the sediments and the basement listed in Table 8.1.

A wide range of RMS$_{GV}$ values were found for the different porosity contrasts and trough depths investigated. For each contrast, the smallest RMS$_{GV}$ always occurs at a trough depth of 1.0 km. The largest RMS$_{GV}$ value occurs at different depths, depending on the porosity contrast, with the largest RMS$_{GV}$ value of 17 occurring at a trough depth of 3.9 km for a 30% contrast. The MT data fit had a much smaller range. For porosity contrasts of 5, 10 and 20%, the RMS$_{MT}$ value was generally less than 2.0, but for the 30% contrast the RMS$_{MT}$ values ranged from 1.6 to 4.1. The equivalent single MT inversions all had an RMS of 1, with the exception of the 30% contrast which had an RMS$_{MT}$ value between 1.3 and 1.6.

It was established in Section 8.1.1 that the gravity component of the joint inversion is sensitive to changes at shallow depth, or large changes of density with depth. Figures 8.9 and 8.10 show the sensitivity distributions for the MT component of the joint inversion for contrasts of 10% and 20%, respectively, with the four plots in each figure corresponding to trough depths of 1, 2, 4 and 7.5 km. These two figures show the progression of increased sensitivity with depth as the bottom of the trough becomes deeper. The reason is that the bottom boundary provides a discontinuity between the conductive sediments to which the MT technique is more sensitive, and

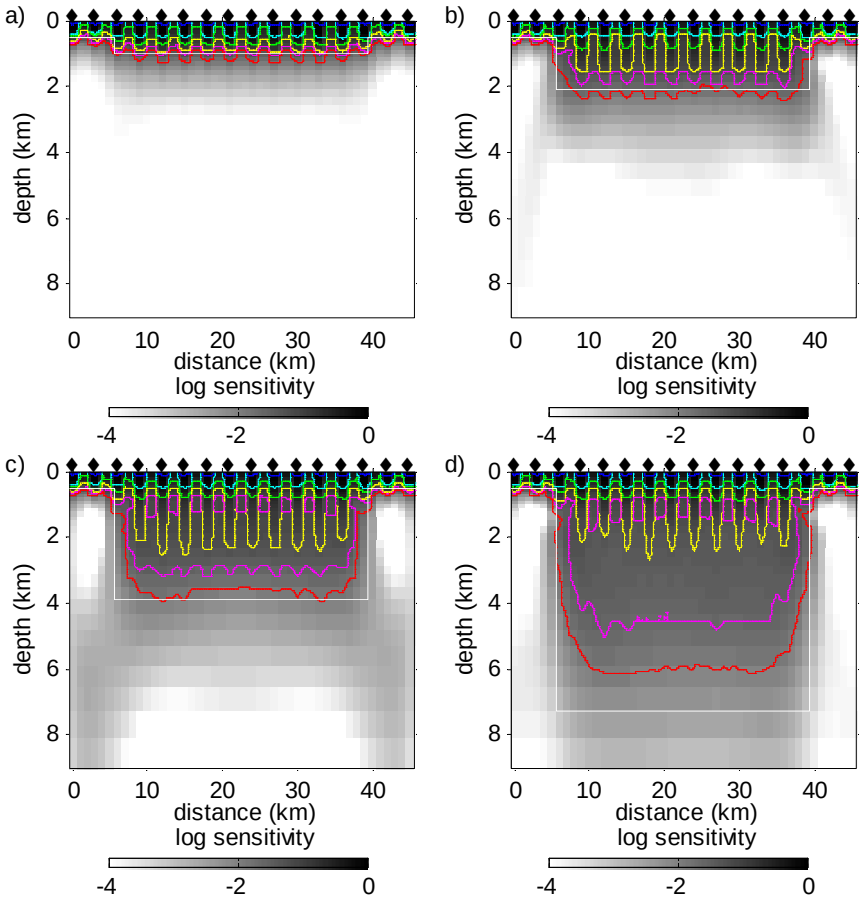

Figure 8.9: The MT sensitivity distribution for the basement model with a contrast of 5% and trough depths of a) 1.0 km, b) 2.1 km, c) 3.9 km and d) 7.3 km. Data change isoclines are indicated, where blue = 1 Ωm, cyan = 5 Ωm, green = 10 Ωm, yellow = 25 Ωm, magenta = 50 Ωm and red = 100 Ωm. All models are from a joint inversion of broadband MT data with an error of 2% and gravity data with an error of 0.06 mGals.

the resistive basement for which the MT technique is less sensitive. There is a point at which increasing the depth of the trough no longer corresponds to an increase in sensitivity with depth. This is indicative of EM attenuation, which is characterised by the skin depth.

There is no correlation between the trough depth and subsequent sensitivities and a large gravity misfit. Incompatibilities between the MT and gravity sensitivities, or their ability to detect and resolve the bottom boundary, are not the cause of the large RMS_{GV} values. The only correlation that exists in the RMS values of the joint inversions undertaken is the higher the contrast, the higher the gravity misfit.

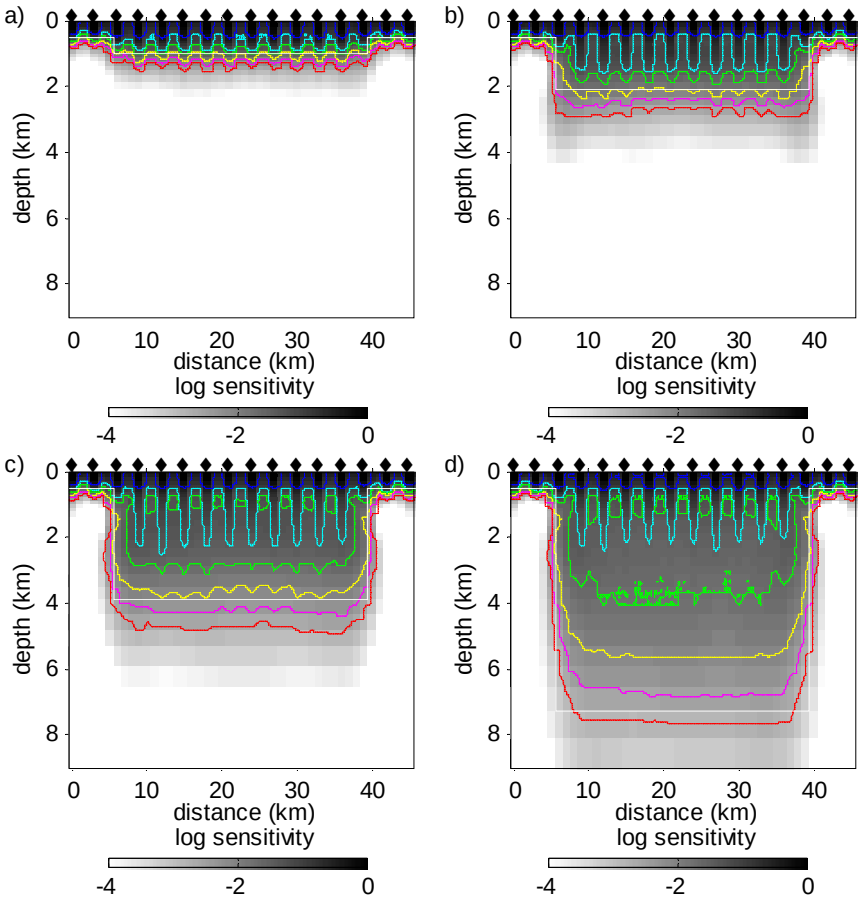

Figure 8.10: The MT sensitivity distribution for the basement model with a contrast of 20% and trough depths of a) 1.0 km, b) 2.1 km, c) 3.9 km and d) 7.3 km. Data change isoclines are indicated, where blue = 1 Ωm, cyan = 5 Ωm, green = 10 Ωm, yellow = 25 Ωm, magenta = 50 Ωm and red = 100 Ωm. All models are from a joint inversion of broadband MT data with an error of 2% and gravity data with an error of 0.06 mGals.

Figure 8.11 shows the computed gravity data for a model with a trough depth of 3 km and porosity contrasts of 5, 10, 20 and 30%. The higher the porosity contrast the larger the amplitude of the gravity response. The joint inversion seems to have difficulties in rectifying the higher amplitudes, which generally involves under-estimating the values situated over the trough. The behaviour could be caused by the smoothness constraint, which means the sharp side boundaries of the trough are not faithfully reconstructed and the smoothing of these boundaries results in an over-estimation of the porosity values.

The trough model in Section 7.1.3 has a gravity response with amplitude of

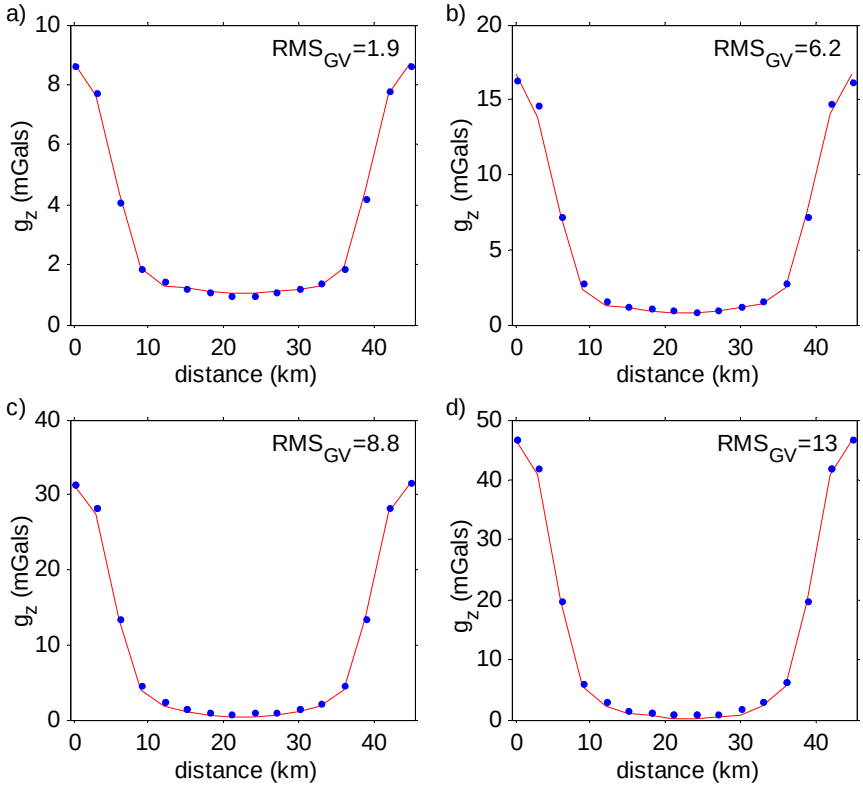

Figure 8.11: The gravity data (blue dots) and model responses (red line) for the basement model having a trough depth of 3.2 km and porosity contrasts of a) 5%, b) 10%, c) 20% and d) 30%. The model response is from a joint inversion of broadband MT data with an error of 2% and gravity data with an error of 0.06 mGals.

34 mGals. This amplitude is similar to a simplified trough model with a depth of 3 km and a contrast of 20%, as shown in Figure 8.11c. It is concluded that the cause of the large gravity misfit in the trough model is due to the inability of the joint inversion to reconstruct the large amplitude of the gravity data. Section 8.3 investigates the effectiveness of weighting the MT and gravity data sets to reduce the gravity data misfit.

8.1.4 Effects of Data Incompatibility

Joint inversions are based on the premise that the two techniques are sensing the same subsurface features. Therefore there is an intrinsic compatibility of signal between the MT and gravity data and the joint inversion only needs to seek one porosity model to satisfy both data sets. In this section the effect of an incompat-

Table 8.2: The MT and gravity synthetic data combinations for the surface, basement and composite models used in a joint inversion.

MT data	gravity data
composite	composite
basement	basement
surface	surface
basement	composite
composite	basement
surface	composite
composite	surface
surface	basement
basement	surface

ible signal in the MT and gravity data sets on the joint inversion is investigated. Although this is unlikely, unless the data sets were acquired in different locations, it is important to understand the complete behaviour of the joint inversion.

To investigate the effects of incompatible data on the joint inversion, MT and gravity data were generated for the three models shown in Figure 8.12. All models have sixteen recording stations with a station spacing of 5 km. They have a porosity-compaction trend appropriate for sandstone, which was determined using Athy's model with a surface porosity of 0.49 and a compaction coefficient of 270 m [163]. Figure 8.12a is referred to as the surface model and incorporates two anomalous blocks having their top located at the surface and a porosity value of 0.25. The right block is 10 km wide and has a bottom boundary at 1 km. The left block also has its bottom boundary at 1 km, but its left side boundary extends to infinity. The basement has no topography and is at a depth of 8.1 km. It has a porosity value of 0.03. Figure 8.12b is referred to as the basement model and has a 3.8 km step in the basement. The top horizon is located at a depth of 4.3 km and the bottom horizon is located at a depth of 8.1 km. Finally, Figure 8.12c is a combination of the surface and basement models and is referred to as the composite model.

Joint inversions were run for a series of data combinations generated from the different models. The data combinations used are listed in Table 8.2. For each of the data combinations, broadband MT data with a 2% error were combined with gravity data, which had an error of 0.06 mGals. The inherent bias in the joint inversion towards fitting the MT data means the models produced from the incompatible MT

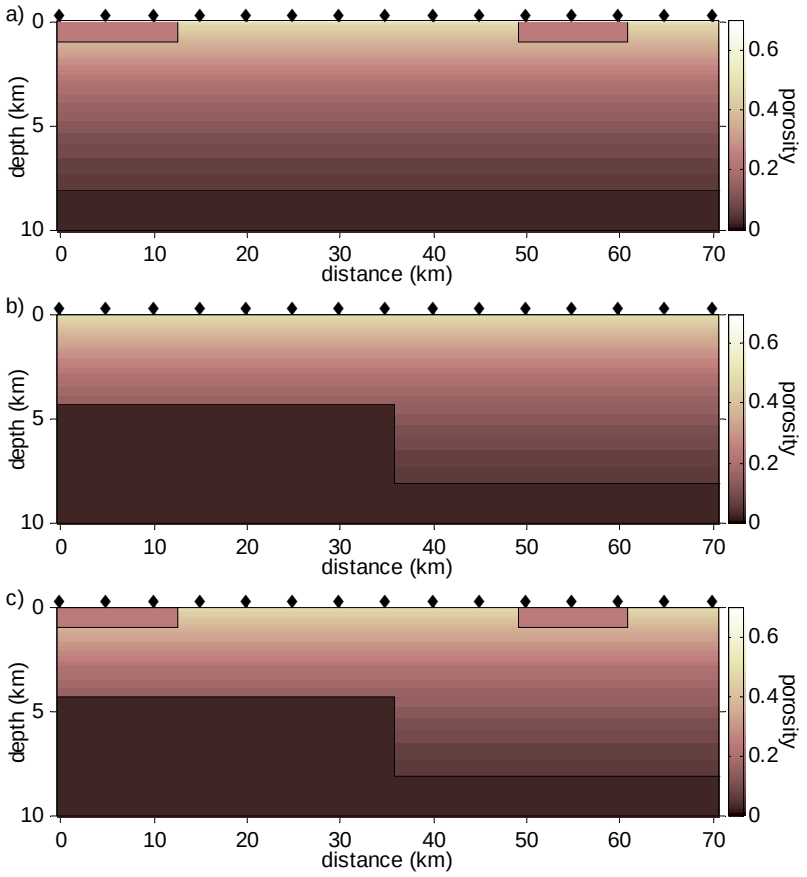

Figure 8.12: Synthetic porosity models referred to as the a) surface model, b) basement model and c) composite model.

and gravity data sets resemble the model from which the MT data are derived. An example of this behaviour is shown in Figure 8.13 for a joint inversion where the MT data corresponded to the surface model and the gravity data corresponded to the composite model. The bias towards fitting the MT data results in a large RMS_{GV} value and the RMS_{GV} value for the joint inversion of the different data combinations varied between 4.5 and 29.4, whereas the RMS_{MT} value only varied between 1.3 and 3.5. Incompatible data joint inversions have RMS values that are always higher than the equivalent compatible data joint inversion. Therefore high RMS values could be indicative of incompatible MT and gravity data sets.

Figure 8.14 shows the joint inversion model for the gravity data corresponding to the composite model and the MT data corresponding to the basement model. There appears to be a zone of slightly higher porosity values at depths (> 8 km)

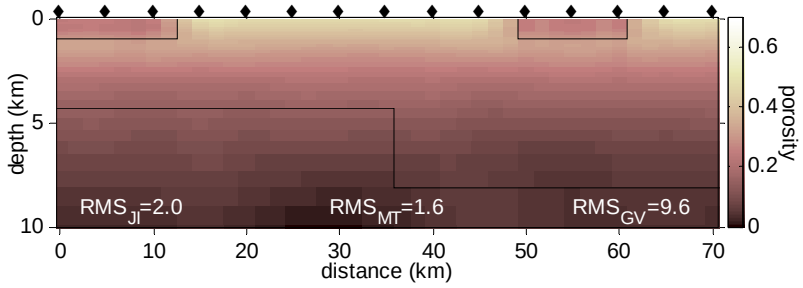

Figure 8.13: The models produced from a joint inversion, where the MT synthetic data were generated from the surface model and the gravity data were generated from the composite model. The gravity error was 0.06 mGals and the MT error was of 2%.

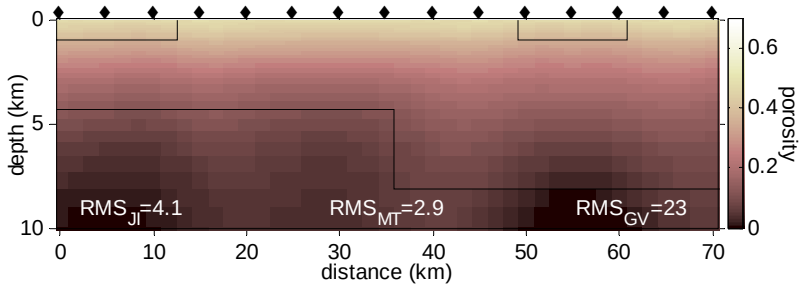

Figure 8.14: The models produced from a joint inversion, where the MT synthetic data were generated from the basement model and the gravity data were generated from the composite model. The gravity error was 0.06 mGals and the MT error was of 2%.

beneath the surface block locations. This is interpreted as the joint inversion trying to reconcile the mismatch between the MT and gravity data. It takes advantage of gravity's inherent non-uniqueness and tries to put the extra mass, needed by the gravity response, in a location that does not interfere with fitting the MT data. This redistribution of mass was observed to varying degrees in models where the gravity data corresponded to surface features and the MT data did not.

8.1.5 Compatibility and Sensitivity Summary

In order to evaluate the sensitivities of the MT and gravity techniques, a new approach was developed to determine effective sensitivity distribution and depth of investigation. A Taylor series expansion was used to determine isoclines of the mag-

nitude of change needed in the model parameters to generate a change in the model response greater than the associated data error. The sensitivity analysis along with MT and joint inversions of broadband and long period MT data, showed that the gravity data aid the long period MT data in reconstructing the subsurface. However, combining broadband MT data with gravity data produces the optimal joint inversion results. It was also established that the joint inversion has a bias towards fitting the MT data, not only due to having more MT than gravity data points, but because the magnitude of the MT partial derivatives in the Jacobian matrix are larger than their gravity counterparts.

The joint inversion preferential bias towards fitting the MT data means that when incompatible MT and gravity data are combined in a joint inversion, the inversion will favour a model in line with the MT data. However, the joint inversion may also try to take advantage of the inherent non-uniqueness of gravity data by redistributing the mass required by the gravity data to such depths that the MT technique is less sensitive.

8.2 Validity of the Petrophysical Relationships

The porosity-density relationship expresses the bulk density of the Earth in terms of fluid density, matrix density and porosity, whereas Archie's Law describes the bulk resistivity of the Earth in terms of the tortuosity factor, cementation constant and porosity. For a given survey area these 'empirical constants' in Archie's Law and the porosity-density relationship might be unknown or difficult to determine. Therefore, this section investigates the ramifications of using the incorrect petrophysical parameters in the joint inversion. There are three parts to this section. Firstly, how an incorrect value distorts the porosity estimate is investigated. Secondly, multiple inversions are performed with incorrect parameters to assess degradation of image quality, and finally the Jacobian matrix is studied to ascertain the invariance of the joint inversion to changes in the petrophysical parameters. The saturation quantity (S) and its exponent (n_s) were not specifically investigated because in Section 5.4, the saturation parameter was assumed to always be 1.

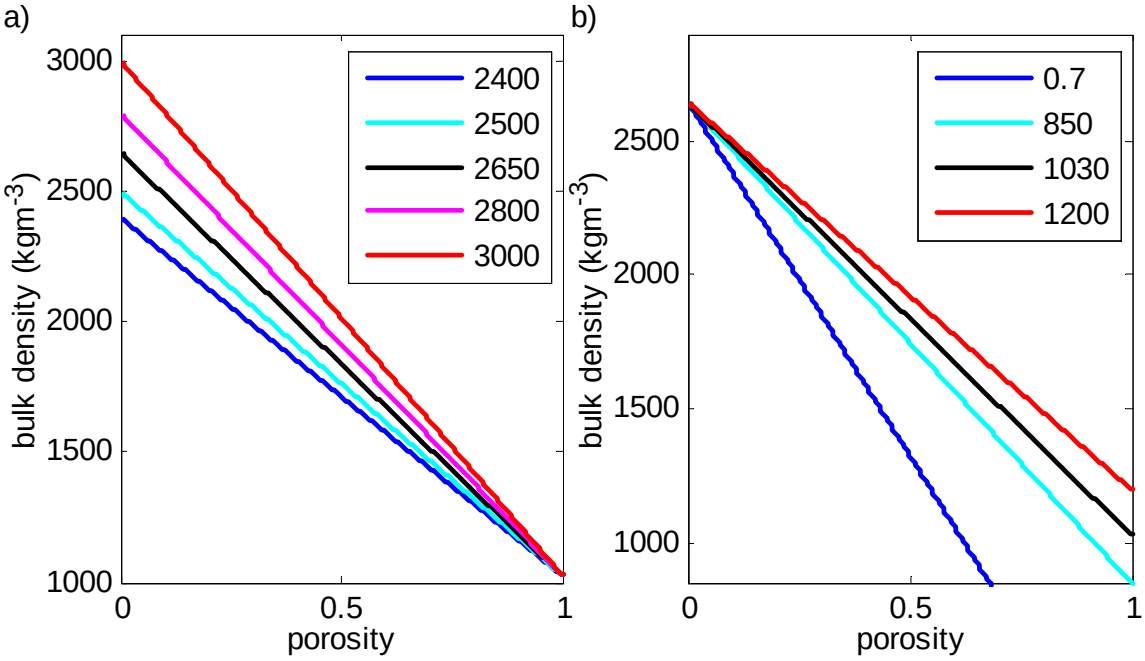

Figure 8.15: The porosity-density relationship for various values of a) matrix density, and b) fluid density.

8.2.1 Parameter Behaviour

Figure 8.15 depicts the linear relationships between bulk density and various matrix and fluid density values, as given by the porosity-density relationship. The fluid densities used in the plot are 0.7, 850, 1030 and 1200 kgm^{-3} and correspond to gas, oil, sea water and hyper-saline fluid, respectively. When the porosity value is high the system is dominated by the fluid and variations in the fluid density have the greatest influence on the bulk density. The maximum porosity that exists in the block, fault and trough models studied to date is 0.6. For such a porosity value one would expect a 210 kgm^{-3} variation in bulk density due to variations in the fluid, but this does not include the case of gas. Consequently, low porosity values mean the system is dominated by the matrix, therefore the variations in the matrix density have the greatest influence on the bulk density. The minimum porosity used in the three synthetic models is 0.02, which represents the basement in the trough model. At this porosity value of 0.02 there is a 588 kgm^{-3} variation in bulk density due to possible variations in the matrix density.

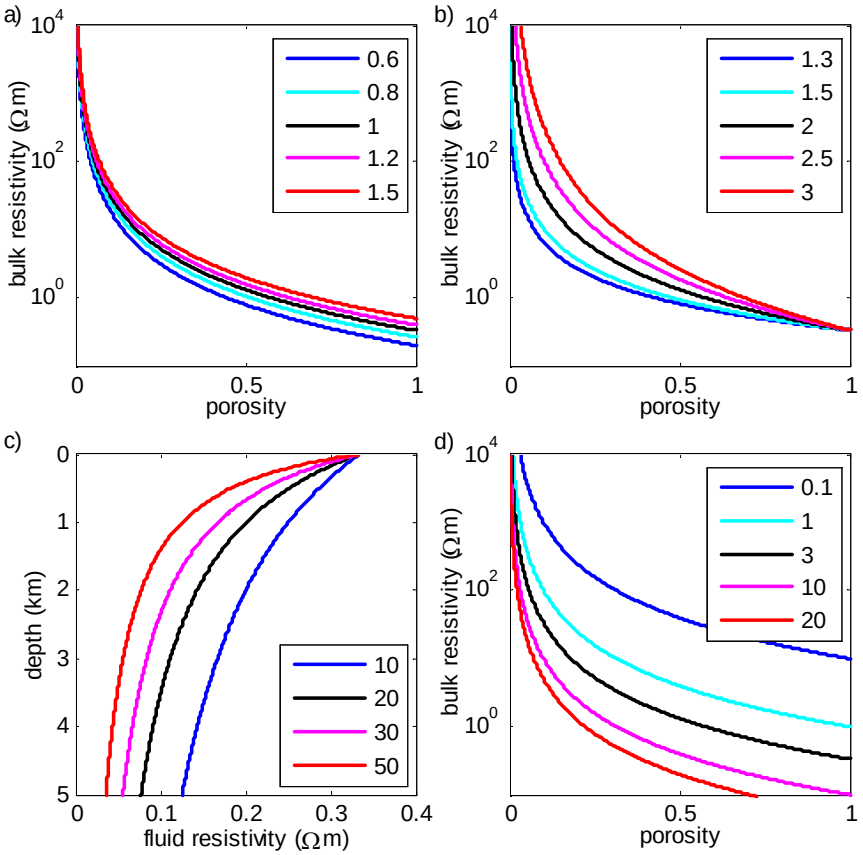

Figure 8.16: Archie's Law showing bulk resistivity vs. porosity for various values of a) the tortuosity a-value, b) the cementation m_{cf}-value and d) the fluid resistivity. c) Shows the fluid resistivity vs. depth using Equation 8.4, for various values of temperature gradients.

Figure 8.16 is a graphical display of Archie's Law, showing how bulk resistivity varies with porosity for various values of the tortuosity factor, the cementation constant and the fluid resistivity. This figure is very similar to Figure 5.7, except it is expressed in terms of resistivity, not conductivity. In sedimentary environments the tortuosity or a-value varies between 0.6 and 1.5 and the cementation constant or the m_{cf}-value ranges between 1.3 and 3.0 [134]. The bulk resistivity values lie between the two extremes of the fluid resistivity (at a porosity of 1) and infinity (perfect insulator) at a porosity of 0. The m_{cf}-value changes the shape and position of the curve between these two end points (see Figure 8.16b), with the largest variations in the bulk resistivity due to the m_{cf}-value occurring in the middle ranges of porosity. The largest variations in the resistivity-porosity relationship due to the

a-value occur when the porosity is 1. As discussed in Section 5.4, at a porosity of 1 the bulk resistivity should equal the fluid resistivity. However, the inclusion of the a-value in Archie's Law means the previous statement is not strictly correct unless the a-value is 1.

In sedimentary environments it has been shown that fluid resistivity is dependent on temperature (see Section 5.4). The fluid resistivity used for the three synthetic models in this chapter and Chapter 7 is based on the relationship,

$$\varrho_w(T) = \varrho_{w_o} + \frac{10}{T} \quad , \tag{8.4}$$

where ϱ_w is the resistivity of water, ϱ_{w_o} is the resistivity of water at zero temperature and fixed salinity and T is temperature. Figure 8.16c shows in graphical form the variation of fluid resistivity with depth according to Equation 8.4, using a surface resistivity of 0.33 Ωm and various temperature gradients of 10, 20, 30 and 50 ^{o}Ckm^{-1}. As the temperature gradient increases, the fluid resistivity decreases. Figure 8.16d shows the change in bulk resistivity due to changes in the fluid resistivity values.

Porosity fluctuations due to changes in the above parameters can be quantified for a joint inversion model. Using the porosity-density relationship, the change in porosity due to an incorrect fluid density value is given by

$$\Delta\phi = \frac{\rho_{bulk} - \rho_{matrix}}{[S\rho_{fluid\_inc} + (1-S)\rho_{air} - \rho_{matrix}]} - \frac{\rho_{bulk} - \rho_{matrix}}{[S\rho_{fluid} + (1-S)\rho_{air} - \rho_{matrix}]} \quad , \tag{8.5}$$

where $\Delta\phi$ is the change in porosity, ρ_{fluid_inc} is the incorrect fluid resistivity and $\frac{\rho_{bulk}-\rho_{matrix}}{[S\rho_{fluid}+(1-S)\rho_{air}-\rho_{matrix}]}$ is the final porosity given by the joint inversion. Similarly, the changes in porosity due to an incorrect matrix density can be calculated using Equation 8.5, except the correct fluid density value and the incorrect matrix density would be used. The change in porosity due to an incorrect a-value is given by

$$\Delta\phi = \left(\frac{a_{inc}S^{-n_s}\varrho_{fluid}}{\varrho_{bulk}}\right)^{\frac{1}{m_{cf}}} - \left(\frac{aS^{-n_s}\varrho_{fluid}}{\varrho_{bulk}}\right)^{\frac{1}{m_{cf}}} \quad , \tag{8.6}$$

where a_{inc} is the incorrect a-value and $\left(\frac{aS^{-n_s}\varrho_{fluid}}{\varrho_{bulk}}\right)^{\frac{1}{m_{cf}}}$ is the final porosity given

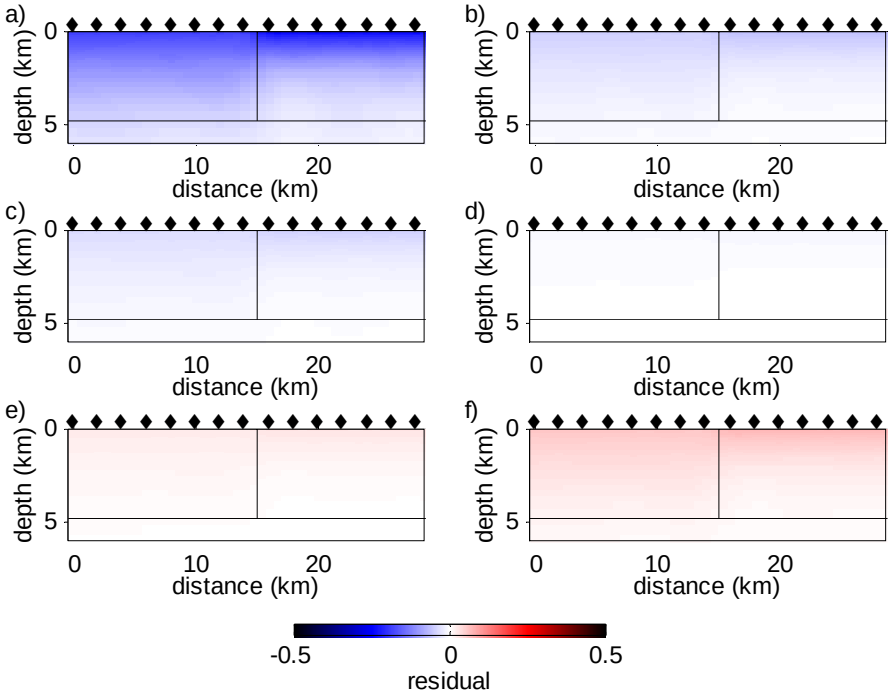

Figure 8.17: The change in porosity for a joint inversion of the synthetic fault model data with an MT error of 2% and a gravity error of 0.06 mGals, using incorrect fluid densities of a) 0.7, b) 850, c) 900, d) 1000, e) 1100 and f) 1200 kgm^{-3}, instead of the correct value of 1030 kgm^{-3}.

by the joint inversion. A similar approach can be taken to determine the deduced porosity for an incorrect m_{cf}-value and an incorrect temperature gradient, with the aid of Equation 8.6.

The changes in the porosity due to incorrect fluid densities, matrix densities, a-values, m_{cf}-values and temperature gradients were calculated for the block, fault and trough joint inversion models with an MT error of 2% and gravity error of 0.06 mGals. The incorrect fluid densities used in the study were 0.7, 850, 900, 1000, 1100 and 1200 kgm^{-3} instead of the correct value of 1030 kgm^{-3}. Figure 8.17 shows the resulting relative changes in porosity for the fault model, where a positive residual value means the incorrect fluid density has caused the porosity to increase, and a negative residual value means the incorrect fluid density has caused the porosity to decrease. When the fluid density value is less than the correct value, the porosity values are under-estimated. However, if the fluid density is greater than the true value, the porosity values are over-estimated. Since there is only a small range to

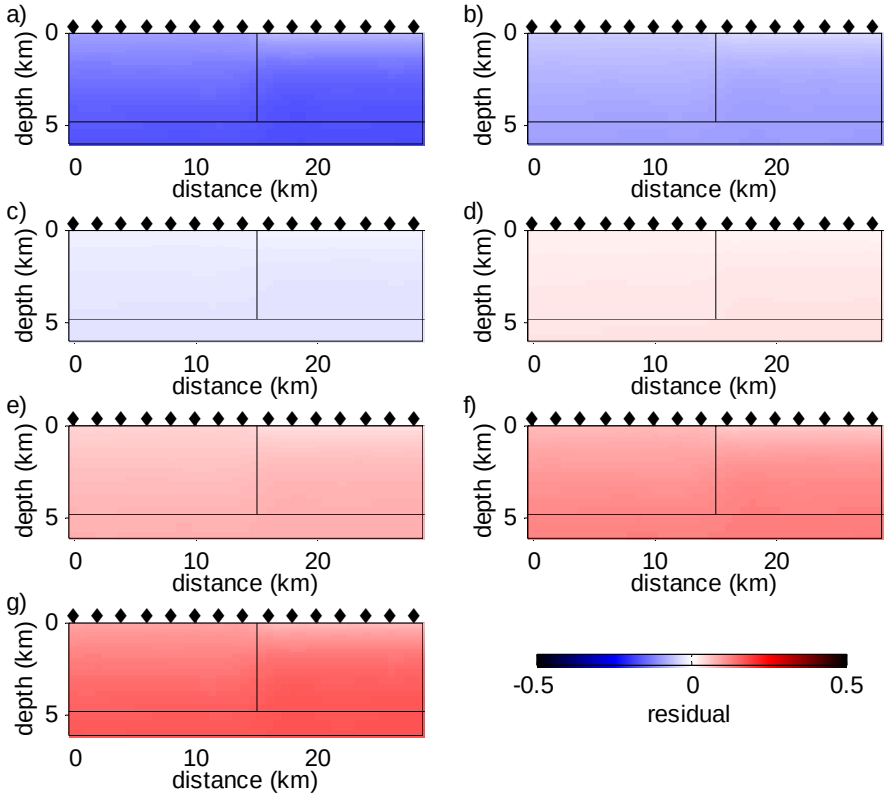

Figure 8.18: The change in porosity for a joint inversion of the synthetic fault model data with an MT error of 2% and a gravity error of 0.06 mGals, using incorrect matrix densities of a) 2400, b) 2500, c) 2600, d) 2700, e) 2800, f) 2900 and g) 3000 kgm^{-3}, instead of the correct value of 2650 kgm^{-3}.

the fluid density, the resulting change (error) in porosity is quite small, except when the fluid is gas (density of 0.7 kgm^{-3}).

The incorrect matrix densities used were 2400, 2500, 2600, 2700, 2800, 2900 and 3000 kgm^{-3} instead of the correct value of 2650 kgm^{-3}. Similar to an erroneous fluid density, low matrix density causes porosity to be under-estimated (see Figure 8.18). There is a slight increase in the porosity variation with depth for a given incorrect matrix density. This type of change would result in an offset in the gravity response by a constant amount, which implies that this type of behaviour could be hidden in the gravity offset term.

Figures 8.19 and 8.20 show the changes in porosity due to erroneous a- and m_{cf}-values, respectively, for the fault model. The correct a-value is 1 but the incorrect a-values used were 0.6, 0.7, 0.8, 0.9, 1.1, 1.2, 1.3, 1.4 and 1.5. The correct m_{cf}-value

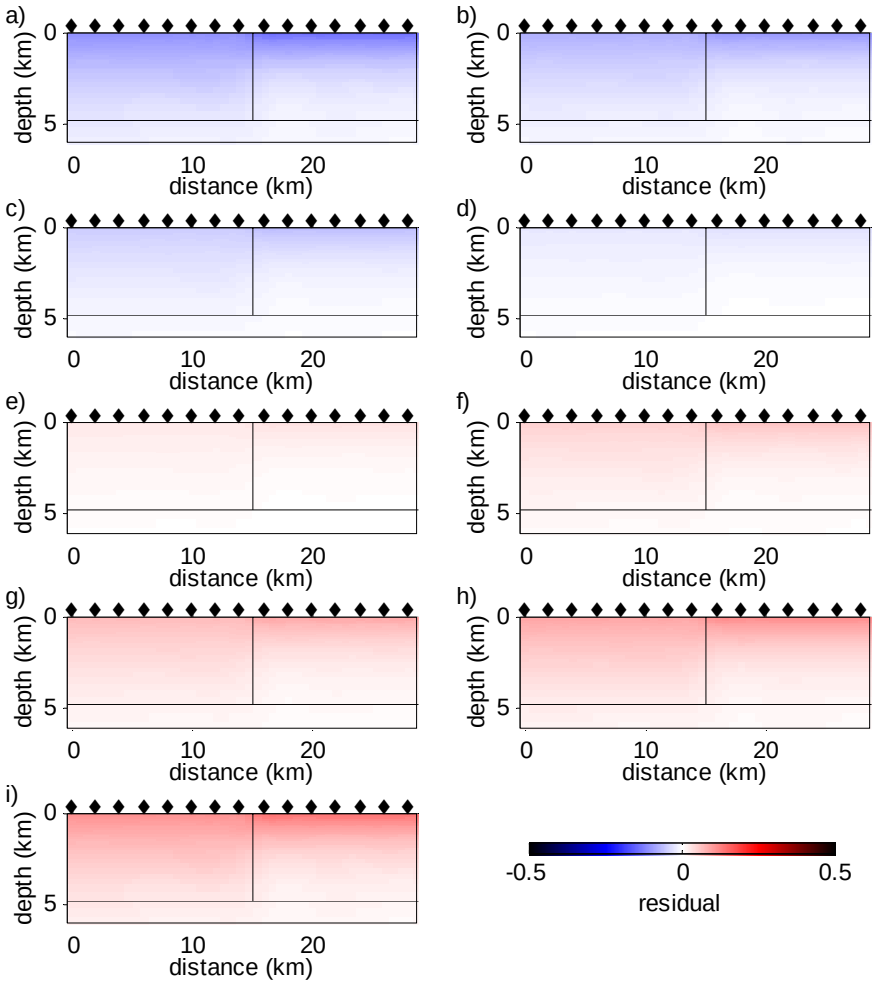

Figure 8.19: The change in porosity for a joint inversion of the synthetic fault model data with an MT error of 2% and gravity error of 0.06 mGals, using incorrect a-values in Archie's law of a) 0.6, b) 0.7, c) 0.8, d) 0.9, e) 1.1, f) 1.2, g) 1.3, h) 1.4 and i) 1.5, instead of the correct value of 1.

is 2, but the incorrect m_{cf}-values used were 1.3, 1.5, 1.7, 1.9, 2.2, 2.4, 2.6, 2.8 and 3.0. When the a-value is smaller than the correct value, the porosity values are lower than expected. Conversely, when the a-value is larger than the true value, the porosity is higher than expected. The greatest change in the porosity values due to the wrong a-value is in the shallow part of the model, where the system is dominated by the fluid properties. The changes in porosity due to an incorrect m_{cf}-value are similar to that of an incorrect a-value, except the change in the porosity value is greater and occurs to a greater depth.

The correct temperature gradient is 20 ^{o}Ckm^{-1}, but the incorrect temperature

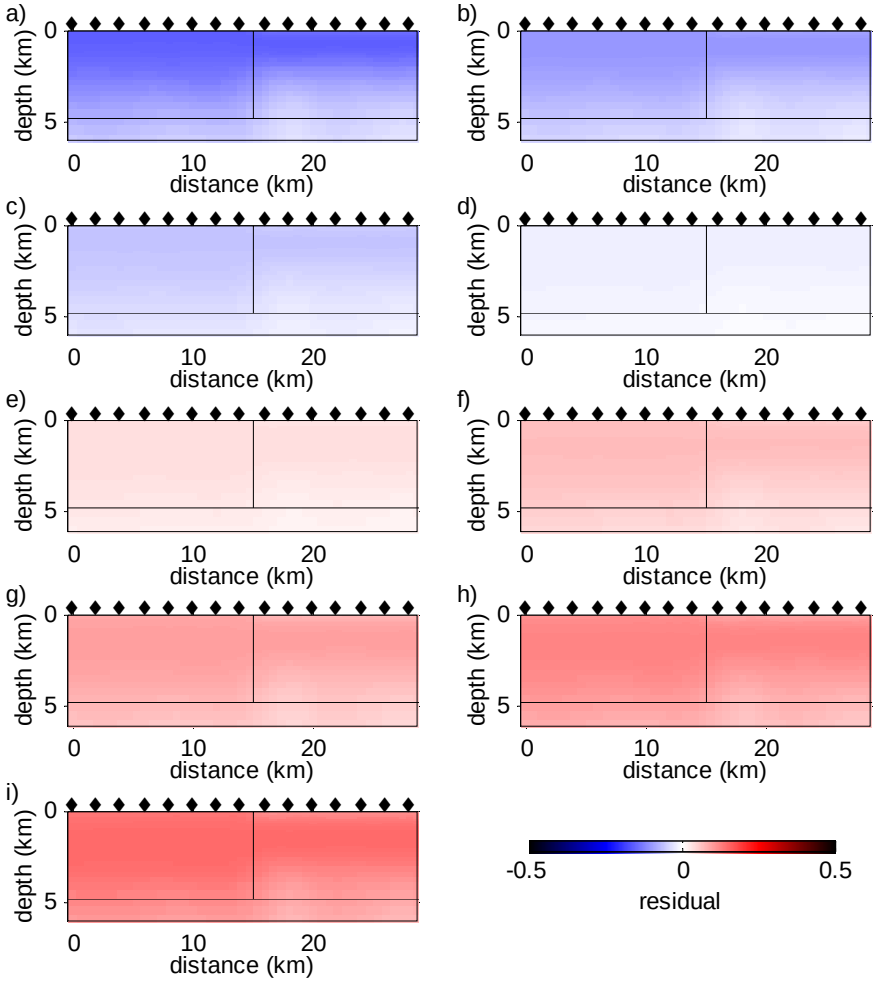

Figure 8.20: The change in porosity for a joint inversion of the synthetic fault model data with an MT error of 2% and a gravity error of 0.06 mGals, using incorrect m_{cf}-value in Archie's law of a) 1.3, b) 1.5, c) 1.7, d) 1.9, e) 2.2, f) 2.4, g) 2.6, h) 2.8 and i) 3.0, instead of the correct value of 2.

gradients tested were 5, 10, 30, 40, 50 and 60 ^{o}Ckm^{-1}. When the temperature gradient is less than the true gradient, the computed porosity values are too high (see Figure 8.21). Conversely, when the temperature gradient is greater than the true value, the deduced porosity values are too low. This is the only parameter in Archie's Law and the porosity-density relationship that exhibits such behaviour. The other parameters underestimate the porosity when the incorrect value is less than the correct value and overestimate the porosity when the incorrect value is greater than the correct value.

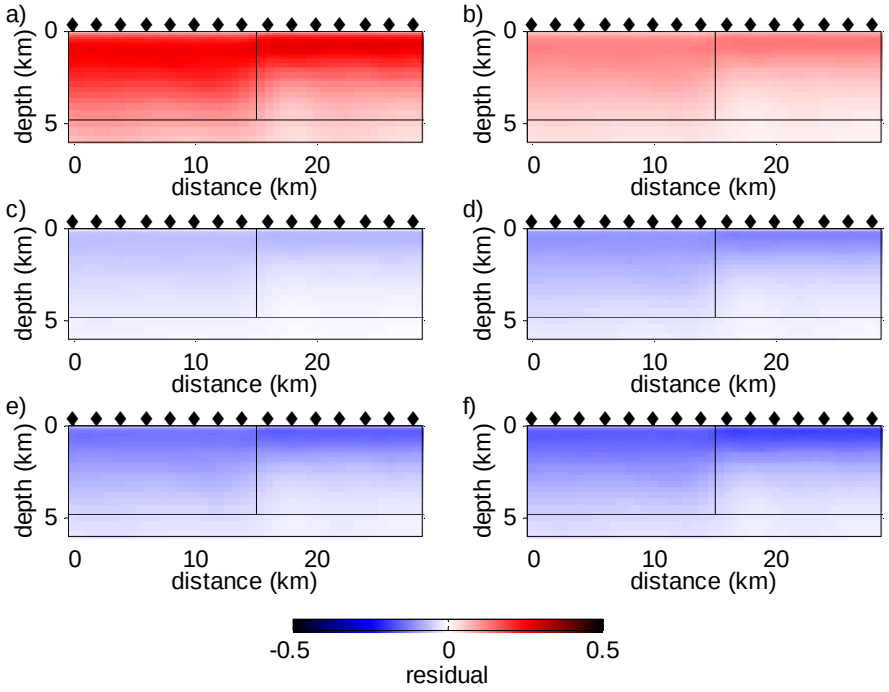

Figure 8.21: The change in porosity for a joint inversion of the synthetic fault model data with an MT error of 2% and a gravity error of 0.06 mGals, using incorrect temperature gradients of a) 5, b) 10, c) 30, d) 40, e) 50 and f) 60 ^{o}Ckm^{-1}, instead of the correct value of 20 ^{o}Ckm^{-1}.

8.2.2 Computational Testing

The effect on the joint inversion of using the incorrect constants (parameters) in Archie's Law and the porosity-density relationship is evaluated in this section by performing multiple joint inversions with different incorrect parameter values. Each parameter is examined in turn, and finally how errors in the observed geophysical data affect the results are examined.

To test the effect of using the incorrect parameters, the block, fault and trough synthetic models were used. For each model type the joint inversions use the same MT and gravity data with an MT error of 2% and a gravity error of 0.06 mGals. In these inversions, except for the stated parameter under examination, all other constants appearing in Archie's Law and the porosity-density relationship were taken to be correct. When evaluating the joint inversion with incorrect parameters, the results are compared to the joint inversion result with the correct value and not the true synthetic model. This enables a more meaningful comparison to be made

against the 'best' possible result, given the restricted survey configuration and data available.

Effect of Incorrect Fluid Density

Joint inversions were re-run with fluid densities of 0.7, 850, 900, 1000, 1100 and 1200 kgm^{-3}, instead of the correct value of 1030 kgm^{-3}. All inversions, regardless of model type, which had a fluid density of 0.7 kgm^{-3} produced a significantly higher total RMS$_{JI}$ than if the correct fluid density was used. The high RMS$_{JI}$ value was largely due to a large misfit of the gravity data, with RMS$_{GV}$ values of 4.6, 2.8 and 31.7 being obtained for the block, fault and trough models, respectively. On the other hand, the RMS$_{MT}$ values were smaller at 2.3, 1.7 and 4.7 for the three respective models, although they are not as small as if the correct fluid density was used. The RMS$_{MT}$ and RMS$_{GV}$ values are in line with the bias of the joint inversion towards fitting the MT data. In this case the bias is beneficial, because the MT component of the joint inversion uses the correct values. Therefore, by fitting this data, the joint inversion yields a model similar to the correct joint inversion.

The joint inversions for all the tested incorrect fluid density values of 850, 900, 1000, 1100 and 1200 kgm^{-3}, produced RMS values close to the RMS values of the joint inversions with the correct fluid density value. From Section 8.2.1, these density values cause little change in the porosity value from that with the correct value. The resulting models look very similar to the correct fluid density model. The smallest RMS$_{JI}$ value for each model type did not occur at the correct fluid density values, but there was no obvious pattern at which fluid density, higher or lower than the correct value, occurred. These results show that the joint inversion is robust against incorrect fluid density values, provided there is no significant gas present.

Effect of Incorrect Matrix Density

Matrix densities of 2400, 2500, 2600, 2700, 2800, 2900 and 3000 kgm^{-3} were used in the joint inversions, instead of the correct value of 2650 kgm^{-3}. There was little variation between the RMS values for the different matrix density values. The resulting inverted models all look very similar to each other, and to the model with the

correct matrix density. The stability in the RMS_{JI} value across the matrix density values is a reflection of the joint inversion bias towards fitting the MT data, which has the correct Archie's Law values. The smallest RMS_{GV} values occur between a matrix density of 2500 and 2800 kgm^{-3}. Outside this range of values it was hard for the joint inversion to find a model that satisfied the gravity data as well as the MT data.

Effect of Errors in the Tortuosity Factor

The correct tortuosity a-value was 1, but the joint inversions were re-run with incorrect a-values of 0.6, 0.7, 0.8, 0.9, 1.1, 1.2, 1.3, 1.4 and 1.5. As shown in Figure 8.22, the inverted models transition from under-estimating the porosity values to over-estimating the porosity values as the a-value increases. The structural boundaries in the models remain the same. This behaviour is consistent with that found in Section 8.2.1. The resistivity values remain the same in order to fit the MT data, but the incorrect a-value precludes the resistivity values from being converted to the correct porosity values.

Inversions with an a-value of 0.6 and 1.5 produced very large RMS_{GV} values and consequently, large total RMS_{JI} values. In between these two a-values the total RMS_{JI} does not vary significantly. The inversions which under-estimate the porosity values correspond to an a-value < 0.8 and have a raised RMS_{GV} value. The inversions which over-estimate the porosity values occur at a-values > 1.3. These models do not have a significant difference in the RMS values when compared to the correct a-value inversion, which makes distinguishing them from the correct a-value model based on the RMS value difficult.

Effect of Errors in the Cementation Constant

Joint inversions were re-executed with cementation m_{cf}-values of 1.3, 1.5, 1.7, 1.9, 2.2, 2.4, 2.6, 2.8 and 3.0, instead of the correct value of 2. The m_{cf}-value results produce a similar pattern to the tortuosity a-value result. As the m_{cf}-values increase from 1.3 to 3.0, there is a transition from inverted models that under-estimate the porosity values, to inverted models that over-estimate the porosity values (see

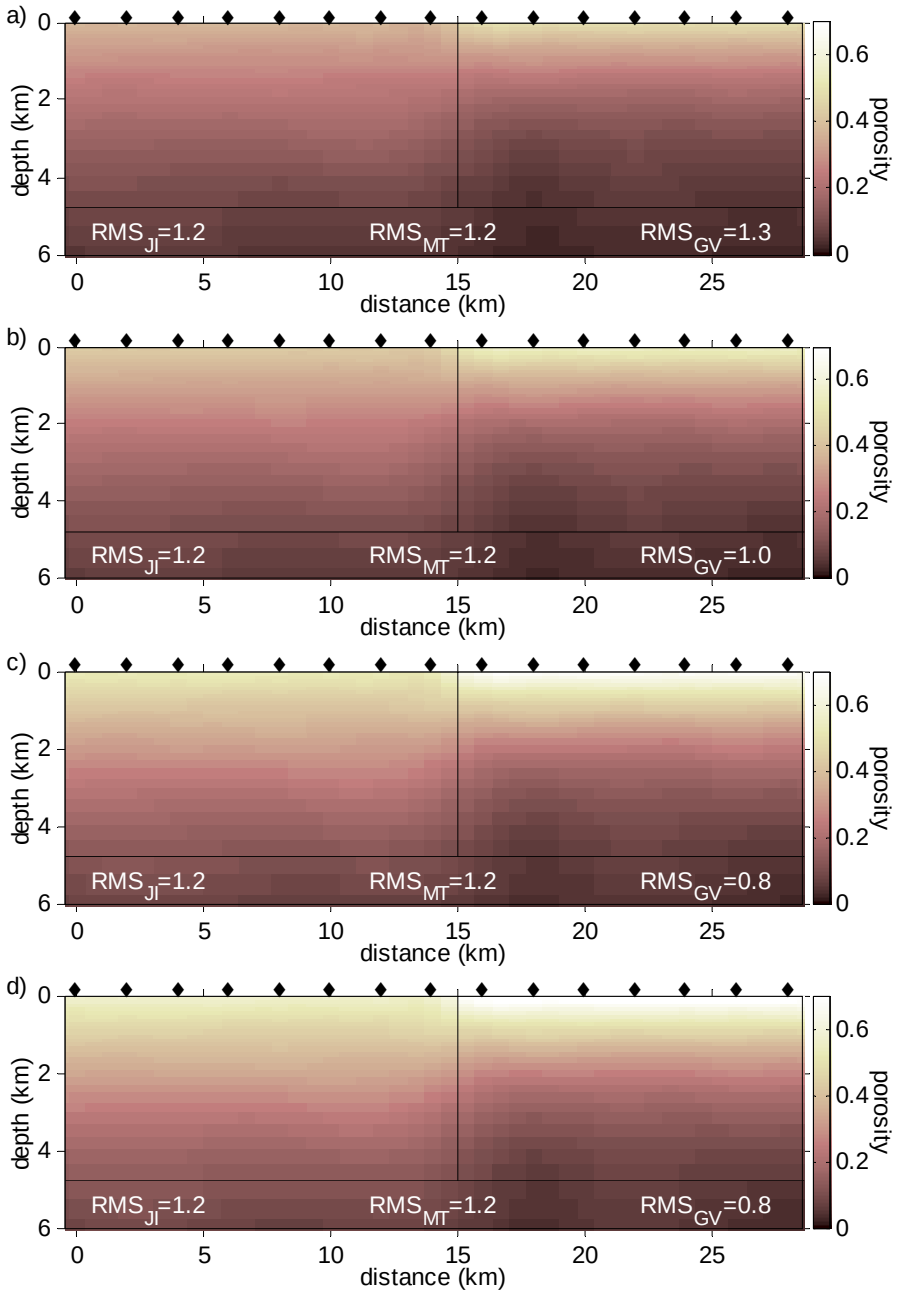

Figure 8.22: The models produced from a joint inversion of the synthetic fault model data with an MT error of 2% and a gravity error of 0.06 mGals, and various a-values in Archie's law of a) 0.6, b) 0.8, c) 1.2 and d) 1.4.

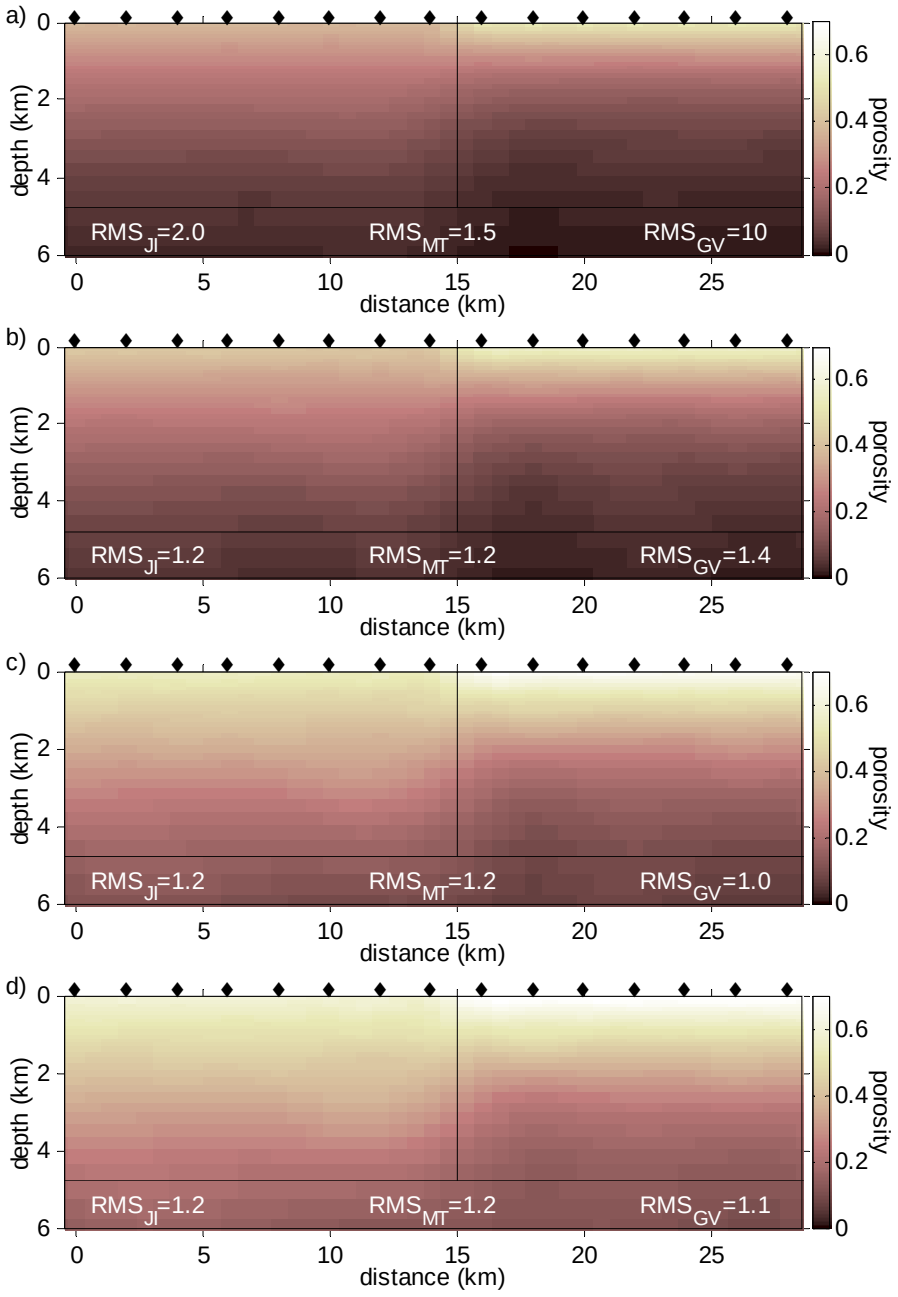

Figure 8.23: The models produced from a joint inversion of the synthetic fault model data with an MT error of 2% and a gravity error of 0.06 mGals, using m_{cf}-values in Archie's law of a) 1.5, b) 1.7, c) 2.4 and d) 2.8.

Figure 8.23) and this behaviour is consistent with the discussion in Section 8.2.1. The structural boundaries are always in the correct locations. For inverted models with an m_{cf}-value < 1.9, which have porosity values too low, the RMS_{JI} values are significantly greater than the RMS_{JI} values of the correct m_{cf}-value model. For the m_{cf}-values of 1.9 and 2.2 the models are similar to the correct value model. Inverted models which have m_{cf}-values above 2.2 over-estimate the porosity values, but do not show a corresponding increase in the RMS_{JI}, RMS_{MT} or RMS_{GV} values. This makes it difficult to determine these models from the correct m_{cf}-value model based on the RMS values.

Effect of Errors in the Temperature Gradient

The correct temperature gradient used in Equation 8.4 by the joint inversion is 20 $^{o}\text{Ckm}^{-1}$. The joint inversion was re-run with incorrect temperature gradients of 5, 10, 30, 40, 50 and 60 $^{o}\text{Ckm}^{-1}$, to establish the effect of such errors. For all three models the correct temperature gradient value had the smallest RMS_{JI}, RMS_{MT} and RMS_{GV} values The inversions with too low temperature gradient values over-estimate the porosity values whereas those with too high temperature gradient values under-estimate the porosity values. Even the temperature gradients of 10 and 30 $^{o}\text{Ckm}^{-1}$, which bracket the true value, produce models which have significantly erroneous porosity values (see Figure 8.24). Although the porosity values were incorrect, the structural boundaries in the models were still correctly located.

The temperature, and consequently the fluid resistivity, has the greatest effect on the bulk resistivity. The above results show that having the correct temperature gradient and the correct fluid resistivity are critical in producing the correct model in a joint inversion. However, they also show that the RMS values are a clear indicator of whether the temperature gradient is correct or not.

8.2.3 Jacobian Matrix Analysis

In this section the Jacobian of the joint inversion is used to test the joint inversion's invariance to changes in the parameters which characterise Archie's Law and the porosity-density relationship.

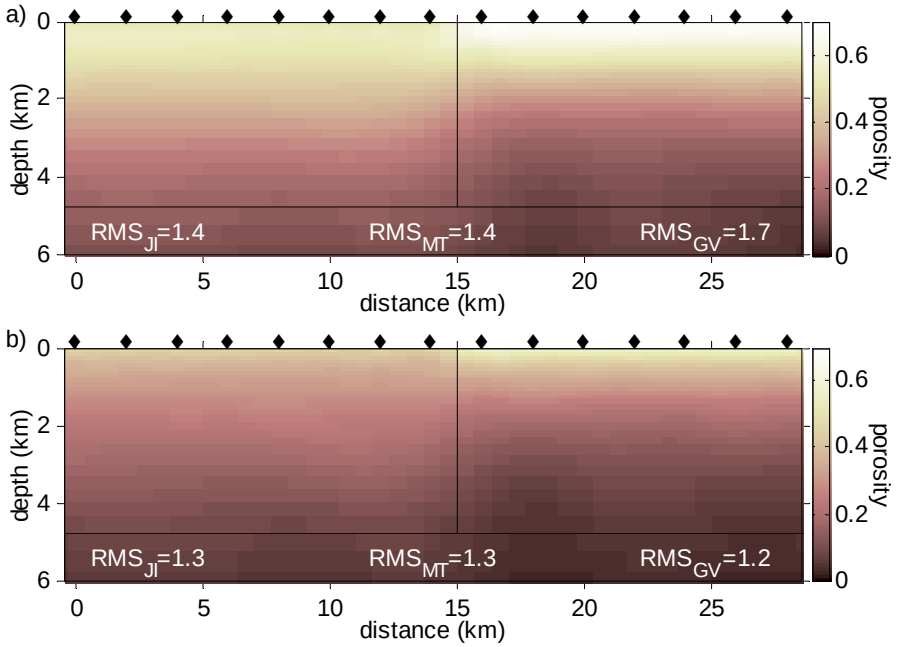

Figure 8.24: The models produced from a joint inversion of the synthetic fault model data with an MT error of 2% and a gravity error of 0.06 mGals, using temperature gradients of a) 10 ^{o}Ckm^{-1} and b) 30 ^{o}Ckm^{-1}.

Porosity-Density Relationship

In Section 6.2.1, the Fréchet derivative (sensitivity) with respect to porosity was ascertained from the single gravity Jacobian and the porosity-density relationship using the differential chain rule. Rather than differentiating the porosity-density relationship directly with respect to porosity, it can be differentiated with respect to the fluid and matrix density values. Doing so obtains

$$\frac{\partial d_{GV}}{\partial \rho_{fluid}} = \frac{\partial d_{GV}}{\partial (\rho)} * \frac{\partial (\rho)}{\partial \rho_{fluid}} = \frac{\partial d_{GV}}{\partial (\rho)} * S\phi \tag{8.7a}$$

$$\frac{\partial d_{GV}}{\partial \rho_{matrix}} = \frac{\partial d_{GV}}{\partial (\rho)} * \frac{\partial (\rho)}{\partial \rho_{matrix}} = \frac{\partial d_{GV}}{\partial (\rho)} * (1-\phi) \quad . \tag{8.7b}$$

Equation 8.7 gives the change in the gravity model response due to changes in the fluid and matrix densities. A sensitivity model can be viewed once the new Jacobian sub-matrices have been calculated. Section 8.1.1 outlined how to calculate the sensitivity distribution, but here there is no normalisation. From these new Jacobian

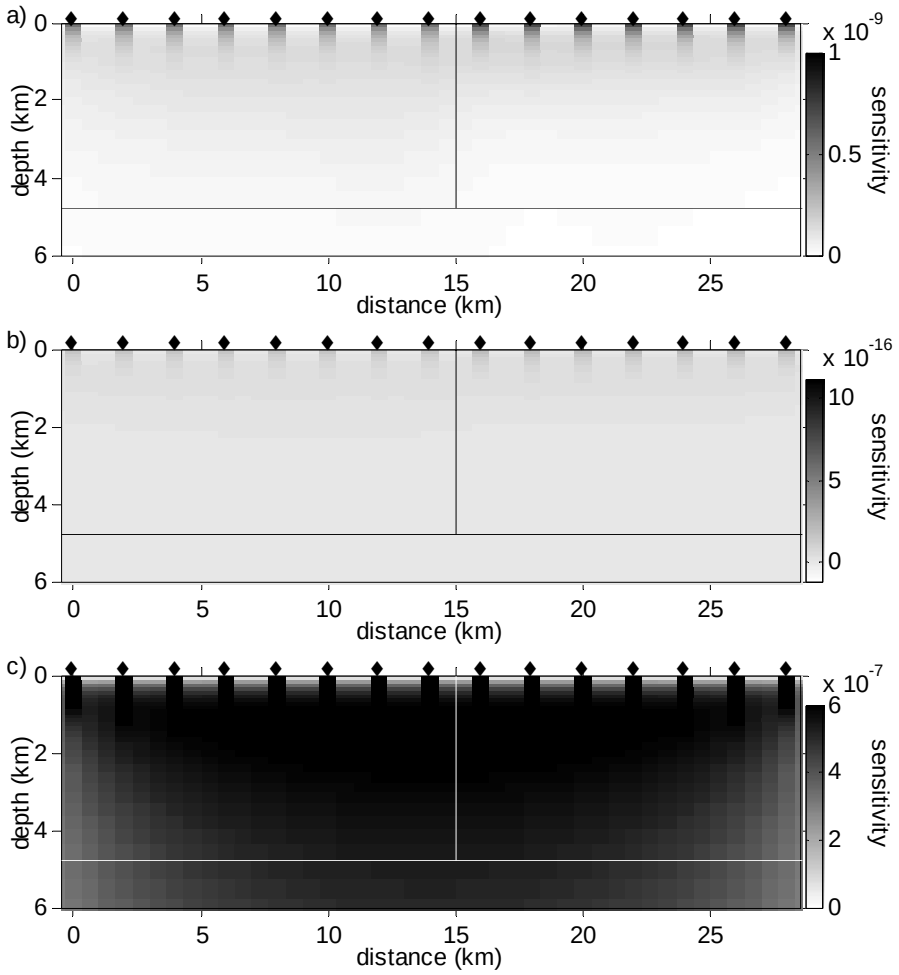

Figure 8.25: The gravity sensitivity distribution produced from a joint inversion of the synthetic fault model data with an MT error of 2% and a gravity error of 0.06 mGals. The sensitivity models are with respect to the a) fluid density, b) matrix density and c) porosity.

matrices, a sensitivity plot can be computed and compared to the sensitivity plot of the original Jacobian with respect to porosity.

The matrix density, fluid density and porosity sensitivity for the fault model joint inversion with an MT error of 2% and gravity error of 0.06 mGals are shown in Figure 8.25. The sensitivity of all plots decreases with depth, however there is a significant difference in the orders of magnitude between the matrix density, the fluid density and the porosity sensitivity values. A change in the model response is significantly more sensitive to a change in porosity than it is to a change in fluid or matrix density. This demonstrates the dependence of density, and hence gravity, on

porosity and their relative invariance to the fluid and matrix densities.

Archie's Law

A similar approach to the above can be applied to the petrophysical parameters in the Archie's Law. The Archie's Law equivalent to Equation 8.7 (with the aid of Equation 8.4) is given by

$$\begin{aligned}
\frac{\partial d_{MT}}{\partial a} &= \frac{\partial d_{MT}}{\partial(\log(\varrho))} * \frac{\partial(\log(\varrho))}{\partial(\varrho)} * \frac{\partial(\varrho)}{\partial a} \\
&= \frac{\partial d_{MT}}{\partial(\log(\varrho))} * \frac{1}{\varrho_j} \log(e) * \phi^{-m_{cf}} S^{-n_s} \varrho_{fluid} \qquad (8.8a) \\
\frac{\partial d_{MT}}{\partial m_{cf}} &= \frac{\partial d_{MT}}{\partial(\log(\varrho))} * \frac{\partial(\log(\varrho))}{\partial(\varrho)} * \frac{\partial(\varrho)}{\partial m_{cf}} \\
&= \frac{\partial d_{MT}}{\partial(\log(\varrho))} * \frac{1}{\varrho_j} \log(e) * -aS^{-n_s} \varrho_{fluid} \phi^{-m_{cf}} \ln(\phi) \qquad (8.8b) \\
\frac{\partial d_{MT}}{\partial T} &= \frac{\partial d_{MT}}{\partial(\log(\varrho))} * \frac{\partial(\log(\varrho))}{\partial(\varrho)} * \frac{\partial(\varrho)}{\partial T} \\
&= \frac{\partial d_{MT}}{\partial(\log(\varrho))} * \frac{1}{\varrho_j} \log(e) * -a\phi^{-m_{cf}} S^{-n_s} \varrho_{fluid} 10 T^{-2} \quad . \qquad (8.8c)
\end{aligned}$$

These equations give the changes in the MT model response due to changes in the a-value, the m_{cf}-value and the temperature (not temperature gradient).

Figure 8.26 shows the sensitivity distributions in the subsurface (models), with respect to the a-value, the m_{cf}-value and the temperature, for the fault model joint inversion with an MT error of 2% and gravity error of 0.06 mGals. These sensitivity plots can be compared to the sensitivity plot of the original Jacobian with respect to porosity. The temperature sensitivity plot shows that only changes in the temperature in the shallower part of the section will affect the model response. The a- and m_{cf}-values have greater sensitivities at depth, but when all four sensitivity plots are compared, the model response is most sensitive to changes in porosity. This validates the joint inversion approach of using porosity, because it is the parameter to which the MT response is most sensitive. The block and trough sensitivity plots (not shown) are consistent with the fault sensitivity findings.

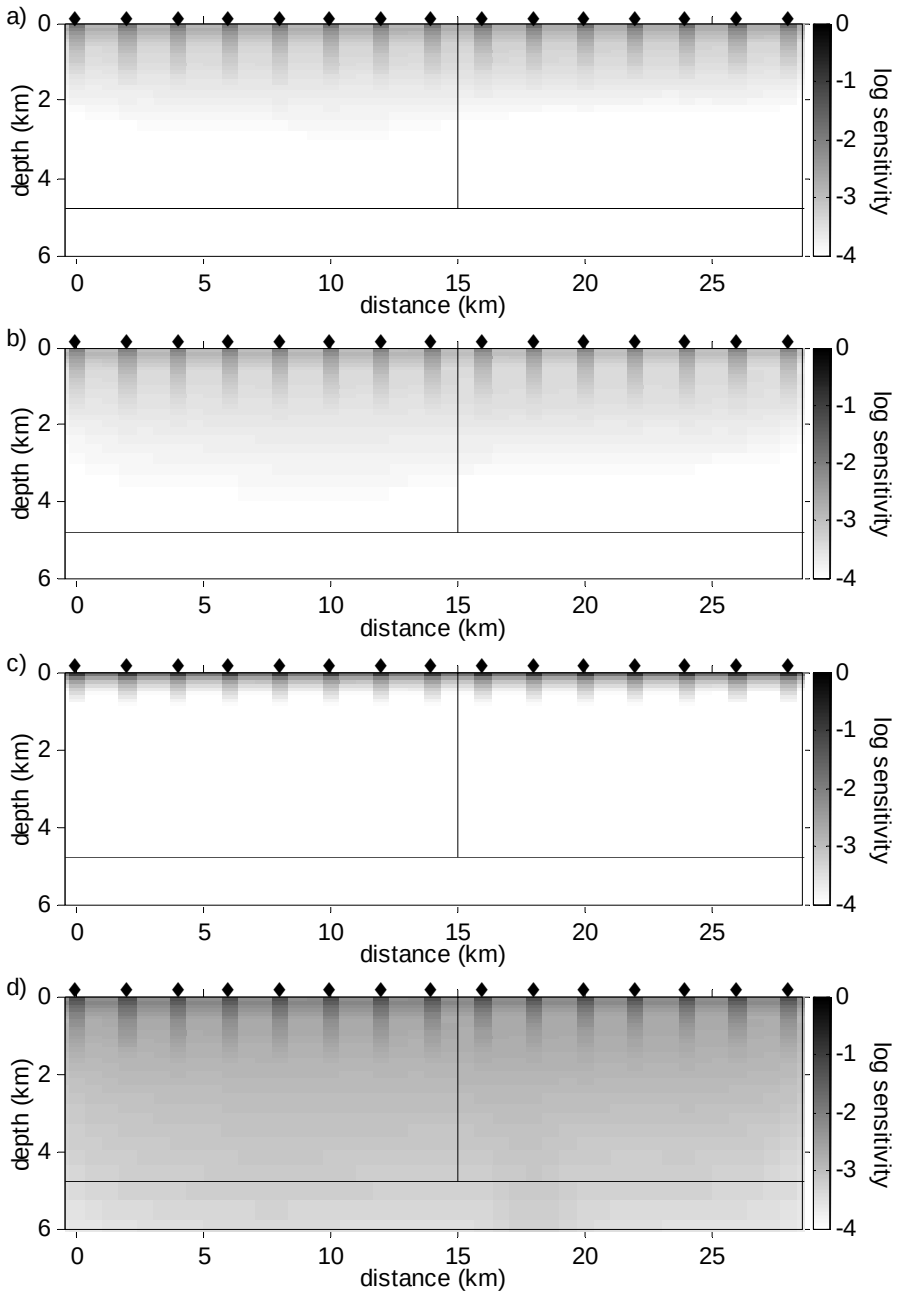

Figure 8.26: The MT sensitivity distribution produced from a joint inversion of the synthetic fault model data with an MT error of 2% and a gravity error of 0.06 mGals. The sensitivity models are with respect to a) the a-value, b) the m_{cf}-value, c) temperature and d) porosity.

8.2.4 Validity of Relationships Summary

The extended Jacobian matrix analysis shows that porosity has the greatest influence on the MT and gravity model responses compared to the other parameters in Archie's Law and the porosity-density relationship. The Jacobian analysis indicates invariance towards a change in the temperature, except at shallower depths. However, the computational investigation, whereby inversions were performed for incorrect values of the petrophysical parameters, shows large variations in the resulting models due to incorrect temperature gradients. The correct temperature gradient produced the smallest joint inversion RMS values, indicating that the RMS values are an indicator of the correct value.

The change in MT data is more sensitive to the variations in the a- and m_{cf}-values than to the temperature gradient. The inversion results showed that if the a- and m_{cf}-values are too small then the joint inversion will under-estimate the porosity and produce a higher RMS than the correct model value. If the a- and m_{cf}-values are too large then the joint inversion will over-estimate the porosity values. However, there are no associated increases in the RMS values.

The joint inversion is quite robust to incorrect values in the porosity-density relationship parameters of fluid density and matrix density. This was both demonstrated computationally and through sensitivity plots. Therefore, if one is unsure of the correct constants to use in Archie's Law and the porosity-density relationship, it is better to encourage the joint inversion to fit the gravity data than the MT data. As the MT and gravity errors increase, the effect of an incorrect parameter in Archie's Law and the porosity-density relationship is less critical.

8.3 Effects of Differential Weighting

In a joint inversion there are essentially two different places where the MT and gravity data sets can be differentially weighted in order to influence the outcome of the joint inversion. The first is the data error (data weighting matrix), which defines the confidence (reliability) of each individual data value. This was discussed in Section 7.2. The second is an overall weighting of each technique (data set) in

formulating the objective function. The reasons for wanting to do this may be to reduce the data fit for one technique or having greater confidence in one technique over the other. To date, the joint inversion was not set up to allow for this type of weighting. In this section the joint inversion scheme is extended to allow for such a differential weighting scheme, and then evaluates the effectiveness of both percentage and Jacobian-based weighting approaches.

8.3.1 Implementing the Weighting

Currently, the joint inversion scheme calculates the RMS according to the formula,

$$\text{RMS} = \left\{ \frac{\sum_{i=1}^{q} \left(\frac{d_i - F[m]_i}{\sigma_i^*} \right)^2}{q} \right\}^{\frac{1}{2}} \quad . \tag{8.9}$$

This expression does not distinguish between the gravity and MT data. However, it would be desirable to be able to weight the MT and gravity data differently by the relationship,

$$\alpha\text{RMS}_{MT} + \beta\text{RMS}_{GV} = \text{RMS}_{total} \quad , \tag{8.10}$$

where RMS_{total} is the RMS that the joint inversion seeks to minimise, RMS_{MT} and RMS_{GV} are the MT and gravity RMS terms respectively, and α and β are the MT and gravity weighting factors, respectively. The α and β weights can influence the RMS calculation in the following way [172],

$$\alpha\text{RMS} = \left\{ \frac{\sum_{i=1}^{q} \left(\alpha \frac{d_i - F[m]_i}{\sigma_i^*} \right)^2}{q} \right\}^{\frac{1}{2}} \quad . \tag{8.11}$$

This is equivalent to calculating the RMS value with an MT data weighting matrix, $\mathbf{W}_{MT}$, redefined as

$$\mathbf{W}_{MT} = diag \left\{ \frac{\alpha}{\sigma_1^*}, \frac{\alpha}{\sigma_2^*}, \ldots, \frac{\alpha}{\sigma_q^*} \right\} \quad , \tag{8.12}$$

and similarly for βRMS using a gravity data weighting matrix $\mathbf{W}_{GV}$ and β. This redefinition of the data weighting matrix replaces the old definition for all steps in

a weighted joint inversion.

The α and β values can vary between 0 and infinity. The larger the α and β values, the higher the contribution from the corresponding technique. However, if they are both equal to 1 then there is no additional contribution. When the β value equals 0, the joint inversion is equivalent to executing a single MT inversion. Similarly, when α equals zero it is equivalent to executing a single gravity inversion.

To be able to weight the MT and gravity data differently, the objective function of the joint inversion needs to be redefined and a distinction made between the MT and gravity data. The new objective function is

$$\begin{aligned} U(\mathbf{m}) &= \left\|\underline{\partial}_y \mathbf{m}\right\|^2 + \left\|\underline{\partial}_z \mathbf{m}\right\|^2 + \mu^{-1}\left\{\left\|\mathbf{W}_{MT}\widehat{\mathbf{d}}_{MT} - \mathbf{W}_{MT}\mathbf{J}_{MT}\mathbf{m}\right]\right\|^2 \\ &\quad + \left\|\mathbf{W}_{GV}\widehat{\mathbf{d}}_{GV} - \mathbf{W}_{GV}\mathbf{J}_{GV}\mathbf{m}\right]\right\|^2 - \chi_*^2\Big\} \quad , \quad (8.13) \end{aligned}$$

where $\mathbf{J}_{MT}$ is the Jacobian corresponding to the MT data points and $\mathbf{J}_{GV}$ is the Jacobian which corresponds to the gravity data points.

Altering the objective function may alter how the model parameters are updated. To determine the effects of the new objective function on the model updates, a similar process to that described in Section 3.1.1 is followed. Equation 8.13 is differentiated and then set equal to zero to give

$$\begin{aligned} &\left(\underline{\partial}_y^T\underline{\partial}_y + \underline{\partial}_z^T\underline{\partial}_z\right)\mathbf{m}_{k+1} + \boldsymbol{\mu}^{-1}\Big\{\left(\mathbf{W}_{MT}\mathbf{J}_{MTk}\right)^T\left(\mathbf{W}_{MT}\mathbf{J}_{MTk}\right)\mathbf{m}_{k+1} \\ &\quad - \left(\mathbf{W}_{MT}\mathbf{J}_{MTk}\right)^T\left(\mathbf{W}_{MT}\widehat{\mathbf{d}}_{MTk}\right) + \left(\mathbf{W}_{GV}\mathbf{J}_{GVk}\right)^T\left(\mathbf{W}_{GV}\mathbf{J}_{GVk}\right)\mathbf{m}_{k+1} \\ &\quad - \left(\mathbf{W}_{GV}\mathbf{J}_{GVk}\right)^T\left(\mathbf{W}_{GV}\widehat{\mathbf{d}}_{GVk}\right)\Big\} = 0 \quad . \quad (8.14) \end{aligned}$$

This is the equivalent expression to the original expression of

$$\begin{aligned} &\left(\underline{\partial}_y^T\underline{\partial}_y + \underline{\partial}_z^T\underline{\partial}_z\right)\mathbf{m}_{k+1} + \mu^{-1}\Big\{\left(\mathbf{W}_d\mathbf{J}_k\right)^T\left(\mathbf{W}_d\mathbf{J}_k\right)\mathbf{m}_{k+1} \\ &-\mu^{-1}\left(\mathbf{W}_d\mathbf{J}_k\right)^T\left(\mathbf{W}_d\widehat{\mathbf{d}}_k\right)\Big\} = 0 \quad . \quad (8.15) \end{aligned}$$

However in Equation 8.14,

$$\begin{aligned} & \left(\mathbf{W}_{MT}\mathbf{J}_{MTk}\right)^T\left(\mathbf{W}_{MT}\mathbf{J}_{MTk}\right)\mathbf{m}_{k+1} + \left(\mathbf{W}_{GV}\mathbf{J}_{GVk}\right)^T\left(\mathbf{W}_{GV}\mathbf{J}_{GVk}\right)\mathbf{m}_{k+1} \\ = \; & \left(\mathbf{W}_d\mathbf{J}_k\right)^T\left(\mathbf{W}_d\mathbf{J}_k\right)\mathbf{m}_{k+1} \qquad (8.16a) \\ & -\left(\mathbf{W}_{MT}\mathbf{J}_{MTk}\right)^T\left(\mathbf{W}_{MT}\widehat{\mathbf{d}}_{MTk}\right) - \left(\mathbf{W}_{GV}\mathbf{J}_{GVk}\right)^T\left(\mathbf{W}_{GV}\widehat{\mathbf{d}}_{GVk}\right) \\ = \; & \left(\mathbf{W}_d\mathbf{J}_k\right)^T\left(\mathbf{W}_d\widehat{\mathbf{d}}_k\right) \qquad . (8.16b) \end{aligned}$$

Therefore, Equations 8.14 and 8.15 are equivalent and the model updates for the weighted joint inversion and the original joint inversion are the same.

8.3.2 Percentage Weighting

Percentage weighing assigns the α and β values to sum to 1. This controls the percentage by which each of the MT and gravity RMS values contribute to the RMS_{total} value. To test the percentage weighting, joint inversions were executed with MT weightings of 0.7, 0.6, 0.5, 0.4 and 0.3 with the corresponding gravity weightings of 0.3, 0.4, 0.5, 0.6 and 0.7. The block, fault and trough models were used. The inversions were run with various combinations of MT errors of 2, 4 or 6% and corresponding gravity errors of 0.03, 0.06, 0.1, 0.3 or 0.5 mGals.

The RMS_{MT} and RMS_{GV} values were tabulated for all weighting factors, model types and error levels. No strong patterns appeared in the RMS values. There was a weak trend observed whereby if the gravity weighting was high then the RMS_{GV} would decrease. Similarly, if the MT weighting was high then the RMS_{MT} value would decrease. When the MT and gravity weights were 0.5 and 0.5, respectively, it did not result in similar RMS_{MT} and RMS_{GV} values. For most inversions, the RMS_{GV} value increased when compared to the corresponding original joint inversion RMS_{GV} value in which no weighting was used. The trough model was of special interest because the original joint inversion (see Chapter 7) produced models with a high gravity misfit. The percentage weighting did not significantly aid in resolving this problem and the RMS_{GV} values were always greater than the RMS_{MT} values.

The percentage weighting scheme removes the original joint inversion bias toward

fitting the MT data due to the greater number of MT data points compared to gravity data points. However, it does not address the bias in the original joint inversion due to the magnitude of the Jacobian values discussed in Section 8.1.1. The next section looks at assigning the α and β values based on the properties of the Jacobian matrix.

8.3.3 Jacobian Weighting

Weighting the RMS values of the joint inversion based on their Jacobian values is an idea suggested by Athanasiou *et al.* [172]. In that paper, the authors simultaneously inverted different arrays of electrical resistivity data. However, the authors found that when they tried to combine different electrode array data without differential weighting, one array type would become dominant and overshadow the contribution of the other array types. This dominant array type had higher Jacobian values. Athanasiou *et al.* found that a Jacobian-based weighting scheme produced a better inverted model than that containing information from all electrode configuration types.

The difference between the inversion of the electrical resistivity data described above, and the joint inversion presented here is that the joint inversion involves two fundamentally different parameters of the Earth (resistivity and density) and different measurements (MT and gravity). Resistivity operates entirely in the model and data space of resistivity (and apparent resistivity), in which all quantities have the same units. Also, the electrical resistivity inversion had suppression of structure from different array types. However the joint inversion does not have this problem. Rather it needs the MT technique to dominate because it contains the vitally important depth information that gravity data does not contain. This section determines whether applying a Jacobian-based weighting is beneficial.

There are two different Jacobian weights which can be used to condition the data. The first is

$$\mathbf{J}_{MTj} = \frac{\sum_{i=1}^{p} |\mathbf{J}_{MTij}|}{p} \tag{8.17a}$$

$$\mathbf{J}_{GVj} = \frac{\sum_{i=1}^{s} |\mathbf{J}_{GVij}|}{s} \tag{8.17b}$$

$$\beta = \sum_{j=1}^{n} \frac{\mathbf{J}_{MTj}}{\mathbf{J}_{GVj}} \quad , \tag{8.17c}$$

where $\mathbf{J}_{MT}$ is the MT component of the Jacobian, $\mathbf{J}_{GV}$ is the gravity component of the Jacobian, p is the number of MT data points, s is the number of gravity data points and n is the number of model parameters. The Jacobian format used here is with respect to porosity, not resistivity and density as in Section 8.1.1. The second Jacobian weight is

$$\mathbf{J}_{MTj} = \frac{\sqrt{\sum_{i=1}^{p} |\mathbf{J}_{MTij}|^2}}{p} \tag{8.18a}$$

$$\mathbf{J}_{GVj} = \frac{\sqrt{\sum_{i=1}^{s} |\mathbf{J}_{GVij}|^2}}{s} \tag{8.18b}$$

$$\beta = \sum_{j=1}^{n} \frac{\mathbf{J}_{MTj}}{\mathbf{J}_{GVj}} \quad . \tag{8.18c}$$

These weighting factors, Equations 8.17 and 8.18, are equivalent to the l_1 and l_2 column norms of the Jacobian matrix for the two different techniques. To implement the Jacobian weighting value in the weighting scheme outlined in Section 8.3.1, α is set equal to 1 and β equals the value shown in Equations 8.17 and 8.18. Since the MT component of the Jacobian changes at each iteration, so too does the β value.

To test the Jacobian weightings both the l_1 and l_2 based weights were applied to the block, fault and trough models. Joint inversions were performed with all combinations of a gravity error of 0.06, 0.1, 0.3 or 0.5 mGals and an MT error of 2, 4 or 6%. Approximately one third of the l_1-weighted joint inversions failed in the first three iterations. Of the remaining joint inversions, the weighting value β varied between 155 and 11300, depending on the model type, error level and number of iterations. In general, the successful block and fault models had RMS_{GV} values of less than 0.6, but the RMS_{MT} values ranged between 12 and 45. The trough model

produced varied RMS values.

The results of the l_2-weighting scheme are similar to those of the l_1-weighting scheme, however the l_2-weighting seemed to give more stable results, with only $\sim 20\%$ of inversions failing in the first three iterations. Also, the variation of the weighting value obtained for a given model type is less across all error levels, as is the RMS value. The block and fault models had RMS_{GV} values of less than 0.3 and the RMS_{MT} values were higher than 6.0. The trough model had RMS_{GV} values of between 0.1 and 5.5, whereas the RMS_{MT} values were between 14 and 61. For all model types the RMS_{GV} value was smaller than the RMS_{MT} value.

Comparing the l_2-weighting results to the original joint inversion results showed that the weighted RMS_{GV} values are always smaller than the original. Conversely, the weighted RMS_{MT} values are always larger than the original. Therefore this improved gravity data fit is occurring at the expense of the MT data fit. The original block and fault models gave good gravity data fits, so it is no surprise that significant weighting towards the gravity data in the l_2-weighting schemes means these values are reduced below the desired RMS of 1. The original trough model in Section 7.1.3 had an RMS_{GV} of 5.0 and an RMS_{MT} of 1.5. The l_2-weighting scheme reduced the RMS_{GV} value to 2.3, however the RMS_{MT} value was increased to 56. The resulting inverted model bears no resemblance to the true synthetic model. In fact, all the inverted models produced by the l_1- and l_2-weighting schemes are a very poor representation of the true models due to the large MT misfits.

Variation

In an attempt to improve the Jacobian weighting results, a column sum of $\mathbf{W}_d\mathbf{J}$ rather than just $\mathbf{J}$ was taken in Equations 8.17 and 8.18. Normalising the Jacobian by the data error makes it dimensionless, and so it was hoped that a comparison between the MT and gravity Jacobian components would produce a better weighting value. However, this was not observed and the results were no different to those discussed above.

8.3.4 Differential Weighting Summary

Weighting the MT and gravity data based on a simple percentage bias has very little effect on influencing the fit of the MT and gravity data. The l_1 and l_2 Jacobian weightings were found to produce similar results to each other. The RMS_{GV} value is smaller than the original joint inversion (with no weighting), but the RMS_{MT} values are significantly higher. Neither the percentage weighting nor the Jacobian-based weighting significantly improved the results over the original unweighted joint inversion.

8.4 Conclusions

Results produced by the joint inversion are robust to incorrect fluid and matrix density values used in the porosity-density relationship. The joint inversion is more susceptible to incorrect petrophysical parameters namely the a-value, the m_{cf}-value and fluid resistivity in Archie's Law. In general, high RMS values are indicative of an incorrect variable being used.

In terms of sensitivity to the same subsurface areas, the gravity data are compatible with the broadband MT data, but less so with the long period MT data. If the MT and gravity data containing information about different subsurface structures, the joint inversion, to reconcile the data mismatch, may take advantage of gravity's inherent non-uniqueness and try to redistribute porosity (density) with depth. It places the porosity needed to produce a better gravity fit at locations that do not interfere with fitting the MT data. Another aspect of incompatible MT and gravity data is that the joint inversion will produce models which favour the MT data. This is due to the bias in the joint inversion towards fitting the MT data.

Weighting the gravity and MT data sets differently was implemented in an attempt to remove the bias towards fitting the MT data and improve the balance between fitting both data sets. Weighting values were assigned using two methods, percentage weighting and Jacobian-based weighting. Disappointingly, neither method improved upon the original joint inversion results.

Chapter 9

Renmark Trough Case Study

The case study selected for the newly developed joint inversion scheme is the Renmark Trough area, shown in Figure 9.1. This area is of particular interest because of its geothermal potential. It is located within the South Australian Heat Flow Anomaly (SAHFA), which has anomalously high heat flow values [173] [174]. Petratherm Pty. Ltd. previously held a geothermal tenement over this study area.

The aim of this case study is to demonstrate the application of the joint inversion approach to real world data. The Renmark Trough area provides a good example because pre-existing geophysical data sets are available, and the geology of the site from a structural point of view is relatively simple. Sandstone is the dominant lithology, which allows Archie's Law to be used. This chapter first provides an overview of the geology and the pre-existing geophysical data sets, then the single gravity and MT inversions are applied to the individual data sets. Finally, the joint inversion scheme is undertaken and the various results discussed.

9.1 Geological Overview

The Renmark Trough area encompasses the Early Permian Nadda Basin and the Early Cretaceous Berri Basin, which both underlie the Tertiary Murray Basin [175]. The sediments filling these basins have been preserved in structures such as the Renmark Trough and the nearby Canegrass Lobe and the Paringa Embayment (see Figure 9.1). A cross-sectional view showing the sequence of sediments in the Ren-

Figure 9.1: Location map of the Renmark Trough survey area, showing major geology and structural features (adapted from [178])

mark Trough is given in Figure 9.2.

The Renmark Trough itself is a north-easterly trending feature that is 24 km wide and extends for over 100 km. It has a depth of approximately 3500 m in the north, decreasing to 2700 m in the south [176]. The southern part of the Trough is poorly documented but is thought to be a half graben with the Hamley Fault delineating the north-western side [177]. The fault has a throw up to 1500 m and extends into the Early Cretaceous sediments. The northern part of the Trough is a graben with its south-eastern side delineated by the Chowilla Fault [177].

The upper few hundred metres of the sequence contained in the Renmark Trough

Figure 9.2: Geological cross section of the Renmark Trough area, adapted from Rogers [178].

are from the Murray Basin. The succession of freshwater, marine, coastal and continental sediments in the Murray Basin covers an area of 300000 km^2 in south-eastern South Australia, south-western New South Wales and north-eastern Victoria [175]. Underlying the Murray Basin sediments are the Berri Basin sediments, which are thought to be a former extension of the Eromanga Basin [178]. The Berri Basin is made up of the Monash Formation. It consists of coarse and fine grained sandstone, siltstone and claystone. However, in the North Renmark 1 drill hole (which is close to the survey area and indicated on Figure 9.3), the unit is dominated by siltstone and sandstone, with only minor claystone interbeds.

The Nadda basin sediments underlie the Berri basin sediments and include the Urana Formation. This formation contains shale, siltstone diamictite and occasional conglomeratic and carbonaceous intervals [177]. There are also variable thicknesses of the Urana Formation across the Renmark Trough area. Drill holes suggest a thickness of 395 m, although seismics suggest this might extend to 900 m in the Renmark Trough [176].

The basement is thought to be the Cambrian Kanmantoo Group and could contain Adelaidean strata. In between the basement and the overlying Urana Formation there is evidence of a clastics layer believed to be Devonian in age [176]. Although no drill hole has intercepted this layer, seismic information suggests it could have a thickness of > 1500 m in the north, decreasing to ~ 600 m in the south.

Geologically the Renmark Trough provides a good testing ground for the joint inversion scheme because it is structurally simple and the sediments are predominantly sandstone and siltstone. There are also minor thin clay based layers, for which Archie's Law will break down. However, these are considered comparatively minor compared to the overall scale of the investigation.

9.2 Geophysical Data Sets

There are currently four different geophysical data sets which exist over the Renmark Trough area. These are reflection seismics, gravity, magnetics and MT. There are also eight drill holes, as shown in Figure 9.3, which range in depth between 200 m and 1380 m. Numerous seismic reflection surveys have been conducted in the Renmark Trough area to evaluate its petroleum potential. The locations of all seismic survey lines are marked on Figure 9.3. After an initial reconnaissance survey, the main seismic survey was conducted in 1965 by Tasman Oil [179]. In the late 1960's other surveys were conducted by Beach Petroleum [180] and Associated Australian Oilfields [181]. In the 1980's there was renewed interest in the area by the International Mining Corp, which surveyed extensively [182].

The latest (2007) total magnetic intensity (TMI) and Bouguer anomaly gravity grids are shown in Figure 9.3 and 9.4, respectively. The grids are at an interval of 100 m and were obtained from Primary Industry and Resources South Australia. The data values and locations of the gravity stations that form the basis of the gravity map were obtained as input for the inversions described in this chapter. Gravity station locations are plotted in Figure 9.4.

The most recent geophysical survey conducted in the area was in 2009 by The University of Adelaide [183]. This was an MT survey which entailed 25 stations along two roughly parallel profiles, as shown in Figure 9.4. The profiles were orientated perpendicular to the north-east trending Renmark Trough. The southern profile coincided with an old seismic line OC 1965-R1. Long period instruments, which measured the E_x, E_y, B_x, B_y, B_z components of the electric and magnetic fields, were deployed at a station spacing of $4-5$ km along the northern profile. Broadband

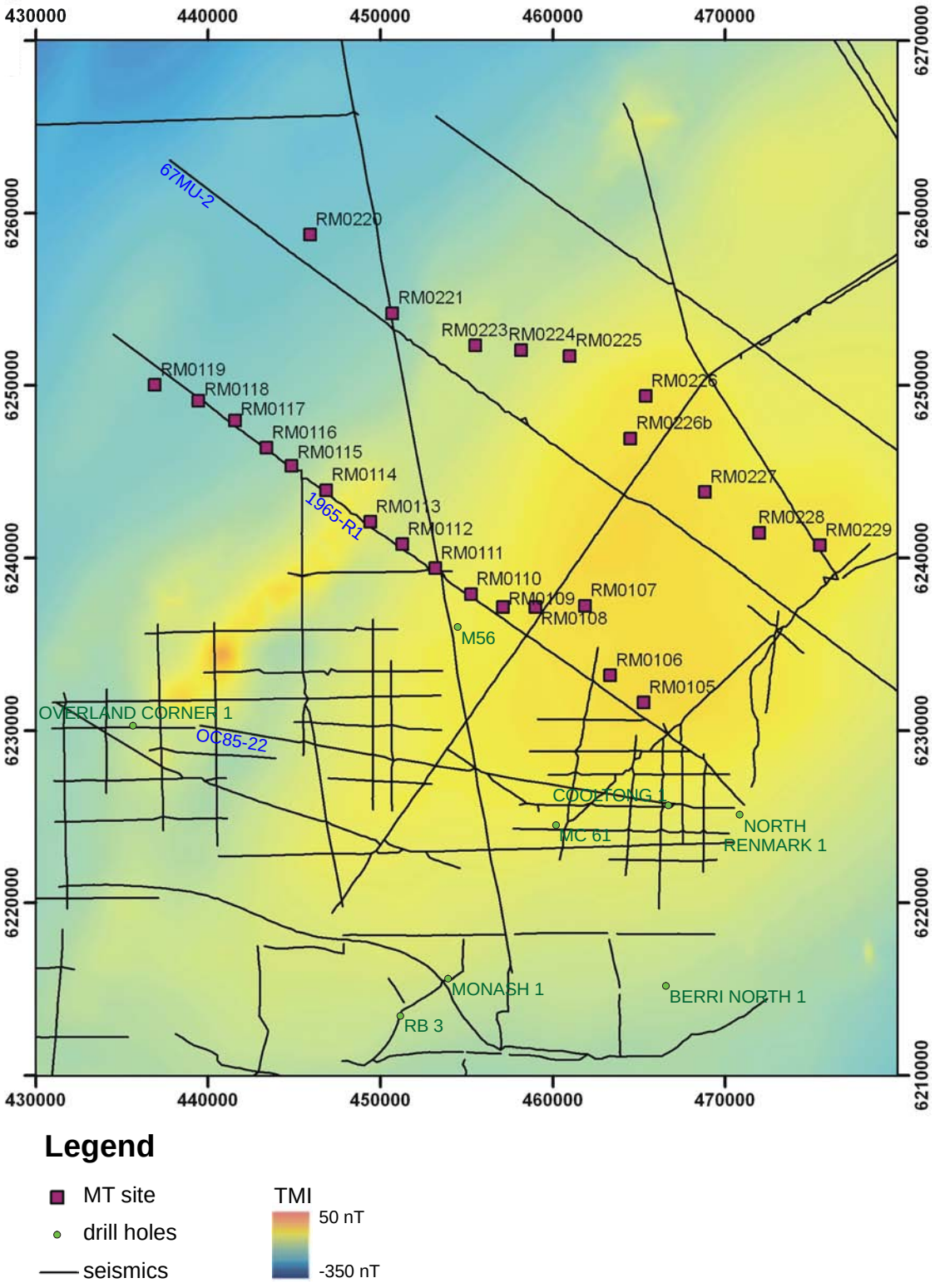

Figure 9.3: Total field magnetic intensity map of the Renmark Trough area, with MT stations, drill holes and seismic lines superimposed.

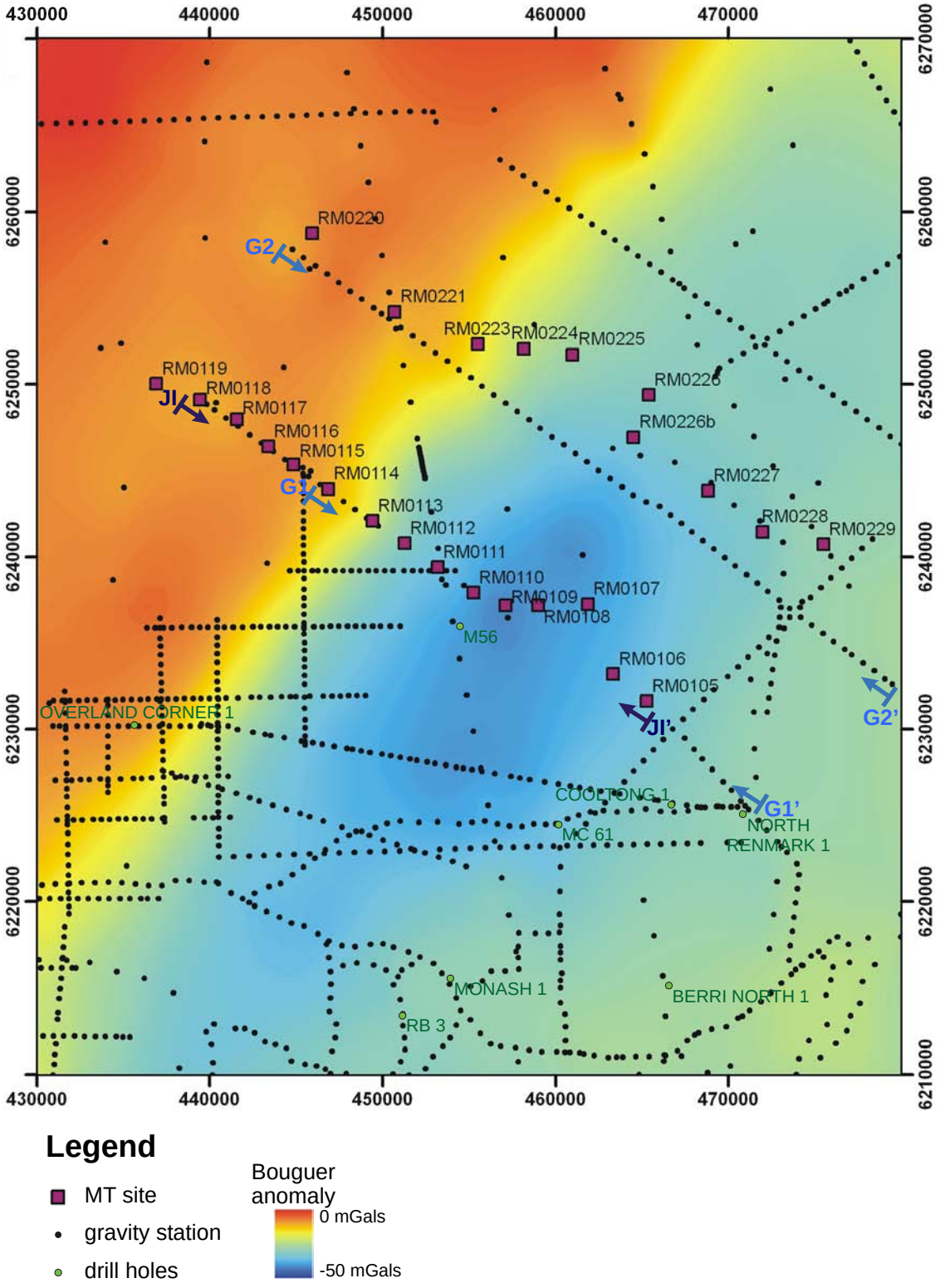

Figure 9.4: The Bouguer gravity anomaly map of the Renmark Trough area. Also shown are the locations of MT stations, gravity stations, drill holes and profile lines for the joint inversion and gravity forward modelling.

instruments which measured the E_x, E_y, B_x, B_y components of the electric and magnetic fields were deployed at a station spacing of $2-3$ km along the southern profile. The raw time series were remote referenced and processed using the Bound Influence Remote Reference Processing code (BIRRIP) of Chave and Thomson [184]. Apparent resistivity and phase data were produced over frequency bands of $0.1-10^{-4}$ Hz for the long period stations and $100-10^{-2}$ Hz for the broadband stations. For further details on the MT acquisition and processing, see Craven [183].

The combination of the gravity station data and the broadband MT data form the basis of the Renmark Trough case study. The long period MT data set was not used because it was of poor quality. The JI profile, on which the gravity, MT and joint inversions are conducted, is shown in Figure 9.4. Station RM0119 is excluded from the discussion below since there is no co-incident gravity station data (preferred over the gridded data) to constrain it in the joint inversion.

9.3 Gravity

The Bouguer anomaly gravity map of the Renmark Trough area is shown in Figure 9.4. The north-east trending Renmark Trough is clearly visible as a gravity low. Its western boundary is a major feature on the gravity map as a sharp transition between high and low gravity values (approximately ~ 35 mGals). This strong gradient delineates the Hamley fault. Away from the Hamley fault there is a gradual increase in the gravity values to the south-east. There is a central gravity low, although its extent is not well constrained due to the sparse gravity station network. The location of the Chowilla fault, which forms the south-east side of the trough, is not clear. North-west of the Hamley fault there is a high in the gravity values that corresponds to the Canegrass Lobe. The magnetic map of the equivalent area (See Figure 9.3) shows a magnetic high along the Hamley fault close to the Overland Corner 1 drill hole. South-east of the Hamley fault there is a large magnetic high, which is thought to be caused by deep regional features. This high masks the magnetic signature of the nearer surface trough, making complementary information unattainable from magnetics.

Figure 9.5: The seismically-constrained gravity forward modelling along profile G1, as shown on Figure 9.4. Adapted from Craven [183].

A recent investigation by Craven [183] used seismic and drill hole data to constrain density models along profiles G1 and G2, as indicated on Figure 9.4. The seismic cross sections (locations given in Figure 9.3) were characterised by very strong reflectors correlating to an unconformity in the Early Cretaceous and the top of the basement. Profile G1 corresponds to the seismic line 1965-R1, which coincides with the last $\sim$ 23 km of the eastern end of the JI profile. The 1965-R1 seismic data were of poor quality and so the interpretation was aided by using seismic line OC85-22 [179] [182]. Profile G2 corresponds to seismic line 67MU-2 [181].

Figures 9.5 and 9.6 show the subsurface density models for profiles G1 and G2. Relatively low density values were used, which were indicated by the drill hole logging. The G1 profile model only contains the seismically-determined boundaries. The base of the trough is at a depth of $\sim$ 3.6 km and is located adjacent to the southerly dipping Hamley fault. From this point there is a sharp depth increase in the basement of the Trough over a horizontal distance range of between 6 km and 8 km, before a gentle rise for the remainder of the profile. The boundary between the Permian and the upper sediments plunges in depth over the Hamley fault, before gradually decreasing in depth for the remainder of the profile. The

Figure 9.6: The seismically-constrained gravity forward modelling along profile G2, as shown on Figure 9.4. Adapted from Craven [183].

gravity data along this profile are incomplete. However, from the available data the model reproduces the observed data over the Hamley fault, but the model response slightly over-estimates the observed data at the southern end of the profile.

In the G2 profile model (Figure 9.6) the seismically defined sediment layers are divided into finer geological units. The M56 and North Renmark 1 drill holes were used to constrain their depths. This model also shows a south-dipping Hamley fault and a relatively flat basement. The model reproduces the general trend of the observed gravity data but does not fit the subtle variations.

For the gravity stations along the JI profile, indicated in Figure 9.4, there is approximately a 20 km gap in coverage in the middle portion of the profile. There is also a much larger gap at the eastern end of the line. The 20 km gap in station coverage is over a significant portion of the Trough, starting just south of the Hamley fault and extending to the east end of the profile. The interpolated gridded gravity values were not used to fill this gap because their values are not well constrained due to the lack of stations in this area. Owing to the continuity of the trough along the strike direction, the gravity stations from the $\sim$ 10 km north-east G2 profile

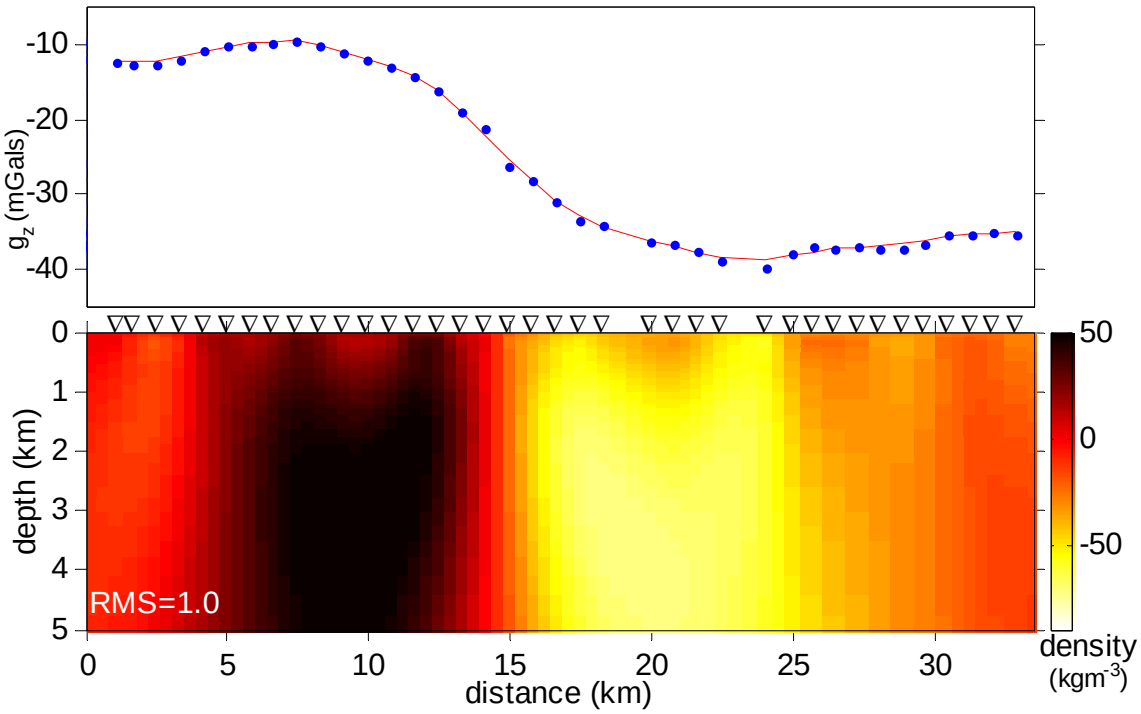

Figure 9.7: Density contrast model produced from an Occam gravity inversion along the JI profile, as shown in Figure 9.4. The observed data is shown by the blue dots and the computed model response is shown by the red line.

were used to fill this gap and to give consistent gravity coverage along the profile. The gravity stations along the JI profile are assigned an error of 0.2 mGals and the gravity stations from the G2 profile are assigned a larger error of 0.4 mGals to allow for any variations in subsurface structure due to the altered locations.

Figure 9.7 shows the results of the Occam gravity inversion along the JI profile. Consistent with this type of inversion, all the structure has been placed at the surface. Between a horizontal distance of 0 km and $\sim$ 5 km, there is an increase in density. At a horizontal distance of $\sim$ 15 km there is a distinct drop in the density contrast of 100 kgm^{-3}, corresponding to the location of the Hamley fault. Proceeding further along the profile at a horizontal distance of $\sim$ 25 km, the density values begin to increase again. Small density variations are used at the top of the model to fit subtle variations in the data.

9.4 Magnetotellurics

9.4.1 Phase Tensor Analysis

Before performing an MT inversion along the JI profile, a phase tensor analysis was conducted on the MT broadband stations [37]. The phase tensor is a second-rank tensor that contains the phase relationships of the MT impedance tensor [37]. An ellipse can be used to graphically represent the phase tensor, with the long axis of the ellipse indicating the direction of maximum current flow. The plot of the phase tensors given in Figure 9.8 is such that the ellipse can be thought of as a compass needle with north fixed at the top (vertical direction) of each figure. When the ellipse appears to be circular there is no direction of preferential current flow and the Earth is electrically homogeneous or 1D.

At small periods (high frequencies) all stations appear to be 1D Figure 9.8a, which is indicative of sedimentary environments. As the period increases the phase tensor decreases in size because there is a transition into a more resistive environment i.e., the basement. The transition into a more resistive environment occurs at successively longer periods as the horizontal distance increases, which means the depth of the overlying sediments is increasing. The phase tensors over the horst (horizontal distance between 0 km and 12 km) at long periods align in a north-east direction, suggesting the current flow is related to the north-east trending Trough. Stations at a horizontal distance of 18 km to 32 km also align but in a more northerly direction. This direction does not correspond with a known structure.

Station RM0111, at a horizontal distance of 17 km, has dissimilar phase tensor characteristics compared to the surrounding stations. The phase tensors align in an easterly direction at long periods. At very long periods adjacent stations sense the same subsurface structure and would be expected to have a similar response. The longest period in this survey is 85 s, which is not long enough to expect a similar response in adjacent stations. Therefore, the unusual behaviour of station RM0111 cannot be disproved and may be due to localised current flow. Both MT and joint inversions were executed with and without station RM0111 and produced similar results. For reasons of completeness, this station has been included in the discussion.

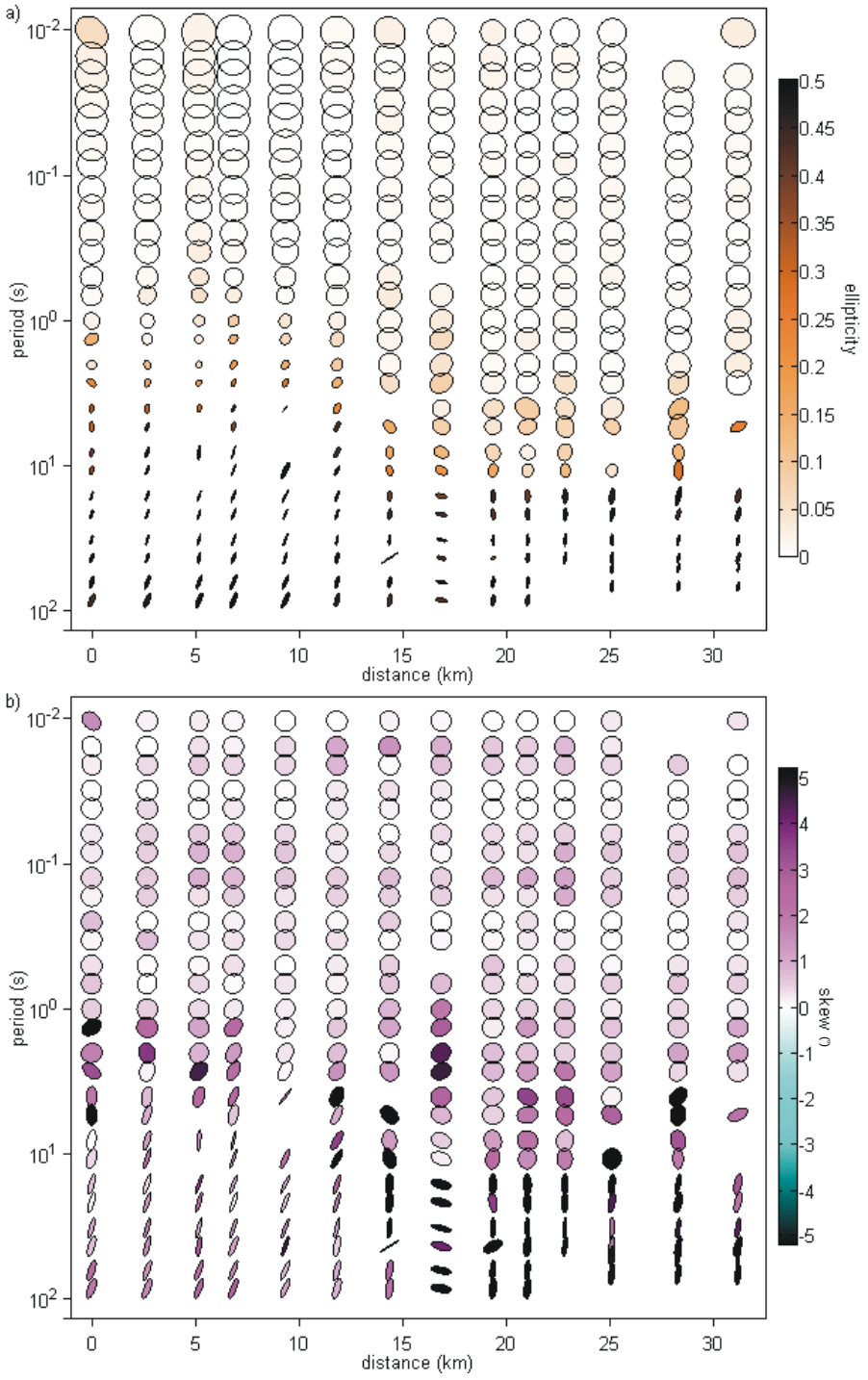

Figure 9.8: Phase tensor plot of the broadband MT data. In a) the phase tensor ellipses are coloured according to their ellipticity values. In b), the phase tensors have been normalised by their maximum axis values and coloured according to their skew angle values.

The phase tensors plotted in Figure 9.8a are coloured in accordance with their ellipticity values. The ellipticity value is a measure of the relationship between the maximum and minimum phase [37] [185]. When the ellipticity value is less than 0.1, it indicates data points that correspond to 1D electrical structure. In Figure 9.8a, when the phase tensors no longer appear circular, their ellipticity value becomes greater than 0.1. This joint phase tensor and ellipticity behaviour clearly defines the presence of the basement in the data. It is unknown if the increase in ellipticity value is due to 2D or 3D structure.

A skew angle is a measure of the tensor's asymmetry. When the skew angle is between $\pm 5^{o}$ the data correspond to 2D subsurface structures, outside of these bounds the data correspond to 3D structure [185]. Figure 9.8b shows the phase tensors coloured in accordance with their skew values. The ellipses have been normalised by their maximum axis value, allowing the skew colour to be visible. The colour scale is such that any black phase tensor relates to a data point that exhibits 3D behaviour. The main region of 3D data points is at long periods and a horizontal distance greater than 10 km. This area corresponds to the phase tensors aligning with an unknown structural feature. The cause of the 3D structure is unknown as the trough itself is primarily a 2D feature. There is insufficient station coverage to conduct a 3D inversion and the removal of the 3D points would significantly reduce the data set. Therefore, as the trough is predominantly 2D, the case study will proceed with a 2D inversion.

9.4.2 MT Model

The results of the MT inversion with a 5% data error, along the JI profile are shown in Figure 9.9. Diagram (a) does not fit the data to within the expected noise level but still has a relatively small RMS of 2.2, as can be seen graphically in Figure 9.10. The model response reproduced the trends and values of the observed data and there was no systematic misfit of the data. The MT model consists of a conductive (< 3 Ωm) zone down to a depth of 1 km, that appears patchy and could contain artifacts. The basement geometry appears to contain two vertical faults, with the west being the Hamley fault. The faults separate two resistive basement blocks

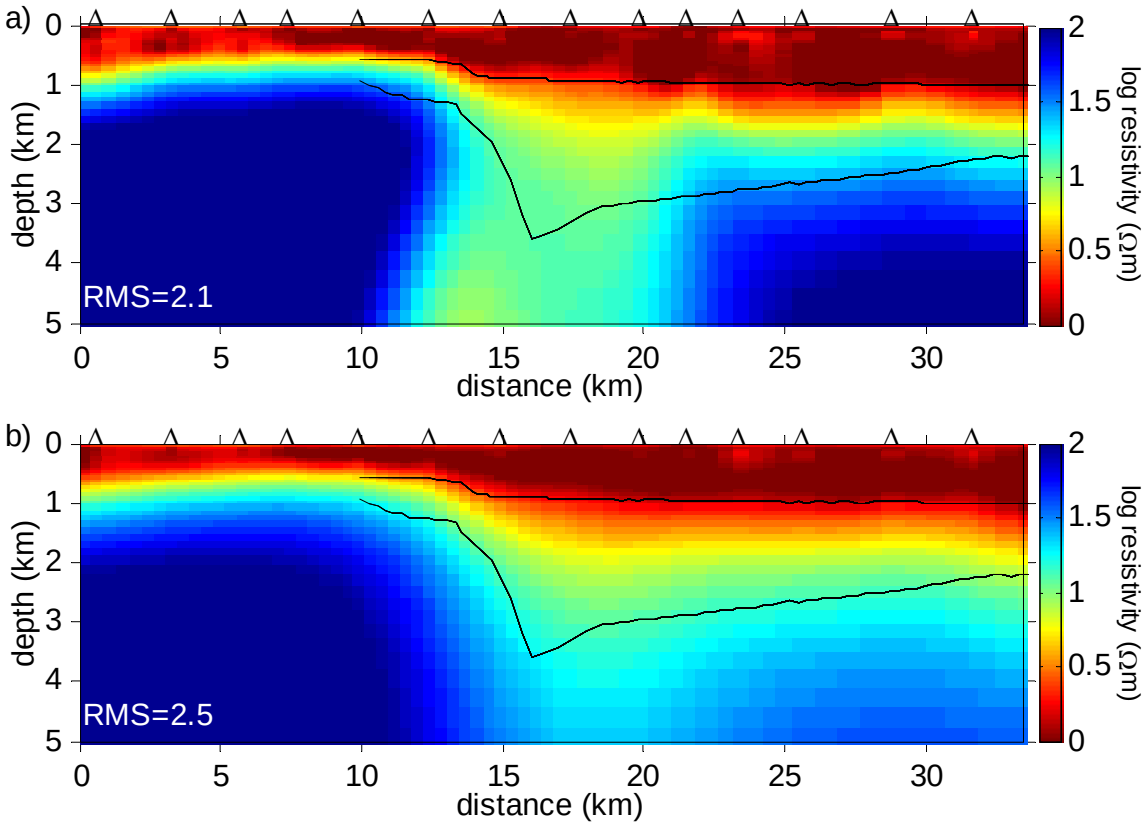

Figure 9.9: The resistivity models obtained from the MT inversions along the JI profile, with a) having a target RMS of 1 and b) a target misfit that is a 20% increase in the RMS of a). The black lines show the boundaries in the seismically-constrained gravity forward modelling from Figure 9.5.

(100 Ωm) from the slightly less resistive ($\sim$ 10 Ωm) trough, with the basement topography seen to be relativity flat. The western block has a depth to basement of $\sim$ 1.9 km and the eastern block has a depth to basement of $\sim$ 0.8 km, which falls away to $\sim$ 1 km at the far east end of the profile. The base of the trough cannot be resolved.

A 20% relaxation of the RMS value in Figure 9.9a was conducted to produce Figure 9.9b. The Hamley fault has now been correctly orientated but all features are heavily smoothed and their exact locations are hard to determine. Without prior knowledge of the area, it would be challenging to interpret the 20% relaxation model and reconcile the severe changes in the geometries of the features from the original MT model.

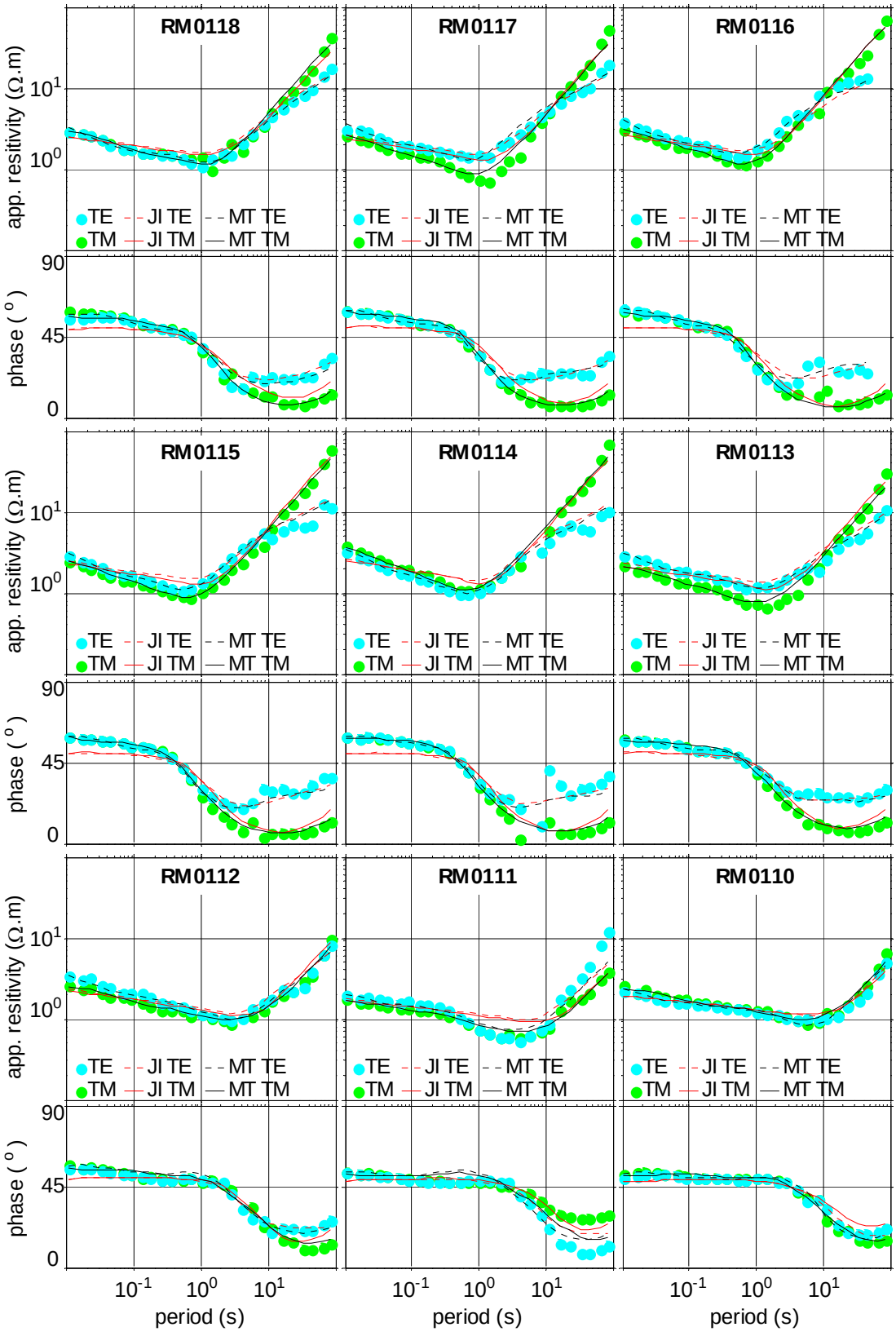

Figure 9.10: The observed MT data for stations along the JI profile, as shown in Figure 9.4. The model responses (amplitude and phase for both TE and TM modes) from the MT inversion are shown in black and the MT model responses from the joint inversion are shown in red.

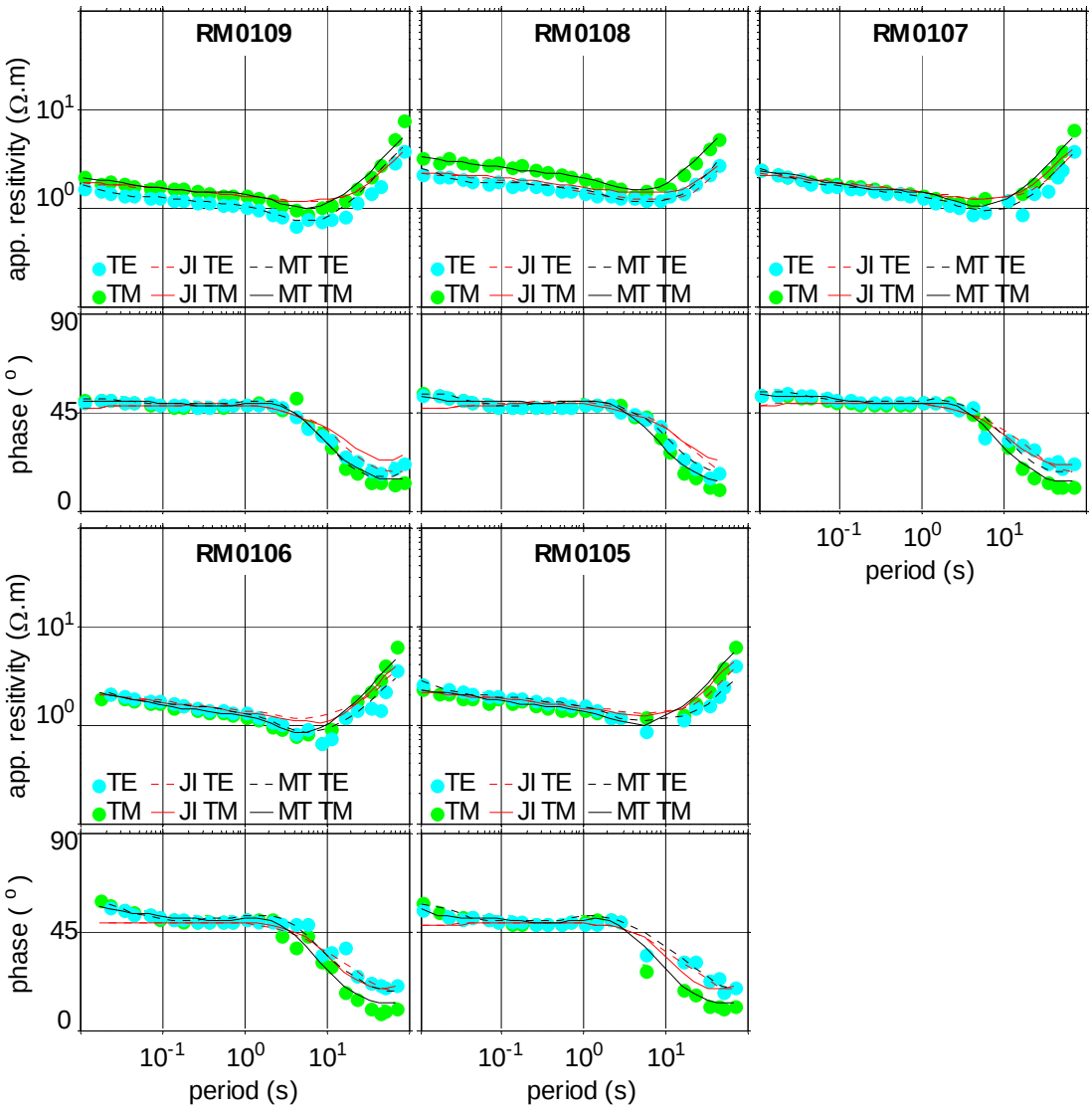

Figure 9.10 continued.

9.5 Joint Inversion

The joint inversion was executed with an MT error of 5%. A differential weighting scheme was applied towards fitting the gravity data to ensure that the MT data were well constrained. Rather than applying the weighting methods described in Section 8.3, which produced indifferent results, the weighting used here simply entailed the reduction of the estimated error level of the gravity data to 0.06 mGals, thus demanding a tighter fit.

In order to carry out the joint inversion, certain assumptions need to be made

about the parameters (constants) that appear in Archie's Law and the porosity-density relationship. Matrix density and fluid density, which appear in the porosity-density relationship, are assigned fixed values of 2400 kgm^{-3} and 1030 kgm^{-3} respectively. The lower matrix density is a reflection of the low density values used in Figure 9.5. The variables which need to be defined in Archie's Law are a, m_{cf} and fluid resistivity, with fractional saturation (S) assumed to be 1. The geological environment described in Section 9.1 indicates using a a- and m_{cf}-value combination from Table 5.1 of $a = 0.62$ and $m_{cf} = 1.72$ (for Mesozoic sediments) or $a = 0.62$ and $m_{cf} = 1.95$ (for Paleozoic sediments). Both sets of value combinations were tried but the joint inversion returned the best results with the more common values of $a = 1$ and $m_{cf} = 2$.

Fluid resistivity measured from the MC56 and Cooltong drill holes, shown in Figure 9.3, were $\sim$ 30 Ωm [186]. These measurements were made in the 1980's. Since that time the Murray River and its surrounds (see Figure 9.1) have undergone significant salinity and water level changes. In 2003 the formation fluid in the Renmark Trough area was listed as very saline, although current salinity or resistivity values are not given [186]. Irrespective of a specific value, these types of values only categorise the near-surface fluid resistivity environment. For the joint inversions, fluid resistivity values to a depth of at least 5 km need to be considered. Therefore, Equation 5.5 is used to define the fluid resistivity with depth. This equation requires a temperature gradient and the resistivity of water (ϱ_{w_o}) to be defined. No temperature information could be obtained for the Renmark Trough area. Given that it is located in SAHFA, high temperature gradients are expected. Through a process of trial and error it was found that the best joint inversion results, having the smallest RMS values, occurred between temperature gradients of 90 ^{o}Ckm^{-1} and 100 ^{o}Ckm^{-1} and a ϱ_{w_o} value between 0.1 and 0.2. It was found that the optimal parameter values, giving the lowest RMS overall, were selected values with a temperature gradient of 90 ^{o}Ckm^{-1} and ϱ_{w_o} value of 1.6 Ωm.

Figure 9.11 shows the porosity model obtained from the joint inversion. The joint inversion model is smooth and artifact free. In order to compare the result with the single gravity and MT inversions, the porosity model is converted to resistivity and

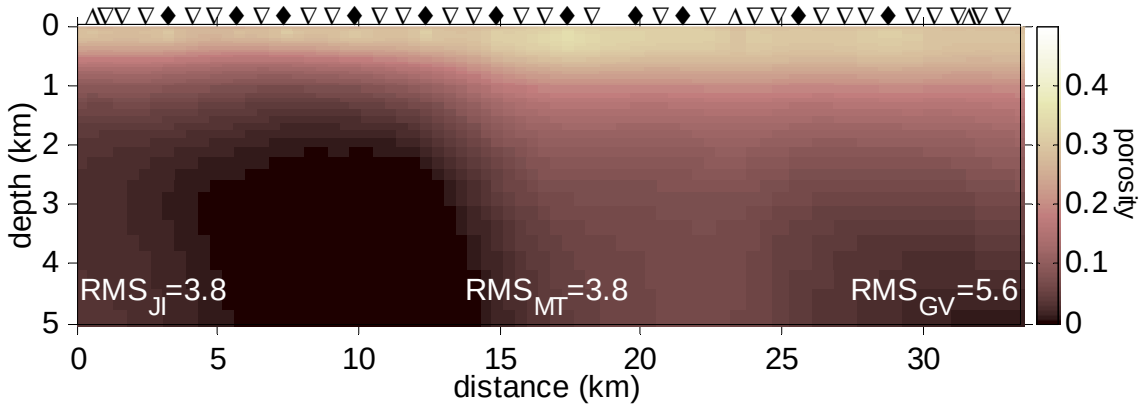

Figure 9.11: The porosity model obtained from a joint inversion along the JI profile. Black diamonds represent co-incident gravity and MT stations, triangles represent just MT stations and upside down triangles represent just gravity stations.

density models using the above discussed parameter values in Archie's Law and the porosity-density relationship. The joint inversion resistivity model is shown in Figure 9.12. Similar to the MT model, the joint inversion model has a conductive zone in the upper $1-2$ km depth range, although the joint inversion model is slightly more resistive. However, the basement structure between the MT and joint inversion resistivity models is significantly different.

In the joint inversion, the Hamley fault appears to have the correct inclination, compared to the vertical orientation in the MT model. The depth to the eastern basement block is also slightly lower in the joint inversion model and becomes less resistive at the far east of the model. This decrease in resistivity (porosity) could be a boundary effect, or more likely the result of lower observed gravity values over this area. The second fault that appears in the MT model is not prominent in the joint inversion model. Rather, the western block is situated at a greater depth. Neither the MT nor the joint inversion models can resolve the base of the trough. The joint inversion does however show higher conductivity values to a greater depth in this zone, indicating the presence of sediments to a greater depth.

In Section 7.1, when considering synthetic data examples, it was shown that the joint inversion is far superior to the Occam gravity inversion in reconstructing the subsurface structure. This is also the case here. However, the joint inversion

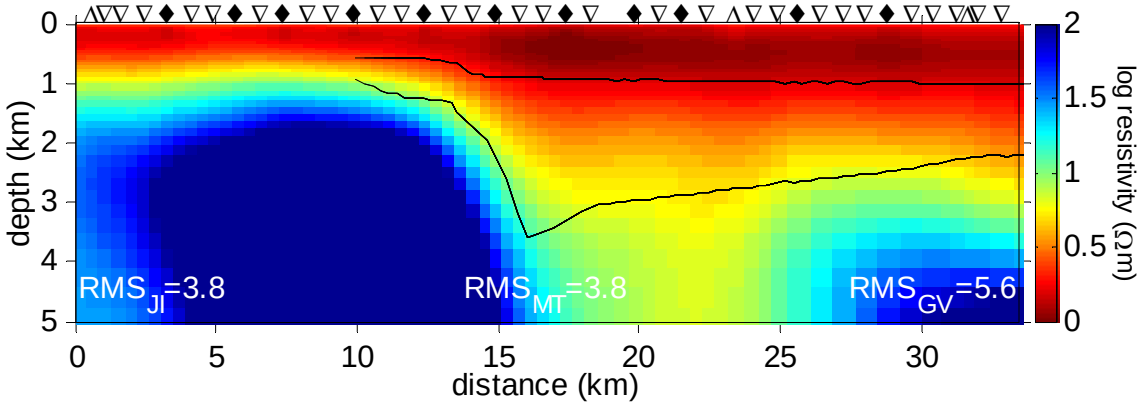

Figure 9.12: The resistivity model obtained from the joint inversion along the JI profile. It was produced by converting the porosity model to resistivity values using Archie's Law. Black diamonds represent co-incident gravity and MT stations, triangles represent just MT stations and upside down triangles represent just gravity stations. The black lines show the boundaries in the seismically-constrained gravity forward modelling in Figure 9.5.

density model, given in Figure 9.13, agrees with the seismically-constrained density model of Figure 9.5. The upper portion of the section has similar orientations and density values. The density values of the Devonian/Permian sediments are hard to compare because the joint inversion has smoothed this layer, while reproducing the basement. The basement geometries are broadly similar, although their actual values are different. The joint inversion cannot reproduce a basement density value of 2800 kgm^{-3}, since the maximum density corresponding to the matrix density is only 2400 kgm^{-3} when the porosity is zero.

The joint inversion model fits the gravity data well, as is evident from Figure 9.14. The computed model response does slightly underestimate the observed data between horizontal distances of 6 km and 15 km, which corresponds to the western basement block. A reason for this could be that a matrix density value of 2400 kgm^{-3} in the porosity-density relationship is adequate for the sediment component of the model, but is too low for the basement, and the porosity-density relationship may not even be applicable to the basement. If the basement topography was flat, it would have a constant gravity response and the gravity offset term would accommodate incorrect density values. At this distance, there is a $>$ 3 km

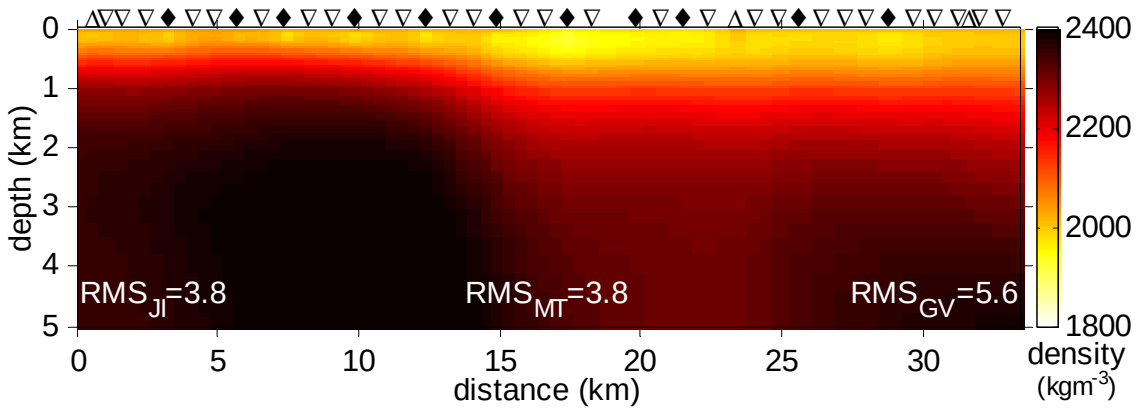

Figure 9.13: The absolute density model from the joint inversion along the JI profile. It was produced by converting the porosity model to density values using the porosity-density relationship. Black diamonds represent co-incident gravity and MT stations, triangles represent just MT stations and upside down triangles represent just gravity stations.

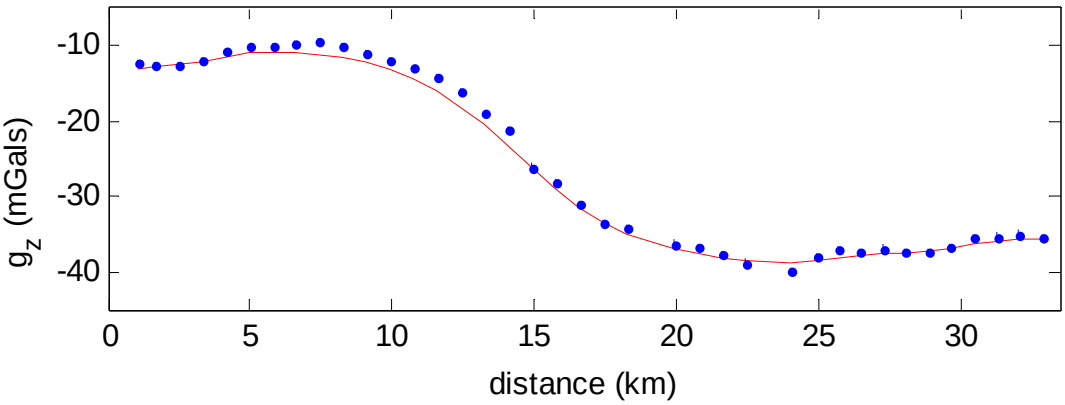

Figure 9.14: The observed gravity data are shown by blue dots and the joint inversion model response is shown by the red line.

topographic relief that cannot be accounted for by the gravity offset term.

The data fit for the single MT data inversion, as well as that of the joint inversion are shown in Figure 9.10. In general, the computed MT data for the joint inversion model reproduce the trends and values of the observed data of all stations rather well. However in the phase response there are two areas where they do not fit. At short periods, the model response underestimates the observed phase, and as the phases become greater than 45°, the observed data indicate a more conductive environment than is found for the joint inversion. At MT stations on the eastern end on the profile (stations RM0111 – RM0105), the model response overestimates the observed TM phase at long periods. This will be discussed further in Section 9.6.

Sensitivity Analysis

In Section 8.2.3 a method of evaluating the effect of the adjustable parameters in Archie's Law and the porosity-density relationship was outlined. This takes advantage of the implicit differentiation through the chain rule that is applied to the sensitivities (Jacobian matrix). Figure 9.15 shows the gravity sensitivity distributions with respect to the various parameters from the porosity-density relationship, viz., fluid density, matrix density and porosity. There are 3 and 10 orders of magnitude difference between the joint inversion sensitivity to porosity and the fluid and matrix densities, respectively. This demonstrates the joint inversion model is more robust to the fluid and matrix values than the porosity values.

The MT sensitivity distributions with respect to the parameters in Archie's Law, a, m_{cf} and temperature, are shown in Figure 9.16. The joint inversion model appears to have the greatest sensitivity to the porosity value. In the upper part of the section (< 1 km) the model has an increased sensitivity to the a- and m_{cf}-values. This could be a contributing factor to the misfit in the phase at short periods, as discussed earlier. The geology in the upper $1-2$ km is Tertiary in age, which normally has a- and m_{cf}-values of 0.88 and 1.37, respectively (Table 5.1). If these values were used in the Tertiary part of the section it would result in an increase in conductivity for the same porosity values. A joint inversion could be executed that has one set of a- and m_{cf}-values above 1 km and another set of a- and m_{cf}-values below 1 km.

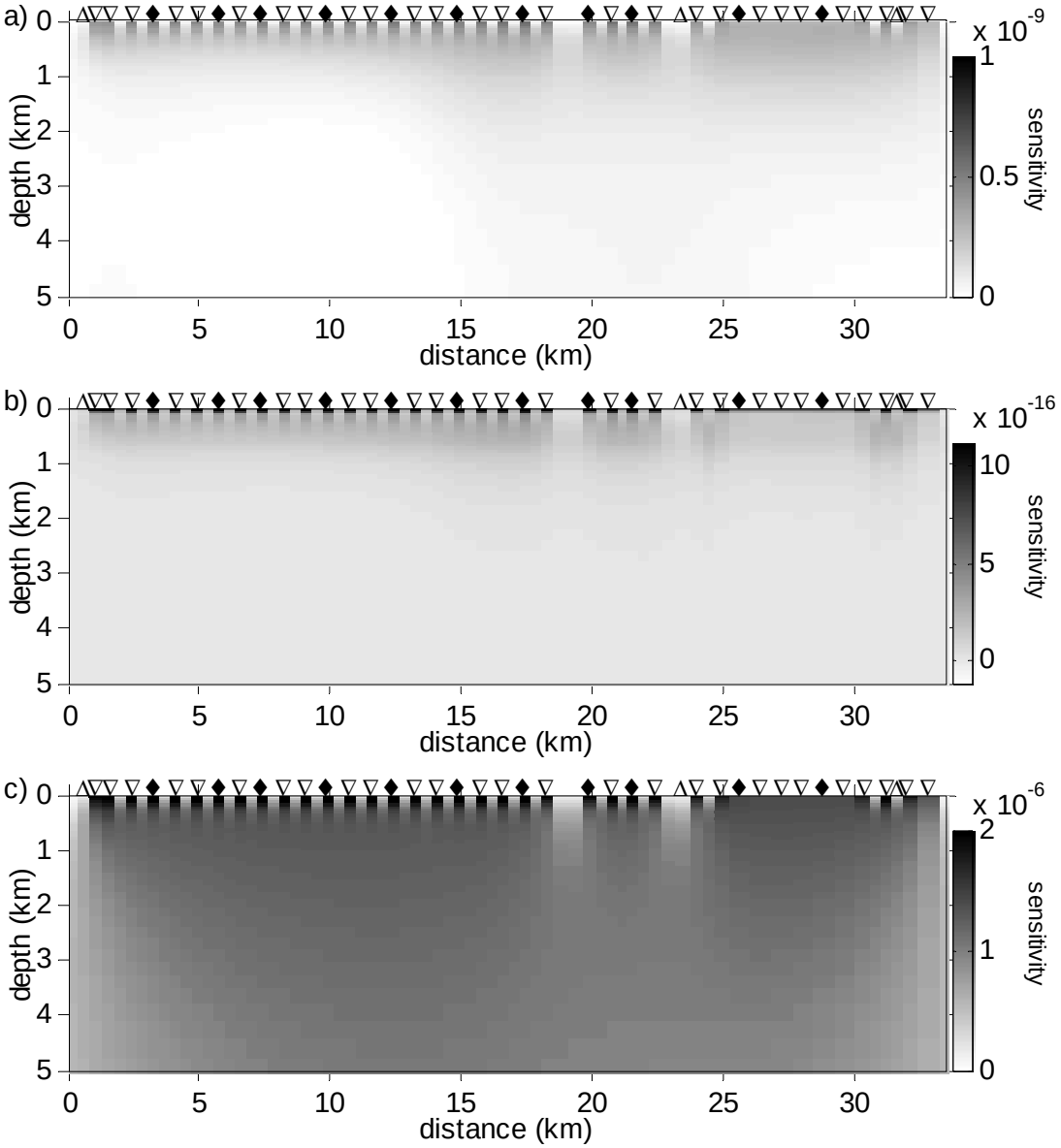

Figure 9.15: The gravity sensitivity distribution produced from a joint inversion of the Renmark Trough data. The sensitivity models are with respect to a) the fluid density, b) the matrix density and c) the porosity. Black diamonds represent coincident gravity and MT stations, triangles represent just MT stations and upside down triangles represent just gravity stations.

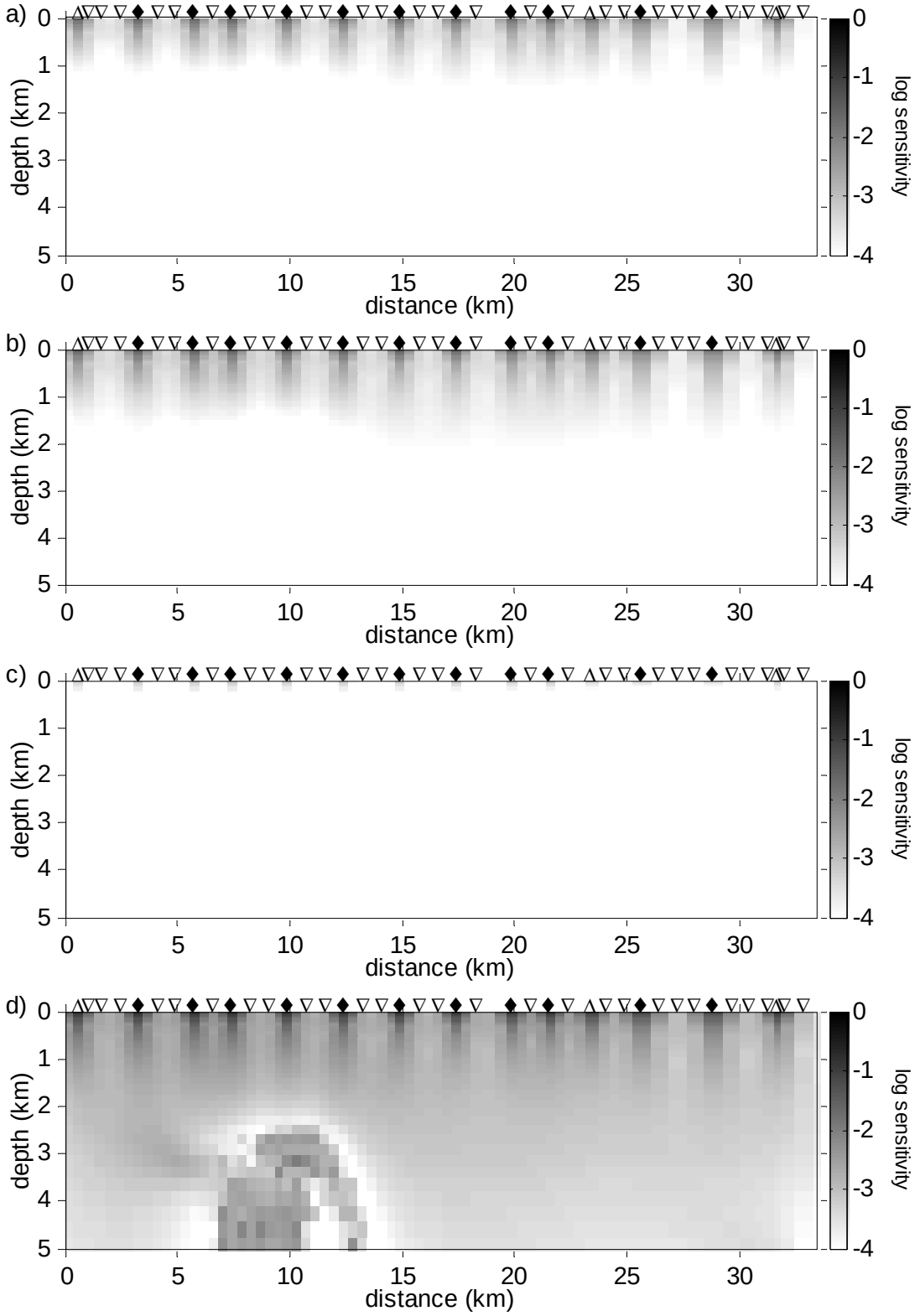

Figure 9.16: The MT sensitivity distribution produced from a joint inversion of the Renmark Trough data. The sensitivity models are with respect to a) the a-value, b) the m_{cf}-value, c) temperature and d) porosity, implicit in Archie's Law. Black diamonds represent co-incident gravity and MT stations, triangles represent just MT stations and upside down triangles represent just gravity stations.

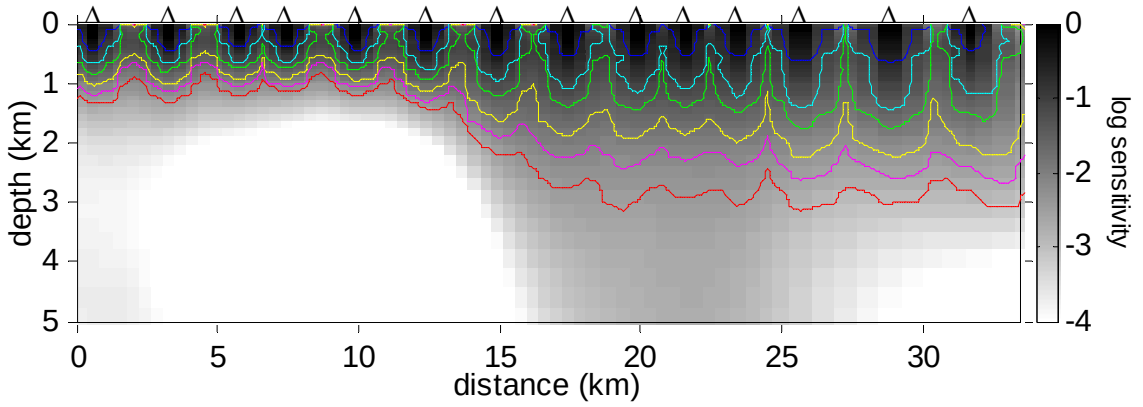

Figure 9.17: The MT sensitivity distribution model for the Renmark Trough joint inversion, with data change isoclines drawn, where blue = 1 Ωm, cyan = 5 Ωm, green = 10 Ωm, yellow = 25 Ωm, magenta = 50 Ωm and red = 100 Ωm.

Future work is to develop the joint inversion to be able to have different parameters in Archie's Law, and the porosity-density relationship, across different parts of the model.

Figure 9.17 was produced in accordance with the method outlined in Section 8.1.1, and shows the Schwalenberg *et al.* [170] style of sensitivity plot for the MT component of the joint inversion Jacobian. It is important to remember that the sensitivity plot is dependent on the final model. This figure shows that the MT data are sensitive to shallow features that are conductive and insensitive to resistive features, which is consistent with the results in Section 8.1.1. What this sensitivity plot suggests is that the MT data are insensitive to the variations in the resistivity of the Trough sediments and that they do not contain enough (long period) information to resolve the base of the Trough.

9.6 Discussion

Overlain on the MT and joint inversion resistivity models of Figures 9.9a and 9.12 respectively, are the seismically constrained boundaries of the gravity model from Figure 9.5. The upper conductive layer in both the MT and joint inversion models is consistent with the topmost 1km of sediments in the gravity model. The basement geometries of the joint inversion model and the gravity model are consistent.

However, the MT single inversion basement geometry is distinctly different, most notably the location and orientation of the Hamley fault and the geometry of the eastern basement block.

The curve of the observed gravity data is indicative of a normal fault. Therefore, constraining the MT data with the gravity data in the joint inversion produces the correct orientation of the Hamley fault. There is no information in the seismic reflection data or the gravity models which extends further south-west than the JI profile, to support a secondary large fault that is present in the MT model.

At the location of the suggested second fault and the eastern basement block in the MT inverted model, two observations correspond: (1) the skew values indicate the presence of 3D structure at long periods, and (2) the joint inversion at long periods does not fit the phase of the TM mode, which is sensitive to resistive boundaries. The presence of 3D structure, as indicated by the skew values, is manifest as a distinct fault and raised basement block in the 2D MT model. The joint inversion forces consistency between the MT and gravity data sets, thereby not fitting the long period TM mode phases as this subsequent structure is not supported by the gravity data. Therefore, the joint inversion does not put a resistive boundary into the model and thus does not estimate the basement depth correctly.

Through the joint inversion process some assumptions are made about the parameters in Archie's Law and porosity-density relationship. Only when these parameter values are correctly chosen as being close to the true subsurface values will an adequate data fit be achieved. This additional information helps to categorise the study area. The Renmark Trough area is being investigated for its geothermal potential and the additional temperature gradient and porosity values are of importance. Extracting this type of information from the individual MT or gravity data sets, without the constraint of a joint inversion, would be extremely difficult.

9.7 Conclusions

The Renmark Tough is a north-east trending half graben structure that was used to test the newly-developed MT and gravity joint inversion scheme. The broadband

MT inversion was hindered by the presence of data points that corresponded to 3D structure, as indicated by a phase tensor analysis. This resulted in a model with a basement geology which was inconsistent with seismically-constrained gravity forward modelling. In the joint inversion, the gravity data aided the MT data in correctly locating the basement features and producing a model that was consistent with all available geophysical data sets.

Chapter 10

Conclusions

The successful development, testing and application of a petrophysical MT and gravity joint inversion scheme has been described in this thesis. This joint inversion approach is based on a common parameter to which both techniques are sensitive, thus providing the effective means for integrating the information contained in both data sets. The MT and gravity joint inversion uses Archie's Law and the porosity-density relationship to express resistivity and density in terms of the common parameter 'porosity'. The 2D MT and gravity joint inversion scheme then produces a single unified porosity model that satisfies both data sets. Detailed synthetic data testing as well as application to field data through the Renmark Trough case study shows that the joint inversion is more effective in reconstructing the subsurface model than the MT and gravity inversions alone.

There is a diverse range of applications for the MT and gravity joint inversion, and these include:

- Determination of sedimentary basin structure, particularly in frontier basins where it offers a cheap alternative to seismics.

- Porosity-based pore pressure predictions, so as to categorise anomalous high porosity values to determine zones of overpressure [154].

- Exploration in sedimentary basins to determine the broad architecture of hydrocarbon and mineralisation systems.

- Application for geothermal exploration, as described through the case study in Chapter 9.

- Extension to applications other than sedimentary environments, since Archie's Law has been previously used to successfully predict the bulk conductivity values of oceanic and continental crust [141] [150] [151] [152].

10.1 Results Summary

A new gravity Occam inversion scheme was developed to form the gravity component of the joint inversion, and was discussed in Chapter 4. The single gravity inversion only places structure at the surface, which is then smeared into the model due to the smoothness constraint. The use of different grid configurations and a depth weighting function only marginally improved the result, highlighting the need for joint inversions in analysis of gravity data.

The benefits of combining MT and gravity techniques in a joint inversion were investigated in Chapter 5. The introduction of porosity, through Archie's Law and the porosity-density relationship, as the link between the MT and gravity data sets was established. This was then followed by a review of Archie's Law and the porosity-density relationship, and an examination of the joint porosity, conductivity and density behaviour.

The new MT and gravity joint inversion that inverts directly for a porosity model was outlined in Chapter 6. The conversion of this porosity model to a resistivity and density model uses Archie's Law and the porosity-density relationship. Responses of the conductivity and density models were calculated and compared to the observed MT and gravity data sets. Then, based on both techniques, the porosity model was updated. These steps were repeated in an iterative fashion until a porosity model was reached that satisfied the data from both techniques.

To test the newly developed joint inversion algorithm, several synthetic models (block, fault and trough models) were used (Chapter 7). It was shown that the joint inversion produced a smooth, artifact free model and yielded a better representation of the subsurface than was possible with single technique (MT or gravity) inversions.

The joint inversion was shown to be particularly useful in extracting coherent information from noisy MT data when the gravity error was small. It was found, by means of numerical experiments, that there is no optimal MT and gravity station configuration, although having an equal or greater number of gravity stations than MT stations produces better results. Better results were also obtained with denser station coverage. The joint inversion has similar resolving characteristics to the MT inversion, since the joint inversion only produced structure that was required by the MT data. However, the joint inversion was beneficial in reducing artifacts, imaging resistivity structures and improving the clarity of the subsurface features.

A new method for viewing the information contained in the Jacobian matrix was developed and used in a sensitivity analysis (Chapter 8). The column sum of absolute values of the Jacobian not only provided a cumulative subsurface sensitivity distribution model but also produced a crude measure of resolution for the MT and gravity techniques. The sensitivity analysis and subsequent joint inversions, using broadband and long period MT data, showed that broadband MT data were more compatible with the gravity data than long period MT data.

The perceived disadvantage of the petrophysical approach (as opposed to the structural approach) of not being able to deal with distinctly different and diverse subsurface environments was also investigated in Chapter 8. Although the new MT and gravity joint inversion algorithm was mainly restricted to sedimentary basin environments, computational testing and Jacobian matrix analysis showed that the joint inversion was robust to inaccuracies in the parameter values in Archie's Law and the porosity-density relationship. In general, the correct parameter values were indicated by the lowest RMS values. Once the appropriate parameters in Archie's Law and the porosity-density relationship had been established, they were able to provide greater understanding of the study area. To obtain this complementary information from the individual MT and gravity data sets (outside of a joint inversion) would be extremely difficult.

The Renmark Trough in South Australia is an area of current geothermal energy interest and provided a case study for the joint inversion which was given in Chapter 9. The single MT inversion produced a model that had basement geometries

conflicting with other geophysical data (seismic, gravity) and geological information in the area. However, the joint inversion produced a model that was consistent with all other geophysical data sets and known geology.

In this thesis, the development and characterisation of a new MT and gravity joint inversion has been achieved, and the petrophysical approach validated. Synthetic testing demonstrated the ability of the joint inversion to provide better reconstructions of the subsurface image than is possible using the single MT and gravity techniques. More importantly, the joint inversion was successfully applied to real world data and provided a greater understanding of this area than was achieved using the single techniques alone.

10.2 Outlook

Joint inversion of geophysical data sets is a topic of current major interest, both in academia as well as industry, for more effectively reconstructing the subsurface geology. The next few years are likely to see increased interest in this field. However until now, the focus of joint inversion research has been on the structural approach, whereby penalty terms are introduced into the objective function to favour models which yield similar structure from the inversion of each data set. In this thesis, it has been shown by means of synthetic and real data inversions that the petrophysical approach is a dynamic and viable joint inversion alternative, which certainly warrants continued research.

The MT and gravity joint inversion scheme could be extended by applying a dynamic weighting scheme, such as that detailed in Doetsch *et al.* [3]. Attempts to individually weight the MT and gravity data sets in the joint inversion (Section 8.3) produced indifferent results. However, dynamic weighting would involve changing the weighting values at each iteration to encourage both the MT and gravity RMS to have a value of 1. Alternatively, a Lagrange multiplier could be used to determine the right balance between the MT and gravity data sets. The inclusion of gravity data in the joint inversion aids in producing a smoother model than is achievable from an MT inversion alone Therefore, the smoothness constraint could be removed

and the Lagrange multiplier used instead to find the optimal balance between the MT and gravity data sets. The removal of the smoothness constraint would require careful consideration in order to prevent destabilising the inversion.

The sensitivity analysis presented in Section 8.1 could be extended to incorporate a resolution analysis by using variants of the singular value decomposition (SVD) method [74] [187] [188]. This resolution analysis could then determine the subsurface features that each technique is resolving, rather than the subsurface area to which each technique is sensitive.

An aim of this research was to develop a general methodology that is not only restricted to MT and gravity techniques. Thus the general methodology developed can be extended to 3D, or even expanded to include three or more techniques. Seismic data could be incorporated into the joint inversion through the Wyllie time-average law or the Gassmann quasi-static poroelastic equation, both of which relate seismic wave speed to porosity. This would enable these three techniques to be combined in a petrophysical joint inversion, which has not been attempted before. The addition of a seismic constraint could also allow the joint inversion to not only solve for porosity but also the fluid resistivity parameter in Archie's Law, thus providing an improved characterisation of the study area, with obvious applications to hydrocarbon exploration and development

Combining two different techniques that are sensitive to the same subsurface petrophysical quantity is not only restricted to MT and gravity data through porosity. Any geophysical data sets that have a common petrophysical link can be inverted in this way. One example is combining electrical resistivity tomography (ERT) and ground penetrating radar (GPR), through moisture content, which affects both the resistivity (for ERT) and the dielectric constant (for GPR wave speed and attenuation). Another alternative is to combine long period MT and seismics in a joint inversion. Here both the seismic wave speed and electrical resistivity have a common anisotropy strike direction in the mantle, due to the alignment of the [100]-axis of the olivine molecules. The research in this thesis lays a critical foundation for developing petrophysical joint inversions in a wide range of areas and applications.

Appendix A

Occam 2D Gravity Inversion User Manual

This manual outlines the file structure and steps involved in executing the 2D Occam gravity inversion from Chapter 4. The Occam gravity inversion reads in Bouguer anomaly data and outputs a density contrast model. The gravity inversion is based on the Occam 2D inversion code for MT data. Professor Steven Constable from the Scripps Institute of Oceanography (SIO) has made the Occam2DMT program is freely available and it can be downloaded from his website (*http://marineemlab.ucsd.edu*). The general Occam procedure is discussed in Constable *et al.* [80] and developed into 2D by deGroot-Hedlin and Constable [90].

A.1 Gravity Inversion Files

A summary of the required and optional INPUT and OUTPUT files are as follows:

Requited INPUT files: Gravity data file, STARTUP, INMODEL and MESH

Gravity data	Houses the gravity data information, including station locations and Bouguer anomaly gravity values and errors.
STARTUP	The inversion parameters and the initial model parameter values are defined here. Contains the name of the INMODEL, Gravity data file and Relate files.

INMODEL	Describes the regularisation grid and contains the name of the MESH file.
MESH	Describes the finite element mesh.

Optional INPUT files: Depth Weighting file and Prejudice file

Depth Weighting	Contains the depth weighting values
Prejudice	Allows the model parameters to be weighted towards a specific model.

OUTPUT files: LogFile.logfile ITERxx.iter, RESPxx.resp

LogFile.logfile	Is a detailed summary of the inversion parameter and steps taken during the inversion process.
ITERxx.iter	Outputted at every iteration it contains the inversion and model parameters for the iteration number given by the xx.
RESPxx.resp	Outputted at every iteration it gives the model response for the iteration number given by the xx.

A.2 File Structure

In developing the Occam gravity inversion minimal changes to the file structure are made in order to allow for easy transition between the MT, gravity and joint inversions. The file structure of the Gravity data file, INMODEL, MESH, Prejudice file, LogFile.logfile ITERxx.iter, RESPxx.resp are the same as the joint inversion, therefore see Appendix B.2 for these file templates. The only difference is in the STARTUP file from Appendix B.2, are the model parameters listed are density value, which make up the density contrast model, and the `MT DATA FILE`, `RELATE FILE` and `GRAVITY OFFSET` items are not required. The gravity inversion only requires one iteration therefore in the startup file the item `ITERATIONS TO RUN:` should always be one.

There is a separate gravity inversion which executes the depth weight discussed in Section 4.5.2. The depth weighting constants are containing in a file that has to be called 'IRUF5values.dat' and has the format below.

`BETA:`	`1.5`	β_* *value*
`Z zero:`	`20`	z_0 *value*

A.3 Programs Required

The programs needed in the gravity inversion procedure are listed below. They are used to set up the input files and view the output files.

Makemodel2D.exe	Fortran90	Creates the STARTUP, INMODEL and MESH files from the input gravity data files. Modified from the SIO program for Occam2DMT.
Occam2DGrav.exe	Fortran90	Main program and executes the MT and gravity joint inversion.
plot2DmodelGrav	MatLab	Plots the density contrast model for a specified iter file, requires iter, INMODEL, MESH, Gravity data files. Modified from the SIO program for Occam2DMT.
plotGVRESP	MatLab	Plots the model response and original data for a specified resp file, requires resp, gravity data files. Modified from the SIO program for Occam2DMT.

A.4 Procedure

Start by creating the gravity data files and ensure the offsets values are accurate. To create the model files the makemodel2D.exe can be used. It requires the gravity data file as input and will output the STARTUP, INMODEL and MESH files. Use the plot2DmodelGrav MatLab program to view the model and to make sure the model parameterisation has the desired characteristics.

To execute the gravity inversion, ensure STARTUP, INMODEL, MESH and gravity data files are in the same folder as the Occam2DGrav.exe executable. Open the executable and in the words of Occam 'sit back and relax'. As Occam runs it will print to the screen information for every μ value and model parameter that has been tested.

The model response compared to the observed data can be viewed using the plotGVRESP. To view the porosity model use the plot2DmodelGrav MatLab program.

Appendix B

Occam 2D Joint Inversion User Manual

This manual outlines the file structure and steps involved in executing a magnetotelluric (MT) and gravity joint inversion. MT is sensitive to the subsurface resistivity distribution, where as gravity is sensitivity to the subsurface distribution of density. Resistivity and density can be related to porosity through Archie's Law and the porosity-density relationship. This joint inversion inverts directly for a porosity model which is constrained by both the MT and gravity data using these equations.

The joint inversion is based on the Occam 2D inversion code for MT data. The Occam2DMT program is freely available, courtesy of Professor Steven Constable from the Scripps Institute of Oceanography (SIO), and it can be downloaded from his website (*http://marineemlab.ucsd.edu*). The 1D Occam procedure is outlined in Constable *et al.* [80] and developed into 2D by deGroot-Hedlin and Constable [90].

B.1 Joint Inversion Files

A summary of the required and optional INPUT and OUTPUT files are as follows:

Requited INPUT files: MT data file, Gravity data file, STARTUP, MESH, INMODEL and Relate file

MT data — Houses the MT data information, including station locations,

	frequencies, TE and TM apparent resistivity and phase values and errors.
Gravity data	Houses the gravity data information, including station locations and Bouguer anomaly gravity values and errors.
STARTUP	The inversion parameters and the initial model parameter values are defined here. Contains the name of the INMODEL MT data file, Gravity data file and Relate files.
INMODEL	Describes the regularisation grid and contains the name of the MESH file.
MESH	Describes the finite element mesh.
Relate	Contains the values of the variables used in Archie's Law and the porosity-density relationship. Weighting of the MT and gravity data sets is defined here.

Optional INPUT files: Statics file and Prejudice file

Statics	Allows for static shift parameters in the MT data to be solved for.
Prejudice	Allows the model parameters to be weighted towards a specific model.

OUTPUT files: LogPlot.logplot, LogFile.logfile ITERxx.iter, RESPxx.resp

LogPlot.logplot	Has a summary of the total RMS, RMS_{MT}, RMS_{GV}, μ value and roughness value for each iteration.
LogFile.logfile	Is a detailed summary of the inversion parameter and steps taken during the inversion process.
ITERxx.iter	Output at every iteration, it contains the inversion and model parameters for the iteration number given by the xx.
RESPxx.resp	Output at every iteration, it gives the model response for the iteration number given by the xx.

B.2 File Structure

In expanding the Occam2DMT inversion to a joint MT and gravity inversion, minimal changes to the file structure are make in order to allow for easy transition between the MT, gravity and joint inversions. Due to the similarity with the original Occam2DMT inversion the majority of the below information is taken directly from the Occam2DMT release notes [168]. Most files are very meticulous about spacing and order of items listed. Unless otherwise stated the order of items must appear as in the template and after any colon Occam assumes that the values begin at or after the 18^{th} character.

B.2.1 Data Files

MT Data File

`FORMAT:`	`OCCAM2MTDATA_1.0`	
`TITLE:`	`Whatever you like`	
`SITE:`	`4`	*Number of stations being used.*
`mt01`		*List of station names in location order, the number*
`mt02`		*of listed names needs to equal the value in* `SITE`.
`mt03`		
`mt04`		
`OFFSETS:`		*List of station locations along the 2D line in meters*
`-1000`		*and ascending order. The spacing between stations*
`0`		*needs to be accurate not their physical location.*
`1000`		*The 1^{st} offset corresponds to the 1^{st} listed station.*
`2000`		
`FREQUENCIES:`	`3`	*Number of frequencies to be used in the inversion.*
`1.000`		*List of frequencies in decreasing order. All of the*
`0.100`		*frequencies need to be used in the the next section*
`0.010`		

```
DATA BLOCKS:  36  Number of data points in the next section.
SITE    FREQ    TYPE    DATUM    ERROR              See below.
1       1       1        2.03    0.43
1       1       2       46.7     2.90
1       1       5        1.97    0.43
1       1       6       45.2     2.90
etc.
```

The columns containing the data information are:

- `SITE` The station of the data point, 1 relates to the 1^{st} station listed, 2 will relate to the 2^{nd} station listed, etc...
- `FREQ` The frequency of the data point, 1 relates to the 1^{st} frequency listed, etc...
- `TYPE` The type of the data point being described, 1 = TE apparent resistivity (log10), 2 = TE phase, 5 = TM apparent resistivity (log10), 6 = TM phase. Other `TYPE` options are available in the Occam2DMT but have not been tested in the joint inversion.
- `DATUM` Data value.
- `ERROR` Error of the data value.

Gravity Data File

```
FORMAT:  OCCAM2GVDATA_1.0
TITLE:   Whatever you like
SITE:    4          Number of stations being used.
gv01                List of station names is location order, the number
gv02                of listed names needs to equal the value in SITE.
gv03
gv04
```

```
OFFSETS:            List of station locations along the 2D line in meters
-500                and ascending order. The spacing between stations
0                   needs to be accurate not their physical location.
500                 The 1st offset corresponds to the 1st listed station.
1000
DATA BLOCKS:  36    Number of data points in the next section.
SITE    TYPE    DATUM    ERROR                  See below.
1       51      10.4     0.06
2       51      11.7     0.06
3       51      11.9     0.06
4       51      13.1     0.06
etc.
```

The data information in the gravity data file is the same as the MT data file, except there is no frequency information and the `TYPE` value corresponds to the vertical location of a station. If the `TYPE` value is `51` the station will get located at the top of the grid. If the `TYPE` value is `52` the station will get located on a user defined topographic or bathymetric surface. Due to the processing required to produce Bouguer anomaly data this option would rarely, if ever get used.

B.2.2 Model Files

STARTUP File

```
FORMAT:             OCCAMITER_FLEX
DESCRIPTION:        Whatever you like
MODEL FILE:         INMODEL      Name of INMODEL file.
MT DATA FILE:       MTfile.dat   Name of MT data file.
GRAV DATA FILE:     GVfile.dat   Name of gravity data file.
RELATE FILE:        relate.dat   Name of relate file.
DATE/TIME:          Dec10
ITERATIONS TO RUN:  25           Number of iterations to run.
```

TARGET MISFIT:	1	
ROUGHNESS TYPE:	1	1 - *No horizontal aspect weighting*
		2 - *No horizontal aspect weighting*
DEBUG LEVEL:	0	*Set to 0 minimizes the amount of "chatter" displayed while running, 1 (default), displays progress, 2 displays diagnostic info and instead of using a "golden section search" to find the minimum RMS during an iteration it uses a brute-force scan which is time consuming, but useful if the inversion is in an area containing local minima.*
ITERATION:	0	*Lets Occam know the iteration number the model parameters correspond to.*
GRAVITY OFFSET:	0	*The optimal gravity offset value*
LAGRANGE VALUE:	5.000	
ROUGHNESS VALUE:	0.100E+11	
MISFIT VALUE:	1000.000	
MISFIT REACHED:	0	*A flag indicating if the target misfit has been reached, 0 is no and 1 is yes.*
PARAM COUNT:	4048	*The number of parameter corresponding*
0.1		*to free blocks in the regularisation grid,*
0.1		*followed by a list of initial porosity values.*
etc.		

The order of the items in the startup file is unimportant, except that the last item must be `PARAM COUNT`, Occam assumes that the model parameter values immediately follow this line. Optional variables that can appear in the STARTUP file are given below. If an option appears in the startup file but not required it can be commented out by placing a `!` at the start of the line.

MODEL LIMITS:	min,max	*Limits on the values that the model parameters may take.*
MODEL VALUE STEPS:	step	*Discretises model parameter space into steps "stepsize" large (e.g. for step=*0.1*, values allowed will be* 0.1, 0.2, 0.3, *etc, subject to whatever* MODEL LIMITS *you have imposed).*
STEPSIZE CUT COUNT:	8	*Limits the number of times Occam cuts the step size in a search for a better fitting model. If this count is exceeded, Occam will end the iteration prematurely on the grounds that the best fitting model may have already been found, even though the* TARGET MISFIT *has not been reached.*
DIAGONAL PENALTIES:	0	*Normally, Occam only calculates roughness penalties horizontally and vertically. If set to 1 diagonal penalties are added to the horizontal and vertical.*

INMODEL File

FORMAT:	OCCAM2MTMOD_1.0	
MODEL NAME:	Whatever you like	
DESCRIPTION:	Descriptive text	
MESH FILE:	MESH	*Name of MESH file.*
MESH TYPE:	PW2D	
STATICS FILE:	none	*Name of static file, no file indicated by none.*
PREJUDICE FILE:	none	*Name of prejudice file, no file indicated by none.*
BINDING OFFSET:	-876.9	*The location along the 2D profile of the right-hand side of the left-most regularisation not MESH model block.*

```
NUM LAYERS:  43
```
Number of model blocks layers defined here.

The following describes how the mesh cell are grouped together to make the regularisation grid and must directly follow `NUM LAYERS`.

```
2   64
```
Above is the first in the pair of lines that describes a layer of regularisation model blocks. The first number is the number of mesh layers that are aggregated in this model layer. The second number is the number of horizontal model blocks in this layer – as described by the next line.

```
7 2 2 2 2 2 2 2 ...  2 2 2 2 2 7
```
Above is the second in the pair of lines that describes a layer of regularisation model blocks. Each number here describes the number of mesh blocks that are aggregated in each model block. The sum of this line must equal the sum of columns in the mesh. This sequence of two lines is repeated `NUM LAYERS` *of times and should account for all cells in the mesh file.*

```
1   33
7 4 4 4 4 4 4 4 ...  4 4 4 4 4 7
...
1   12
7 10 10 10 10 ...  10 10 10 10 7
...
4  4
7 62 62 7
Number Exceptions:  -45
288  289  0
298  299  0
```

It is usual in MT to make the model bricks larger as the layers go deeper in the model. The model should narrow down to a half-space or nearly one at the bottom. However, the Occam code requires that the model block boundaries line up with the boundaries of the blocks above. If this is not the case, the program will still run, but roughness penalties will not be calculated properly for the lower blocks.

Discontinuities or changes in the roughness penalty calculations can be specified using the `Number Exceptions` in this file (default `0`). This allows you to specify blocks between which there should be either no penalty or modified penalty. There are two ways to do this, the easiest of which is shown here. If you specify a negative number of exceptions, then Occam expects the line to be followed by three columns of numbers: block #1, block #2, weight on the exception between them. Use the MatLab routine plot2DModelPoro to show the block numbers in your model. By specifying a zero weight, you remove the penalty between the blocks. Weight less than 1 decreases the penalty between blocks, while weight greater than 1 increases the penalty. Also, you can create new relationships between two blocks (for example, the left and right edges of the model) by specifying block numbers and a weight of 1.0.

MESH

`0 153 83 0 0 2`	*Mesh specification, see below.*
`15000 11000 7000 1000 500`	*Column widths in meters.*
`250 250 250 250 250`	
`250 250 250 250 ...`	
`12 12 25 25 50 50`	*Layer heights in meters.*
`100 100 150 150 200 200`	
`250 250 300 300 350 ...`	
0	*Always a zero.*
`????????????????????????????`	*Parameter specification, see below.*
`????????????????????????????`	
`????????????????????????????`	
`????????????????????????????`	

The mesh specification are as follows:

1^{st} value	Always zero
2^{nd} value	Number of horizontal "nodes" (columns +1)

3^{rd} value	Number of vertical "nodes" (layers +1)
4^{th} value	Number of fixed porosities in the mesh, can have up to 34 which does not including seawater. Value usually zero but if not the next line is a list of the fixed porosity values.
5^{th} value	Always zero
6^{th} value	Always two

Parameter specification is tedious. There must be four lines of '?' for each layer in the mesh. The four lines contain symbols which represent the value of four triangles in each mesh cell. Imagine that each mesh cell is cut by two diagonal lines, making four triangles. These four lines stand for the top, left, bottom, and right-hand triangles of each call in a layer. The character indicates what porosity value is to be assigned to the triangle. '?' means that the triangle is a free parameter to be calculated. 'Z' means that the triangle contains seawater and '0' (zero) means that it contains air. Numbers '1' through to '9' and other letters 'A' through 'Y' indicate fixed porosity values as specified above.

Fixing mesh cell values and subsequent regularisation blocks means there is a reduction in the number of free model parameters. This means the number of parameters in the STARTUP file will also be reduced. Fixing structure required a dance between the MESH, INMODEL and STARTUP file to maintain consistence.

B.2.3 Relate File

There are two file formats depending on if fluid properties are fixed with depth, OCCAM2DPAJI_FIXED or changing with depth, OCCAM2DPAJI_DEPTH.

```
FORMAT:            OCCAM2DPAJI_DEPTH
DESCRIPTION:       Whatever you like
MT misfit weight:  1   Used for weighting data sets, see below.
MT jac weight:     1   Used for weighting data sets, see below.
GV misfit weight:  1   Used for weighting data sets, see below.
GV jac weight:     1   Used for weighting data sets, see below.
```

`base switch:`	0	*Always zero.*
`termination:`	`semi`	*Fluid property depth termination options, see below.*
`matrix density:`	2650	*Matrix density in* kgm^{-3}.
`air density:`	0	*Air density in* kgm^{-3}.
`temp gradient:`	20	*Temperature gradient, in* $^{\circ}\mathrm{Ckm}^{-1}$, *used to calculate fluid resistivity.*
`surface temp:`	20	*Surface temperature, in* $^{\circ}\mathrm{C}$, *used to calculate fluid resistivity.*
`press gradient:`	9.9	*Pressure gradient, in* MPakm^{-1}, *used to calculated fluid density.*
`surface press:`	1	*Surface pressure, in* MPa, *used to calculate fluid density.*
`salinity:`	35	*Salinity, in* gl^{-1}, *used to calculate fluid density*
`archies s:`	1	*Fractional saturation.*
`archies a:`	1	*Tortuosity factor.*
`archies m:`	2	*Cementation factor.*
`archies n:`	2	*Saturation exponent and has to be last item.*

`FORMAT:`	`OCCAM2DPAJI_FIXED`	
`DESCRIPTION:`	`Whatever you like`	
`MT misfit weight:`	1	*Used for weighting data sets, see below.*
`MT jac weight:`	1	*Used for weighting data sets, see below.*
`GV misfit weight:`	1	*Used for weighting data sets, see below.*
`GV jac weight:`	1	*Used for weighting data sets, see below.*
`base switch:`	0	*Always zero.*
`matrix density:`	2650	*Matrix density in* kgm^{-3}.
`air density:`	0	*Air density in* kgm^{-3}.
`fluid density:`	1030	*Fluid density in* kgm^{-3}.
`fluid resis:`	0.1	*Fluid resistivity, in* $\Omega\mathrm{m}$.

`archies s:` `1` *Fractional saturation.*

`archies a:` `1` *Tortuosity factor.*

`archies m:` `2` *Cementation factor.*

`archies n:` `2` *Saturation exponent and has to be last item.*

The order of items is unimportant except `archies n` must always be the last item listed.

There are currently two joint inversion programs that are identical, except one incorporates the weighting factors of the MT and gravity data sets as outlined in Chapter 8. For the program which does not execute the weighting, the weights should be `1`. When weighting the joint inversion a positive `MT misfit weight` value weights the MT data points according to this value, similarly with the `GV misfit weight` value and the gravity data points. A `-98` or `-99` value for both MT and gravity weighting will execute the l_2 and l_1 Jacobian weighting, respectively. Jacobian weighting is discussed in Chapter 8. The `MT jac weight` and `GV jac weight` can be used to weight their respective components of the Jacobian. This alters how the model space is searched without weighting the data and subsequent RMS values. A direct Jacobian weighting value of `1` would normally be used.

The joint inversion calculates fluid resistivity and density using values of the pressure and temperature items above. The fluid resistivity with depth is calculated using Equation 8.4. This equation only holds true when temperature is < 300 °C. The fluid density with depth can be calculated with an Equation 5.2, similarly it holds true with temperatures between 20 °C and 350 °C and pressures between 5 MPa and 100 MPa. The `termination` item gives four options on how to terminate the fluid property calculation with depth in order to keep with in the temperature and pressure bounds. The fluid resistivity and density values on termination are the value used for the remainder of the depths. The options are as follows.

`none` The calculation for the fluid properties is not terminated, which means the temperature and pressure values will exceed their bounds.

`depth` Terminates the fluid properties calculations at a specified depth and requires the `term depth` item, in m, to be in relate file.

`value` Terminates the fluid properties calculations at a specified temperature and pressure value and requires the `max temp` item, in °C, and `max press` item, in MPa, to be in the relate file.

`semi` The fluid density is fixed and requires the `const flu den` item, in kgm^{-3}, to be in the relate file. The fluid resistivity calculations are terminated at a specified depth and requires the `term depth` item, in m, to be in the relate file.

B.2.4 Optional Input Files

The statics and prejudice files are optional files which are called in the INMODEL file.

Statics File

`FORMAT:`	`OCCAM2MTSHIFT_1.0`	
`DESCRIPTION:`	`Whatever you like`	
`DATA FILE:`	`Data.dat`	*Not used.*
`CONSTRAINT TYPE:`	`0`	*Type of summing constraint available in static processing, 0 = no summing constraint, 1 = add a constraint involving the TE+TM sum, 2 = add separate constraints for TE+TM sum.*
`CONSTRAINT ERROR:`	`0.1`	*Error value used for the sums if the* `CONSTRAINT TYPE` *is* `1` *or* `2`
`NO. SHIFT BLOCKS:`	`12`	*Number of rows of data below.*

`SITE`	`TYPE`	`SHIFT`	`INVERT/NOT`	*Shift data see below.*
`1`	`1`	`0.0`	`1`	
`1`	`5`	`0.0`	`1`	
`2`	`1`	`0.0`	`1`	

etc.

The shift data identifies the shift data. The `SITE` and `TYPE` are the same as the MT data file. The `INVERT/NOT` flag indicates whether to invert for this parameter

(flag = 1) or to accept the value in the SHIFT column (flag = 0). Static shift data are output in the iteration files following the spatial model parameters.

Prejudice File

FORMAT:	OCCAM2MTPREJ_2.0	*Specifies this file format*
NO. PARMS:	27	*Number of rows below.*
32 0.70	1.0	*See below.*
33 0.70	1.0	
34 0.65	0.8	

etc.

The three columns of listed numbers correspond to the parameter number, prejudice value, and prejudice weight. The parameter number is the 1-based number of the model parameter or static shift parameters. Static shift parameter numbers begin after the model parameter numbers.

B.2.5 Output Files

The iteration file has the same file format as the startup file such that it could be used as the startup file in subsequent inversions. The LogFile and LogPlot are self-explanatory when opened. The resp file contains the models response for all given MT and gravity data points. In the resp file, the rows correspond to MT data points, which is followed by the gravity data points. There are seven columns in the resp file and, using heading form the data files, are as follows.

SITE FREQ TYPE *zeros* DATUM model response $\frac{\text{DATUM}-\text{model response}}{\text{ERROR}}$

The SITE value is the value used in the MT or gravity data file. That means station 1 for MT data is not the same as station 1 for the gravity data. Use the TYPE value to know if MT or gravity data are being described. The gravity data contain no frequency information, therefore the FREQ column will be zero for a gravity data point.

B.3 Programs Required

The programs needed in the joint inversion procedure are listed below. They are used to set up the input files and view the output files.

Makemodel2D.exe	Fortran90	Creates the STARTUP, INMODEL and MESH files from the inputted MT and gravity data files. Modified from the SIO program for Occam2DMT.
Occam2DJI.exe	Fortran90	Main program and executes the MT and gravity joint inversion.
plot2DmodelPoro	MatLab	Plots the porosity model for a specified iter file, requires iter, INMODEL, MESH MT and gravity data files. Modified from the SIO program for Occam2DMT.
plotJIRESP	MatLab	Plots the model response and original data for a specified resp file, requires resp, MT and gravity data files. Modified from the SIO program for Occam2DMT.

B.4 Procedure

Setup Input Files

Start by creating the MT and gravity data files. Ensure the MT data have been rotated to the direction of the survey line. The magnetic and electric fields of the TE and TM mode should be either parallel or perpendicular to the survey line. Take care in ensuring the MT and gravity offsets values are accurate and are in relation to the same 2D survey line and reference point. The number of MT and gravity stations and their location does not have to be the same.

To create the model files the makemodel2D.exe can be used. It requires the MT and gravity data files as input and will output the STARTUP, INMODEL and MESH files. Use the plot2DmodelPoro MatLab program to view the model and to make sure the model parameterisation has the desired characteristics. Using

makemodel2D.exe will ensure there is a node (or MESH block boundary) at every MT and gravity station location.

Execute Joint Inversion

To execute the joint inversion, ensure STARTUP, INMODEL, MESH, relate, MT and gravity data files are in the same folder as the Occam2DJI.exe executable. Open the executable and in the words of Occam 'sit back and relax'. As Occam runs it will print to the screen information for every μ value and model parameter that has been tested. This information including the frequency number from calculating the MT forward model, the maximum and minimum porosity values, the gravity offset value, the μ value, and the total, MT and gravity RMS values. For each iteration Occam will also output the associated ITERxx.iter and RESPxx.resp files in the same folder as the executable. These files can be viewed while the inversion is still running to monitor its progress.

View Results

The model response compared to the observed data can be viewed using the plotJIRESP. To view the porosity model use the plot2DmodelPoro MatLab program. It has four options as follows.

Porosity	Plots the porosity values in the iter file.
Porosity Residual	Subtracts a specified model from the porosity values in the iter file and plots this.
Resistivity	Uses the relate file to convert the porosity value in the iter file to a resistivity value and plots this.
Density	Uses the relate file to convert the porosity value in the iter file to a density value and plots this.

Optimising Results

Below is a list of things to try to optimise the results of the joint inversion.

- Check how that model is fitting the data, and if there are any bad data points or stations that need to be removed.

- If the maximum number of iterations is reached, the inversion can be restarted from one of the iter files (easiest way is to just change the iter file name to STARTUP and away you go).
- Change the initial model parameters in the STARTUP file to ensure that the different initial models all converge to the same final model.
- Once you think the minimum misfit has been reached change the `MISFIT REACHED` value to `1` in corresponding ITERxx.iter file. Then use this as the startup file for another Occam inversion. This will give you the smoothest model at this misfit.
- Try an inversion with a 20% increase in the smallest RMS reached to (generally not required)
- Play around with the item values in the relate file (the temperature values used to calculate fluid conductive has the most effect)

Bibliography

[1] E Haber and D Oldenburg, "Joint inversion: a structural approach", *Inverse Problems*, vol. 13, pp. 63–77, 1997.

[2] J Zhang and F Morgan, "Joint seismic and electrical tomography", *EEGS Proceedings of the Symposium on the Application of Geophysics to Engineering and Environmental Problems*, vol. 10, pp. 391–396, 1997.

[3] J Doetsch, N Linde, I Coscia, S Greenhalgh, and A Green, "Zonation for 3D aquifer characterization based on joint inversions of multimethod crosshole geophysical data", *Geophysics*, vol. 75, pp. G53–G64, 2010.

[4] L Gallardo and M Meju, "Characterization of heterogeneous near-surface materials by joint 2D inversion of dc resistivity and seismic data", *Geophysical Research Letters*, vol. 30, pp. 1658, 2003.

[5] L Gallardo and M Meju, "Joint two-dimensional DC resistivity and seismic travel time inversion with cross-gradients constraints", *Journal of Geophysical Research*, vol. 109, pp. B03311, 2004.

[6] W Telford, L Geldart, and R Sheriff, *Applied Geophysics*, Cambridge University Press, Cambridge, 2nd edition, 1990.

[7] F Santos and S Sultan and P Represas and A El Sorady, "Joint inversion of gravity and geoelectrical data for groundwater and structural investigation: application to the northwestern part of Sinai, Egypt", *Geophysical Journal International*, vol. 165, pp. 705–718, 2006.

[8] M Jegen, R Hobbs, P Tarits, and A Chave, "Joint inversion of marine magnetotelluric and gravity data incorporating seismic constraints: preliminary

results of sub-basalt imaging off the Faroe Shelf", *Earth and Planetary Science Letters*, vol. 282, pp. 47–55, 2009.

[9] S Constable, "Geomagnetism", in *Treatise on Geophysics*, G Schubert and M Kono, Eds. 2007, vol. 5, pp. 237–276, Elsevier, Amsterdam.

[10] M Dobroka, A Gyulai, T Ormos, J Csokas, and L Dresen, "Joint inversion of seismic and geoelectric data recorded in an underground coal mine", *Geophysical Prospecting*, vol. 39, pp. 643–665, 1991.

[11] A Hering, R Misiek, A Gyulai, T Ormos, M Dobroka, and L Dresen, "A joint inversion algorithm to process geoelectric and surface wave seismic data. Part I: basic ideas", *Geophysical Prospecting*, vol. 43, pp. 135–156, 1995.

[12] A Manglik and S Verma, "Delineation of sediments below flood basalts by joint inversion of seismic and magnetotelluric data", *Geophysical Research Letters*, vol. 25, pp. 4015–4018, 1998.

[13] M Kis, "Generalised Series Expansion (GSE) used in DC geoelectric-seismic joint inversion", *Journal of Applied Geophysics*, vol. 50, pp. 401–416, 2002.

[14] L Gallardo-Delgado and M Pérez-Flores and E Gómez-Treviño, "A versatile algorithm for joint 3D inversion of gravity and magnetic data", *Geophysics*, vol. 68, pp. 949–959, 2003.

[15] M Bosch and R Meza and R Jiménez and A Hönig, "Joint gravity and magnetic inversion in 3D using Monte Carlo methods", *Geophysics*, vol. 71, pp. G153–156, 2006.

[16] M Moorkamp, A Jones, and D Eaton, "Joint inversion of teleseismic receiver functions and magnetotelluric data using a genetic algorithm: are seismic velocities and electrical conductivities compatible?", *Geophysical Research Letters*, vol. 34, pp. L16311, 2007.

[17] M Moorkamp, A Jones, and S Fishwick, "Joint inversion of receiver functions, surface wave dispersion, and magnetotelluric data", *Journal of Geophysical Research*, vol. 115, pp. B04318, 2010.

[18] N Linde, A Binley, A Tryggvason, L Pedersen, and A Revil, "Improved hydrogeophysical characterization using joint inversion of cross-hole electrical resistance and ground-penetrating radar traveltime data", *Water Resources Research*, vol. 42, pp. W12404, 2006.

[19] L Gallardo and M Meju, "Joint two-dimensional cross-gradient imaging of magnetotelluric and seismic traveltime data for structural and lithological classification", *Geophysical Journal International*, vol. 169, pp. 1261–1272, 2007.

[20] L Gallardo, "Multiple cross-gradient joint inversion for geospectral imaging", *Geophysical Research letters*, vol. 34, pp. L19301, 2007.

[21] D Colombo, M Mantovani, S Hallinan, and M Virgilio, "Sub-basalt depth imaging using simultaneous joint inversion of seismic and electromagnetic (MT) data: a CRB field study", *SEG Expanded Abstracts*, vol. 27, pp. 2674–2678, 2008.

[22] N Linde, A Tryggvason, J Peterson, and S Hubbard, "Joint inversion of crosshole radar and seismic traveltimes acquired at the South Oyster Bacterial Transport Site", *Geophysics*, vol. 73, pp. G29–G37, 2008.

[23] E Fregoso and L Gallardo, "Cross-gradients joint 3D inversion with applications to gravity and magnetic data", *Geophysics*, vol. 74, pp. L31–L42, 2009.

[24] W Hu, A Abubakar, and T Habashy, "Joint electromagnetic and seismic inversion using structural constraints", *Geophysics*, vol. 74, pp. R99–R109, 2009.

[25] C Tiberi and M Diament and J Déverchère and C Petit-Mariani and V Mikhailov and S Tikhotsky and U Achauer, "Deep structure of the Baikal rift zone revealed by joint inversion of gravity and seismology", *Journal of Geophysical Research*, vol. 108, pp. 2133, 2003.

[26] J Lees and J VanDecar, "Seismic tomography constrained by Bouguer gravity anomalies: applications in Western Washington", *Pure and Applies Geophysics*, vol. 135, pp. 31–52, 1991.

[27] G Hoversten, F Cassassuce, E Gasperikova, G Newman, J Chen, Y Rubin, Z Hou, and D Vasco, "Direct reservoir parameter estimation using joint inversion of marine seismic AVA and CSEM data", *Geophysics*, vol. 71, pp. C1–C13, 2006.

[28] H Tseng and K Lee, "Joint inversion for mapping subsurface hydrological parameters", *SEG Expanded Abstracts*, vol. 20, pp. 1341–1344, 2001.

[29] L Cagniard, "Basic theory of the magneto-telluric method of geophysical prospecting", *Geophysics*, vol. 18, pp. 605–635, 1953.

[30] A Tikhonov, "The determination of the electrical properties of deep layers of the Earths crust", *Doklady Akademii Nauk SSSR*, vol. 73, pp. 295–297, 1950.

[31] F Simpson and K Bahr, *Practical Magnetotellurics*, Cambridge University Press, Cambridge, 2005.

[32] R McPherron, "Magnetic Pulsations: their sources and relation to solar wind and geomagnetic activity", *Surveys in Geophysics*, vol. 26, pp. 545–592, 2005.

[33] K Vozoff, "The magnetotelluric method", in *Electromagnetic methods in applied geophysics - Applications*, M Nabighian, Ed. 1991, vol. 2, pp. 641–711, Society of Exploration Geophysicists, USA.

[34] W Parkinson, *Introduction to Geomagnetism*, Elsevier, Amsterdam, 1983.

[35] D Halliday, R Resnick, and J Walker, *Fundamentals of Physics*, John Wiley and Sons, New York, 4th edition, 1993.

[36] A Orange, "Magnetotelluric exploration for hydrocarbons", *IEEE Proceedings*, vol. 77, pp. 287–317, 1989.

[37] H Bibby, G Caldwell, and C Brown, "Determinable and non-determinable parameters of galvanic distortion in magnetotellurics", *Geophysical Journal International*, vol. 163, pp. 915–930, 2005.

[38] J Ledo, P Queralt, and J Pous, "Effects of galvanic distortion on magnetotelluric data over a three-dimensional regional structure", *Geophysical Journal International*, vol. 132, pp. 295–301, 1998.

[39] R Groom and R Bailey, "Decomposition of magnetotelluric impedance tensors in the presence of local three-dimensional galvanic distortion", *Journal of Geophysical Research*, vol. 94, pp. 1913–1925, 1989.

[40] Z Hashin and S Shtrikman, "A variational approach to the theory of the elastic behaviour of multiphase materials", *Journal of the Mechanics and Physics of Solids*, vol. 11, pp. 12–140, 1963.

[41] Z Hashin and S Shtrikman, "A variational approach to the theory of the effective magnetic permeability of multiphase materials", *Journal of Applied Physics*, vol. 33, pp. 3125–3131, 1962.

[42] Z Hashin and S Shtrikman, "A variational approach to the theory of the elastic behaviour of polycrystals", *Journal of the Mechanics and Physics of Solids*, vol. 10, pp. 343–352, 1962.

[43] H Waff, "Theoretical considerations of electrical conductivity in a partially molten mantle and implications for geothermometry", *Journal of Geophysical Research*, vol. 79, pp. 4003–4010, 1974.

[44] M Luo, J Wood, and L Cathles, "Prediction of thermal conductivity in reservoir rocks using fabric theory", *Journal of Applied Geophysics*, vol. 32, pp. 321–334, 1994.

[45] N Beekmans and L Heyne, "Correlation between impedance, microstructure and compositions of calcia-stabilized zirconia", *Electrochim. Acta*, vol. 21, pp. 303–310, 1976.

[46] J Macdonald, *Impedance Spectroscopy: Emphasing Solid Materials and Systems*, John Wiley and Sons, New York, 1987.

[47] T Shankland and H Waff, "Partial melting and electrical conductivity anomalies in the upper mantle", *Journal of Geophysical Research*, vol. 82, pp. 5409–5417, 1977.

[48] J Warren and A Price, "Flow in heterogeneous porous media", *Transactions AIME (SPEJ)*, vol. 222, pp. 153–183, 1961.

[49] G Archie, "The electrical resistivity log as an aid in determining some reservoir characteristics", *Petroleum Transactions AIME*, vol. 146, pp. 54–62, 1942.

[50] S Arrhenius, "Über den Einfluss des Atmosphärischen Kohlensäurengehalts auf die Temperatur der Erdoberfläche", in *Royal Swedish Academy of Science, Stockholm*, 1896, vol. 22, pp. 1–101.

[51] W Winsauer and W McCardell, "Ionic double-layer conductivity in reservoir rocks", *Transactions AIME*, vol. 198, pp. 129–134, 1953.

[52] J Maxwell, *A Treatise on Electricity and Magnetism*, Clarendon, Oxford, 2nd edition, 1881.

[53] K Wagner, "Explanation of the dielectric fatigue phenomenon on the basis of Maxwell's concept", in *Archiv für Electrotechnik*, H Schering, Ed. 1914, Springer-Verlag, Berlin.

[54] H Fricke, "The Maxwell-Wagner dispersion in a suspension of ellipsoids", *Journal of Physical Chemistry*, vol. 57, pp. 934–937, 1953.

[55] J Watt, G Davies, and R O'Connell, "The elastic properties of composite materials", *Review of Geophysics and Space Physics*, vol. 14, pp. 541–563, 1976.

[56] S Constable, T Shankland, and A Duba, "The electrical conductivity of an isotropic olivine mantle", *Journal of Geophysical Research*, vol. 97, pp. 3397–3404, 1992.

[57] S Constable, "SO3: A new model of olivine electrical conductivity", *Geophysical Journal International*, vol. 166, pp. 435–437, 2006.

[58] A Jones, R Evans, and D Eaton, "Velocity-conductivity relationships for mantle mineral assemblages in Archean cratonic lithosphere based on a review of laboratory data and Hashin-Shtrikman extremal bounds", *Lithos*, vol. 109, pp. 131–143, 2009.

[59] L Hirsch, T Shankland, and A Duba, "Electrical conduction and polaron mobility in Fe-bearing olivine", *Geophysical Journal International*, vol. 114, pp. 36–44, 1993.

[60] R Blakely, *Potential Theory in Gravity and Magnetic Applications*, Cambridge University Press, Cambridge, 1995.

[61] L Nettleton, "Determination of density for reduction of gravimeter observations", *Geophysics*, vol. 4, pp. 176–183, 1939.

[62] R Bell, "Gravity gradiometry", *Scientific American*, vol. 278, pp. 74–79, 1998.

[63] I Newton, *Isaac Newton's Philosophiae Naturalis Principia Mathematica*, A Koyré and I Cohen, Ed., Harvard University Press, Massachusetts, 3rd edition, 1972.

[64] Y Li and D Oldenburg, "3-D inversion of gravity data", *Geophysics*, vol. 63, pp. 109–119, 1998.

[65] P Wynne, *Index of gravity surveys*, Geoscience Australia Publication-Record, Canberra, 2nd edition, 2009.

[66] C Farquharson, M Ash, and H Miller, "Geologically constrained gravity inversion for the Voiseys Bay ovoid deposit", *The Leading Edge*, vol. 27, pp. 64–69, 2008.

[67] A Reid, J Allsop, H Granser, A Millet, and I Somerton, "Magnetic interpretation in three dimensions using Euler deconvolution", *Geophysics*, vol. 55, pp. 80–91, 1990.

[68] L Nettleton, "Regionals, residuals and structures", *Geophysics*, vol. 19, pp. 1–22, 1954.

[69] C Lee, "Compositional variation of density and seismic velocities in natural peridotites at STP conditions: implications for seismic imaging of compositional heterogeneities in the upper mantle", *Journal of Geophysical Research*, vol. 108, pp. 2441, 2003.

[70] T Duffy and D Anderson, "Seismic velocities in mantle minerals and the mineralogy of the upper mantle", *Journal of Geophysical Research*, vol. 94, pp. 1895–1912, 1989.

[71] T Jordan, "Structure and formation of the continental tectosphere", *Journal of Petrology (Special Lithosphere Issue)*, pp. 11–37, 1988.

[72] R Parker, "Understanding inverse theory", *Annual Reviews of Earth and Planetary Sciences*, vol. 5, pp. 35–64, 1977.

[73] J Scales and M Smith, *Introductory Geophyscial Inverse Theory*, Samizat, Colorado, 1994.

[74] R Aster, B Borchers, and C Thurber, *Parameter Estimation and Inverse Problems*, Elsevier, Amsterdam, 2005.

[75] S Greenhalgh, B Zhou, and A Green, "Solutions, algorithms and inter-relations for local minimization search geophysical inversion", *Journal of Geophysics and Engineering*, vol. 3, pp. 101–113, 2006.

[76] A Tarantola and B Vallette, "Generalized non-linear inverse problem solved using the least-squares criterion", *Reviews of Geophysics and Space Physics*, vol. 20, pp. 219–232, 1982.

[77] D Marquardt, "An algorithm for least-squares estimation of nonlinear parameters", *Journal of the Society for Industrial and Applied Mathematics*, vol. 11, pp. 431–441, 1963.

[78] G Backus and J Gilbert, "Numerical applications of a formalism", *Geophysical Journal of the Royal Astronomical Society*, vol. 13, pp. 247–276, 1967.

[79] R Parker, *Geophysical Inverse Theory*, Pinceton University Press, New Jersey, 1994.

[80] S Constable, R Parker, and C Constable, "Occam's inversion: a practical algorithm for generating smooth models from electromagnetic sounding data", *Geophysics*, vol. 52, pp. 289–300, 1987.

[81] R Ellis and D Oldenburg, "Applied geophysical inversion", *Geophysical Journal International*, vol. 116, pp. 5–11, 1994.

[82] A Kirsch, *An Introduction to the Mathematical Theory of Inverse Problems*, Springer, Basel, 1996.

[83] J Shewchuk, "An introduction to the conjugate gradient method without the agonizing pain", Tech. Rep., School of Computer Science, Carnegie Mellon University, http://www.cs.cmu.edu/ jrs/jrspapers.html, 1994.

[84] C Farquharson and D Oldenburg, "A comparison of automatic techniques for estimating the requlariza tion parameter in nonlinear inversion problem", *Geophysical Journal International*, vol. 156, pp. 411–425, 2004.

[85] W Siripunvaraporn, G Egbert, Y Lenbury, and M Uyeshima, "Three-dimensional magnetotelluric inversion: data-space method", *Physics of The Earth and Planetary Interiors*, vol. 150, pp. 3–14, 2005.

[86] R Parker and K Whaler, "Numerical methods for establishing solutions to the inverse problem of electromagnetic induction", *Journal of Geophysical Research*, vol. 86, pp. 9574–9584, 1981.

[87] F Wu, "The inverse problem of magnetotelluric sounding", *Geophysics*, vol. 33, pp. 972–979, 1968.

[88] D Jupp and K Vozoff, "Stable iterative methods for the inversion of geophysical data", *Geophysical Journal of the Royal Astronomical Society*, vol. 42, pp. 957–976, 1975.

[89] J Smith and J Booker, "Magnetotelluric inversion for minimum structure", *Geophysics*, vol. 53, pp. 1565–1576, 1988.

[90] C deGroot Hedlin and S Constable, "Occam's inversion to generate smooth, two-dimensional models from magnetotelluric data", *Geophysics*, vol. 55, pp. 1613–1624, 1990.

[91] W Siripunvaraporn and G Egbert, "An efficient data-subspace inversion method for 2-D magnetotelluric data", *Geophysics*, vol. 65, pp. 791–803, 2000.

[92] J Smith and J Booker, "Rapid inversion of two- and three-dimensional magnetotelluric data", *Journal of Geophysical Research*, vol. 96, pp. 3905–3922, 1991.

[93] W Rodi and R Mackie, "Nonlinear conjugate gradients algorithm for 2-D magnetotelluric inversion", *Geophysics*, vol. 66, pp. 174–187, 2001.

[94] D Jupp and K Vozoff, "Two-dimensional magnetotelluric inversion", *Geophysical Journal of the Royal Astronomical Society*, vol. 50, pp. 333–352, 1977.

[95] T Smith, M Hoversten, E Gasperikova, and F Morrison, "Sharp boundary inversion of 2D magnetotelluric data", *Geophysical Prospecting*, vol. 47, pp. 469–486, 1999.

[96] C deGroot Hedlin and S Constable, "Inversion of magnetotelluric data for 2D structure with sharp resistivity contrasts", *Geophysics*, vol. 69, pp. 78–86, 2004.

[97] C Farquharson, "Constructing piecewise-constant models in multidimensional minimum-structure inversions", *Geophysics*, vol. 73, pp. K1–K9, 2008.

[98] G Newman and D Alumbaugh, "Three-dimensional magnetotelluric inversion using non-linear conjugate gradients", *Geophysical Journal International*, vol. 140, pp. 410–424, 2000.

[99] D Avdeev, "Three-dimensional electromagnetic modelling and inversion from theory to application", *Surveys in Geophysics*, vol. 26, pp. 767–799, 2005.

[100] M Bott, "The use of rapid digital computing methods for direct gravity interpretation of sedimentary basins", *Geophysical Journal of the Royal Astronomical Society*, vol. 3, pp. 63–67, 1960.

[101] D Oldenburg, "The inversion and interpretation of gravity anomalies", *Geophysics*, vol. 39, pp. 526–536, 1974.

[102] Y Chai and W Hinze, "Gravity inversion of an interface above which the density contrast varies exponentially with depth", *Geophysics*, vol. 53, pp. 837–845, 1988.

[103] S Reamer and J Ferguson, "Regularized two-dimensional Fourier gravity inversion method with application to the Silent Canyon Caldera, Nevada", *Geophysics*, vol. 54, pp. 486–496, 1989.

[104] V Barbosa, J Silva, and W Medeiros, "Gravity inversion of basement relief using approximate equality constraints on depths", *Geophysics*, vol. 62, pp. 1745–1757, 1997.

[105] L Pedersen, "Constrained inversion of potential field data", *Geophysical Prospecting*, vol. 27, pp. 726–748, 1979.

[106] R Moraes and R Hansen, "Constrained inversion of gravity fields for complex 3D structures", *Geophysics*, vol. 66, pp. 501–510, 2001.

[107] W Green, "Inversion of gravity profiles by use of a Backus-Gilbert approach", *Geophysics*, vol. 40, pp. 763–772, 1975.

[108] B Last and K Kubik, "Compact gravity inversion", *Geophysics*, vol. 48, pp. 713–721, 1983.

[109] A Guillen and V Menichetti, "Gravity and magnetic inversion with minimization of a specific functional", *Geophysics*, vol. 49, pp. 1354–1360, 1984.

[110] M Talwani, J Worzel, and M Landisman, "Rapid gravity computations for two-dimensional bodies with application to the Mendocino submarine fracture zone", *Journal of Geophysical Research*, vol. 64, pp. 49–59, 1959.

[111] M Talwani and M Ewing, "Rapid computation of gravitational attraction of three-dimensional bodies of arbitrary shape", *Geophysics*, vol. 25, pp. 203–225, 1960.

[112] D Nagy, "The gravitational attraction of a right rectangular prism", *Geophysics*, vol. 31, pp. 362–371, 1966.

[113] C Barnett, "Theoretical modeling of the magnetic and gravitational fields of an arbitrarily shaped three-dimensional body", *Geophysics*, vol. 41, pp. 1353–1364, 1976.

[114] M Okabe, "Analytical expressions for gravity anomalies due to homogeneous polyhedral bodies and translations into magnetic anomalies", *Geophysics*, vol. 44, pp. 730–741, 1979.

[115] R Parker, "The rapid calculation of potential anomalies", *Geophysical Journal of the Royal Astronomical Society*, vol. 31, pp. 447–455, 1972.

[116] B Russell, *History of Western Philosophy*, George Allen and Unwin Ltd., London, 1946.

[117] P Wannamaker, J Stodt, and L Rijo, "A stable finite-element solution for two-dimensional magnetotelluric modeling", *Geophysical Journal of the Royal Astronomical Society*, vol. 88, pp. 277–296, 1987.

[118] W Press, S Teukolsky, W Vetterling, and B Flannery, *Numerical Recipes in Fortran*, Cambridge University Press, Cambridge, 2nd edition, 1992.

[119] M Oristaglio and M Worthington, "Inversion of surface and borehole electromagnetic data for two-dimensional electrical conductivity models", *Geophysical Prospecting*, vol. 28, pp. 633–657, 1980.

[120] P de Lugao and P Wannamaker, "Calculating the two-dimensional magnetotelluric Jacobian in finite elements using reciprocity", *Geophysical Journal International*, vol. 127, pp. 806–810, 1996.

[121] S Thiel and G Heinson, "Crustal imaging of a mobile belt using magnetotellurics: an example of the Fowler Domain in South Australia", *Journal of Geophysical Research*, vol. 115, pp. B06102, 2010.

[122] S Constable, K Key, and L Lewis, "Mapping offshore sedimentary structure using electromagnetic methods and terrain effects in marine magnetotelluric data", *Geophysical Journal International*, vol. 176, pp. 431–442, 2009.

[123] A Jones and J Craven, "The North American Central Plains conductivity anomaly and its correlation with gravity, magnetics, seismic, and heat flow data in the Province of Saskatchewan", *Physics of the Earth and Planetary Interiors*, vol. 60, pp. 196–194, 1990.

[124] B Tapley, S Bettadpur, M Watkins, and C Reigber, "The gravity recovery and climate experiment: mission overview and early results", *Geophyscial Research Letters*, vol. 31, pp. L09607, 2004.

[125] National Collaborative Research Infrastructure Strategy (AuScope), "Investment plan for the research capability: Structure and evolution of the australian continent", Tech. Rep., The Australian Federal Government, http://www.auscope.org.au/res/file/downloads/auscope/AuScopePlan.pdf, 2010.

[126] S Constable and C Weiss, "Mapping thin resistors and hydrocarbons with marine EM methods: insights from 1D modeling", *Geophysics*, vol. 71, pp. G43–G51, 2006.

[127] P Wright, S Ward, H Ross, and R West, "State-of-the-art geophysical exploration for geothermal resources", *Geophysics*, vol. 50, pp. 2666–2699, 1985.

[128] L Nettleton, "Geophysics, geology and finding oil", *Geophysics*, vol. 14, pp. 273–289, 1949.

[129] E Hinze, G Will, and L Cemič, "Electrical conductivity measurment on synthetic olivines and on olivine, enstatite, and diopside from Dreiser Weiher, Eifel (Germany) under defined thermodynamic activities as a function of temperature and pressure", *Physics of the Earth and Planetary Interiors*, vol. 25, pp. 245–254, 1981.

[130] M Rider, *The Geological Interpretation of Well Logs*, Whittles Publishing Services, United Kingdom, 1986.

[131] J Hanor, "Origin of saline fluids in sedimentary basins", in *Geofluids: Origin, Migration and Evolution of Fluids in Sedimentary Basins*, J Parnell, Ed. 1994, vol. 78, pp. 151–174, Geological Society of London, Special Publications.

[132] J Adams and S Bachu, "Equations of state for basin geofluids: algorithm review and intercomparison for brines", *Geofluids*, vol. 2, pp. 257–271, 2002.

[133] M Batzle and Z Wang, "Seismic properties of pore fluids", *Geophysics*, vol. 57, pp. 1396–1408, 1992.

[134] R Sheriff, *Encyclopedic Dictionary of Applied Geophysics*, Society of Exploration Geophysicists, USA, 4th edition, 2002.

[135] W Winsauer, H Shearin, P Masson, and M Williams, "Resistivity of brine-saturated sands in relation to pore geometry", *Bulletin of the American Association of Petroleum Geologists*, vol. 36, pp. 253–277, 1952.

[136] G Keller, "Rock and mineral properties", in *Electromagnetic Methods in Applied Geophysics Theory*, M Nabighian, Ed. Tulsa, Okla 1987, vol. 1, pp. 13–51, Society of Exploration Geophysicists, USA.

[137] D Kennedy, "The porosity-water saturation-conductivity relationship: an alternative to Archie's model", *Petrophysics*, vol. 48, pp. 335–361, 2007.

[138] B Nesbitt, "Electrical resistivities of crustal fluids", *Journal of Geophysical Research*, vol. 98, pp. 4301–4310, 1993.

[139] A Quist and W Marshall, "Electrical conductances of aqueous sodium chloride solutions from 0 to 800 ° and at pressures to 4000 bars", *The Journal of Physical Chemistry*, vol. 72, pp. 684–703, 1968.

[140] P Dickey, "Increasing concentration of subsurface brines with depth", *Chemical Geology*, vol. 4, pp. 361–370, 1969.

[141] K Becker and R Von Herzen and T Francis and R Anderson and J Honnorez and A Adamson and J Alt and R Emmermann and P Kempton and H Kinoshita and C Laverne and M Mottl and R Newmark, "In situ electrical resistivity and bulk porosity of the oceanic crust Costa Rica Rift", *Nature*, vol. 300, pp. 594–598, 1982.

[142] R Von Herzen and T Francis and K Becker, "In situ large-scale electrical resistivity of ocean crust, hole 504b", *DSDP Initial Reports*, vol. 69, pp. 237–244, 1983.

[143] P Jackson, D Taylor-Smith, and P Stanford, "Resistivity-porosity-particle shape relationships for marine sands", *Geophysics*, vol. 43, pp. 1250–1268, 1978.

[144] G Keller and F Frischknecht, *Electrical methods in geophysical prospecting*, Pergamon Press, Oxford, 1966.

[145] A Duba, A Piwinskii, M Santor, and H Weed, "The electrical conductivity of sandstone, limestone and granite", *Geophysical Journal of the Royal Astronomical Society*, vol. 53, pp. 583–597, 1978.

[146] M Wyllie, *The Fundamentals of Well Log Interpretation*, Academic Press, New York, 3rd edition, 1963.

[147] Ó Flóvenz and L Georgsson and K Árnason, "Resistivity structure of the upper crust in Iceland", *Journal of Geophysical Research*, vol. 90, pp. 10136–10150, 1985.

[148] V Spichak and A Manzella, "Electromagnetic sounding of geothermal zones", *Journal of Applied Geophysics*, vol. 68, pp. 459–478, 2009.

[149] P Glover, M Hole, and J Pous, "A modified Archie's Law for two conducting phases", *Earth and Planetary Science Letters*, vol. 180, pp. 369–383, 2000.

[150] J Roberts and J Tyburczy, "Partial-melt electrical conductivity: influence of melt composition", *Journal of Geophysical Research*, vol. 104, pp. 7055–7065, 1999.

[151] R Hyndman and M Drury, "Physical-properties of oceanic basement rocks from deep drilling on Mid-Atlantic Ridge", *Journal of Geophysical Research*, vol. 81, pp. 4042–4052, 1976.

[152] W Brace, A Orange, and T Madden, "Relation of elastic properties of rocks to fabric", *Journal of Geophysical Research*, vol. 70, pp. 5669–5678, 1965.

[153] M Giles, S Indrelid, and D James, "Compaction - the great unknown in basin modelling", in *Basin Modelling: Practice and Progress*, S Düppenbecker and J Iliffe, Ed. 1998, vol. 141, pp. 15–43, Geological Society of London, Special Publications.

[154] M Tingay, R Hillis, R Swarbrick, C Morley, and A Damit, "Origin of overpressure and pore-pressure prediction in the Baram province, Brunei", *Bulletin of the American Association of Petroleum Geologists*, vol. 93, pp. 51–74, 2009.

[155] J Atkins and E McBride, "Porosity and packing of Holocene river, dune, and beach sands", *Bulletin of the American Association of Petroleum Geologists*, vol. 76, pp. 339–355, 1992.

[156] D Beard and P Weyl, "Influence of texture on porosity and permeability of unconsolidated sand", *Bulletin of the American Association of Petroleum Geologists*, vol. 57, pp. 345–369, 1973.

[157] G Dickinson, "Geological aspects of abnormal reservoir pressures in Gulf Coast Louisiana", *Bulletin of the American Association of Petroleum Geologists*, vol. 37, pp. 410–432, 1953.

[158] W Galloway, "Deposition and the diagenetic alteration of sandstone in northeast Pacific arc-related basins. Implications for graywacke genesis", *Bulletin of the Geological Society of America*, vol. 85, pp. 379–390, 1974.

[159] P Nagtegaal, "Sandstone instability as a function of burial diagenesis", *Journal of the Geological Society of London*, vol. 135, pp. 101–105, 1978.

[160] B Baldwin and C Butler, "Compaction curves", *Bulletin of the American Association of Petroleum Geologists*, vol. 69, pp. 622–626, 1985.

[161] D Falvey and M Middleton, "Passive continental margins: evidence for a pre-break-up deep crustal metamorphic subsidence mechanism", in *Proceedings 26th International Geological Congress, Geology of Continential Margins Symposium*, 1981, pp. 103–114.

[162] L Athy, "Density, porosity and compaction of sedimentary rocks", *Bulletin of the American Association of Petroleum Geologists*, vol. 14, pp. 1–24, 1930.

[163] J Sclater and P Christie, "Continental stretching: an explanation of the post-mid-Cretaceous subsidence of the central North Sea basin", *Journal of Geophysical Research*, vol. 85, pp. 3711–3739, 1980.

[164] P Carrion, "Generalized non-linear elastic inversion with constraints in model and data spaces", *Geophysical Journal*, vol. 96, pp. 151–162, 1989.

[165] B Zhou, S Greenhalgh, and C Sinadinovski, "Iterative algorithm for the damped minimum norm, least-squares and constrained problem in seismic tomography", *Exploration Geophysics*, vol. 23, pp. 497–505, 1992.

[166] P Stark and R Parker, "Bounded-variable least-squares: an algorithm and applications", *Computational Statistics*, vol. 10, pp. 129–141, 1995.

[167] Y Li and D Oldenburg, "Fast inversion of large-scale magnetic data using wavelet transforms and logarithmic barrier method", *Geophysical Journal International*, vol. 152, pp. 251–265, 2003.

[168] "Occam 2D MT File Format Notes", Tech. Rep., Marine EM Laboratory, Scripps Institution of Oceanography, http://marineemlab.ucsd.edu/Projects/Occam/index.html, 2006.

[169] "A guide to using winglink", Tech. Rep., Geosystems SRL, Italy, 2002.

[170] K Schwalenberg, V Rath, and V Haak, "Sensitivity studies applied to a two-dimensional resistivity model from the Central Andes", *Geophysical Journal International*, vol. 150, pp. 673–686, 2002.

[171] P Wannamaker, G Hohmann, and S Ward, "Magnetotelluric responses of three-dimensional bodies in layered earths", *Geophysics*, vol. 49, pp. 1517–1533, 1984.

[172] E Athanasiou, P Tsourlos, C Papazachos, and G Tsokas, "Combined weighted inversion of electrical resistivity data arising from different array types", *Journal of Applied Geophysics*, vol. 62, pp. 124–140, 2007.

[173] N Neumann, M Sandiford, and J Foden, "Regional geochemistry and continental heat flow: implications for the origin of the South Australian heat flow anomaly", *Earth and Planetary Science Letters*, vol. 183, pp. 107–120, 2000.

[174] R Hillis, M Hand, S Mildren, J Morton, P Reid, and S Reynolds, "Hot dry rock geothermal exploration in Australia", *PESA Eastern Australasian Basins Symposium II*, pp. 413–421., 2004.

[175] P Rogers, J Lindsay, N Alley, S Barnett, K Lablack, and G Kwitko, "The geology of South Australia. Vol. 2, The Phanerozoic: Tertiary: Southern Marine Basins: Murray Basin", *South Australia Geological Survey Bulletin*, vol. 54, pp. 157–163, 1995.

[176] R Thorton, "Hydrocarbon potential of western Murray Basin and infrabasins. South Australia", *South Australia Geological Survey Quarterly Geological Notes*, vol. 44, pp. 5–11, 1974.

[177] N Alley, "The geology of South Australia. Vol. 2, The Phanerozoic: Late Palaeozoic: Nadda Basin", *South Australia Geological Survey Bulletin*, vol. 54, pp. 70, 1995.

[178] P Rogers, J Lindsay, N Alley, S Barnett, K Lablack, and G Kwitko, "The geology of South Australia. Vol. 2, The Phanerozoic: Mesozoic: Jurasic-Cretaceous Epicratonic Basins: Berri Basin", *South Australia Geological Survey Bulletin*, vol. 54, pp. 127–129, 1995.

[179] Tasman Oil Pty. Ltd., "Renmark seismic survey final report reconnaissance photogeomorphic evaluation of a part of OEL 35", Tech. Rep., Primary Industries and Resources South Australia Envelope No. ENV00532, 1965.

[180] Beach Petroleum NL, "1966 Murray Basin provinces seismic survey, final report", Tech. Rep., Primary Industries and Resources South Australia Envelope No. ENV00639, 1966.

[181] Associated Australian Oilfileds NL, "1967 Hamley seismic survey, final report", Tech. Rep., Primary Industries and Resources South Australia Envelope No. ENV00824, 1967.

[182] International Mining Corporation NL, "1985 Overland corner (OC85) seismic survey, final report", Tech. Rep., Primary Industries and Resources South Australia Envelope No. ENV06331, 1985.

[183] E Craven, "Crustal imaging of prospective geothermal basins using magnetotellurics: a case study of the Renmark Trough in South Australia", *B.Sc Honours Thesis, The University of Adelaide*, 2009.

[184] A Chave and D Thomson, "Bounded influence estimation of magnetotelluric response functions", *Geophysical Journal International*, vol. 157, pp. 988–1006, 2004.

[185] T Caldwell, H Bibby, and C Brown, "The magnetotelluric phase tensor", *Geophysical Journal International*, vol. 158, pp. 457–469, 2004.

[186] A Fabris, "North-western Murray Basin geological synthesis, South Australia", Tech. Rep., Primary Industries and Resources South Australia Report Book 2003/13, 2003.

[187] T Kalscheuer and L Pedersen, "A non-linear truncated SVD variance and resolution analysis of two-dimensional magnetotelluric models", *Geophysical Journal International*, vol. 169, pp. 435–447, 2007.

[188] W Menke, *Geophysical Data Analysis: Discrete Inverse Theory*, Academic, New York, 1984.